# Morphodynamics of Sand Mounds in Shallow Flows

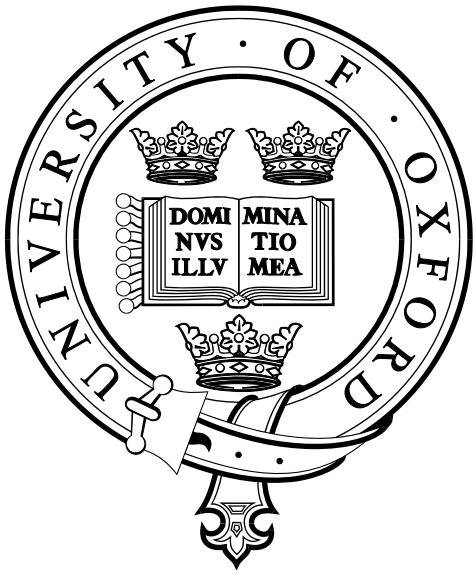


**M. Isabel García-Hermosa**

**St Edmund Hall**

**Hilary Term, 2008**

*Thesis submitted in partial fulfilment for the degree of Doctor of Philosophy at the University of Oxford*

**Department of Engineering Science**

**University of Oxford**

We shall not cease from exploration,
and the end of all our exploring
will be to arrive where we started
and know the place for the first time

*Little Gidding*, T. S. Elliot

# Morphodynamics of Sand Mounds in Shallow Flows

Thesis submitted in partial fulfilment for the degree of
Doctor of Philosophy at the University of Oxford

By M. Isabel García-Hermosa, St Edmund Hall, Hilary Term 2008

## Abstract

Large-scale bed features are often encountered in coastal waters, and include sandbanks and spoil heaps. The morphodynamic development of such features involves complicated nonlinear interactions between the flow hydrodynamics, sediment transport, and bed profile. Numerical modelling of the morphodynamic evolution and migration of large-scale bed features is necessary in order to understand their long-term behaviour in response to changing environmental conditions.

This thesis describes detailed measurements of the morphodynamics of sand mounds in unidirectional and oscillatory (tidal) flows, undertaken at the U.K. Coastal Research Facility (UKCRF). High quality data were collected, including water velocities, water levels and overhead images. The parameters tested are: three types of mound shape (circular and elliptical in plan shape, and Gaussian, cosine and triangular in cross-section); underlying fixed or mobile bed conditions; and initial crest height (submerged, surface-touching and surface-piercing). Peak flow velocities are about 0.5 m/s, the sand median grain size is 0.454 mm, and transport occurring mostly as bedload. When analysing the data, the bed contours are determined by digitising the shoreline at different water levels. From these plots, the volume, height, and centroid position of the mound are calculated. A large-scale fit method, based on a Gaussian function has been used to separate small-scale ripples from the large-scale bed structure during the evolution of an isolated sand mound or spoil heap. The bed profile after the ripples are removed is comparable to typical predictions by shallow-flow numerical solvers. The UKCRF experiments investigated the morphodynamic response of a bed mound to hydrodynamic forcing: shape changes, migration rates, volume decay and sediment transport rates.

The measured migration rate and decay of a submerged sand mound in the UKCRF are found to be in satisfactory agreement with results from various theoretical models, such as the analytical solution derived by De Vriend. Numerical predictions of mound evolution by a commercial code, PISCES, are also presented for a fully submerged sand mound; the bed evolution is reasonably similar to that observed in the UKCRF.

The data provided as a result of the research reported in this thesis provide insight into the behaviour of sand mounds in steady and unsteady flows at laboratory scale, and should also be useful for benchmark (validation) purposes to numerical modellers of large-scale morphodynamics.

# ACKNOWLEDGMENTS

First and foremost, I would like to thank my supervisors, Professors Alistair Borthwick, Richard Soulsby and Paul Taylor, not only for giving me the opportunity to work with them, but also for all I have learned from them, both academically and personally. I will always be in debt with them for their guidance, kindness, patience and encouragement; and for sharing their wisdom, suggestions and stories with me during these years.

I am very grateful to Dr Jingmin Huang, for her contributions to the project. I must thank the research partners from the Mechanical, Aerospace and Civil Engineering Department in the University of Manchester: Professor Peter Stansby for his contributions to the project and his incessant drive, and Dr. Jianguo Zhou for his cooperation during the experimental phase.

I wish to thank the staff from HR Wallingford that made the experiments in the Reversing Flume and the UKCRF possible, Dr James Sutherland, Tom Stevenson, John Collins and Phil Small. Their useful suggestions and timely help were invaluable.

Thanks to the Engineering and Physical Science Research Council (EPSRC) for the funding via grants GR/S73396 and GR/S73402.

I am very grateful I had the chance to work with the Coast and Estuaries Group in HR Wallingford. A great bunch that helped me deal with *the indomitable*, albeit user friendly Telemac suit. Their generosity, kindness and warmth took me through the writing up.

A very warm thank you goes to all (current and former) colleagues from the Ocean Engineering and Dynamics Group. I wish them all the best. Special thanks are due to my office mates.

I could never thank enough those friends (present, gone and lost on the way) in Oxford, the UK, Spain and the rest of the world that put up with me during these years, and were there in the darkest and happiest hours, for discussions (always lively), decision making, or for fun. Special mentions go to: Celine, Virginie, Lucy, Tania, Irene and Haris, Lorraine & the gang, Los Payasos Borrachos, Regina and Belen, Schini & Yoko, Belen, MCR colleagues, HR friends, housemates, etc.

Last but not least, there is not much I can write to demonstrate my gratitude to my parents, siblings and family. Without them I would not be here today, and certainly I could not have finished my doctoral studies. I will also be forever grateful to those that had a determinant influence in my life, and are not here any more. I hope they would be proud.

**NOTATION LIST**

| | |
|---|---|
| $A$ | generic bedload equation coefficient |
| $A_N$ | Nielsen bedload equation coefficient |
| $A_{MPM}$ | Meyer-Peter-Müller bedload equation coefficient |
| $a$ | cylinder radius [L] |
| $d$ | sieve diameter of grains [L] |
| $d_{50}$ | median grain diameter [L] |
| $F_r$ | Froude number |
| $g$ | acceleration due to gravity [$L/T^2$] |
| $H$ | undisturbed water depth [L] |
| $H$ | global measure of the height of the large scale fit of the mound [L] |
| $h(t)$ | height of the mound [L] |
| $h_{max}$ | initial crest height of the mound in morphodynamic timescale (Hudson *et al.*, 2005) [L] |
| $h_0$ | initial crest height [L] |
| $k_s$ | Nikuradse equivalent sand grain roughness |
| $L_x$ | global measure for width of the large scale fit of the mound in the stream-wise direction [L] |
| $L_y$ | global measure for width of the large scale fit of the mound in the cross-flow direction [L] |
| $m$ | velocity coefficient in transport equation |
| $n$ | ($s$,$n$) coordinate reference system for De Vriend's analytical solution |
| $q_0$ | initial flow discharge [$L^3/T$] |
| $q_b$ | volumetric sediment transport [$L^3/LT$] |
| $R_e$ | Reynolds Number |
| $r$ | distance from the cylinder [L] |
| $s$ | ratio of density between grain and water |
| $s$ | ($s$,$n$) coordinate reference system for De Vriend's analytical solution |
| $s_x$ | measure of the inverse width of the mound in the stream-wise direction [1/L] |
| $s_y$ | measure of the inverse width of the mound in the cross-flow direction [1/L] |
| $S_{tot}$ | sediment transport from the de Vriend's analytical solution [$L^3/LT$] |
| $T_{m1}$ | Hudson *et al.* (2005) morphodynamic timescale [T] |
| $T_{m2}$ | Huang *et al.* (2008) morphodynamic timescale [T] |
| $T_E$ | elapsed time [T] |
| $T_v$ | experimental morphodynamic timescale for the decay of volume [T] |
| $T_{va}$ | analytical morphodynamic timescale for the decay of volume [T] |
| $T_h$ | morphodynamic timescale (RF experiments) [T] |
| $T_0$ | oscillation time period [T] |
| $t$ | Time [T] |
| $U_{cr}$ | velocity corresponding to the threshold for sediment motion [L/T] |

| | |
|---|---|
| $\overline{U}$ | depth averaged velocity [L/T] |
| $u$ | velocity component in $x$-axis [L/T] |
| $u_r$ | radial velocity component (polar coordinates) [L/T] |
| $u_*$ | friction velocity |
| $u_\theta$ | tangential velocity component (polar coordinates) [L/T] |
| $u_\infty$ | velocity of undisturbed flow [L/T] |
| $u_0$ | velocity of undisturbed flow [L/T] |
| $V$ | depth averaged flow velocity [L/T] |
| $v$ | velocity component in $y$-axis [L/T] |
| $w_s$ | settling velocity of isolated grains [L/T] |
| $z_0$ | bed roughness length [L] |
| $\alpha$ | spreading angle from star-shape feature in De Vriend's analytical solution [deg] |
| $\varepsilon$ | bed porosity |
| $\theta$ | Shields parameter |
| $\theta_{cr}$ | critical Shields parameter |
| $\kappa$ | von Kármán constant (= 0.40) |
| $\nu$ | kinematic viscosity of water [$L^2/T$] |
| $\nu_{00}$ | global measure of the volume of the large scale fit of the mound |
| $\rho$ | density of water [$M/L^3$] |
| $\rho_s$ | grain density |
| $\tau_{cr}$ | critical bed shear stress [Mass /$L^2$ $T^2$] |
| $\phi$ | angle of velocity vector in polar coordinates [rad] |
| $\Psi$ | stream function in polar coordinates |
| $\Phi$ | dimensionless transport rate |
| $\xi$ | parameter describing the star-shape feature in De Vriend's analytical solution |
| $\eta$ | parameter describing the star-shape feature in De Vriend's analytical solution |

# CONTENTS

# 1. INTRODUCTION and BACKGROUND

## *1.1. Introduction*

The seabed is a dynamic environment, changing constantly with the forcing of waves and currents. When the flow velocity is sufficiently large, the near bed sediment becomes mobile and may be moved; creeping, rolling, hopping (saltating) or even in suspension. The bed then changes shape due to deposition or erosion of the sediment. These modify the flow field. As early as 1887 Osborne Reynolds built a model of an idealised estuary and simulated the effect of tides on the morphology of an estuary (developing channels and shoals) to improve the understanding of flow-sediment interactions (Reynolds, 1887).

Many large-scale coastal bed features have been generated by mechanisms not present today. Examples include sandbanks that originated during periods when the sea-level was lower or when the dominant hydrodynamic conditions were different. These large-scale features are maintained by, and evolve with, the combined present-day hydrodynamic forcing (relaxation effect, timescales of evolution). Other features are man-made, such as spoil heaps or dredged pits. If their spatial scales are large, such features may affect the hydrodynamics over and around them. The resulting changes in morphology can then trigger further dramatic variations in the regional hydrodynamic field (Roos, 2004), perhaps affecting the propagation of the tide over them.

An understanding of the interaction of large-scale bed features with the hydrodynamic field has become increasingly relevant due to the following factors:

- The increased pressure due to human activities in the estuarine, coastal and near-shore areas. These regions hold most of the world's population, valuable assets and infrastructures, and are very sensitive to changes (environmental, hydrodynamic or meteorological).
- Changes in climate that will have an effect on sea levels, making land near the coast more prone to flooding. Increased storminess may also occur, adding to the threat of inundation; and
- Scientific and technological advances: (i) that facilitate in-depth studies of processes; (ii) larger computational power to study complex problems; and (iii) the shift of interest to marine renewable energies and their effect on the seabed.

Anthropogenic activities taking place in coastal and estuarine environments that impact on morphodynamics include dredging and the construction of coastal structures. Dredging activities often involve maintenance of navigational channels, as well as aggregate dredging (e.g. on sandbanks). Other human activities include civil engineering construction of structures that are either protective (e.g breakwaters, groynes, seawalls, beach recharges, etc.) or functional (e.g. offshore wind farms, tidal barrages, renewable energy devices, bridge piers, etc.).

Future changes in sensitive riverine, estuarine and coastal regions may have important economic and sociological consequences. A proper risk analysis is needed to provide effective countermeasures, warning systems and insurance to minimise potential social and economic costs. The impacts of large-scale morphodynamic change need to be assessed, minimised and mitigated to protect and maintain the value of the infrastructure/asset. To this end, it is paramount to understand the role of large-scale bed features within the morphodynamic system. For each proposed scheme it is essential to investigate the before (baseline) and after (effect of proposed changes) scenarios. During the evaluation of a typical proposal it is necessary to predict accurately what will be the outcome at the various phases of the development and at the final stage.

Considering the present state of knowledge, there is a need for improved prediction tools for large-scale morphodynamic evolution. Numerical models, if reliable, can provide comprehensive information regarding (short- and mid-term) predictions for hydrodynamic and morphodynamic problems in large areas. Although hydrodynamic modelling of tidal flows is quite mature; a considerable amount of further understanding is still required about the interaction of hydrodynamics, sediment transport and bed morphology. Furthermore this interaction becomes even more complex when human intervention is taken into account. Experimental research is needed to advance the present understanding and knowledge of large-scale morphodynamics, and to provide a high-quality benchmark dataset for the purpose of numerical model validation.

## *1.2. Background*

The term *morphodynamics*, as it is interpreted in this thesis refers to the change of shape of sediment features in fluvial, estuarine or coastal beds due to the hydrodynamic processes taking place.

### 1.2.1. Morphodynamic features in detail: spoil heaps and sandbanks

Coastal and estuarine morphodynamic features are affected by waves and/or currents. Although the work presented in this thesis deals with current-dominated processes (for simplicity of interpretation), this section also mentions features caused by wave forcing. Most of the following generic morphodynamic features, some rhythmic, result from complex interactions between waves, currents and the bed topography. Certain morphodynamic features occur where and when currents are dominant: ripples, mega-ripples, sand waves, dunes, single or multiple sandbanks, shoreface-connected ridges. Other features in the near-shore regions result from wave forcing such as: wave ripples, beach cusps, crescentic bars, oblique and shore parallel bars with rip channels, spits, capes, ridges and long bed waves. It is not clear whether these are due to external forcing or self-organisation (Battjes, 2005). All the above-mentioned features have characteristic spatial and temporal scales of evolution. From Dodd *et al*. (2003), Table 1.1 presents characteristic wavelengths, heights, migration speeds and evolution timescales of rhythmic bedforms in coastal seas.

Spoil heaps and sandbanks are two types of morphodynamic features on which the present research is focused. These display different morphological characteristics, origins and scales of evolution (temporal and spatial). Both these features can be found in various hydrodynamic conditions.

Spoil heaps are disposed material bi-product from dredging operations. As such, the material may be transported to a specific licensed site (e.g. in the UK) where its impact will be minimised. Typically the disposal sites are in shallow water (not too far from the dredging site, for economic reasons) with sufficiently large local currents to disperse the sediment. The grain size and characteristics of the sediment may be different to that of the underlying bed material. Spoil heap shapes and sizes vary greatly, typically spoil heaps are fully submerged. There is little scientific literature on the dispersion of spoil heaps, and their long-term evolution. To date, monitoring of dredged spoil heaps has been infrequent.

Sandbanks are quintessential bed features of estuaries, coastal areas and shallow-seas where there is sufficient supply of sediment and the currents are strong enough to shift it (Off, 1963), and are the largest-scale bedforms. They have been described and studied for the last fifty years (Off, 1963; Allen, 1968; Stride, 1982; Dyer and Huntley, 1996; Whitehouse, 2001). The characteristics of sandbanks vary with their location, origin and classification. For instance linear sandbanks range up to tens of kilometres in length, have widths of the order of kilometres, and heights of tens of metres with the crest generally found orientated at an angle to the main flow direction and a few metres under the water

surface. The timescales of change may vary: some sandbanks may respond to short-lived extreme events, others may remain moribund offshore for hundreds of years (Dyer and Huntley, 1999). The grain size distribution varies spatially, from crests to troughs. Stride (1982) argued that moribund sandbanks are composed of sand and some shell material, and that the coarser material with mud on top is found on the troughs and lower flanks. Dronkers (2005) noted that active sandbanks have coarser sediment on the crests and finer in the troughs. Usually, the orientation of the crest of the bank is counter-clockwise in the northern hemisphere, with a clockwise current generated around the bank. However, observations in the Northern Hemisphere of both clockwise (e.g. the Sandettie bank and the Zeeland banks) and counter-clockwise rotation (e.g. Norfolk banks) with respect to the main flow direction have proven this is not always the case. Offshore sandbanks protect shorelines from wave action especially in storm conditions. Changes to sandbanks and the nearby wave characteristics have an obvious knock-on effect on coastal defence structures. Conversely, the addition of man-made structures may drastically affect the morphological evolution of sandbanks, and amplify the impacts on the adjacent coastline (Williams *et al*., 2000). In certain cases, coastal defences might become obsolete; in others, new defences would need to be constructed.

### 1.2.2. Present knowledge of the evolution of spoil heaps

As mentioned in Section 1.2.1 few scientific references are available regarding the evolution of spoil heaps (also called dredge disposal sites). There is generic reference knowledge regarding aggregate sites licensed in the English Channel (Posford Haskoning, 2003). Wienberg and Hebbeln (2005) investigated the effect of dredged material disposed over a dune system in the German Bight. The disposed material infilled the troughs of the dunes and buried certain dunes. The system was monitored and regenerated within a few months, by evolving to a new dynamic equilibrium state. Drapeau *et al*. (2003) studied a disposal place in the St Laurence river/estuary, following the evolution of the material with bathymetric data and sea bed sampling.

### 1.2.3. Present knowledge of sandbanks

Dyer and Huntley (1999) and Whitehouse (2001) reviewed the state of knowledge of sandbanks. During the last twenty years a concerted effort has been made to study such large-scale features, and understand their interactions with the coastal systems to which they belong. Part of this effort has been a series of research projects funded by the European

Union that investigate sandbanks, or subjects related to sandbanks: RESECUSED[1], CSTAB[2], STARFISH[3], COAST3D[4], HUMOR[5], SANDPIT[6], EUMARSAND[7], and in the UK, the BLINKS[8] project. Currently, in the UK, there are programmes that involve the systematic surveying of three banks: East Hoyle, Nash and Helwick Banks. Figure 1.1 presents the distribution of large-scale bedforms in the Southern North Sea, and English Channel areas (Dyer and Huntley, 1996).

**Origins and classification**

Depending on their origin and evolution, sandbanks can be found in shallow seas, estuary mouths or along the coast, in such instances where the currents are strong enough to mobilise sediment and there is sufficient sediment supply (Off, 1963). Williams *et al.* (2000) and Off (1963) identified the worldwide distribution of sandbanks, and Velegrakis *et al*. (2000) listed existing sandbanks in European shelf waters. Hu and Cooke (1997) compiled a database of sandbanks along the coasts of England and Wales. In 1996 Dyer and Huntley presented a comprehensive study of the then state-of-the-art knowledge. They described previous classifications of sandbanks by Swift (1975), Belderson (1986), and Pattiaratchi and Collins (1987), and proposed their own classification. Dyer and Huntley (1996) consider there to be three distinct types of sandbanks, classified according to the origin and evolutionary state (Table 1.2).

Dyer and Huntley (1996, 1999) also described a selection of theories of sandbank formation and maintenance: seabed stability analysis (which relates to Type I banks, e.g. Huthnance, 1982 and Hulscher *et al*., 1993), vorticity from shoreline irregularity (that applies to Type 3 banks), and ebb and flood channels in estuary mouths (relevant to Type II banks). Dyer and Huntley also provided an introduction to the main effects of the sandbank on local hydrodynamic processes.

Whitehouse (2001) (as part of Offshore Sand Banks: Basic Processes and Effects on Long-term Coastal Morphodynamics, funded by MAFF, UK) provided a review of the

[1] RESECUSED (1990-1992) Relationship between sea or currents and sediment mobility in the South-North Sea [MAST I]
[2] CSTAB (1992-1995) Circulation and Sediment Transport around Banks [MAST II]
[3] STARFISH (1993-1995) [MAST II]
[4] COAST3D (1997-2001) Coastal Study of 3-dimensional sand transport processes and morphodynamics.
[5] HUMOR (2002-2004) Human Interaction with Large Scale Coastal Morphological Evolution [EU-FP5]
[6] SANDPIT (2002-2005) Sand Transport and Morphology of Offshore Sand Mining Pit/Areas
[7] EUMARSAND (2002-2005) European Sand and Gravel Resources Evaluation and Environmental Impact of Extraction [EU-FP5]
[8] BLINKS (2005-2007) Beach Links to Sandbanks [NERC]

methods used to investigate sandbanks, analysed the deficiencies of these methods and posed a set of questions regarding the knowledge of sandbank evolution. The report stated that present understanding regarding prediction of long-term evolution was limited, and pointed at the lack of information regarding the biological effects of changes in sandbank morphology. It provided a brief but useful description of factors involved in the short-, medium- and long-term sandbank evolution and their interaction with the coastline; a methodology for the assessment of the role of sandbanks in the coastal system; and a summary of outstanding matters. The report highlighted the need for better appreciation and identification of the principal physical processes in the evolution and maintenance of sandbanks. It also flagged the lack of thoroughly tested morphodynamic numerical models by which to predict the evolution of sandbank, and other large-scale features.

### 1.2.4. Methodologies and techniques to study sandbanks

Over the last 30 years, semi-quantitative research has been carried out (Whitehouse, 2001). However, present knowledge of sandbank origins and long-term evolution is rather sketchy, and based mostly on qualitative findings. Observations sometimes support existing theories for the origin or maintenance of sandbanks, at other times contradict the theories, and occasionally findings are inconclusive.

**Fieldwork and other observations**

A portion of this knowledge is based on the analysis of data: investigating bathymetric charts (of areas with sufficient tidal velocities, and sediment supply, Off, 1963), carrying out historical chart analysis (numerous consultancy studies), and *in situ* observation using instrumentation to study the hydrodynamics, bedform orientation and symmetry, grain size variation, sediment pathways, etc. (Stride, 1982; Caston, 1972; Caston and Stride, 1970; Harris *et al.*, 1992; Collins *et al.*, 1995; Williams *et al.*, 2000; Vanvesenbeek and Lanckneus, 2000; and Lankver *et al.*, 2003). The limitations of field data are the time and spatial constraints regarding data coverage. The processes captured in the data are snapshots of the conditions in which the data were collected (short-term information).

Bedform asymmetry is used in the interpretation of sediment transport and morphological changes (transverse bedform migration occurs towards the steepest side). To ensure the validity of the technique, it is necessary to check that hydrodynamic conditions are associated with bedform orientation, as the latter could be a relict feature that does not

correspond to present conditions. Observations of bedform asymmetry by Collins *et al.* (1995) and Vanwesenbeek and Lanckneus (2000) support Huthnance's maintenance theory for the existence of a mean circulation around the bank with a convergence at the crest. However, other techniques to elucidate the sediment pathways such as grain size trend analysis (Van Lanckner *et al*., 2003) do not agree with the information derived from bedform asymmetry.

**Data analysis**

Data from surveys or navigation charts have been used to investigate the past evolution of sand banks: in particular to identify trends or the presence of cyclical processes. Geographical Information Systems (GIS) have been used by Kemp and Brampton (2007) to study the temporal rate of change of the bathymetry of the Nash Bank. Sophisticated statistical analysis based on principal component analysis (or empirical orthogonal eigenfunctions, EOF) was initially used in meteorology to identify cyclic weather patterns. It has since been applied to identify the main components in the temporal and spatial evolution in the bathymetry of the Dutch coast (Wijnberg and Terwindt, 1995), and more recently of the Great Yarmouth banks (Reeve, 2001). EOFs are useful to identify periodic patterns in the evolution of the bathymetric data. This technique has also been used in the investigation of channel-shoal shift mechanisms in the Humber Estuary (Horrillo-Caraballo *et al*., 2002).

Analysis of historical data from a Lowestoft bank (Dolphin *et al*., 2007) indicated that there were two types of bank morphological state (deltaic and elongated). The existence of the two states may be related to the regional morphology of the Norfolk banks, which alters the local tidal currents and hence affects downstream features (such as the Lowestoft bank).

The weaknesses of these techniques are scarcity of data and gaps in the dataset, which add uncertainty to the results. It is not easy to ascertain whether changes are due to episodic events (storms), or to the typical conditions. Such techniques are not suitable for predicting long-term evolution, as extrapolation would be required. Instead they contribute to data reduction by identifying the important forcing processes (De Vriend, 1993). Data-based modelling (applied to barred beach evolution by Gunawardena, 2007) is a useful technique to study large-scale morphodynamics, which could be applied to studying sandbank evolution. This technique requires frequent datasets to validate the model.

**Conceptual model of sandbank growth**

Huthnance (1973) proposed a mechanism for sandbank growth and maintenance using a hydrodynamic model describing an infinite tidal ridge (after observations from Caston, 1972). Huthnance described two mechanisms capable of generating mean currents that can play a role in the maintenance of the bank. The balance between frictional and pressure gradients, and separately the effect of Coriolis forces on friction generate mean currents around the bank that converge at the crest. Later, Huthnance (1982a) proposed hypotheses for the growth of a sinusoidal bedform, and equilibrium profiles that depend on the wind-wave activity, the angle of the bank to the peak tidal flow and the sediment supply. Huthnance also proposed an empirical formula regarding the calculation of bank separation based on the water depth, slightly different to Off (1963), who assumed the spacing to be proportional to water depth). Huthnance argued that secondary flows generated by a gently sloping bed were not likely to have a great influence in comparison to the mean currents.

**Stability analysis**

Stability analysis is a tool that allows for the distinction as to whether changes in a system are due to internal or external forcing (Dronkers, 2005). Unfortunately this technique so far, cannot describe the sandbank's response to present environmental conditions. Following Huthnance (1982b), Hulscher (1993, 1996) and Dodd *et al*. (2003) applied linear stability analysis to large-scale, long-term evolution of rhythmic morphodynamic features, in particular the growth (and later location of occurrence) of large-scale features such as sandbanks. Linear stability analysis couples equations describing the hydrodynamic fluid motion (including tide propagation) with a sediment transport equation. The method tests a range of wavelengths as small bed perturbations and studies their stability, and identifies the wavelengths that have preferential growth. One of the method's limitations is that it cannot predict the amplitude of the sandbank wavelength (or crest height).

Besio *et al*. (2006) developed further the linear stability model by improving the representation of the flow near the bed, the eddy viscosity, taking the time-derivatives into account and the acceleration terms in the momentum equations. These terms are of the same order of magnitude as the Coriolis, and the latter has been shown to have an effect on sandbank formation. The model is able to predict sandbank wavelength and the orientation of the crests to the main flow direction (both clockwise and counter-clockwise) as compared to observations.

Idier and Astruc (2003) compared analytical and numerical investigations on sandbanks using stability analysis. Their model was capable of predicting equilibrium amplitude and timescales as well as indicating the migration rates. This model assumes the cross-section of the banks are symmetric, which is not the case in reality.

Roos *et al*. (2004) extended the capability of Hulscher's model by adding non-linear theory to be able to predict equilibrium profiles. Roos *et al*. also studied the influence of $M_2$ and $M_4$ tidal components on the profile shape, the differences in resulting shape with bedload[9] or suspended[10] load transport, and compared their predictions with observed data in the Southern North Sea. They also added parametrically the effect of wave stirring of the sediment (by adding a depth-dependent factor).

Idier *et al*. (2007) investigated the effect of varying grain size and included the threshold for transport in the calculations. This improved the model predictions of the amplitudes and location of sandbanks.

**Numerical modelling**

Numerical modelling (process-based) is the most widely used tool to predict evolution of large-scale morphodynamics such as sandbanks (and spoil heaps). Flow models have reached a high degree of sophistication due to the processes being fairly well understood. However, sediment transport is highly complex and interactions between hydrodynamics and sediment are not fully understood. Transport rate predictions are highly dependent on the expression used, and produce results with a large range of variability. The key is the interpretation of the processes. A recent overview of numerical modelling in the context of scour (Sumer, 2007) provides insight into the complexity of the morphodynamic problem.

For the study of long-term evolution, all the processes involved (including the nature of non-linear interactions between them) need to be taken into account. Predictions of long-term evolution with process-based numerical models are not very reliable when used on their own due to the complexity of the system. Nevertheless, there are techniques that can be applied to improve long-term morphodynamic predictions (De Vriend, 1993). The forecast of long-term evolution improves when using a combination of techniques to check results (e.g. coastal area models and regime models). Morphodynamic numerical models are rarely validated for prediction of long-term evolution, and their results are of varying quality.

[9] Bedload transport: takes place by grains rolling, hoping and sliding along the bed in response to the friction, and in the case of sloping beds to gravity (Soulsby, 1997).
[10] Suspended load transport: If the flow or waves are large enough, and the grains fine enough, sand will be put in suspension, and be carried by the currents (Soulsby, 1997).

Thus, testing morphodynamic models against a benchmark dataset would improve predictions.

Dyer and Huntley (1999) identified numerical modelling as perhaps the most useful tool by which to broaden the understanding of Type 2 banks, their generation mechanisma and evolution are the least understood. Dyer and Huntley suggested that sensitivity analysis be used to investigate the important processes involved in sandbank evolution.

Process modelling has been satisfactorily applied to the study of sandbanks. Williams *et al*. (2000) investigated the evolution of Middlekerke bank on the Belgian coast. The observations and modelling suggested the presence of a clockwise circulation around the bank, supporting existing theories. However, the measured residuals did not show a counter-clockwise circulation. Results from O'Connor *et al*. (1996, CSTAB) modelling wave effects on the sandbank showed that bed levels increased in calm conditions whereas levels decreased during storm conditions. O'Connor *et al*.'s findings suggested that the results are more sensitive to wave period and height than to wave direction. The simulation of a scenario representing dredging on the bank, predicted that wave heights will decrease immediately after the dredged site and increase at the sides. Sand extraction has the potential to modify bank morphology, and hence the impacts of future dredging or other activities need to be closely evaluated and monitored. Coughlan *et al*. (2007) recently investigated the effect of the tidal stage in the wave energy inshore of a breakwater, and its relationship with the long-shore transport and the beach evolution. Coughlan *et al*. found that the stage of the tide had a greater influence on the wave climate than the tidal currents. The greatest long-shore transport took place at high waters.

Carbajal *et al*. (2005) investigated the influence of geometry in the formation of periodic seabed features using a 2-D non-linear hydrodynamic model coupled with bedload sediment transport. The model predicted the existence of periodic features (i.e. sandbanks) for a simplified geometry of the Southern North Sea. From the results, it followed that the location where sandbanks occur depends on the geometry of the basin, and where a Kelvin wave (a long wave, like the tide) is diffracted.

Damgaard and Chesher (1997) used a 2-D depth averaged model to predict the evolution of Helwick Bank over a twenty year period. The technique may be too sensitive for the long-term prediction because the model becomes unstable. Smoothing techniques could be used to remove the instability, although then the non-deterministic effects occurring at long-term scales in nature would not be taken into account.

Signell *et al*. (2000) found through the use of a 3-D numerical model, that the generation mechanisms for headlands associated banks were due to shear stress and sediment flux, rather than residual circulation. This disagrees with the popular hypothesis of "tidal stirring" (also known as "teacup effect", the tea leaves gather in the centre of the cup after stirring it) when the convergence in the centre of a residual eddy is due to the inwardly directed pressure gradient. The banks formed were symmetric and not strongly affected by Coriolis force. Further to Signell *et al*., Jones (2007) suggested that the process responsible for the asymmetry of headland associated banks was the Coriolis effect and that secondary flows were not important in the generation of headland associated banks.

Hayes and Nairn (2004) proposed wave-bathymetry interaction as a method for the maintenance of tidal ridges in the continental shelf and Gulf area of the USA. Hayes and Nairn used a phase-resolving Boussinesq-type model to investigate this. Refraction of waves over banks produced non-linear orbital velocity that had a stronger component towards the shallower waters; this would preferentially transport (coarser) sediment to the crest of the ridge.

Horrillo-Caraballo (2005) investigated the hydrodynamics around the Great Yarmouth banks. By means of a numerical model, Horrillo-Caraballo evaluated the long-term evolution, and assessed the impact of residual currents and eddy vorticity on the sediment transport in the area. It was found that vorticity affected the residual currents and in turn enhances sediment transport, which can affect the morphology.

The effect of an offshore wind farm in the local morphodynamics was assessed by Van der Veen *et al*. (2007). An analytical model, that parameterises a wind farm as flow resistance, was used to investigate the changes in size of the area affected by the wind farm (i.e. larger area affected implies a greater impact). Changes in size of the area affected were investigated as a function of varying environmental parameters (water depth, flow velocity, grain size and orientation of the farm with respect to the main flow direction). Van der Veen *et al*. also studied the influence of the wind farm design parameters (turbine diameter, spacing between them and drag coefficient) on the size of the disturbed area.

Self-organisation models, such as Cellular Automata techniques applied to trench recovery by Schinaia (2007), could have a potential use in the investigation of long-term evolution of sandbanks. For this method there is the need for quantitative data and a manner of defining the time-scale of evolution.

**Experimental work**

Some experimental work has been carried out to collect and analyse detailed information on the velocity and turbulence field over fixed 2D bedforms (Nelson *et al.*, 1993; McLean *et al.*, 1994; or Bennett and Best, 1995). Bed load sediment transport is sensitive to changes in the velocity and turbulence field in the boundary layer. The bedform affects the sediment transport and the flow field in its vicinity, and the flow modifies the sediment transport and the bedform shape. Bennett and Best (1995) lists experimental research carried out from the sixties on flow over fixed bedforms. These kind of experimental work is related to large-scale bedforms although is not directly related to the morphodynamics, that is the topic of this thesis.

**Concluding remarks**

To the best of the author's knowledge there has been no experimental study to date investigating the large-scale morphodynamics of idealised sand banks/spoil heaps in controlled conditions under steady and tidal flow. Previous attempts to carry out laboratory experiments of this kind were flawed by the presence of laboratory-scale ripples that interfered with the studied features (personal communication from Professor H. J. de Vriend regarding experiments in LNH, France). The present work aims to fill this gap in knowledge. The experimental data collected in the UKCRF can be used as a comprehensive standard test case to validate morphodynamic numerical models. This would improve their capability and provide understanding of their shortcomings when applied to real-scale problems.

### 1.2.5. The bed mound

From Chapter 2 onwards the term bed mound will be used to represent an idealised description of a bed feature (sandbank or spoil heap). The bed mound was described by a simple mathematical formula (circle or ellipse in plan view, and Gaussian, cosine or trianglular in cross-section). This was done for simplicity of interpretation and ease of representation in a numerical model. Unlike *in situ* sandbanks, in the UKCRF experiments, the bed surrounding the mound was bare in most cases and there was no source of sediment, nor was there any maintenance mechanism (only erosion and destruction mechanisms affected the experimental bed mound).

The bed mound is subject to a simplified version of the complex physical processes that affect naturally occurring sandbanks or spoil heaps, hence the interpretation is subject to

certain limitations. Even so, the results provide insight into the large-scale morphodynamics. Their interpretation requires consideration of what processes are present or not in the experiments: the similarities and differences in the morphology of sandbanks and spoil heaps to the bed mound, and what processes drive the evolution of sandbanks or spoil heaps. Due to the limiting factors mentioned above, the bed mound in the experiments resembles more directly a spoil heap than a real sandbank. Several of the findings are applicable to the morphodynamic evolution of a spoil heap, and others provide significant qualitative information about sandbank evolution.

**Similarities and differences between full-scale sandbanks and the bed mound**

Similarities include: (i) the mound length and width: typically linear sandbanks are longer than wider, and can be tens of kilometres long and up to a few kilometres wide - the elliptical mound had a long axis of 6 m long and a short axis of 2.5 m wide; (ii) the slopes of the mound (length-to-height ratio): generally sandbank slopes are asymmetric, and can have angles from about 1 to 6 º - in the case of the submerged elliptical mound (6 m in length, and 0.15 m in height), the slopes (though symmetric) are of the same order of magnitude (the same applies to the submerged Gaussian hill); (iii) the range of mound heights relative to the water depth (submerged to surface piercing): can be interpreted as representative of the varying stages of the tide, although not all sandbanks become exposed during the tidal cycle; (iv) the mobile bed surrounding the mound: typically sandbanks are found in areas where there is a mobile sediment layer. The mound was assumed to be in dynamic equilibrium with the hydrodynamic conditions. Despite the foregoing similarities, there was no account taken of formation processes or maintenance mechanisms in the experiments. The influence of the Coriolis effect could not be taken into account due to the limitations in laboratory facilities available. The effects of the wave climate were not included for simplicity. It should be noted that it is impossible to apply scaling techniques to flows and waves with sediment transport. The underlying concrete bed (fixed bed) cases do not represent the conditions of the environment where sandbanks occur.

**Similarities and differences between spoil heaps and the bed mound**

There is no typical shape or configuration for spoil heaps, which are bed features that are not in equilibrium with the surrounding conditions (the disposed material). The flow changes the shape of the spoil heap causing barchan-like features to form, with ripples further afield. The fixed bed is more representative of the prototype conditions where spoil heaps occur,

and the disposed sediment may not interact with the underlying bed material. Typically wave processes are not dominant, therefore they have not been taken into account. The water surface-piercing and surface-touching mounds cannot be interpreted as spoil heaps.

## 1.3. Objectives of the research

The aim of the research presented in this thesis is to improve the knowledge and understanding of the evolution of large-scale morphodynamic features through analysis and interpretation of experimental results (i.e. insight into sandbank dynamics and spoil heap evolution). Objectives of the present work were: to identify the key processes taking place during the dynamic evolution of the bed mound; to collect a benchmark dataset of laboratory experimental measurements of flow velocity, free surface elevation and time-dependent bathymetries, in controlled idealised conditions in the UK Coastal Research Facility (UKCRF); to interpret the results from the experimental tests; to compare existing analytical and empirical expressions regarding the migration and decay in volume of the mound to experimental observations; to use the benchmark dataset to provide a comprehensive standard check, for numerical modellers to improve the quality of predictions of full-scale morphodynamic problems. The data is expected to be made publicly available in 2009.

## 1.4. Relevance to Engineering Science

At present there is a lack of experimental data on the morphodynamic evolution of large-scale seabed features. There is also the need for a benchmark dataset that allows for a comprehensive evaluation of the predictive capability of existing morphodynamic numerical models. This check should lead to improved numerical model predictions for full-scale problems. Improvement of the prediction tools would reduce uncertainty in the decision making process. The dataset collected can also provide a test by which to compare the capabilities of different numerical models, 2-DH or 3-D.

This work also presents a comparison between existing analytical solutions (Chapter 5) and the experimental data. The comparison improves the understanding of large-scale morphodynamics of a bed mound in steady flow.

## 1.5. Thesis outline

The thesis consists of three main parts: (i) set up, instrumentation and procedure followed during the experiments and the analysis and interpretation of the results; (ii) comparison of experimental data to theoretical formulae (an analytical solution and three morphodynamic timescale calculations); and (iii) comparison of the experimental data with numerical predictions. The contents of each chapter are described briefly as follows:

**Chapter 1** State of knowledge of large-scale morphodynamics. Introduction to sandbank and spoil heaps (bed mound). Techniques and methods to study sandbanks and spoil heaps. Objectives and relevance of the research to the engineering community.

**Chapter 2** Set up, experimental procedure and results form the pilot experiments in the Reversing flume.

**Chapter 3** Set up, instrumentation and experimental procedure for the experiments in the UKCRF.

**Chapter 4** Analysis and interpretation of the UKCRF experimental data from images, slice analysis and coloured sand tests. Comparison of experimental sediment transport rates with empirical formulae using modelled velocity and water depths.

**Chapter 5** Description of an analytical solution developed by de Vriend (1987) using the method of characteristics applied to the 2D shallow-water equations, and its comparison to the experimental results. The comparison of semi-empirical expressions for morphodynamic timescale and volume decay calculation with experimental results.

**Chapter 6** Brief description of the modelling exercise carried out to appraise a commercial 2-DH morphodynamic model (PISCES).

**Chapter 7** Discussion, conclusions and future work

## 1.6. Contributions to the research

The overall project was funded by the Engineering and Physical Science Research Council (EPSRC), and undertaken jointly by the University of Oxford (A.G.L. Borthwick, P.H. Taylor, R.L. Soulsby; and the author), and the University of Manchester (P.K. Stansby, D. Apsley, J. Zhou, later replaced by J. Huang and the author). The distribution of the research was as follows:

- Pilot experiments in the Reversing Flume: Phase I and II: J. Zhou and the author; and Phase III: the author.
- Large-scale experiments in the UKCRF: J. Zhou and the author
- Data analysis and interpretation: the author
- Development of the Large scale fit tool: P. H. Taylor and J. Huang.
- PISCES model calibration and numerical study: the author

**Table 1.1 Characteristic wavelengths, heights, migration speeds and evolution timescales of rhythmic bedforms in coastal seas (from Dodd *et al*., 2003).**

| Bedform | Spacing (m) | Height (m) | Speed (m/yr) | Time-scale |
|---|---|---|---|---|
| *Ripples* | 0.1 – 1 | 0.01 – 0.1 | - | Hours |
| *Beach cusps* | 1 – 100 | 0.1 – 1 | - | Hours-days |
| *Nearshore bars* | 50 – 500 | 1 – 5 | 0-100 | Days-weeks |
| *Shoreface-connected sand ridges* | 5000 - 8000 | 1 – 5 | 1/10 | Centuries |
| *Sandwaves* | 300 - 700 | 1 – 5 | 1/10 | Decades |
| *Long bed waves* | 1500 | 5 | Unknown | Centuries |
| *Tidal sandbanks* | 5000 - 10000 | 5 – 15 | - | Unknown |

**Table 1.2 Sandbank classification according to Dyer and Huntley (1996)**

Type 1 Open shelf linear sandbanks

Type 2 Estuary mouth
- A Linear banks (wide mouth)
- B Ebb tidal delta (narrow mouth):
  - i. Without migration
  - ii. With migration (shore-face connected ridges)

Type 3 Headland associated banks
- A Banner banks (non-recessional headland)
- B Alternating banks (recessional headland)

The figure originally presented here cannot be made available via ORA for copyright reasons. It can be found in: Dyer, K.R. and D.A. Huntley, 1999. The origin, classification and modelling of sand banks and ridges. Cont. Shelf Res., Vol. 19, 1285-1330.

**Figure 1.1 Map of sandbank distribution in the North Sea, original from Dyer and Huntley (1996)**

# 2. PILOT EXPERIMENTS IN THE REVERSING FLUME

This chapter describes the setting up, instrumentation and procedure that were followed during the pilot experiments carried out in the Reversing Flume at HR Wallingford, UK from March to June 2004. The experiments were designed to identify primary factors influencing the morphodynamic evolution of the bed mound (described in Chapter 1) under laboratory conditions, and so help plan the large-scale experiments in the UK Coastal Research Facility (UKCRF).

## *2.1. Objectives of the pilot experiments*

The main objectives of the pilot experiments were:

- To assess the dynamics of different sediment grain sizes in order to gather information for the large-scale experiments;
- To identify and understand the key sediment and flow parameters driving the morphodynamic changes to the bed mound (migration and morphological changes); and
- To evaluate the transport rate of the selected sediment grain size chosen for the UKCRF experiments.

The experimental schedule consisted of three phases:

*Phase I* – Exploratory tests. Involved setting up the test rig in the Reversing Flume; preparation of the instrumentation and operating system; calibrating the flow to determine the relationship between voltage (applied to a pumping system) and velocity. Phase I consists of two sets of experiments:

First set - Tests were undertaken for different oscillation periods (ranging from 5 to 40 min), water depths, and two sediment grain sizes.

Second set - Using the information collected during the first set, the response of the bed mound (built with four different grain sizes) to the conditions was tested. The repeatability of the tests was also assessed. The parameter study considered the initial mound shape, overall test duration (elapsed time), flow condition (i.e. unidirectional or reversing) and bed characteristics (i.e. fixed or mobile).

*Phase II* – A series of tests were carried out in the Reversing Flume to gather detailed information about the transport rate for the sediment selected for the large-scale tests in the UKCRF (Garside 21). The median sediment grain size was 0.454 mm, corresponding to medium to coarse-grained sand (according to the Wentworth scale).

## 2.2. Description of the experiments

### 2.2.1. Test facility

The Reversing Flume used for the pilot experiments (Figure 2.1) consisted of a 29 m long, 0.605 m wide channel with a reversible flow pumping system capable of producing oscillatory flow conditions. This small-scale facility was straightforward to control and thus ideal for parameter testing in preparation for the larger-scale experiments that were to be carried out later in the UKCRF. For ease of interpretation, orientation in the photographs is related to compass directions in the figures.

The Reversing Flume channel had smooth walls and flow guides at each end to maintain approximately uniform flow conditions across the channel (i.e. avoid pronounced boundary layer effects). Water was re-circulated from the downstream end of the flume to the upstream entry via an adjacent pipe-work system. The freshwater flow was driven by a constant speed axial flow pump of maximum discharge 0.13 $m^3s^{-1}$ whose blades were continuously adjustable between full forward and reverse pitch. The pitch of the blades in the impeller could be controlled manually or by a computer-based servo-control system (Whitehouse, 1998). This meant that a time series of variable flow speed and direction could be programmed into the system, typically a sinusoidal signal with peak flow of approximately 0.5 m/s.

The Reversing Flume was dismantled immediately after the experiments were completed, as part of HR Wallingford's site redevelopment programme.

### 2.2.2. Instrumentation/Equipment

The instruments used in the pilot experiments were:

- One miniature propeller current meter (MPCM) used initially to measure the depth-averaged velocity during the calibration process, and positioned at an elevation of two-thirds the water depth above the bed.
- Up to three acoustic Doppler velocimeters (ADV) to measure the water particle velocities at an elevation 40 % of the total depth above the bed.

- A Vernier point gauge for taking spot levels of the bed mound, along the length and width of the flume, at regular intervals when the flow was stopped.
- Signal wave generator – Software developed by HR Wallingford Ltd was used to input a voltage signal to a transducer and produce a flow discharge at the pump in the flume. The values of peak voltage correspond to peak flow speeds for the test (this relation was found by flow calibration).
- Cameras:
    1) Scientific high-resolution black and white camera, used to obtain particle tracking velocimetry (PTV) photographs, and mounted in a fixed position approximately 1 m above the flume and looking vertically downwards;
    2) Scientific lower resolution black and white video camera, used to record the evolution of the bed mounds through the glass side-wall of the flume;
    3) Hand held video camera (available in some tests); and
    4) Digital colour camera used to obtain overhead images.

### 2.2.3. Measured velocity

The velocity collected by the ADVs in the Reversing Flume, was taken to be representative of the depth-averaged velocity (assumed power-law profile).

### 2.2.4. Errors

The main sources of errors during the experiments were due to instrumentation and the experimental procedure. The Vernier gauge used to measure the mean water depth and the bed mound profile had an accuracy of ± 0.0005 m. The accuracy of flow velocity measurements is 0.01 m/s for MPCM and either 0.5 % (or ± 0.001 m/s) for the ADV. The ADV's error in the measurements is a function of the accuracy of the positioning of the gauge (in the horizontal and vertical axis as well as the alignment to the main flow direction, and the water depth). During Phase II of the experiments, the sediment was collected very carefully, at low flow conditions there were smaller volumes of sediment transported, and as the volumes were smaller the error (being constant due to keeping to the procedure) can be percentage-wise larger. More details about errors and instrumentation are given in Chapter 3.

### 2.2.5. Sediment

Several sediment types and grain sizes were considered during the pilot experiments, to identify a suitable (i.e sufficiently mobile and transported mostly as bed load) sediment size for the large-scale UKCRF tests. The sand type used most frequently was "Garside 21", a medium to coarse-grained natural sand. The density of the quartz based sediment was assumed to be 2650 kg/m$^3$, the density of anthracite was assumed to be 1400 kg/m$^3$. Table2.1 lists the median grain size ($d_{50}$), the associated settling velocity ($w_s$) for the range of water temperatures, and the critical bed shear stress ($\tau_{cr}$) for each sediment type used in the pilot experiments (calculated according to Soulsby, 1997, Eqs. 102, 74, 77). Table 2.1 shows that larger grain sizes have less potential for suspension by oscillatory currents. The sand samples used were relatively well sorted and it was assumed that particle distribution would not have a large effect.

## *2.3. Flow calibration*

Flow calibration involved finding the relationship between the input voltage to the pumping system and the output flow velocity. The pumping system could be controlled either manually or by inputting a curve into the software. Accurate calibration was essential in order to provide the correct input voltage information. To create a calibration curve, the pumping system was controlled manually as the voltage was ramped up and down in stages to produce steady unidirectional flow. Then this process was repeated to calibrate the flows in the opposite direction. Then, a curve of velocity versus voltage was plotted. Two calibration curves were produced, corresponding to still water depths of 0.10 and 0.20 m (measured before the start of the test) in the flume (Figures 2.2a and 2.2b). In Figure 2.2 the velocity is negative when the water flows westward and positive when eastward. To obtain oscillatory flows, a sinusoidal voltage curve was input into the software, by giving the peak voltage (to produce approximately 0.5 m/s velocities). Figure. 2.3 shows a typical record of measured velocity obtained by an ADV for oscillatory flow in the Reversing Flume. The signal has most noise at times of maximum flow. The magnitude of this fluctuation was identified as an indication of turbulence in the velocity.

## 2.4. Experimental procedure

During the pilot experiments, photographs and video footage of the evolving sand mound were collected, as well as bed mound profiles and flow velocity and water depth measurements. Two kinds of photographic data were obtained. First, still overhead images were taken at a frequency of 0.25 Hz and converted into animations. Second, still images were obtained of the evolving bed mound from various viewpoints every slack water (half cycle in oscillatory flows). In certain cases, digital and analogue video data were also collected of the behaviour of the mound. Sand surface profiles were measured using a Vernier gauge attached to a trolley system (in the stream-wise and cross-flow directions). During the first set of experiments, profiling was undertaken at slack water at the end of full cycles. Due to limitations in the signal generation software, the flow always had to start from one direction (westward). The signal generation software was modified for the second set of experiments, throughout which, profiles could be taken during any slack water period (i.e. every half or full cycle). The ADVs were situated at two or three locations along the flume (Figure 2.1). During test runs two ADVs were used, one at either side of the false floor approximately 2.5 m from the location of the mound. During calibration a third ADV was placed over the false floor. Velocity data collected during the sediment transport rate experiments were converted to depth-averaged velocities using the method recommended by Soulsby (1997, eq. 28a).

The initial mound was built up by placing sand on the wooden false floor of the flume and moulding the heap by hand. The sand of the mound was loosely packed. In all tests, the mound had approximately the same initial shape and height, though the profile was not moulded as precisely as it was in the large-scale tests in the UKCRF experiments which followed. The initial dimensions were approximately: height 0.05 m and diameter 0.30 m (using cupfuls of sand the volume measured was $1.17 \times 10^{-3}$ m$^3$). The plan shape was mostly circular except for Tests 14, 15, 16 where the procedure differed slightly (as did the shape and initial volume). For Test 19, a mobile sand bed was first prepared and carefully screeded to make it level. Next, the bed mound was placed on top of the mobile bed following the same procedure as with the fixed wooden bed. The flume was then filled with water at a slow rate in order not to disturb the mound or the mobile bed. Once the water reached the prescribed test depth, the initial surface profile of the mound was measured. As the mound was not moulded in a very precise manner, the calculated volume based on the assumption of a conical shape, gave an over-prediction compared to the actual volume of

sediment used (measured as cupfuls of sediment). After the initial profiling was completed, the test started. Consecutive profiles were taken when the flow was stopped (at the end of selected full cycles in the first set of experiments and at selected half cycles in the second set of experiments).

## 2.5. Pilot experiments: Test program

Tables 2.2, 2.3 and 2.4 list the test cases, outlining the parameters that characterise the pilot experiments conducted in Phases I, and II.

## 2.6. Pilot experiments: Results

This section discusses the photographic and bed profile data collected from the experiments in the Reversing Flume. Detailed black-and-white photographs were taken using an overhead PTV camera, and colour photographs were taken every half cycle. Measurements of the bed mound height were taken with a Vernier gauge mounted on a trolley that was positioned over the flume in the cross- and along-flume directions ($y$ and $x$ respectively).

To identify whether the flow was laminar or turbulent, the Reynolds number was calculated from:

$$\mathrm{Re} = \frac{\overline{U}\ H}{\nu} \tag{2.1}$$

in which $\overline{U}$ is the depth-averaged flow velocity, $H$ is the water depth, and $\nu$ is the kinematic viscosity of water. For practical purposes, open channel flow is laminar when $R_e < 500$; transitional when $500 < R_e < 2000$; and fully turbulent when $R_e > 2000$ (though the upper value is arbitrary) (Chow, 1973). During the experiments, the flow changed from laminar conditions at slack water to fully turbulent for much of the cycle. Typical $R_e$ at maximum velocity was between $10^4$ and $10^5$, thus well within the turbulent regime.

The threshold of motion of the sediment due to current flow was calculated using the method developed by Shields (1936) (as cited by Soulsby, 1997). Shields' approach is based on the ratio of forces acting on a sediment grain (i.e. gravity and the shear stress due to the current flow). In order for the grain of sediment to move, the bed shear stress must overcome the gravitational forces that keep it in equilibrium. To determine when this happens, it is necessary to calculate the threshold Shields parameter from:

$$\theta_{cr} = \frac{\tau_{cr}}{g(\rho_s - \rho)d} \tag{2.2}$$

where $\tau_{cr}$ is the threshold bed shear stress, $g$ the acceleration due to gravity, $\rho_s$ is the grain density, $\rho$ is the water density and $d$ the grain diameter. For Garside 21 sand of 0.454 mm diameter, $\theta_{cr}$ is 0.0336 (see the Soulsby and Whitehouse method, eq. 77 in Soulsby, 1997).

Typically the sand moved mostly as bed load transport, though a small quantity of sand may have been entrained in the water column for short periods of time. The exception was the case of fine sand with $d_{50}$ 0.111 mm (Test 8 in the second set of experiments), where a large portion of the sand travelled as suspended load in the vicinity of the mound.

### 2.6.1. Reversing Flume experiments: Phase I; First set

The tests in the first set of experiments assessed the relevance of the oscillation period and overall elapsed time from the start of the first flow cycle on the morphological evolution of the bed mound. Profile measurements were carried out before the test started, at the end of the first cycle, and at the end of the test. Each test lasted six cycles, except Tests 2 and 4 which were of 12 and 3 cycles, respectively.

#### *Evolution of bed mound after one cycle*

Figure 2.4a to 2.4f shows photographic images of the plan-form shape of the bed mound after one cycle for Tests 1 to 6 inclusive. The photographs were taken at different elapsed times from the beginning of each test, according to the oscillation period (which ranged from 5 to 40 minutes). The photographic images were oriented so that the left hand side corresponds to the west. Immediately before the photograph was taken the flow was going towards the east.

Figures 2.4a to 2.4d, corresponding to Tests 1 to 4, compare the effect of different oscillation periods on a bed mound of sand of median diameter 0.454 mm in a water depth of 0.20 m. There are similarities in the shapes of the mounds even if the oscillation periods range from 5 to 40 minutes. In each case the upstream side of the mound retains much of its original 'conical' shape. The rear of the mound is eroded by a pair of vortices, aligned symmetrically with respect to the flume centreline, leaving scour holes and a pair of curved headlands. A trail of sand extends to the east.

Figure 2.4c shows the mound for Test 3 (20 min oscillation period). After 1 cycle the mound in Test 3 evolved further than for Tests 1 and 2, which have shorter periods. In Test 3, the velocity is above the threshold of sediment motion for longer time than Tests 1

and 2 so sand is available to move for longer during the cycle. Two detached dunes formed in the lee as the headlands became cut off from the bed mound. A pronounced tail can be seen behind the mound to the east, along the flume centreline. These features are a by-product of strongly vortical flows that swirl behind the bed mound. The duration of the oscillation period in Test 3 was sufficient for headlands to form and detach within the same half cycle.

Figure 2.4d for Test 4 (the longest oscillation period, 40 min) shows the mound has reached an advanced stage of development; two detached dunes are evident on the downstream side (east) and one on the upstream side (west) (residual from the previous half cycle). There is a sand trail to the lee, east of the mound.

Figure 2.4e for Test 5 shows a mound built with finer sand ($d_{50}$ = 0.230 mm) and 10 min oscillation period, water depth of 0.20 m. The results are qualitatively different to those of the other tests. The sand is spread over a larger area, an effect expected due to the higher mobility of finer sediment. During the first half cycle, a series of ripple-like appendages developed on the west side of the bed mound. In the second half cycle, a further pair of appendages formed in the lee of the mound (east). There are trails of sand towards both sides. Note that none of the appendages detached from the bed mound (the sediment moved but the appendages did not detach).

Figure 2.4f presents results for Test 6 run with sand with $d_{50}$ = 0.454 mm, flow oscillation period 10 min, and water depth reduced to 0.10 m. A barchan (crescentic) shape developed in the first half of the cycle. Highly sheared secondary flows due to eddies behind the mound formed lateral ridges and a set of wings on the first half cycle. As the flow reversed the sediment wings shifted to the east and the barchan shape became less distinct. Figure 2.4f indicates that the mound remained essentially intact, with evidence of a sand wave or ripple superimposed (Figure 2.4g). No significant trail of sand can be observed.

### *Bed mound evolution after 10 minutes*

Results obtained for Tests 1 to 6 after 10 minutes run time (Figure 2.5) are very similar to those in Figure 2.4. It should be noted, of course, that Figures 2.5a, 2.5e and 2.5f are the same as Figures 2.4a, 2.4e and 2.4f where the oscillation period coincides with the 10 min run time.

Results shown in Figures 2.5a and 2.5b (Test 1 and 2) are similar to each other. There are 2 appendages and a trail of sand at the lee of the mound. Results in Figures 2.5c

and 2.5d (Test 3 and 4) are also similar to each other, the appendages that formed have since detached and the plan shape is quasi-circular.

### *Bed mound evolution after one hour*

Results for Test 1 to 6 after one hour run time are presented in Figure 2.6. Figures 2.6a to 2.6d appear to be alike; these show the evolved bed mounds with sand with $d_{50}$ = 0.454 mm, in 0.20 m water depth. In each case, the bed mound retained much of the initial material. Ripples of various lengths (but approximately equal widths) extend laterally from the mound. The similarity indicates that long-term motion of the sand and morphodynamics of the mounds are more sensitive to the elapsed time from the start of the run than to the flow oscillation period (within the range of parameters covered by the Reversing Flume tests). This was an important finding, which had implications for the larger-scale tests in the UKCRF. Figure 2.6e (Test 5) shows the mound of finer sand breaking down into ripples. In Test 6 (Figure 2.6f) the shear stress enhancement due to the reduction in water depth (0.10 m) led to a complex shape of mound, caused by increased strength of eddies shed from main body of the mound in the earlier stages of the run.

As an example, Figure 2.7 shows the typical time evolution of a bed mound in the Reversing Flume (for about 2 hr), each image corresponds to half a cycle.

### *Analysis of profiles*

Profiles were taken as described in Section 2.4. Figure 2.8 shows the changes in height of the mound with time for all tests carried out during The first set of experiments. Tests 1 to 4 were run with different oscillation periods (more detail in Table 2.2). Test 5 was run with a smaller grain size material ($d_{50}$ 0.230 mm), water depth of 0.20 m. Test 6 was run with the same grain size as Tests 1 to 4 ($d_{50}$ 0.454 mm) with a different water depth of 0.10 m.

Decay rates for Tests 1 to 4 are similar (Figure 2.8). The reduced water depth (Test 6) shows greater height decay in the first cycle than for any other test. After 10 minutes elapsed time the height of the mound reduced by over 44 % (Table 2.5), after which the decay became more gradual (similar to tests 1, 2 and 4). In general the trends in Tests 1, 2, 3, 4, 6 are similar considering the envelope of decay rates. In Test 5 (finer sediment) the mound height showed a sharp decline, the sediment rapidly dispersed due to greater transport rate (bed load and some suspended load in this case).

At the time of running the tests, it appeared that sand repeatedly piled up at the top of the bank during the first half cycle and then collapsed by an avalanche mechanism. The collapse line moved downstream of the reversing flow. In Tests 1, 2 and 5, an increase in

height occurred after the first cycle (Figure 2.8). It should be noted that data were only collected at the end of the first cycle for the longer oscillation period tests (i.e. Tests 3 and 4 at 20 and 40 minutes, respectively), and so it cannot be ascertained whether the mound height fluctuates between spot measurements during the initial stages of these tests.

### *Effect of oscillation period on mound evolution*

In order to assess whether the oscillation period influenced changes to the morphology of the mound, the bed mound height was plotted against the oscillation period. Typically during the tests the sampling of the mound height was taken at the start of the test, after the first cycle, and at the end of the test. The experiments were run with four different oscillation periods: 5, 10, 20 and 40 min. To compare the influence of the oscillation period, two sampling times, 10 and 60 min were chosen. The mound height $h$ was estimated for times when measuring data were unavailable from the exponential decrease function:

$$h(t) = h_0 \; e^{-t/T_h} \tag{2.3}$$

in which $t$ is time, $h_0$ is the mound height at time $t_0$, and $T_h$ is the morphodynamic timescale (i.e. the time at which $\ln\left(h(t)/h_0\right) = (-0.2793) = -e$ for Test 1, Table 2.6). The data from Tests 1 to 6 were fitted to Equation 2.3, and the resulting regression lines plotted in Figure 2.8, along with the equation and the corresponding correlation coefficient. Table 2.6 shows the regression fit coefficients of the regression lines for these datasets.

To assess the relationship between mound evolution and oscillation period, (Figure 2.9) bed mound height at 10 and 60 min elapsed time ($T_E$) were plotted against oscillation period ($T_o$) 5, 10, 20 and 40 min. Due to profiling frequency, there were no measurements at 10 and 60 min for all the tests, so the intermediate points were predicted using the exponential decrease formula (Eq. 2.3). In Figure 2.9, the mound's height at 60 min is roughly 20 % lower than the corresponding mound height at 10 min, regardless of the oscillation period ($T_o$). For low $T_o$ (5, 10 min), $h$ reduces with increasing values of $T_o$. For high $T_o$ (20, 40 min), $h$ does not vary greatly (at 10 min) or reduces slightly (at 60 min). The decrease in mound height seems largely influenced by the elapsed time ($T_E$) and does not seem strongly dependent on the oscillation period ($T_o$). The morphological evolution of the mound was not greatly influenced by the oscillation period. When the oscillation period was 10 min there was significant morphological change, and the shorter oscillation period meant the potential to run more tests in less time. It was therefore decided to standardise on a 10 min oscillating period for the second set of experiments tests.

### *Blockage of flow due to bed mound*

Regarding flow blockage due to the mound, measurements were undertaken for two water depths (0.20 and 0.10 m) during the first set of the pilot experiments. Tests 1 to 5 were run with water depth 0.20 m and Test 6 with 0.10 m. Typically for depths of 0.20 m the blockage was 6 % of the cross-section. Test 6 however blocked 12.5 % of the total cross section depth causing the flow to move faster around and over the mound. Blockage had an important effect. The flow structure around the mound in the shallower case was more turbulent with strong eddy shedding occurring from the apex of the mound. These eddies enhanced sand transport and caused the mound height to reduce more rapidly in the initial stage until it reached a streamlined shape. Then the decay became more gradual as the flow became less affected by the mound's obstruction.

### *Summary*

The shallower water depth influenced the morphological evolution, accelerating it compared to deeper water, by forcing the flow to go faster around the mound. The acceleration of the morphology did not generally entrain sediment into suspension, hence remaining within bed load transport regime for $d_{50}$= 0.454 mm sand. As it provided sufficient rate of change in the morphology, 0.10 m was set as the testing water depth in the second set of experiments.

## 2.6.2. Reversing Flume experiments: Phase I; Second set

All the tests in the second set were undertaken for the same oscillation period of ten minutes (for further details see Table 2.3). Flow conditions were set to 1.5 times the threshold velocity for each material (Table 2.7). Tests 7 to 11 were run with different sediment types. Tests 12 and 13 were run to ascertain repeatability of the results. Tests 14 to 16 considered different initial shapes of mound. Tests 17 and 18 examined the behaviour of the mound in unidirectional flow. Test 19 dealt with a mound on a mobile bed.

Surveys of the mound profile were obtained at the same frequency intervals for Tests 7 to 11 (i.e. at the start of the test, $t$=0 min; after the first cycle, $t$=10 min; and at the end, $t$=60 min). Tests 12 and 13, were repeats of Tests 9 and 10 and were surveyed more frequently and run for longer (data collected at 0, ½, 1, 3/2, 2, 3, 4, 6, 8, 10 cycles).

Although tests were programmed for equivalent flow conditions - for both water depths - slight variations in flow velocity occurred due to the pumping system. As a consequence there was an unintentional asymmetry in the flow, with a slightly stronger flow

towards the west that was evident in long runs (Table 2.8). Probe 0 was located 2.5 m west of the centre point of the flume, and Probe 2 was located 2.5 m east of the centre point. Probe 1 was used on occasions and was located eastwards of Probe 2.

***Bed mound evolution after 10 minutes.***

Figure 2.10 shows the evolved bed mound shapes obtained using different sediment types for identical hydrodynamic conditions (oscillation period 10 min, flow depth 0.10 m, see Table 2.3). Figures 2.10b, 2.10c, 2.10d and 2.10a, present results for sediment of increasing median diameter 0.110, 0.230, 0.454 and 0.800 mm respectively.

For the finest sand sample (Figure 2.10b), the bed mound spread a considerable distance as sediment was transported partly in suspension as well as bed load. Large trails of sand containing many ripples showed in relict wake zones to the west and the east of the bed mound, which itself had a complicated shape due to vortical flows scouring holes and creating headlands (appendages) to the north and south (perhaps as sand waves). The results for the coarser sands are similar to each other in that the bed mound remained fairly compact with only thin trails of sand forming. The finer the sediment the more the bed mound degenerates into ripples (Figure 2.10).

The bed mounds of sand with median diameters 0.110 and 0.230 mm behaved differently. This was possibly due to the mechanism by which sand was transported, changing from suspended load to bed load. Figure 2.10c shows that the mound had a smooth front face (with respect to the most recent flow direction) and a blunt tip, where the flow accelerated over the mound in a streamlined manner. The flow separated at the crest of the mound and the swirling effect of the two symmetric vortices appeared to have eroded sand in the wake, except for the trail. There was evidence of small sand heaps being deposited immediately behind the zone of influence of the vortices.

Figures 2.10d and 2.10e are very similar as the sand moved predominantly by bed load. The vortex action was more complex, and there may be two pairs of vortices shedding. Almost all sand remained in the mound.

Figure 2.10e shows the results obtained for a 50:50 mixture of two sediments (0.230 and 0.454 mm). The results were very similar to those for uniform sand of diameter 0.454 mm, indicating that the coarser sand seemed to dominate the morphodynamic changes. The similarity between the evolved shapes obtained in Figures 2.10c and 2.10f for the 0.230 mm sand (and Figures 2.10d and 2.10g for the 0.454 mm sand) demonstrate that the tests are reasonably repeatable.

### *Bed mound evolution after one hour.*

The shape of the bed mound after one hour was complex (Figure 2.11). No results are shown for the finest sand, after 30 minutes the sediment had dispersed greatly and the test had to be stopped. For sand of median diameter 0.230 mm, the bed mound degenerated into ripples (Figures 2.11c and 2.11f).

Figures 2.11c, 2.11d, 2.11e and 2.11a show the effect of increasing the grain size was to reduce the production of ripples and to preserve the compactness of the mound. It should be noted that anthracite, used in Test 7 (Figure 2.11a), has different density (1400 kg/m$^3$) than the other sediment types and this had the effect of a lack of ripple development.

The differences between the patterns in Figures 2.11c and 2.11d (and e, f, g) confirmed that strong non-linearity of bed morphodynamics, feedback between the ripple profiles and the local flow conditions meant the end pattern was highly sensitive to small changes in initial conditions. After one hour, the results (2.5d vs. 2.5g; 2.5c vs. 2.5f) were not repeatable due to the influence of ripple formation, though the initial conditions were almost identical and the evolved shapes after 10 min were similar.

The level of disintegration of the mound is similar amongst Figures 2.11c, 2.11f and 2.11g. In these figures there is no part of the mound that is significantly more important than others, unlike in Figures 2.11a, 2.11d, 2.11e.

Figures 2.11d and 2.11e show a smaller level of disintegration of the mound (than in c, f and g). A recognizable part of the mound remained at the centre. These seem to show an earlier stage in the mound evolution. If these tests were run for sufficient time, the final image would resemble Figures 2.11c, 2.11f, 2.11g.

Figure 2.11 also shows a bias of the flow towards the west side, only evident after one hour of run time (see Figures 2.11a, 2.11d, 2.11f and 2.11g). The flow was marginally stronger towards the west side in most cases (Table 2.8) due to the asymmetry in the pumping system.

### *Analysis of profiles*

Figure 2.12 shows the time histories of mound height for all the second set of experiments. Tests 7 to 11 were carried out with different sediment types, and the flow conditions were set to 1.5 times the threshold velocity for each material, for more detail see Table 2.3.

Anthracite was used in Test 7 and the mound's height remained stable at about 0.05 m for 20 min, then reduced gently (20 %) until the end of the test (Table 2.9).

The initial decay rate (between $t$=0 and $t$=10 min) for Test 8 was larger than for coarser sediment (Table 2.9), as also happened in the first set of experiments with this particular sediment type (see Section 2.6.1). Due to the high decay rate and the high sediment mobility (largely as suspended load) the flow was run only for three cycles.

In Tests 9, 10 and 11 there was a small increase in mound height after the first cycle, unlike the other tests where the mound height decreased monotonically. It should be noted that Test 11 was run with a mixture 50:50 of two median grain diameters ($d_{50}$ 0.230 and 0.454 mm).

Test 11 exhibited similar overall decay rates to Tests 10 and 13. Table 2.9 indicates that the heights decreased by between 36 to 41 % during Tests 10, 11 and 13. There was no major difference in the decay of mound height between the coarse sand and the sediment mixture.

Tests 12 and 13 were repetitions of Tests 9 (0.230 mm) and Test 10 (0.454 mm) respectively. The mound evolution during Test 12 and 13 is different to that in Test 9 and 10 over the first 2 cycles (20 min). The mound height oscillated from the start of the flow until the end of the second cycle. After that the height decreased monotonically like in other tests. Both pairs of tests, Test 9 and 12, and Test 10 and 13 show decay rates of the same order of magnitude (Figure 2.12 and Table 2.9). The repeated pairs of tests indicated similar percentage decrease in height with time (Table 2.9), thus confirming there is an element of repeatability in the tests regarding mound height.

### *Other exploratory tests*

During The second set of experiments a number of exploratory tests were carried out. These tests either did not start with a circular mound, or had significantly different conditions (Table 2.3). The purpose of these tests was to investigate the potential influence of the wall effect; the influence of the flow history (with the flow starting from the opposite direction); the mound morphodynamics under unidirectional flow; the reaction of the mound to variable unidirectional flow conditions; and the evolution of a mound on a flat mobile bed.

Test 14 involved an ellipse-shaped mound, under oscillatory flow conditions. The elliptical mound was built with a large amount of sediment, though its behaviour proved to be similar to that of the circular mound. Due to the larger amount of sediment used for this test in comparison to the standard bed mound, the sediment spread in the cross-flume direction, confirming that there were no significant wall effects (Figure 2.13).

Test 15 considered a sand bar across the flume under oscillatory flow (first cycle flow from east, and then alternating west and east), and run for six cycles. Test 16 had the same conditions as Test 15, except that the flow started from the opposite direction (first cycle flow from the west, and then alternating east and west) and lasted only two cycles. The aim was to study whether there was any difference in the bar evolution due to the initial flow direction (Figures 2.14a-2.15a and 2.14b-2.15b respectively). Results from Tests 15 and 16 do not show that the walls have a large effect on the evolution in the initial stages of the run. Moreover, the sand bar dynamics were fairly repeatable in a mirrored sense (i.e. given the initial flow direction when comparing the two tests). The tests also indicated that the sandbar deformation during the first half cycle had a strong influence on where sediment moved afterwards; i.e. there was a memory effect on the sand dynamics. The sandbar initially was 0.05 m height, with length 0.30 m along the $x$-axis, and 0.605 m along the $y$-axis (across the flume). Once the flow reversed and secondary flows developed with strong 3-D effects, the mound behaviour in Tests 15 and 16 started to diverge. During the first half cycle the sandbar flattened out to become a two-dimensional feature (of height about 0.02 m, and length ~ 0.5 m along the $x$-axis). During the first half cycle, the sandbar obstructed the flow, causing the velocity to increase locally by continuity and sand to move downstream of the crest of the sandbar, flattening it out. The transverse flow velocity profile across the width of the flume was almost uniform, without appreciable effects from the flume walls during the early stages of the run.

The repetition of Test 15 with the flow starting in the first half cycle from the west is shown in Test 16, Figure 2.16. The repeatability of the sand bar response is high in the initial stages of evolution. The sand travels in the flow direction and the bar becomes a flatter and smoother slope that spreads towards the direction of the flow. The direction of the flow in the first half cycle leaves an imprint on the mound, because it influences the sand transport and defines the direction in which the sand bar develops in the first stages (i.e. become a 1-D smooth slope of sand). Therefore, the initial evolution of the bar (when the sand bar is flattened, and the largest changes in height happen) is crucial for its subsequent evolution. There will be more sand towards the side where the flow acts first. That would be the imprint.

Test 17 comprised a circular mound under unidirectional flow conditions. A continuation of which was Test 18, that studied further the evolution when the flow conditions changed. The flow was stopped every five minutes in order to profile the mound. The peak velocity was 0.45 m/s for a total of 30 min (Figure 2.17). Initially the centroid of

the mound hardly migrated downstream, though the mound changed shape as energy was used to transform the initially circular/'conical' mound into a more hydrodynamically streamlined (crescent) shape. The mound then retained roughly the same shape and translated downstream with a small loss of sand towards the lee. It was then decided to increase the velocity from 0.45 m/s to 0.50 m/s for Test 18 (starting with the evolved mound geometry of Test 17). Figure 2.17f shows the initial shape of the mound at the start of Test 18, Figure 2.18 shows the mound evolution after a further thirty minutes of non-stop unidirectional flow. As the velocity changed, the mound reacted by changing shape again to accommodate the new conditions and became more streamlined (lost height by spreading), and developed longer appendages at its lee. The mound formed a barchan dune, and travelled downstream keeping its overall shape, but with a slight loss of sand transported in suspension (due to the strong vertical flows generated at the downstream end of the mound).

Test 19 comprised an initially circular mound on a flat mobile bed consisting of a 0.05 m layer (of the same sand as in Test 18). This mound was subject to oscillatory flow. Figure 2.19 shows the plan view after every half cycle. Early on, at the beginning of the first cycle, the flat bed became rippled. After the first cycle, the mound evolved to become another ripple and was indiscernible to the naked eye by the rippled bed when viewed from above. However, it was possible to identify which of the bed forms was the mound from the profiles and the side view. Afterwards, there was a net drift of the mound in the direction of the slightly stronger flows (to the west, left side in the images). Figures 2.20a and 2.20b show the side-view of the Reversing Flume, to put the mound in the context of the mobile bed.

### 2.6.3. Reversing Flume experiments: Phase II

During the second phase of the Reversing Flume experiments, a series of tests was carried out in order to gather information about the sediment transport corresponding to the sediment $d_{50}$, range of water depths and velocities typical of the UKCRF experiments. The intention of Phase II, was to provide a measure of the representative sediment transport for the experiments in the UKCRF, where due to the large scale of the facility it is difficult to visualise the sediment movement. Phase II was carried out solely for steady unidirectional flows.

### *Test rig*

The Reversing Flume test rig was modified in order to provide a source and a sink for the sediment to be released from and trapped respectively (Figure 2.21). A board (marked as 'a' in Figure 2.21) of the elevated false floor on the upstream side of the flume was removed to provide the sediment source (about 1.22 m long and 0.05 m deep). This space was filled up with sand that was levelled with the false floor. The sediment trap (marked with 'b' in Figure 2.21) on the downstream side of the flume (where another board with the same dimensions than that of the source, was removed). In the sediment trap, a purpose built mesh 0.45 m in width, and 0.10 m in length was placed horizontally, aligned as close to the wooden board as possible, to minimise flow disturbance. Between source and sink there was a 2.44 m long boarded area, marked with a grid . The sediment transported over this board travelled mainly as bed load . The sediment transport was assumed to start at the beginning of the gridded board, immediately after the sediment source. The sediment collected, was that settled over the central 0.40 m of the gridded board (avoiding the 0.1 m close to the flume walls) plus that captured by the mesh at the end of the board.

### *Experimental sediment transport rates*

Several tests were carried out to examine the range of movement of sediment of median size 0.454 mm and to determine the transport rate for this sediment size. Three tests were carried out for velocities of about 0.32, 0.41 and 0.52 m/s, and two water depths 0.10 and 0.20 m that cover the range of conditions in Phase I. During these tests an approximate value for the velocity for the threshold of sediment motion was identified. Further tests were undertaken to identify the error in the sediment transport due to ramping up the velocity to the selected peak value. The collected sediment was carefully gathered, dried and weighed after each test. Table 2.11 and Figures 2.22 and 2.23 present the results from these experiments.

Important information on the threshold of sediment movement was gathered during these experiments. Using Sandcalc[1] (Soulsby, 1997), the theoretical threshold velocity for this sediment grain size for a depth of water of 0.10 m, was 0.24 m/s and for a depth of 0.20 m, was 0.26 m/s. For a water depth of 0.10 m, the following was observed, using the criteria devised by Delft Hydraulics (1972) as cited by Van Rijn (1993, pp 4.8): No sediment movement occurred below 0.27 m/s; at 0.30 m/s there was occasional grain movement; at ~ 0.31 m/s, much of the surface of the sediment source began to move most of the time, corresponding to threshold of motion. For a water depth of 0.20 m, the observations were as

[1] Sandcalc: Sediment calculation software

follows: No movement was observed for a flow velocity below ~ 0.27 m/s; in the range 0.32 to 0.33 m/s, the grains occasionally moved; at about 0.36 m/s, much of the surface area of the sediment source moved most of the time, corresponding to the threshold of motion. The experimental thresholds of motion differed from the theoretical values calculated by Sandcalc. In all cases the sediment moved as bed load within the range of velocities considered. The highest sediment transport rates were achieved with the largest flow velocities and shallowest water depth. Transport rates at 0.10 m water depth were nearly twice those at 0.20 m water depth.

Due to the test arrangement, a noticeable amount of sediment moved before the desired velocity was reached. It was impossible to increase the velocity to reach the desired value sufficiently fast so as not to affect the sediment source, and so a number of short ramped tests were undertaken in order to correct the data for this effect. The short tests were carried out to correct the ~0.4 and ~0.5 m/s measured velocity tests. It was unnecessary to correct tests involving a velocity of ~0.3 m/s as this value was very close to the threshold velocity of sediment motion.

Sediment transport during the oscillatory tests is obviously not as straight forward as with unidirectional flow. In steady flow, sediment transport reaches an equilibrium state as long as there is a continuous source of sediment, and sufficient time. It is assumed that bed load transport reaches equilibrium quasi-instantaneously with the changes of flow velocity. The majority of the present experiments consider sediment transport in oscillatory flow, where the equilibrium state is not achievable. Hence the results of the experiments will provide a sensible first approximation by which to calibrate the numerical model. The values presented here are valid as first order estimates, though it should be noted that accurate measurement of sediment transport rates in unsteady flow is very difficult to achieve.

### *More about the sediment transport measurements*

The measurements from the Phase II of the Reversing Flume experiments are compared to two existing sediment transport formulae derived by Nielsen (1992) and Meyer-Peter-Müller (1948). Nielsen's formula is:

$$\Phi = 12\ \theta^{1/2}\left(\theta - \theta_{cr}\right) \tag{2.4}$$

where $\Phi$ is the dimensionless sediment transport rate, $\theta$ is the Shields parameter and $\theta_{cr}$ is its threshold value. Meyer-Peter-Müller formula (MPM) is:

$$\Phi = 8\ \left(\theta - \theta_{cr}\right)^{3/2}; \tag{2.5}$$

where $\theta_{cr}$ has a fixed value of 0.047.

During the experiments, the measured velocity was assumed to represent the depth-averaged velocity. Figure 2.22 shows the relationship between the measured transport and the measured velocity. A relationship of the type $\left(U^2 - U_{cr}^2\right)^{3/2}$ was fitted to the measured data, and the power of the velocity was found to be higher than the typical value. Paintal (1971) presented transport equations with very high powers in the shear stress when not taking the threshold shear stress into account. Paintal explains that extrapolating the Shields curve to the value of shear stress equivalent to $q_b = 0$ is not realistic, since there is movement of sediment particles at low values of shear stress, and there is no lower-limit of shear stress for which there is no particle movement. Although Paintal argues that there is no unique value under which there is no transport, he also agrees that it is necessary from a practical point of view to use a critical value and proposes to use the $\tau_0$ at the intersection between the curves of the power of 16 and 2.5. Some of Paintal's results are presented in Van Rijn (1993) and show that the transport is a function of a high power of the bed shear stress ($\tau_b = f(\theta)$, $\theta^{16}$), and hence the velocity is also subject to a high power $u^{32}$ (the drag coefficient is a function of the velocity, whilst the flow is rough turbulent, then the drag coefficient is constant and $\theta$ ($\sim u^2$). Due to this high power the sediment transport is very sensitive to the Shields parameter at low shear stresses, so the extrapolation can produce large errors (Van Rijn, 1993). A small change in shear stress will yield a large change in bed load transport (Paintal, 1971). The conditions that Paintal used to develop his formulae are, $\theta < 0.06$ and $d_{50}$ from 1 to 25 mm, fully turbulent flow, over artificially flattened floor. Paintal's estimation of the 16-power works only up to values of $\tau_{0*} = 0.05$ N/m$^2$, from then on the power would be 2.5.

The data collected in the Reversing Flume were converted into dimensionless sediment transport, to be plotted against the Shields parameter. The bed shear stress was estimated using:

$$\tau = \rho\ u_*^2 \tag{2.6}$$

where $\rho$ is the water density and $u_*$ is the friction velocity, that was calculated assuming a power law profile such as:

$$u_* = 1/7 \left( \frac{d_{50}}{H} \right)^{1/7} \overline{U} \qquad (2.7)$$

where $d_{50}$ is the median grain size, $H$ is the undisturbed water depth and $\overline{U}$ is the depth average velocity. The Shields parameter was calculated using the bed shear stress and then Equation 2.2. The measured dimensionless sediment transport was compared to two existing bed load sediment transport formulae from Nielsen and MPM (Figure 2.23). The results from the Reversing Flume experiments (Figure 2.23) agree with the predictions from the MPM formula, whilst the Nielsen data overestimates the transport.

## 2.7. Discussion and Conclusions

This section summarizes the main findings from the pilot experiments in the Reversing Flume.

### Oscillation period and test time length

The overall elapsed time had a major influence on the evolution of the mound, more so than the oscillation period. However, the mound evolution was not so sensitive to the oscillation period. The reduction in crest height of the mound showed a stronger dependence on the elapsed time than on the oscillation period.

It should be noted that the oscillation period chosen to run the majority of the tests was a compromise between capacity of the pumps (achieving flows that would provide sufficient motion of the sediment during the tests) and run time constraints.

### Sediment size

The coarser the grain size, the less likely sediment was to be moved at a certain flow velocity. Finer sediment was therefore more mobile than coarser sediment, and so the mound tended to evolve further into sand ripples and trails. For the majority of the tests, the sediment size was selected to minimize the suspended load, while achieving sufficient sediment motion as bed load to alter the mound morphology.

Mound height decay during these experiments was assumed (satisfactorily) to fit an exponential decaying function (Eq. 2.3). The rate of decrease in mound height depended on the sediment type, the finer the sediment the more rapid the rate of decrease for the same water depth. The long-term evolution of the mound showed that finer sand evolved into

smaller bed forms, such as ripples, in a shorter time. With the negative exponential function, a morphodynamic timescale ($T_h$) was inferred. $T_h$ reduced with sediment size, i.e. the temporal rate of decrease in mound height depended on the sediment size.

### Effects of the slope, depth of water and blockage of the water column

At lower water depths, the flow velocity increased and significant part of the water column was blocked by the mound (for a given size of mound). Under these conditions, the sediment mobility increased due to the faster flows and the presence of eddies shed by the mound. The slope of the mound (1:3) generated eddy structures (secondary flow structures) at the lee of the mound that enhanced sediment transport and controlled the long term evolution of the mound.

When the mound was constructed from coarser sand and subject to lower water depths (hence higher flow velocities) it evolved faster, breaking up into small bed forms. Higher flows meant increased mobility and a faster rate of mound decomposition.

### Repeatability of the tests

During the second set in Phase I, two tests were run to assess repeatability. These were run with the same initial conditions (as far as possible). In the initial stages, the mound crest height results were repeatable quantitatively, but progressively less so after about two or three cycles. The mound's crest height and the degree of decomposition of the mound decreased with elapsed time. Different local bed form patterns appeared, even if the overall mound structure was similar.

### Sediment transport

Sediment transport rates were calibrated against flow speed. The sediment threshold of motion has been identified based on visual observation broadly using the criteria devised by Delft Hydraulics (1972) as referred to by Van Rijn (1993, pp 4.8).

| Sediment type | Grain size $d_{50}$ (mm) | Settling velocity (*) $w_s$ (m/s) | Critical bed shear stress (*) $\tau_{cr}$ (N/m$^2$) |
|---|---|---|---|
| Anthracite | 0.800 | 0.040 | 0.102 |
| Garside 21 | 0.454 | 0.056 | 0.247 |
| 5/11B | 0.230 | 0.023 | 0.182 |
| Redhill 110 | 0.111 | 0.006 | 0.145 |

(*) Values derived according to the methods of Soulsby, 1997 – ($w_s$, pp102, $\tau_{cr}$, pp74 & 77).

**Table 2.1. Characteristics of sediments used in the pilot experiments**

| Test No | Sediment name | Oscillation period (min) | Initial water depth (m) | $d_{50}$ (mm) | Velocity § (m/s) | No. cycles | Test time (min) |
|---|---|---|---|---|---|---|---|
| 0 | G21 | 10 | 0.20 | 0.454 | 0.5 | 5.5 | 55 |
| 1 | G21 | 10 | 0.20 | 0.454 | 0.5 | 7 | 70 |
| 2 | G21 | 5 | 0.20 | 0.454 | 0.5 | 12 | 60 |
| 3 | G21 | 20 | 0.21 | 0.454 | 0.5 | 6 | 120 |
| 4 | G21 | 40 | 0.20 | 0.454 | 0.5 | 3 | 120 |
| 5 | 5/11B | 10 | 0.20 | 0.230 | 0.5 | 6 | 60 |
| 6 | G21 | 10 | 0.11 | 0.454 | 0.5 | 6 | 60 |

§ Target velocity. In all cases, the initial plan shape of the mound was circular.
G21: Garside 21 sand; 5/11B: 5/11B sand

**Table 2.2 Phase I – first set of experiments (15 March to 8 April 2004)**

| Test No | Sediment name | Initial plan shape | Initial water depth (m) | $d_{50}$ (mm) | Velocity § (m/s) | No. cycles | Test time (min) |
|---|---|---|---|---|---|---|---|
| 7 | Anthacite | Circular | 0.11 | 0.800 | 0.3 | 6 | 60 |
| 8 | R110 | Circular | 0.11 | 0.111 | 0.4 | 3 | 30 |
| 9 | 5/11B | Circular | 0.11 | 0.230 | 0.45 | 6 | 60 |
| 10 | G21 | Circular | 0.11 | 0.454 | 0.45 | 6 | 60 |
| 11 | G21+5/11B | Circular | 0.11 | 0.230+0.454 | 0.45 | 6 | 60 |
| 12 | 5/11B (r) | Circular | 0.11 | 0.230 | 0.45 | 10 | 100 |
| 13 | G21 (r) | Circular | 0.11 | 0.454 | 0.45 | 10 | 100 |
| 14 | G21 | Ellipse | 0.11 | 0.454 | 0.45 | 6 | 60 |
| 15 | G21 | Bar | 0.11 | 0.454 | 0.45 | 6 | 60 |
| 16 | G21 | Bar | 0.11 | 0.454 | 0.45 | 2 | 20 |
| 17 | G21 | Circular | 0.11 | 0.454 | 0.45 (∇) | - | 30 |
| 18 | G21 | Circular | 0.11 | 0.454 | 0.5 (∇) | - | 34 |
| 19 | Mobile bed (G21) | Circular | 0.16 | 0.454 | 0.45 | 6 | 60 |

G21: Garside 21; 5/11B: 5/11B sand; R110: Redhill 110; (∇) unidirectional flow; (r) repeated test.
§ Target velocity.

**Table 2.3. Phase I – second set of experiments (4 to14 May 2004). $T_E$ = 10 min.**

| Sample No. | Depth of water (m) | Velocity (*) (m) | Weight (kg) | Time (sec) |
|---|---|---|---|---|
| 1 | 0.100 | 0.54 | 2.41 | 648 |
| 2 | 0.100 | 0.40 | 0.29 | 900 |
| 3 | 0.100 | 0.35 | 0.08 | 1902 |
| 5 | 0.200 | 0.55 | 1.16 | 632 |
| 6 | 0.200 | 0.43 | 0.17 | 900 |
| 7 | 0.200 | 0.39 | 0.04 | 1967 |

(*) Depth averaged velocity;

All tests in Phase II were carried out with sand of median grain diameter $d_{50}$ = 0.454 mm

**Table 2.4. Tests carried out in Phase II (10 to 15 June 2004)**

| Test No. | Oscillation period (min) | Initial height (m) $h_0(t_0)$ | Height (m) t =10 min | Height (m) t = 120 min | % decrease Δt =(10'-0') | % decrease Δt =(20'-10') |
|---|---|---|---|---|---|---|
| 1 | 10 | 0.054 | 0.051 | 0.031 | 2 | 40 |
| 2 | 5 | 0.060 | 0.057 | 0.037 | 12 | 35 |
| 3 | 20 | 0.050 | 0.045 | 0.034 | 6 | 24 |
| 4 | 40 | 0.051 | 0.048 | 0.025 | 4 | 48 |
| 5 | 10 | 0.065 | 0.056 | 0.010 | 8 | 82 |
| 6 | 10 | 0.031 | 0.030 | 0.026 | 44 | 13 |

**Table 2.5 Decay in height, Phase I – first set of experiments**

| Test No. | Oscillation period (min) | Initial height $h_0(t_0)$ (m) | $R^2$ | Morphodynamic timescale $T_m$ (hr) |
|---|---|---|---|---|
| 1 | 10 | 0.054 | 0.998 | 3.58 |
| 2 | 5 | 0.060 | - | 4.07 |
| 3 | 20 | 0.050 | 0.943 | 6.28 |
| 4 | 40 | 0.051 | - | 2.86 |
| 5 | 10 | 0.065 | - | 1.04 |
| 6 | 10 | 0.031 | - | 2.88 |

**Table 2.6 Morphodynamic timescale as calculated from Phase I - first set of the Reversing Flume experiments**

| Test No. | Sediment type | $U_{cr}$ (m/s) § | $U^*$ (m/s) | $U/U_{cr}$ |
|---|---|---|---|---|
| 7 | Anthracite | 0.141 | 0.20 | 1.42 |
| 8 | Redhill 110 | 0.223 | 0.32 | 1.43 |
| 9 | 5/11B | 0.225 | 0.37 | 1.64 |
| 10 | Garside 21 | 0.238 | 0.35 | 1.47 |
| 11 | Mixed sediment | 0.238 | 0.36 | 1.51 |
| 12 | 5/11B | 0.225 | 0.37 | 1.64 |
| 13 | Garside 21 | 0.238 | 0.36 | 1.51 |

* (actual velocity, averaged through 6 cycles); (§) Calculated using Sandcalc

**Table 2.7. Threshold velocity and actual velocity used in the tests**

| | Probe 0 | | | Probe 1 | | |
|---|---|---|---|---|---|---|
| | Flow towards (m/s) | | | Flow towards (m/s) | | |
| Test No. | East | West | % | East | West | % |
| 7 | 0.20 | 0.23 | 12 | 0.20 | 0.21 | 4 |
| 10 | 0.33 | 0.35 | 5 | 0.37 | 0.37 | 0.5 |
| 12 | 0.33 | 0.40 | 17 | 0.37 | 0.40 | 7 |
| 13 | 0.33 | 0.40 | 17 | 0.37 | 0.39 | 6 |

**Table 2.8. Average flow speed to the east and west showing that flow to the west is slightly stronger.**

| Test No | $d_{50}$ (mm) | Initial height (m) $h_0(t_0)$ | Height (m) t =10' | Height (m) t = 60' | %decrease Δt =(10'-0') | % decrease Δt =(20'-10') | |
|---|---|---|---|---|---|---|---|
| 7 | 0.800 | 0.053 | 0.052 | 0.042 | 2 | 20 | |
| 8 | 0.110 | 0.049 | 0.032 | 0.030* | 34 | 7 | |
| **9** | **0.230** | **0.051** | **0.052** | **0.024** | -2 | 54 | ◊ |
| **10** | **0.454** | **0.052** | **0.055** | **0.035** | -5 | 36 | ♦ |
| 11 | 0.230+0.454 | 0.051 | 0.053 | 0.036 | -3 | 32 | |
| **12** | **0.230** | **0.051** | **0.051** | **0.024** | 2 | 52 | ◊ |
| **13** | **0.454** | **0.052** | **0.050** | **0.029** | 5 | 41 | ♦ |

(*) t = 30 min (end of simulation)

**Table 2.9 Decay in height, Phase I - second set of the Reversing Flume experiments**

| Test No. | Grain size ($d_{50}$) | Initial height $h_0(t_0)$ | $R^2$ | Morphodynamic timescale $T_m$ (hr) |
|---|---|---|---|---|
| 7 | 0.800 | 0.054 | - | 3.83 |
| 8 | 0.111 | 0.033 | - | 4.49 |
| 9 | 0.230 | 0.061 | - | 1.07 |
| 10 | 0.454 | 0.060 | - | 1.90 |
| 11 | 0.230+0.454 | 0.057 | - | 2.14 |
| 12 | 0.230 | 0.056 | 0.951 | 1.31 |
| 13 | 0.454 | 0.049 | 0.919 | 1.96 |

**Table 2.10 Morphodynamic timescale Phase I (second set of the Reversing Flume experiments)**

| Sample No. | Water Depth (m) | Velocity (*) (m/s) | STR (i) (kg $m^{-1}$ $s^{-1}$) | STR (i) ($m^3$ $m^{-1}$ $s^{-1}$) |
|---|---|---|---|---|
| 1 | 0.10 | 0.54 | 0.013993 | 5.28E-06 |
| 2 | 0.10 | 0.40 | 0.000795 | 3.00E-07 |
| 3 | 0.10 | 0.35 | 0.000107 | 3.80E-08 |
| 5 | 0.20 | 0.55 | 0.006890 | 2.60E-06 |
| 6 | 0.20 | 0.43 | 0.000565 | 2.13E-07 |
| 7 | 0.20 | 0.39 | 0.000054 | 2.00E-08 |

(*) Depth averaged velocity;

(i) STR: Sediment transport rate

**Table 2.11 Results of sediment transport rate experiments (Phase II)**

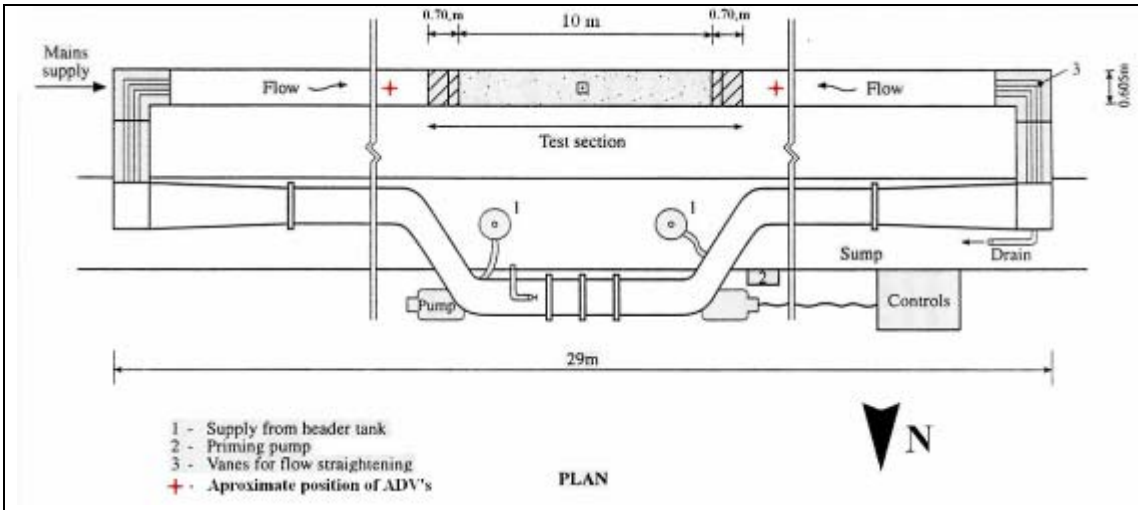


Figure 2.1. Layout and dimensions of the Reversing Flume (modified from Escarameia, 1999)

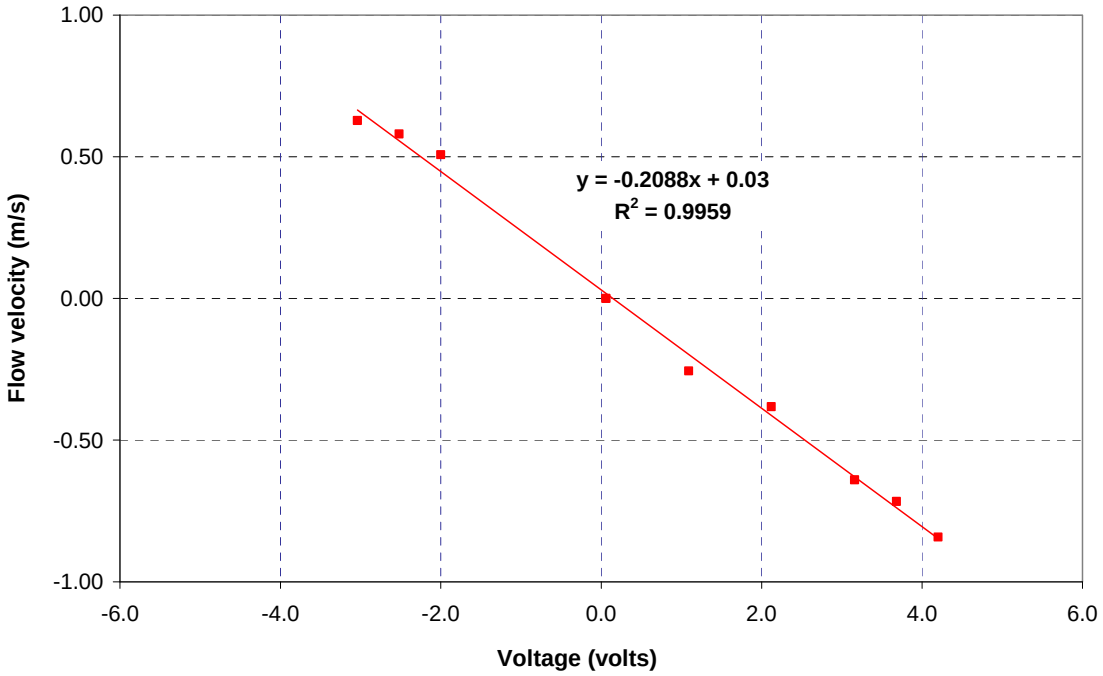


Figure 2.2a Voltage-velocity calibration curve for 0.10 m water depth

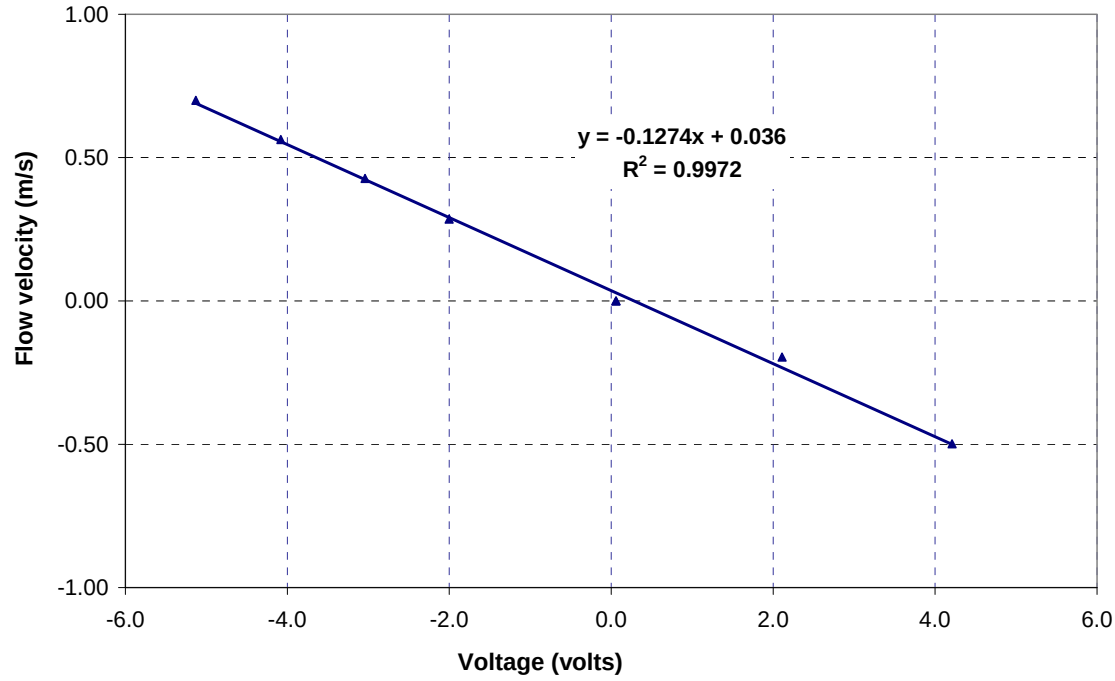


Figure 2.2 b Voltage-velocity calibration curve for 0.20 m water depth

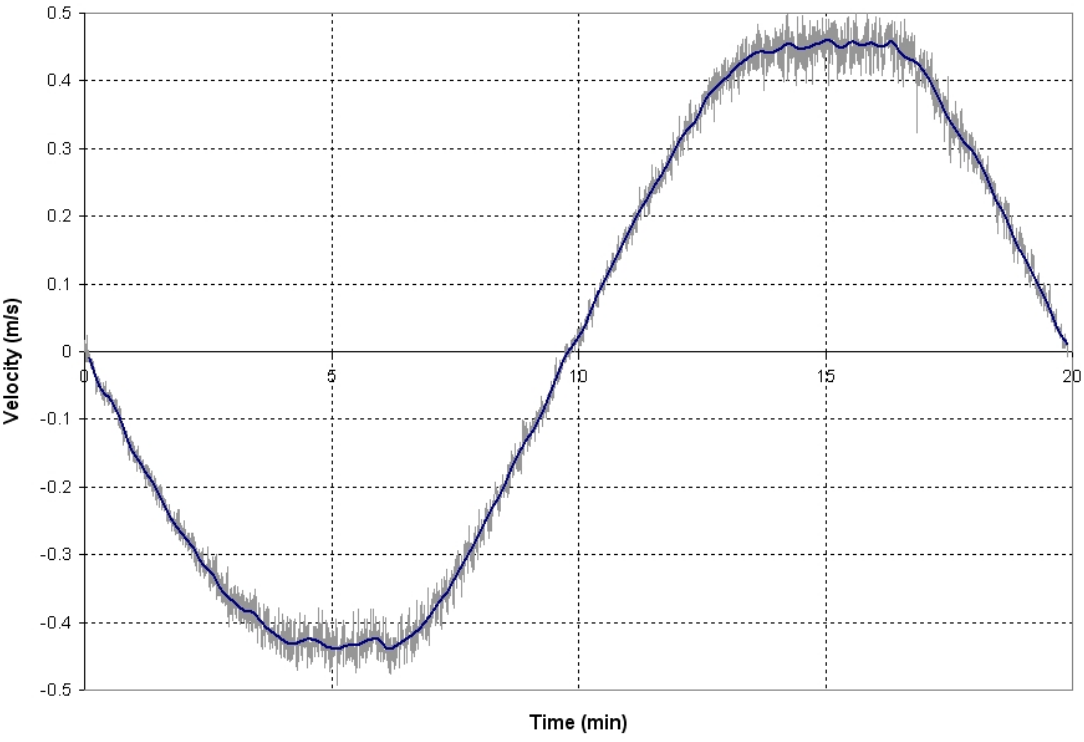


Figure 2.3. Velocity time history measured during a typical oscillatory flow test.

2.4a - Test1 – $T$ = 10 min
$d_{50}$ = 0.454 mm H = 0.2 m

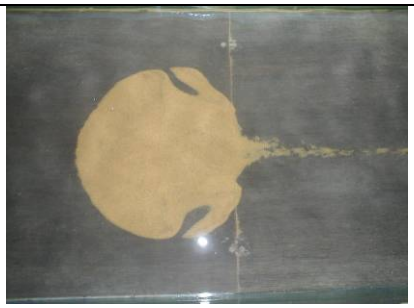

2.4b - Test 2 – $T$ = 5 min
$d_{50}$ = 0.454 mm H = 0.2 m

2.4c - Test 3 – $T$ = 20 min
$d_{50}$ = 0.454 mm H = 0.2 m

2.4d - Test 4 – $T$ = 40 min
$d_{50}$ = 0.454 mm H = 0.2 m

2.4e - Test 5 – $T$ = 10 min
$d_{50}$ = 0.230mm H = 0.2 m

2.4f - Test 6 – $T$ = 10 min
$d_{50}$ = 0.454 mm H = 0.1 m

Figure 2.4 Evolution of the bed mound after one cycle (elapsed time) (Phase I – first set). $T$ is the period of oscillation.

Figure 2.4g - Side view of the Reversing Flume, corresponding to Test 6 after one cycle.

2.5a - Test1 – $T$=10 min
$d_{50}$ = 0.454 mm H = 0.2 m

2.5b - Test 2 – $T$ =5 min
$d_{50}$ = 0.454 mm H = 0.2 m

2.5c - Test 3 – $T$ =20 min
$d_{50}$ = 0.454 mm H = 0.2 m

2.5d - Test 4 – $T$ =40 min
$d_{50}$ = 0.454 mm H = 0.2 m

2.5e - Test 5 – $T$ =10 min
$d_{50}$ = 0.230 mm H = 0.2 m

2.5f - Test 6 – $T$ =10 min
$d_{50}$ = 0.454 mm H = 0.1 m

Figure 2.5 Evolution of the bed mound after 10 min elapsed time (Phase I – first set). $T$ is the period of oscillation.

2.6a - Test1 – $T$ = 10 min
$d_{50}$ = 0.454 mm H = 0.2 m

2.6b - Test 2 – $T$ = 5 min
$d_{50}$ = 0.454 mm H = 0.2 m

2.6c - Test 3 – $T$ = 20 min
$d_{50}$ = 0.454 mm H = 0.2 m

2.6d - Test 4 – $T$ = 40 min
$d_{50}$ = 0.454 mm H = 0.2 m

2.6e - Test 5 – $T$ = 10 min
$d_{50}$ = 0.230 mm H = 0.2 m

2.6f - Test 6 – $T$ = 10 min
$d_{50}$ = 0.454 mm H = 0.1 m

Figure 2.6 Evolution of the bed mound after 60 min elapsed time (Phase I – first set). $T$ is the period of oscillation.

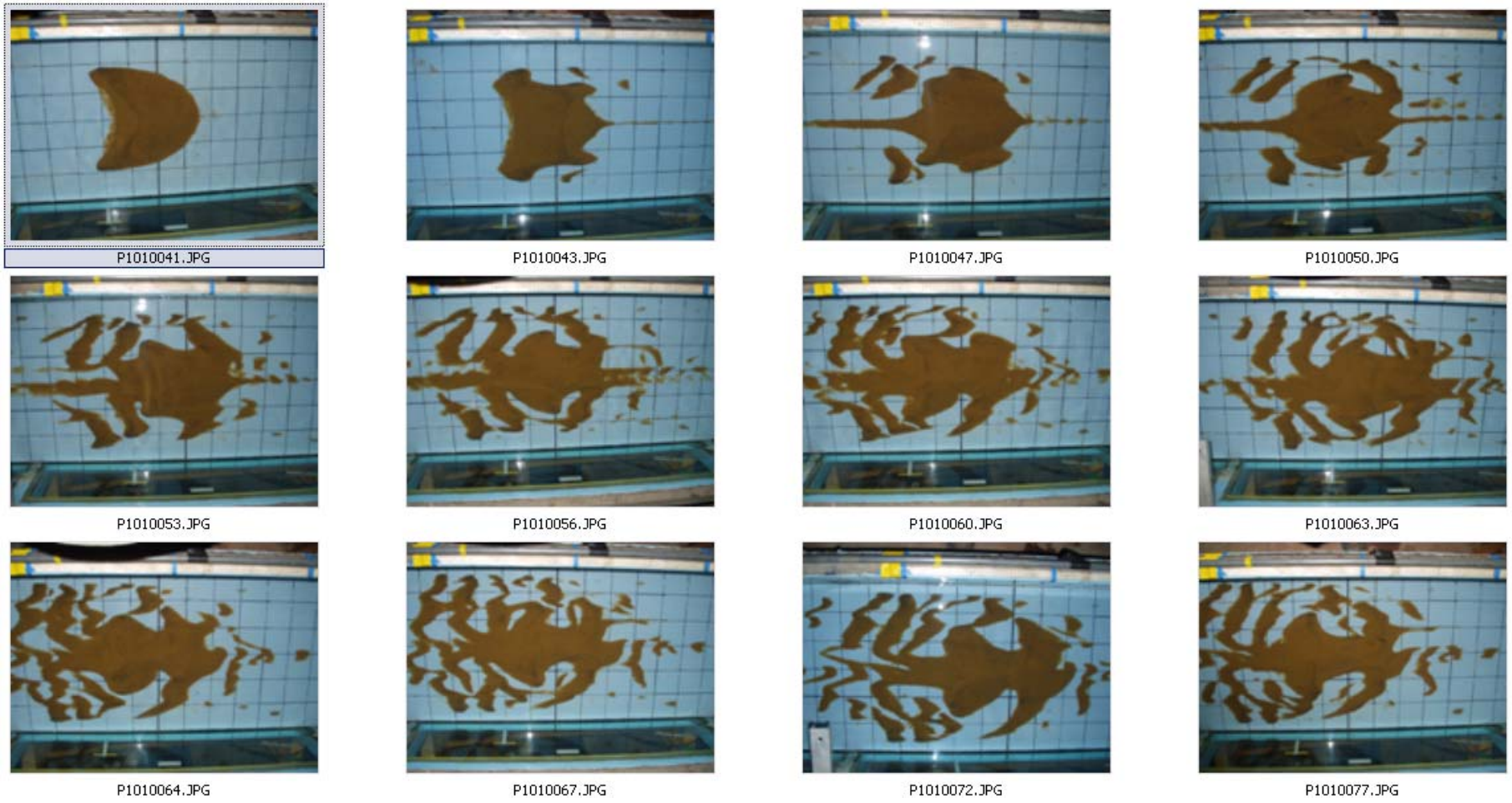


Figure 2.7 Bed evolution of circular mound (from left to right, top to bottom) Test 10, *T*=10 min; water depth = 0.10 m; $d_{50}$ = 0.454 mm; and target velocity 0.45 m/s.

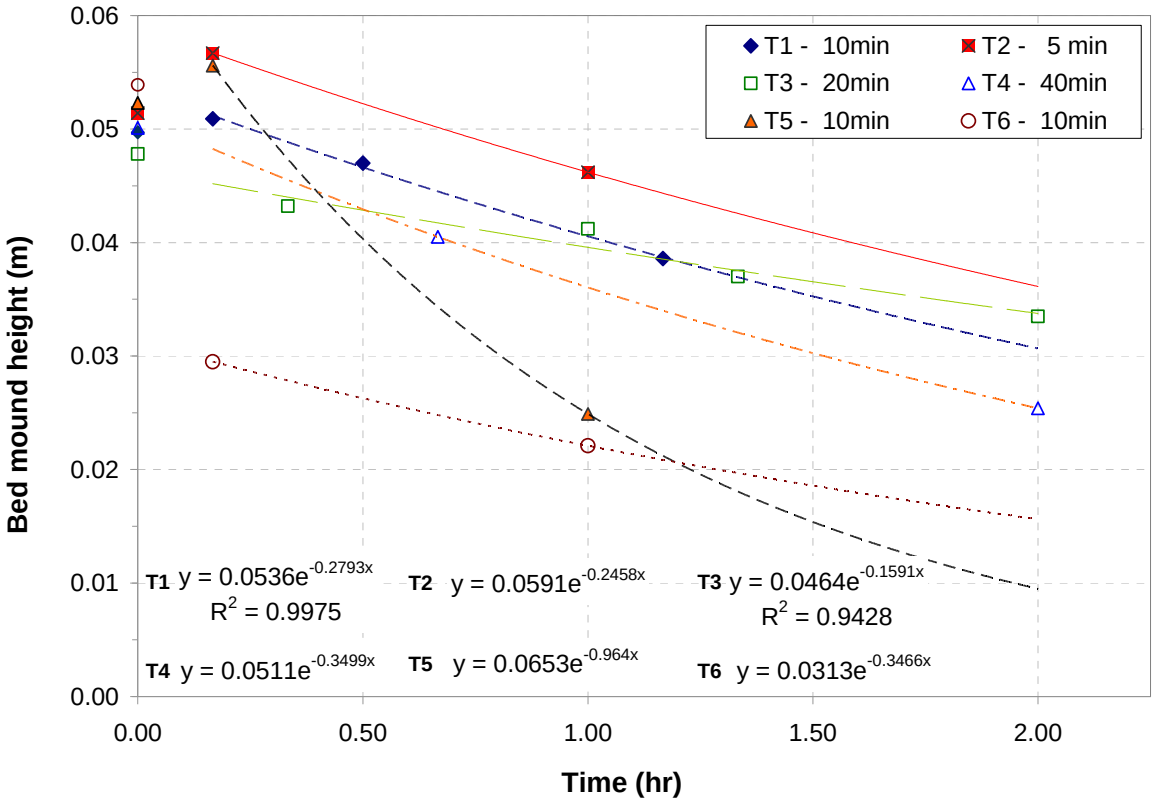


Figure 2.8 Decay rates of maximum mound height with time (Phase I – first set) – height of mound at apex

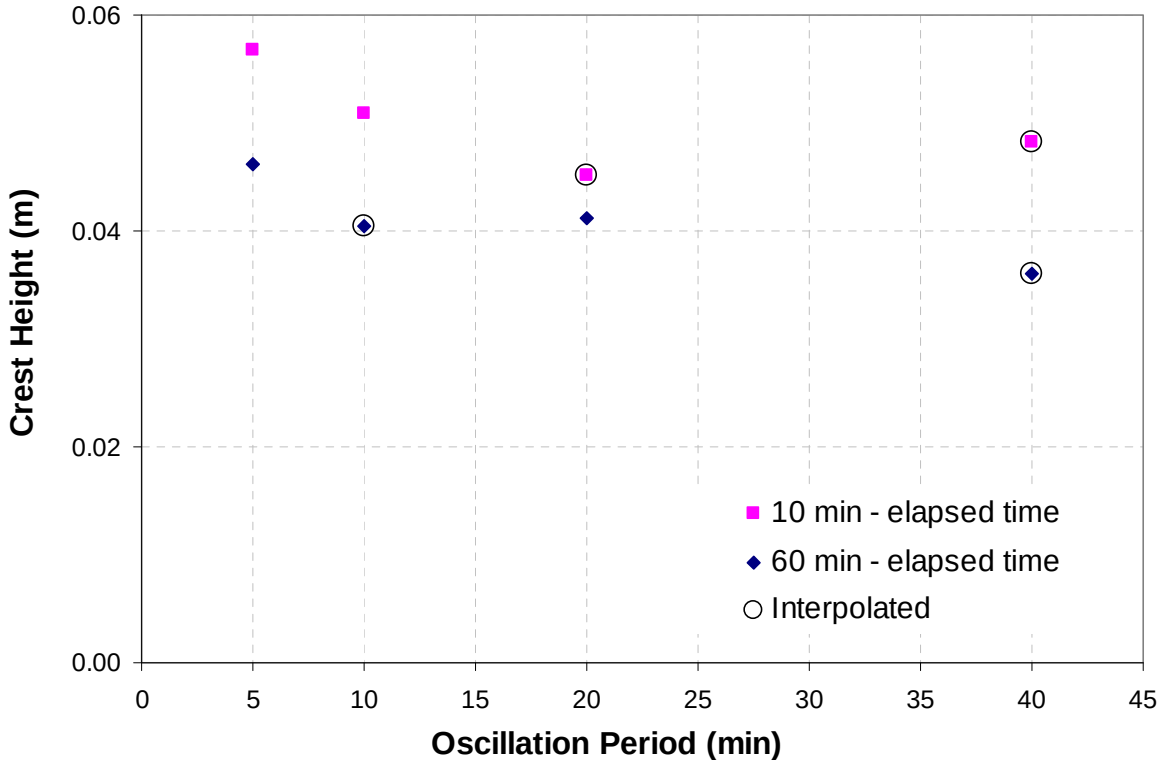


Figure 2.9 Mound crest height against oscillation period for sand grain size of 0.454 mm, 0.20 m water depth.

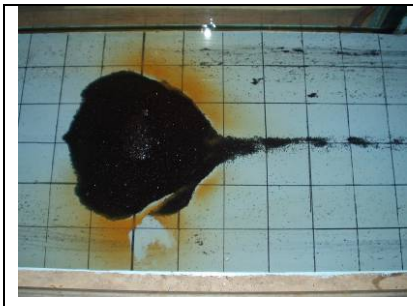

2.10a Test7 – $d_{50}$= 0.800 mm

2.10b Test 8 – $d_{50}$= 0.110 mm

2.10c Test 9 – $d_{50}$= 0.230 mm

2.10d Test 10 – $d_{50}$= 0.454 mm

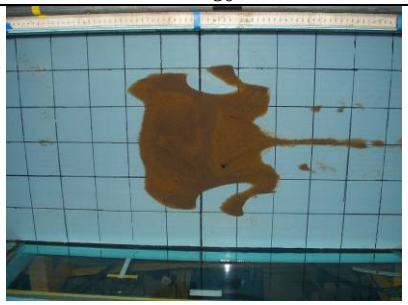

2.10e Test 11 - $d_{50}$= 0.230 + 0.454 mm

2.10f Test 12 – $d_{50}$= 0.230 mm

2.10g Test 13 – $d_{50}$= 0.454 mm

The tests were run with $H$ = 0.1 m, $T$ = 10 min and approximately $U$ = 0.45 m/s.

Figure 2.10 Evolution of the bed mound after 10 min elapsed time (Phase I – second set).

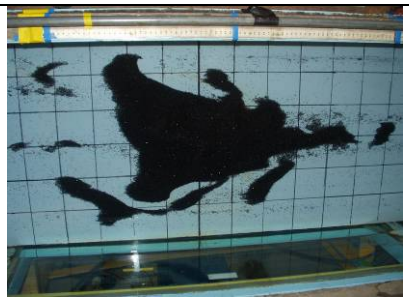

2.11a Test7; $d_{50}$= 0.800 mm

2.11c Test 9; $d_{50}$= 0.230 mm

2.11d Test 10; $d_{50}$= 0.454 mm

2.11e Test 11; $d_{50}$= 0.230+0.454 mm

2.11f Test 12; $d_{50}$= 0.230 mm

2.11g Test 13; $d_{50}$= 0.454 mm

Figure 2.11 Evolution of the bed mound after 60 min elapsed time (Phase I – second set). Note that there is no image for Test 8 (it run for 30 min elapsed time).

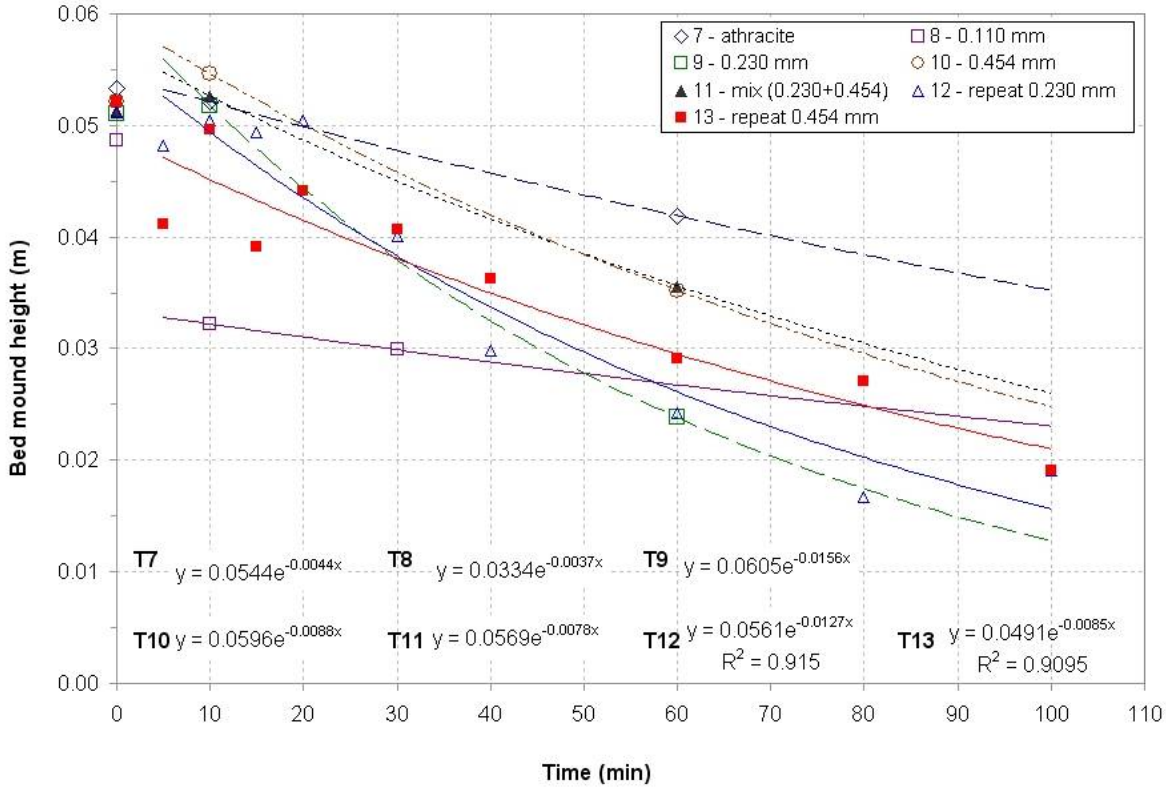


Figure 2.12. Evolution of mound height with time for Tests 7 to 13 (Phase I – second set).

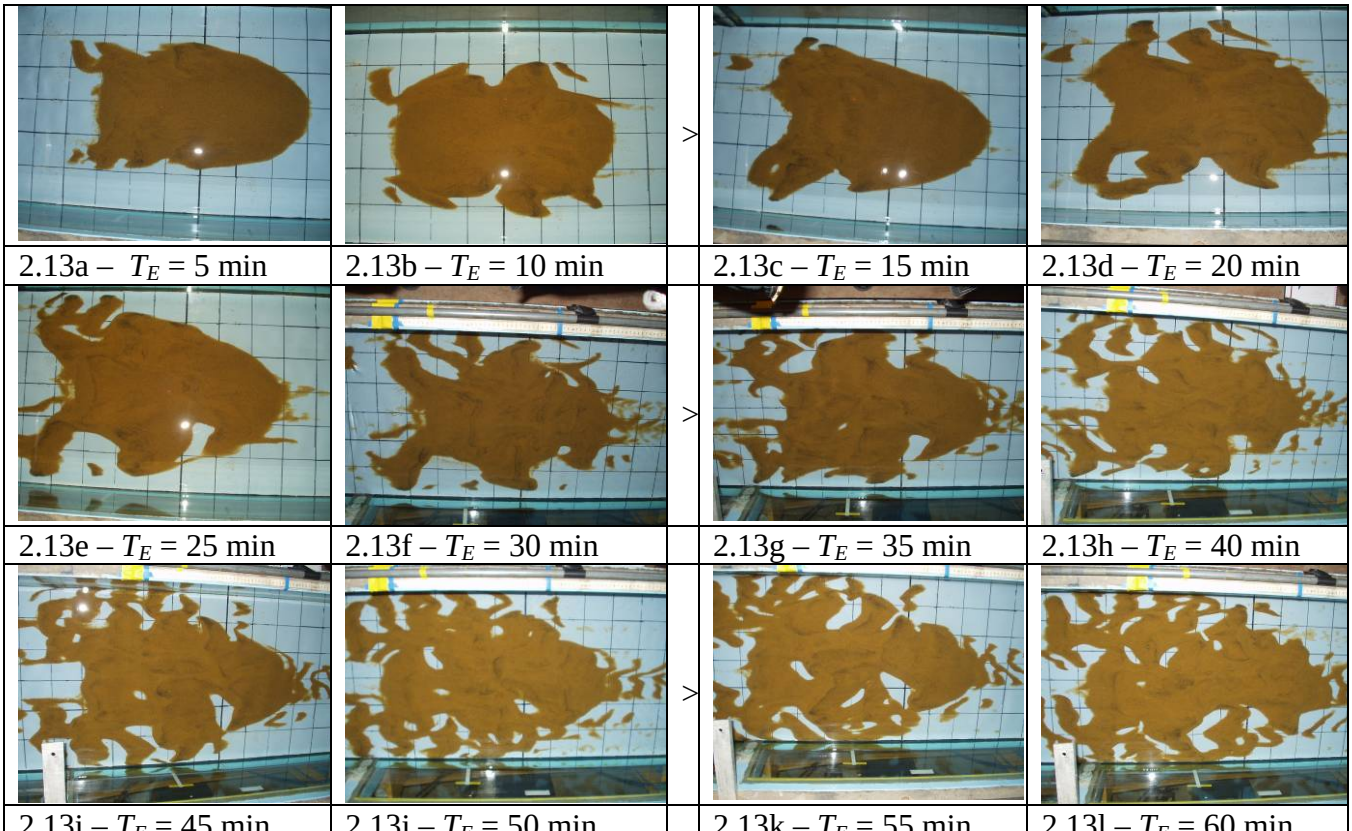

| | | | | |
|---|---|---|---|---|
| 2.13a – $T_E$ = 5 min | 2.13b – $T_E$ = 10 min | > | 2.13c – $T_E$ = 15 min | 2.13d – $T_E$ = 20 min |
| 2.13e – $T_E$ = 25 min | 2.13f – $T_E$ = 30 min | > | 2.13g – $T_E$ = 35 min | 2.13h – $T_E$ = 40 min |
| 2.13i – $T_E$ = 45 min | 2.13j – $T_E$ = 50 min | > | 2.13k – $T_E$ = 55 min | 2.13l – $T_E$ = 60 min |

Figure 2.13 Bed evolution of an elliptical mound (Test 14) from left to right and top to bottom. ($T_E$, elapsed time), $H$ = 0.1 m, $d_{50}$ = 0.454 mm and approximately $U$ = 0.45 m/s.

**Test 15**

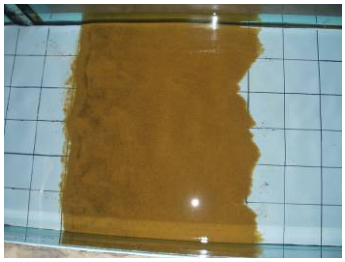

2.14a – $T_E$ = 5 min

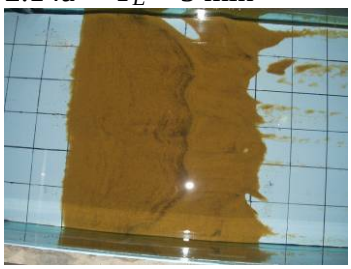

2.14b – $T_E$ = 10 min

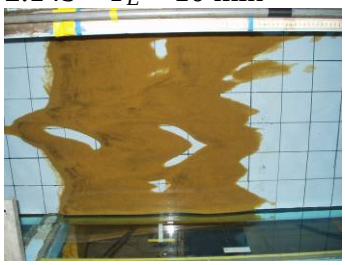

2.14c – $T_E$ = 15 min

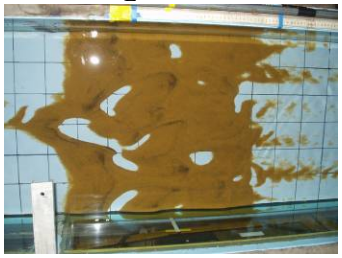

2.14d – $T_E$ = 20 min

Figure 2.14 Test 15


**Test 16**

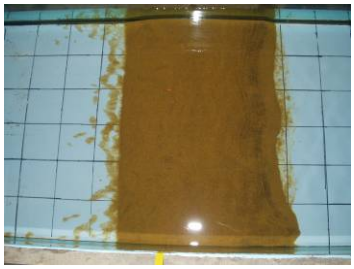

2.15a – $T_E$ = 5 min

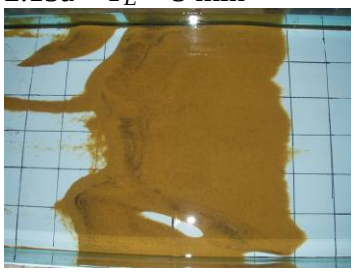

2. 15b – $T_E$ = 10 min

2. 15c – $T_E$ = 15 min

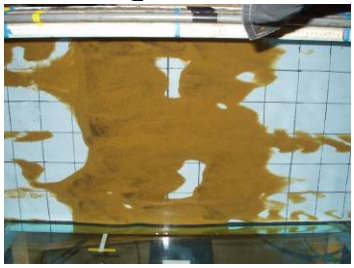

2. 15d – $T_E$ = 20 min

Figure 2.15 Test 16

Comparison of the bed evolution of a sand bar across the flume from $T_E$ = 5 min to $T_E$ = 20 min of Test 15 (flow starting from the east) and Test 16 (flow starting from the west).
$T$ = 10 min, $H$ = 0.1 m, $d_{50}$ = 0.454 mm and approximately $U$ = 0.45 m/s.

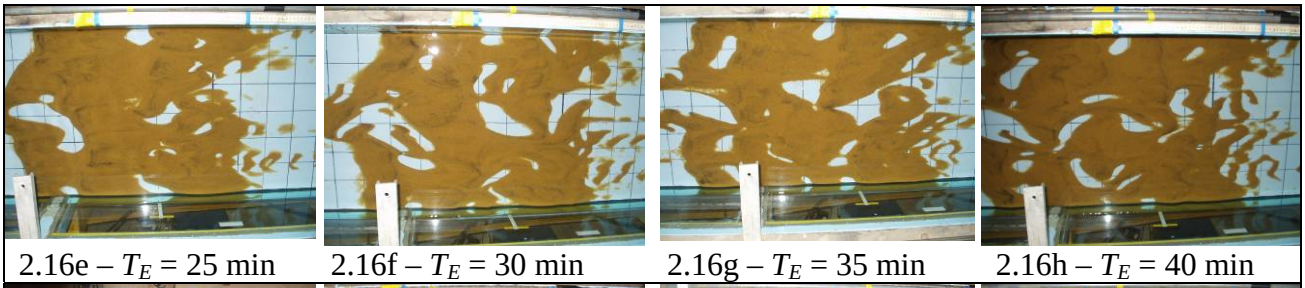

2.16e – $T_E$ = 25 min | 2.16f – $T_E$ = 30 min | 2.16g – $T_E$ = 35 min | 2.16h – $T_E$ = 40 min

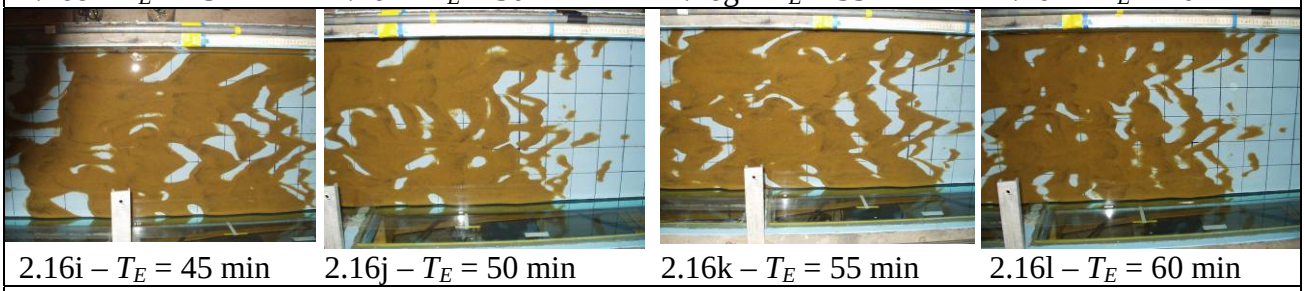

2.16i – $T_E$ = 45 min | 2.16j – $T_E$ = 50 min | 2.16k – $T_E$ = 55 min | 2.16l – $T_E$ = 60 min

Figure 2.16 Bed evolution of a bar across the flume (Test 15) from $T_E$ = 25 min to $T_E$ = 60 min, flow initially from east ($T_E$, elapsed time), $T$ = 10 min, $H$ = 0.1 m, $d_{50}$ = 0.454 mm.

2.17a - $T_E$ = 5 min | 2.17b - $T_E$ = 10 min | 2.17c - $T_E$ = 15 min

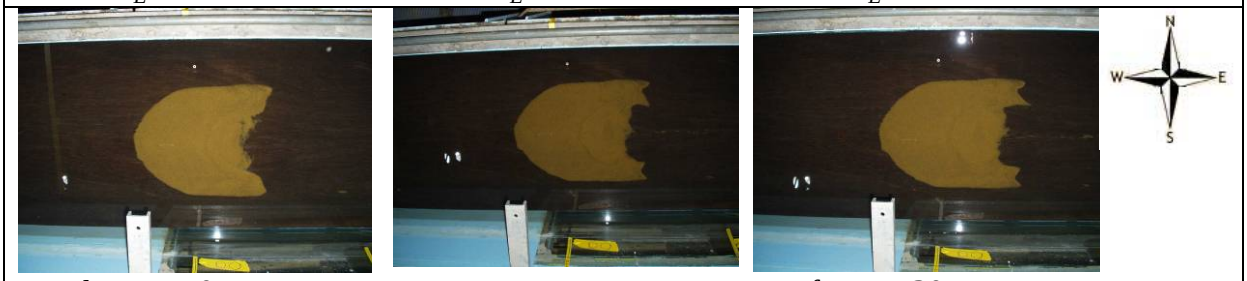


2.17d - $T_E$ = 20 min | 2.17e - $T_E$ = 25 min | 2.17f - $T_E$ = 30 min

Figure 2.17 Bed evolution of a circular mound in unidirectional flow conditions (Test 17), flow from the left, (peak velocity 0.45m/s) ($T_E$, elapsed time), $H$ = 0.1 m, $d_{50}$ = 0.454 mm.

Plate 2.18 Bed evolution (Test 18, continuation of Test 17), flow from the left (peak velocity = 0. 5m/s), $T_E$ = 60 min, $H$ = 0.1 m, $d_{50}$ = 0.454 mm.

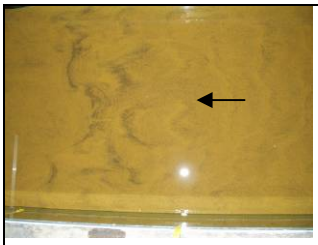

$T_E$ = 5 min
1st cycle

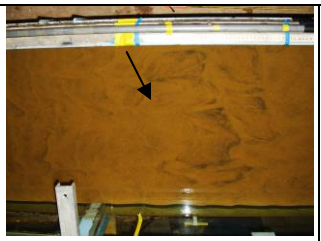

$T_E$ = 10 min

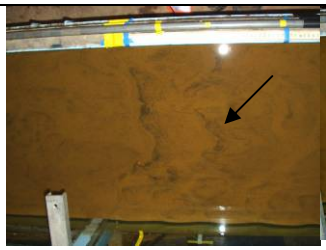

$T_E$ = 15 min
2nd cycle

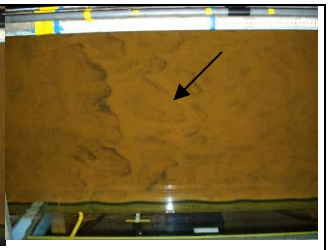

$T_E$ = 20 min

$T_E$ = 25 min
3rd cycle

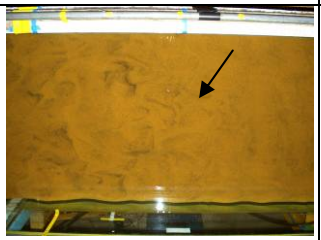

$T_E$ = 30 min

$T_E$ = 35 min
4th cycle

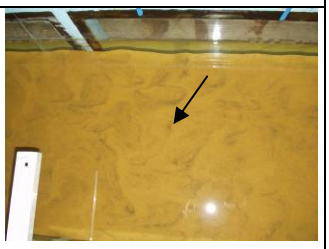

$T_E$ = 40 min

$T_E$ = 45 min
5th cycle

$T_E$ = 50 min

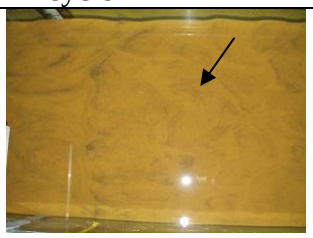

$T_E$ = 55 min
6th cycle

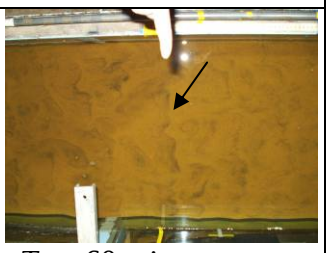

$T_E$ = 60 min

Figure 2.19 Bed evolution of a circular mound on mobile bed (Test 19), from left to right and top to bottom, flow initially from the right ($T_E$, elapsed time), $T$ = 10 min, $H$ = 0.1 m, $d_{50}$ = 0.454 mm.

Profiling at $T_E$ = 10 min (from the left)

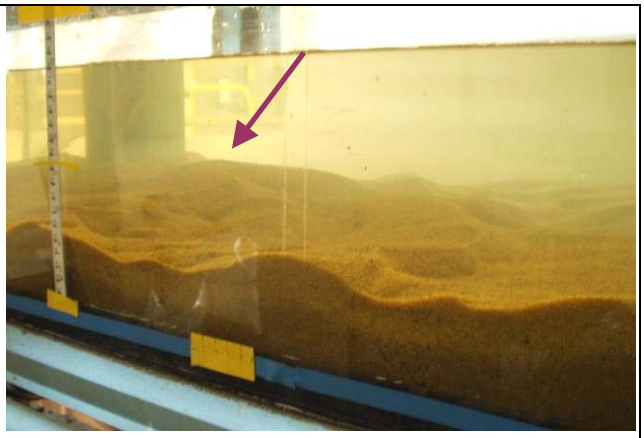

$T_E$ = between 50 - 60 min (flow from the right)

Plate 2.20 Side views of the Reversing flume, bed evolution of a circular mound on mobile bed (Test 19), ($T_E$, elapsed time).

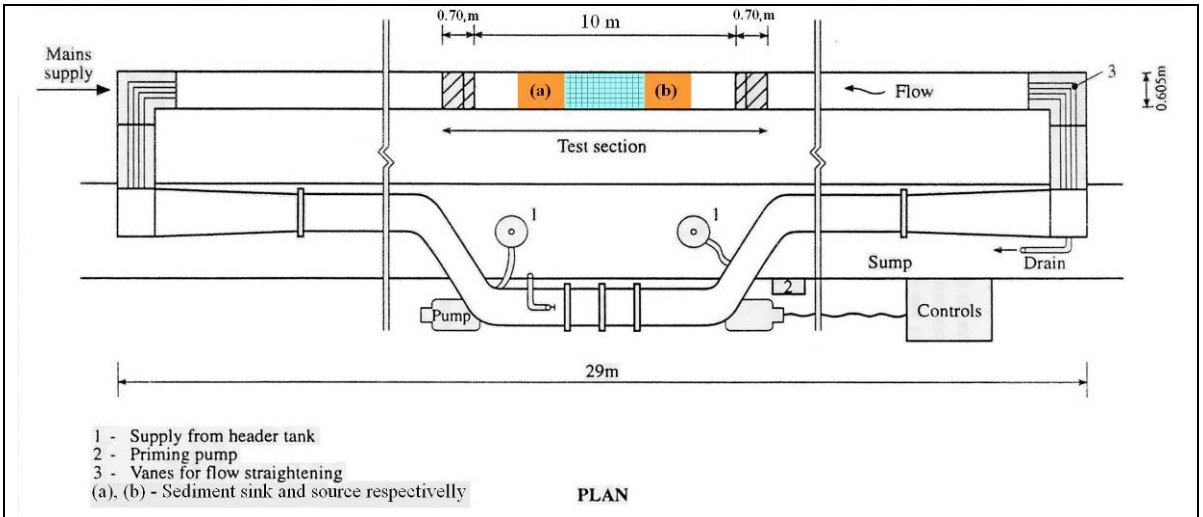


Figure 2.21 Layout of the Reversing Flume set up for Phase II (modified from Escarameia, 1999).

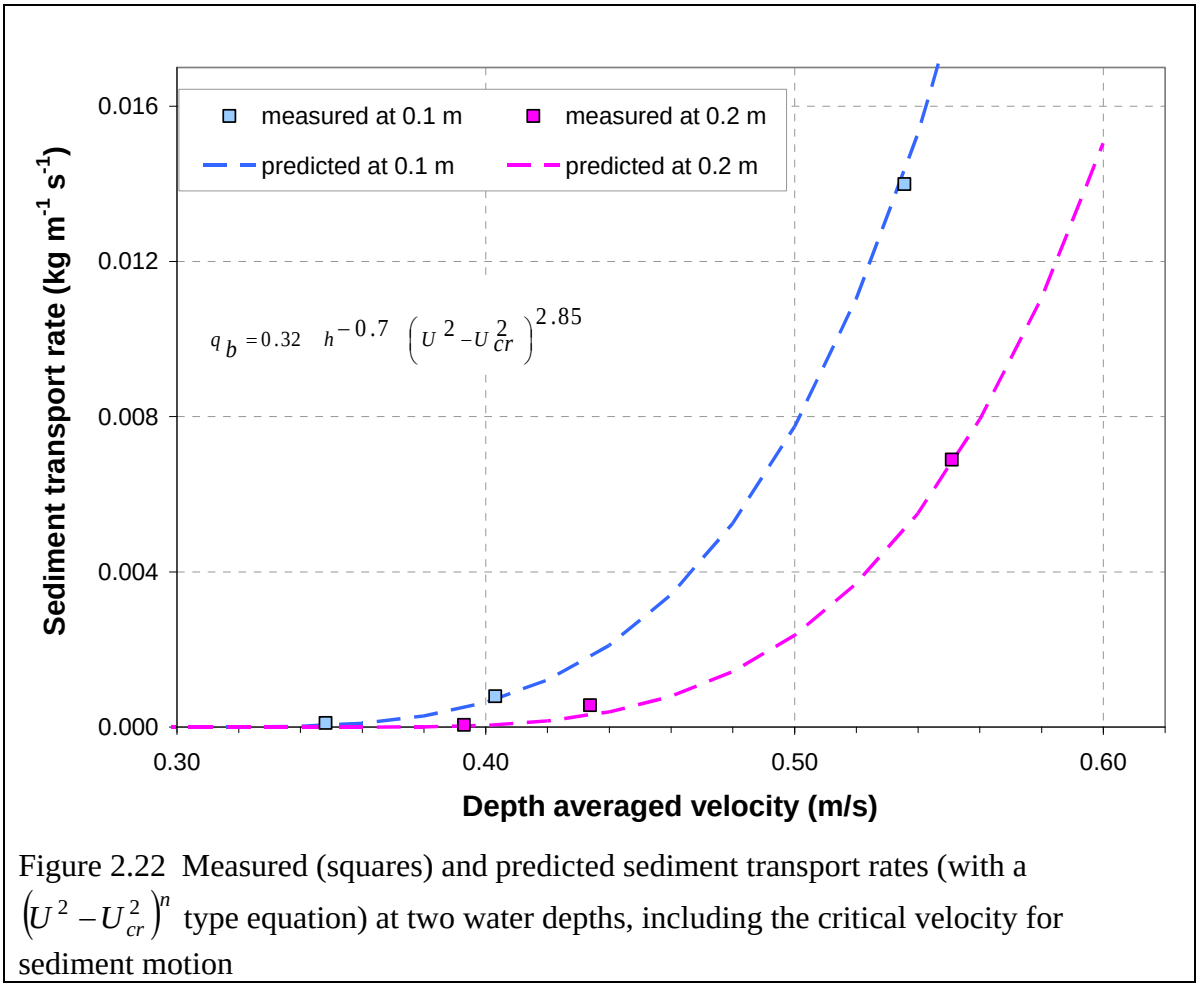


Figure 2.22 Measured (squares) and predicted sediment transport rates (with a $\left(U^2 - U_{cr}^2\right)^n$ type equation) at two water depths, including the critical velocity for sediment motion

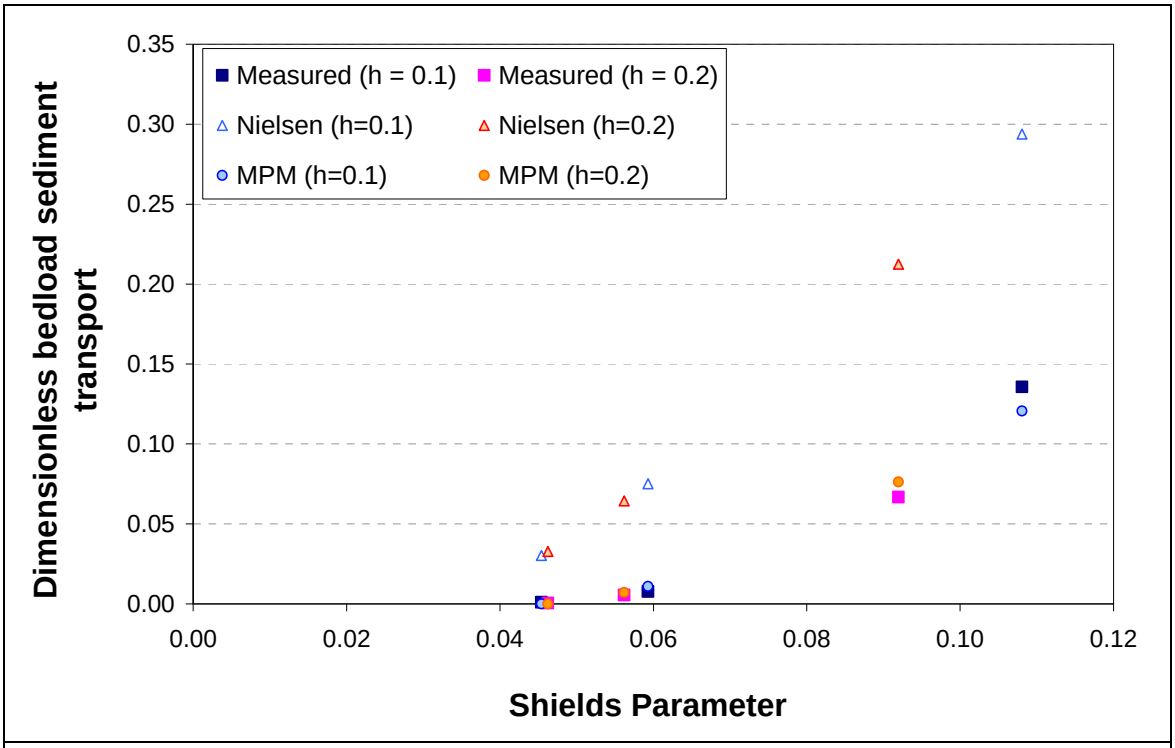


Figure 2.23 Measured (squares) and predicted dimensionless bed load sediment transport rates using Nielsen (triangles) and MPM (circles) at two water depths.

# 3. UK COASTAL RESEARCH FACILITY

This chapter presents details of laboratory-scale physical model tests carried out in the UK Coastal Research Facility (UKCRF) at HR Wallingford from August 2004 to January 2005. The results from the Reversing Flume experiments (presented in Chapter 2) fed back in the planning of these full-scale experiments. The chapter contains the description of the UKCRF, the layout of the test rig, the instrumentation, the methodology and procedure followed during the data collection phase.

The physical tests focused on the evolution of an idealized large-scale feature (sandbank or spoil heap). The persistence of sandbanks and their evolution relies on the growth and destruction mechanisms being in equilibrium. During the experiments only destruction mechanisms were present, leading to the gradual breaking down of the bed mound. The lack of sediment sources and growth mechanisms means that the evolution of the bed mound corresponds more closely to that of a spoil heap.

During the UKCRF experiments, tests were run with different characteristics:

- Initial bed mound shapes: Circular plan view with (i) cosine and (ii) Gaussian cross-section, and elliptical plan view with triangular cross-sections.
- Initial heights: Submerged, surface touching, surface piercing.
- Flow conditions: Steady unidirectional and oscillatory flow.
- Bed conditions: Fixed non-erodible and mobile bed.

## *3.1. Objectives of the large-scale experiments*

The overall aim of the present research is to improve the understanding of the long-term evolution of sandbanks. To achieve this aim, high quality data were obtained from large-scale physical model tests in the U.K. Coastal Research Facility (UKCRF) on the behaviour of an idealised sandbank (bed mound) under controlled conditions. These benchmark data are particularly useful for the calibration and verification of 2-DH and 3-D numerical models used to predict coastal morphodynamic processes such as the evolution of bed mound.

## *3.2. Description of the UK Coastal Research Facility.*

The U.K. Coastal Research Facility (UKCRF) basin is 36 m long by 28 m wide (Figure 3.1). Its original layout was altered in order to achieve the desired flow discharge condition using

two parallel lateral training walls with parabolic ends as depicted in Figure 3.2. The walls guided the flow through a slightly elevated (by about 0.05 m) section 9 m wide and 12 m long, located in the central part of the basin. The bed mound was built in the middle section. At both ends of the elevated area of the basin, the floor sloped downward for about 1 m into a deeper stretch of the basin. The distance from the bottom of the slope to the flow guides was approximately 6 m. The floor was painted a light grey colour in order to obtain maximum contrast with the sand. A 1 x 1 m grid was marked on the floor on the central section to aid visualization and interpretation of the changing bed mound morphology. In certain places the grid was further subdivided into 0.25 m x 1 m cells. The water entered and exited via guide vanes.

A computer controlled pumping system was used to set up either unidirectional or oscillatory flows by means of three re-circulating pumps, across the length of the basin. The flow velocity/discharge could be input as a time series (sine curve for oscillatory flow) or manually (ramping value for unidirectional flow). Three independently controlled pumps were used with a maximum combined capacity of 0.9 $m^3/s$. The water depth in the section was 0.20 m for all tests, and the maximum attainable velocity was approximately 0.5 m/s. The pumping system was calibrated to obtain the desired velocity.

## *3.3. Instrumentation*

The instruments used during the large-scale experiments were:

- Velocity probes to measure the flow velocity (ADV);
- Wave gauges to measure the free surface elevation during the test runs and the water depth during profiling; and
- Cameras to capture images during the running of the tests and the profiling of the mound, and to capture images for PTV (particle tracking velocimetry) purposes.

### 3.3.1. Velocity probes

Two acoustic Doppler velocity meters Nortek (ADV) measured point velocity. The ADVs were positioned on two beams that straddled the (west-east) width of the basin about 8.5 m either side of the middle of the basin along the north-south centreline (Figure 3.2). The two side-looking probes were placed at 40 % of the water depth (0.08 m above the bed). The velocity measured at these points is taken to be representative of the depth averaged velocity. The sampling volume of the ADV is a cylinder with the long-axis oriented horizontally at

0.05 m from the sensor, and is approximately 0.03 by 0.03 m and 0.01 m diameter. The velocity was sampled at a point and typically at a frequency of 4 Hz, with a velocity range (0 to 1.0 m/s). Water temperature measurements were taken using a thermometer and the measurements stored in the associated ADV data files. The error associated with the measurement with the ADVs could be up to 0.01 m/s, and can be related to the positioning of the gauge, the sampling rate, the velocity range, the signal-to-noise ratio and the measurement of the temperature.

### 3.3.2. Water level gauges

Six resistance-type wave probes (HR Wallingford) were used to measure the free surface during the test runs and during profiling. These probes consisted of two thin metal rods, and the probe measured the voltage between the probes.

Three probes were located on either end of the basin, mounted on the same beam as the ADV. One probe was located along the stream-wise centreline of the flume, and the other two probes 2.3 m either side of the centreline (Figure 3.2). The wave probes were calibrated over an immersion range of ±0.04 m, which extended beyond the expected maximum range of variation of the water level during the tests. During testing the sampling frequency of the probes was 10 Hz. A typical record is shown in Figure 3.3 and captures the the variation of the water level. The wave probe data were collated as DATS files at Wallingford. A calibration curve was prepared to convert voltage to water elevation.

Another probe was used to measure the water depth when the water level was lowered or raised to profile the bed mound, whilst synchronised images of the bed mound were captured. This 'profiling probe' was mounted on the southwest side of the basin, as indicated in Figure 3.2, to avoid influencing the flow field. The sampling interval was typically 10 s, and the frequency was 10 Hz. The profiling probe was calibrated to cover the full range of the water depth, and the data were averaged over the sampling time to obtain the water level value associated with each photograph.

The error associated with the wave gauge measurements is related to the calibration, the range of accuracy of the wave probes and the distance between the metal rods**.** The typical maximum error in the measurement using wave probes is ± 0.2 mm.

### 3.3.3. Voltage input to pumping system

A voltage signal generator, controlled using software developed by HR Wallingford Ltd, was used to input a signal to a transducer and produce a flow discharge at the pumps in the basin. The peak voltages correspond to peak flow speeds for the test, using relations found through flow calibration. The input could be done manually or through a time series file. For steady unidirectional flow cases, the voltage was input manually using calibrated values. For oscillatory flows, a time series voltage curve was input with an associated oscillation period of 20 min and peak voltage in order to drive the required oscillatory flow conditions (with a peak velocity of approximately 0.5 m/s).

### 3.3.4. Cameras

The cameras used during the experiments to capture still or moving images were:

- A scientific high resolution Cohu 7900 CCD Camera with 2048 x 2048 pixel black and white camera, used to obtain PTV overhead photographs, and mounted in a fixed position approximately 6 m above the basin, covering an area of 5.5 m by 5.5 m (Camera 1);
- A high resolution (3200 x 2400 pixels) digital colour camera used to obtain overhead images during profiling and running of the experiments, at a fixed position approximately 6 m above the basin, covering an area of 8.5 m by 6 m (Camera 2);
- A high resolution colour video camera (Canon XL1s) mounted on a tripod to capture the movement of individual particles during the particle tracking tests (Camera 3); and
- A hand-held colour photographic camera, to take images of the bank morphology from within the basin (Camera 4).

The sampling interval for each set of images varied. In most cases, colour images were taken at five-minute intervals. Whilst profiling, the image sampling frequency varied with the speed of the water draining or filling up the basin. In general it was every 2 minutes. The black and white camera generally captured frames every 5 s (for more detail see García-Hermosa and Borthwick, 2006).

### 3.3.5. Sediment

The sediment used in the experiments was Garside 21 (supplier Garside Sands) sand of median size 0.454 mm, $d_{10}$ = 0.291 mm and $d_{90}$ = 0.653 mm. The sand was either of natural

colour or else dyed blue, red or green. The sand grain size was selected according to the findings from the pilot experiments, so that the sediment transport should be primarily bed-load over the range of test conditions. Figure 3.4 shows the grain size distribution of the sand used in the experiments. Table 3.1 lists the sediment characteristics. The parameters $w_s$, $\tau_{cr}$, $\theta_{cr}$ and $U_{cr}$ were calculated using methods given by Soulsby (1997, using equations: 102, 77, 74 and 72a respectively).

## 3.4. Flow conditions

### 3.4.1. Flow blockage, Reynolds and Froude number

The mound causes a blocking effect on the flow, the larger the projected frontal area of the bed mound, the greater the blockage. The blockage can be expressed as a ratio between the projected area of the obstacle and the cross-sectional area of the basin in the absence of the obstacle. This section quantifies the blockage effect of the basin's width on the flow velocity.

A blockage of 1/6 of the cross section is considered (understood through common practice) to have an effect on the flow velocity that is acceptably small; otherwise the effect of flume sidewalls should normally be taken into account. For the test with a circular footprint, the initial dimensions of the bed mound were 0.15 m in height at the apex, 2 m in radius, and its slope was about 1:13. In this case the flow blockage was about 1/6 and occupied 17 % of the cross section, with an equivalent cylinder radius of 0.75 m. Certain other tests had a higher surface-piercing apex, at 0.25 m so that the blockage effect was larger, and the eddy shedding properties were amplified. The largest blockage ratio was about ¼, which corresponds to a blockage of 25 % of the cross sectional area of the UKCRF (9 m wide), which will exert a larger effect on the velocity flow field. This blockage effect is equivalent to that of a cylinder of 1.125 m radius.

***Effect of the mound on the flow in the UKCRF basin.***

To investigate the effect of the mound on the flow velocity, the blockage ratio of the mound was represented as that of cylinder with the same cross sectional blockage ratio. The effect of the flow around a cylinder in an infinitely wide basin has been extensively studied, e.g. Sumer and Fredsøe (1997). Then the infinitely wide basin case (Figure 3.5) was compared to the case of a finite basin with the layout of the UKCRF (Figure 3.6).

To calculate the flow velocity around a cylinder in a basin of width *b* the method of images was used to include the effect of the walls in the flow velocity (with 3 cylinders separated a distance *b*, the two on the top and bottom represent the effect of the walls, Figure 3.6).

The stream function:

$$\Psi = u_\infty y - \frac{u_\infty a^2}{r}\sin\theta - \frac{u_\infty a^2}{r_1}\sin\theta_1 - \frac{u_\infty a^2}{r_2}\sin\theta_2 \tag{3.1}$$

where a is the cylinder radius, $r$, $r_1$ $r_2$ are distances from the central cylinder to the upper image and lower image cylinders respectively, and $\theta$, $\theta_1$, $\theta_2$ are the polar angles respect to the centre of each cylinder. The terms on the right hand side of the equation represent respectively, uniform flow, the disturbance due to the centre cylinder, the disturbance due to the upper image cylinder, and the disturbance due to the lower image cylinder. Given that:

$$u = \frac{\partial\Psi}{\partial y};\ v = -\frac{\partial\Psi}{\partial x} \tag{3.2}$$

and conversions from polar to Cartesian coordinates are:

$$r = \sqrt{x^2 + y^2};\ r_1 = \sqrt{x_1{}^2 + y_1{}^2};\ r_2 = \sqrt{x_2{}^2 + y_2{}^2}$$

$$sin\theta = {}^{y}\!/_{r};\ \ sin\theta_1 = {}^{y_1}\!/_{r_1};\ \ sin\theta_2 = {}^{y_2}\!/_{r_2}$$

The velocity varying in the *y*-axis, after conversion to Cartesian from polar coordinates, the stream-wise velocity component is

$$u = u_\infty\left[1 - a^2\left(\frac{x^2 - y^2}{\left(x^2 + y^2\right)^2} + \frac{x^2 - (y-b)^2}{\left(x^2 + (y-b)^2\right)^2} + \frac{x^2 - (y+b)^2}{\left(x^2 + (y+b)^2\right)^2}\right)\right] \tag{3.3}$$

where *b* is the distance between the cylinders. Hence:

$$u = u_\infty\left[1 + a^2\left(\frac{1}{y^2} + \frac{1}{(y-b)^2} + \frac{1}{(y+b)^2}\right)\right]. \tag{3.4}$$

The free flow velocity ($u_\infty$) is assumed to be 0.5 m/s. The effect the mound blockage on the flow velocity due to the walls is given by the percentage difference calculated between the velocity assuming an infinitely wide basin and the one taking into account the effect of the walls (Table 3.2). Due to the constriction of the flow by the walls there is an increase in velocity in comparison to the infinite width basin (Figure 3.7). The maximum calculated disturbance of the flow velocity occurs nearest to the walls, and is of the order of 6 %. In the vicinity of the cylinder the disturbance is much smaller (< 2 %). This confirms that the walls exert an effect, however small, on the velocities near the mound. An increase in the flow velocity may have a non-linear effect on the sediment transport, enhancing it.

The results for a cylinder with a blockage ratio of 1/6 (blocking 17 % of the cross section, with an equivalent radius 0.75 m) are shown in Table 3.3. Note that the maximum disturbance in the velocity is 3 %. The smaller the flow blockage the lower the velocity disturbance. A flow disturbance of 3 % (the maximum is found at the wall, where the effect on the sediment is minimal) was considered acceptable. To put it into context, the enhancement in sediment transport owing to the flow disturbance will be within the range of variation given by different sediment transport formulae.

***Reynolds and Froude number***

The mound acts as a bluff body, and so leads to potential flow separation, eddy generation and subsequent re-circulation patterns in the wake. The eddies and re-circulation zones play important roles in scour and deposition, and enhance the sediment transport rate due to the increased turbulence developed by such vortical flow structures.

The Reynolds number during the UKCRF experiments (described previously in Section 2.6) for a water depth of 0.2 m, peak flow velocity of 0.5 m/s, and a kinematic viscosity coefficient of $10^{-6}$ $m^2/s$, is $10^5$. The limits of the regimes for open channel flow were described in Section 2.6.

The Froude number is:

$$Fr = \frac{u_0}{\sqrt{gH}} \tag{3.5}$$

where $u_0$ is the undisturbed flow velocity, $H$ is the water depth and $g$ the acceleration of gravity. $Fr$ is the ratio between the mean flow velocity and that of a gravity wave travelling over the surface. If $Fr = 1$ the speed of the surface wave and that of the flow is the same, defined as critical flow. For $Fr > 1$ the flow is supercritical and for $Fr < 1$ the flow is subcritical. For water depth of 0.2 m and depth-averaged velocity away from the mound of 0.5 m/s the flow remains subcritical. However, the flow velocity will be affected in the vicinity of the mound. Due to the decrease in the water depth above the mound the flows will accelerate and the flow can become critical, or even supercritical near the mound's crest.

### 3.4.2. Flow calibration

The pumping system was controlled by voltage signal input software. The signal generation system was used in two modes: (i) for oscillatory flow; and (ii) for unidirectional flow.

The flow calibration exercise consisted of finding the relationship between input voltage to the pumping system and the output flow velocity. Accurate calibration was

essential in order to provide the correct input voltage information, and thereby to provide known current flows. In order to calibrate the flows, a side looking ADV was attached to a beam located along the centreline across the basin and placed at several fixed points along it, always keeping the probe at 40 % of the total depth from the floor. The convention used in the measurements is that: positive values represent southward flows, and negative values represent northward flows.

### 3.4.3. Oscillatory flow

Calibration of the oscillatory flow was carried out first. The system was set up with a sinusoidal voltage curve for each pump. The oscillation period and peak voltage were prescribed for each curve for both flow directions (positive and negative). The curves were input to the program, and the pumps generated the flow accordingly.

### 3.4.4. Oscillation period

Initially the oscillating flow tests were run with a 10-minute flow reversal period. However, this setting did not output the desired velocity: there was a deformity in the curve. When the flow was starting, the rate of increase in velocity slowed to zero before increasing again. This problem appeared also when the flow reversed direction. The undesirable kink in the velocity occurred for velocities above the threshold of sediment motion, and so disrupted the sediment dynamics. Either long wave reflections due to basin modes or hunting of the pumping system may have been responsible. After considering several options, the oscillation period was incremented to 20 minutes as this appeared to minimize the long wave reflection and its effect on sediment transport (Figure 3.8). Although the deformity in the velocity record remained visible in the curve for $T$ = 20 min, it occurred when the velocity was below the threshold of motion, and so the sediment motion was not affected.

Figure 3.8 shows a typical ADV velocity measurement with 10 and 20 min oscillation period collected in the UKCRF. The signal has greatest fluctuations at times of maximum flow. These fluctuations are due to turbulence and were also observed during the Reversing Flume experiments.

### 3.4.5. Calibration

The velocity was recorded over at least a full cycle using the ADV at different positions across the flume. Several calibration velocity-time curves were investigated in order to achieve the required flow velocity in the centre of the basin. Four calibration curves for a

20-minute oscillation period covered a range of peak flow velocities from approximately 0.30 m/s to 0.55 m/s.

### 3.4.6. Uniformity of the flow across the basin

A series of tests were carried out to assess the cross-basin uniformity of the flow velocity. The aim of this exercise was to make the velocity across the flume as uniform as possible.

ADVs fixed on a beam across the centre of the basin measured the velocity at three positions. One ADV was located in the centre of the basin, the other two nearer the sidewalls, approximately 3.5 m from the centreline (Figure 3.2).

Initially there was a velocity gradient across the basin, in the boundary layers at the lateral walls of the basin. The measured horizontal velocity component in the main flow direction was slightly higher near the sidewalls than at the centre of the basin due to the contraction effect of the parabolic entry walls.

In order to minimize the velocity gradient, a series of 'tuning tests' was carried out, varying the voltage curves corresponding to each of the three pumps. Eventually it was possible to reduce the gradient substantially, though not altogether. The velocity across the basin after ‘tuning’ was quite uniform. Figure 3.9 shows the transverse profile of horizontal stream-wise water particle velocity component across the basin. The difference in velocity measured by the three gauges ranged from 0.04 to 0.07 m/s. This variation in the velocity distribution across the basin could be due to the layout of the pumps in the basin and the effectiveness of the training walls.

### 3.4.7. Unidirectional flows

For unidirectional flows, the voltage was ramped up slowly using the user interface software. No curve was input, instead values were typed into the computer and the voltage increased incrementally. During calibration the flows were measured at the centre of the basin with an ADV probe. The unidirectional flow was calibrated in the north to south direction.

### 3.4.8. Vertical profile of horizontal velocity

The horizontal water particle velocity component was measured at 5 elevations above the bed during steady unidirectional flow. The measurements were taken at the north end of the basin (see Figure 3.2). Profile information was collected at 0.03 m intervals, except for the final measurement, which was taken close to the water surface. Due to the size of the arms of the side-looking probe, and restrictions due to the sampling volume in the vicinity of the

bed, the vertical profile commenced at approximately 0.05 m above the bed (and so no information was collected in the bed boundary layer). Above this point (0.05 m) the vertical profile of the horizontal water particle velocity component is relatively uniform through the depth.

The voltage input was set to reach a target peak velocity in the centre of the basin of about 0.50 m/s. The peak velocity measured at the probe's position was 0.475 m/s (Figure 3.10), and the depth averaged velocity was 0.467 m/s, the difference is just below 2 %. The measured velocity can be considered to be representative of the depth averaged velocity.

## 3.5. Experimental procedure

The following section details the steps taken when conducting the morphodynamic tests in the UKCRF. Figure 3.11 indicates the procedure followed in a typical test. Table 3.4 presents the experimental program.

### 3.5.1. Test procedure

The bed mound was constructed using purpose-built templates (ellipse, circular or Gaussian shape) from Garside 21 sand. Two different template systems were used. The Gaussian and cosine shape mounds were built using radial templates (approximately every 30 degrees, Figures 3.12a). The elliptical mounds were built using parallel templates half a metre apart (Figures 3.12b and 3.12c). The formula used to build the cross-sectional templates of the Gaussian mound are:

$$h = h_0 \ \exp\left( \ ar^2 \right) \tag{3.6}$$

where $h_0$ was 0.15 m, and $a$ is $\ln(1/2)$ and controls the width of the Gaussian. The templates for constructing the mound were truncated at $r$ = 2.5 m where $h$ = 0.001 m. The cosine cross-sectional templates followed the curve:

$$h = h_0 \ 0.5\left( \frac{\cos \ 2\pi \ r}{L} + 1 \right) \tag{3.7}$$

where $h_0$ was also 0.15 m, and $L$ was 4 m, the diameter of the mound. Figures 3.13 to 3.15 provide details of the template sections used to build the mounds.

In cases where natural sand was used, the sand was wetted *in situ* before moulding. However, in the tests where coloured sand was used (Table 3.4) , the sand had to be wetted

before it was transported into the basin, the surface tension properties seemed to change with the dyeing process. This did not have a noticeable effect on the evolution of the sand. The sand was placed in the basin and moulded into shape using the wooden templates as guides, and screeding over them. Hence, the sand was somewhat compacted. In order to minimize the labour and time costs involved in removing sand from the basin between tests, the order of the tests was arranged where possible according to increasing size of bed mounds.

Subsequently the ADVs' locations and depths were checked. The wave probes measuring the variations in the free surface were also checked to make sure they were operating properly. A further check was carried out to ensure the wave probe used as a profiler (profiler probe) worked correctly.

Following these checks, the basin was then filled. Initially the water was added at maximum rate until the water level reached the toe of the mound. After that, filling was undertaken at a slower rate. This was done to (i) allow water level measurements to be taken synchronized with image capturing; and (ii) to avoid the mound being changed by the flow during profiling. The water level measurements synchronised with the image capture were taken using the profiler probe, which sampled at 10 Hz for 20 s duration each photograph. Water depth values were averaged and the mean value for the interval corresponded to that at the time when photograph was taken. The time interval between the photographs depended on the speed at which the basin was filled. Photographs and water levels were taken until the mound was fully covered. Typically a spot water level measurement was taken when the mound's apex was fully covered. Then, the water intake was opened to the maximum to fill the basin to the required depth (i.e. 0.20 m in most cases). If the test was carried out with a mound of 0.20 m or higher, the basin was filled gently to profile its full height and then the water was drained to the operating water depth. The water level spot measurements were always taken with a graded ruler at the same place in the basin to keep measurements consistent, as the bed of the basin had small irregularities (approx ± 0.003 m). Next, the profiler probe was calibrated for different water depths, accounting for the full height of the mound. Similarly, the wave probes calibration was undertaken covering a range of ± 0.04 m, in 0.02 m intervals up and down from the undisturbed water depth. The sampling rate of the probes was 10 Hz and the recording interval was between 20 and 30 s. The average value for each 20-30 s interval was used to determine a conversion curve to calculate water depth.

Once the voltage curves were loaded in the signal generation software, the water level and ADV data acquisition started. The test commenced the moment the pumping

system started to operate. The two overhead cameras captured images at a prescribed frequency, for the duration of the test. During those tests with floats (white hollow spheres approximately 0.01 m diameter) the black-and-white camera recorded the floats as they passed underneath, and the colour camera recorded the evolution of the bank. After a prescribed number of cycles, the pumping system, the image capturing and the data acquisition software was stopped. At set intervals the bed mound was profiled (typically after 1, 3, 6, 9, 12 cycles in tidal flow or equivalent time intervals for steady flow) according to the following procedure. The pumps were stopped coinciding with slack water in the tidal cycle for the oscillatory flow tests, or by slowly turning off the pump for the unidirectional flow tests. The water level was reduced by removing water from the basin through a drainage valve, until the top of the mound began to pierce the water surface. The water depth was measured using the profiler probe, and an image was captured of the free surface contour. The water level was again lowered gently to a new level, and the profiler probe readings taken and further free surface images recorded. Usually this was repeated until the water depth was about 0.02 m from the bed. In certain tests, a series of hand held photographs of the bank were then taken from around or within the UKCRF basin. The infill valve was then opened and the basin refilled to the correct level. Occasionally a second spot water level measurement was taken when the water was close to the mound crest, to confirm the crest height. The test then recommenced.

Most of the tests used a mound of sand placed on the concrete bed of the flume (i.e. 'fixed bed') this minimised the quantity of sand used, reduced the setting-up time, and gave a better visual impression of the mound evolution. In two cases, the mound was placed on a bed of sand covering the operational area of the flume screeded to a depth of 0.025 m in Test 13, and hand flattened to an approximate depth of 0.025 m in Test 14 (the layer height ranged approximately between 0.01 to 0.03 m). These tests are more representative of natural occurring bed mounds. The water depth was 0.2 m in all cases except for the mobile bed cases where the level was raised up to 0.225 m. For each test, profiles were recorded at prescribed times, typically: initial profile; 1$^{st}$ cycle (or 20 min interval); 3$^{rd}$ cycle (60 min interval); 6$^{th}$, 9$^{th}$, 12$^{th}$, 15$^{th}$ and final profile.

### 3.5.2. Processing of contoured data

The profiling method used in the UKCRF experiments was a combination of synchronised image capturing and data collection. This allowed for a more comprehensive dataset to be collated in a shorter time period (though it meant longer post-processing times) than with

conventional methods. With a conventional method to contour the mound, like a profiler (2 D or 3-D), the data collected comprises an array of finite number of points. The number of samples and the sampling interval usually depends on the time available for profiling.

An overhead camera took images using a computerized remote control. The outflow rate was such that the water depth did not change rapidly whilst capturing the images and measuring the water level. The remote control could be set to take photographs at fixed time intervals whilst simultaneous measurements of water depth were taken using the profiler probe (writing measured voltage into a file). Each file corresponded to an image. The voltage in each file was converted to water depth using a calibration curve. The water depth in each record was averaged to find the corresponding water depth for each image (and each contour). Corrections were applied in order to make sure the manually logged information matched the results.

### *Estimate of volume and centroid coordinates*

The contours in the images were digitised manually. The contour information was converted from pixels into metres, then a correction for radial distortion was carried out using a simple algorithm, based on regression analysis of the distance from the centre of the image. The contours were interpolated using triangular linear interpolation (within Surfer) and plotted as 2-D contours and 3-D surfaces, and cross sections were obtained. The volume of the mound was calculated as the volume of sand included within the footprint of the mound, with a script built in Surfer, the centroid was also calculated.

### *Float image capture*

The intention was to use PTV images to get comprehensive information about the surface flows around the mound. The black and white images were not used, as there were sufficient data from the coloured photographs. Coloured photographs were used to estimate the magnitude of the surface flow velocity. Certain images that included float tracks were digitised and the length of the tracks determined and the velocity estimated from the aperture timings $1/5$ or $1/2$. This information was used in the analysis of the results and could be used to assess the performance of a numerical model.

### *Colour image analysis*

Images from the coloured sand tests were used in the interpretation of the experimental results and to deepen understanding of the morphological processes taking part in the evolution of the bed mound.

### 3.5.3. Experimental error and uncertainty in the measurements

During the course of the experimental phase and data collection there were several sources of uncertainty and error. The deviation between the true value of the property to be measured and the measurement represents the uncertainty in the measurements. During the experiments, the experimental error was taken as being a combination of the following: (i) observational error (systematic, random, human); (ii) error due to instrument limitations; (iii) uncertainty in the measurements;

***Observational error***

The error in observations may be due to two contributions, the systematic error and the random error (due to the difference between the measurement and the true value of the variable measured). The systematic error arises every time a measurement is taken, when every repeated measurement gives slightly different results (due to incorrect offsetting; measuring the same variable using different devices every time). Keeping a tight procedure can minimize observational error.

***Error due to instrument limitations***

The error in the measurements taken with the velocity probes may be due to the vertical positioning of the ADV (± 0.002 m), and the positioning angle of the probe to the main flow direction (< 3-5 degrees). The resolution of the measurement is about 0.1 mm/s and the velocity bias may be ± 0.5 %. The noise may be about 1 % of the velocity range when the velocity is measured at 25 Hz (measurements were taken at 4 Hz). The uncertainty in the ADV velocity measurement was about ±0.01 m/s. The measurements of water depth and free surface were carried out using wave gauges, and a graded ruler. The error in measurements due to the use of the graded ruler was approximately ± 0.001m. The uncertainty in the measurement of free surface using wave gauges was of the order ± 0.1 to 0.2 mm.

***Error due to digitisation procedure***

An initial assessment of the error in the digitising of the photographs may be made by considering the error in ascertaining the interface between the sand and the water. A pixel is approximately 0.003 m. The error in the digitising is approximately ± 2 * 2 pixels (in the *x* and *y*-axis). Human errors due to the digitisation procedure, were assessed by a check on two datasets collected by different people. The variance between the areas covered by the

selected contours varied between ± 0.5 - 8 %. The larger the area covered by the contours, the smaller the error. Contours for the upper parts of the mound yielded larger variability in the position of the points and hence more uncertainty. The variation in the contour area was not of overall importance as the contours were used to calculate integral properties, such as total volume of the mound. The variation of mound volumes calculated from profiles digitised by different people was between ± 2 and 8 %.

### *Occasions when there was uncertainty in the measurements*

When starting to profile, occasionally there was a lag between the time when the tip of the bank became exposed and the time the first photo and surface elevation measurement were taken; Input of the velocity via a voltage curve; concluding the flow was stronger on one side than the other have slightly biased the results. Part of the human error that corresponds to the digitising error is due to the interpretation by the digitising person of the location of the interface between water and sand, and the delimitation of the footprint contour.

| $d_{50}$ (mm) | Settling velocity $w_s$ (m/s) | Critical bed shear stress $\tau_{cr}$ (N/m$^2$) | Critical Shields parameter $\theta_{cr}$ | Critical velocity $U_{cr}$ (m/s) | Measured velocity* $U$ (m/s) | $U/U_{cr}$ |
|---|---|---|---|---|---|---|
| 0.454 | 0.0564 | 0.2467 | 0.035 | 0.262 | 0.5 | 1.91 |

**U* was averaged over 6 cycles

**Table 3.1 Characteristics of sediment used in the pilot experiments.**

| $y$ (m) | $u(y)$ ∞ width (m/s) | $u(y)$ UKCRF (m/s) | % difference |
|---|---|---|---|
| 4.5 | 0.53 | 0.57 | -6.5 |
| 4 | 0.54 | 0.57 | -5.4 |
| 3.5 | 0.55 | 0.58 | -4.5 |
| 3 | 0.57 | 0.59 | -3.9 |
| 2.5 | 0.60 | 0.62 | -3.3 |
| 2 | 0.66 | 0.68 | -2.8 |
| 1.75 | 0.71 | 0.72 | -2.5 |
| 1.5 | 0.78 | 0.80 | -2.2 |
| 1.375 | 0.83 | 0.85 | -2.0 |
| 1.25 | 0.91 | 0.92 | -1.8 |
| 1.125 | 1.00 | 1.016 | -1.6 |

**Table 3.2 Theoretical flow velocity $u(y)$ calculated transverse to a cylinder of radius 1.125 m, with a blockage ratio of ¼ in a basin of infinite width, across width of the UKCRF. The free stream velocity was 0.5 m/s.**

| $y$ (m) | $u(y)$ ∞ width (m/s) | $u(y)$ UKCRF (m/s) | % difference |
|---|---|---|---|
| 4.5 | 0.51 | 0.53 | -3.0 |
| 4 | 0.52 | 0.53 | -2.5 |
| 3.5 | 0.52 | 0.53 | -2.1 |
| 3 | 0.53 | 0.54 | -1.8 |
| 2.5 | 0.55 | 0.55 | -1.6 |
| 2 | 0.57 | 0.58 | -1.4 |
| 1.5 | 0.63 | 0.63 | -1.2 |
| 1.25 | 0.68 | 0.69 | -1.1 |
| 1.125 | 0.72 | 0.73 | -1.0 |
| 1 | 0.78 | 0.79 | -0.9 |
| 0.875 | 0.87 | 0.87 | -0.8 |
| 0.75 | 1.00 | 1.007 | -0.7 |

**Table 3.3 Theoretical flow velocity $u(y)$ calculated transverse to a cylinder of radius 0.75 m with a blockage ratio of $\frac{1}{6}$ in a basin of infinite width, across the width of the UKCRF. The free stream velocity was 0.5 m/s.**

| Test No. | Plan shape | Cross-section | Crest height (m) | Flow cond. | Test duration |
|---|---|---|---|---|---|
| 1 | Circular | Cosine | 0.15 | Tidal | 9 cycles |
| 2 | Ellipse | Triangular | 0.15 | Tidal | 12 cycles |
| 3 | Ellipse | Triangular | 0.25 | Tidal | 58 cycles |
| 4 | Ellipse | Triangular | 0.20 | Tidal | 12 cycles |
| 5 | Circular | Cosine | 0.25 | Tidal | 12 cycles |
| 6 | Circular | Cosine | 0.15 (slope 1:3) | Tidal | 6 cycles |
| 7 | Ellipse | Triangular | 0.15 | Steady | 3 hr |
| 8 | Circular | Gaussian | 0.15 | Tidal | 61 cycles |
| 9 | Circular | Gaussian | 0.15 | Steady | 3 hr |
| 10 | Ellipse | Triangular | 0.25 | Steady | 3 hr |
| 11 | Ellipse (C) | Triangular | 0.15 | Tidal | 61 cycles |
| 12 | Ellipse (C) | Triangular | 0.15 | Tidal | 61 cycles |
| 13 | Circular (C, M) | Gaussian | 0.15 | Steady | 1 hr |
| 14 | Ellipse (M) | Triangular | 0.15 | Tidal | 6 cycles |

(C) colour sand
(M) mobile bed

**Table 3.4 Test program of the UKCRF experiments**

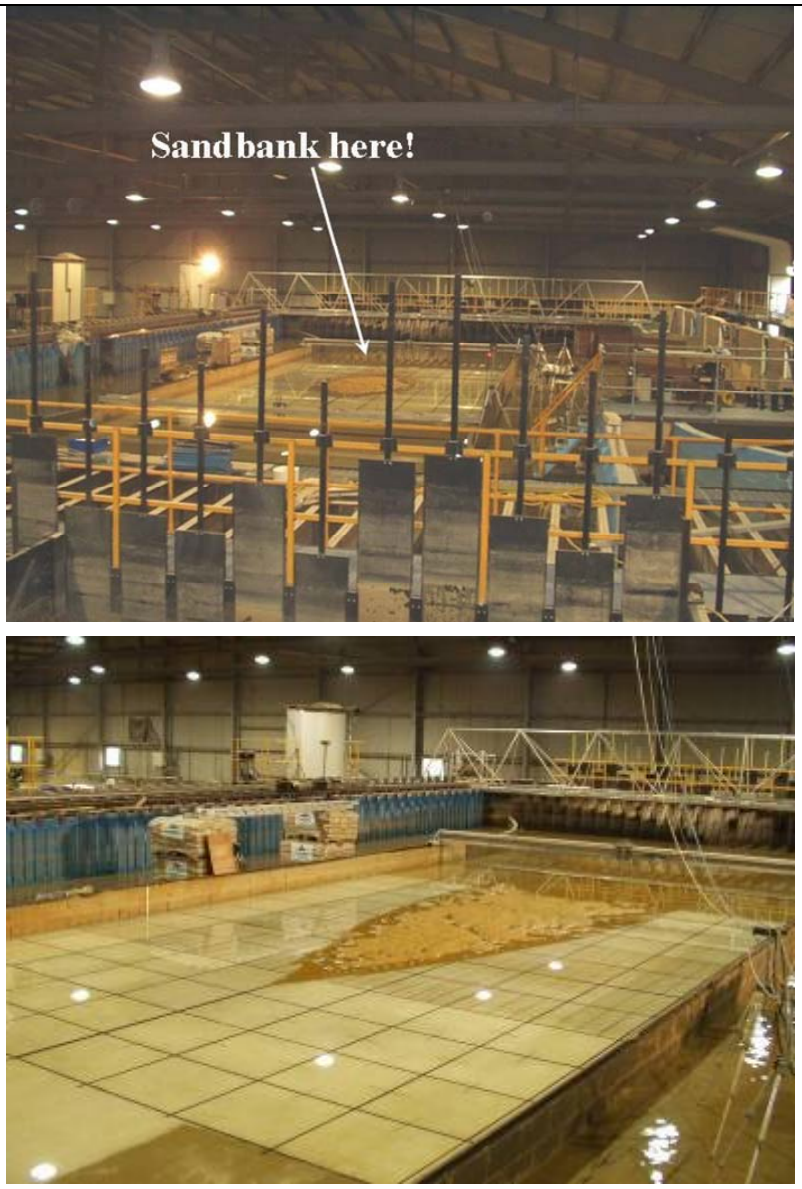


Figure 3.1 UKCRF with mound (top), UKCRF and bed mound after a test (bottom)

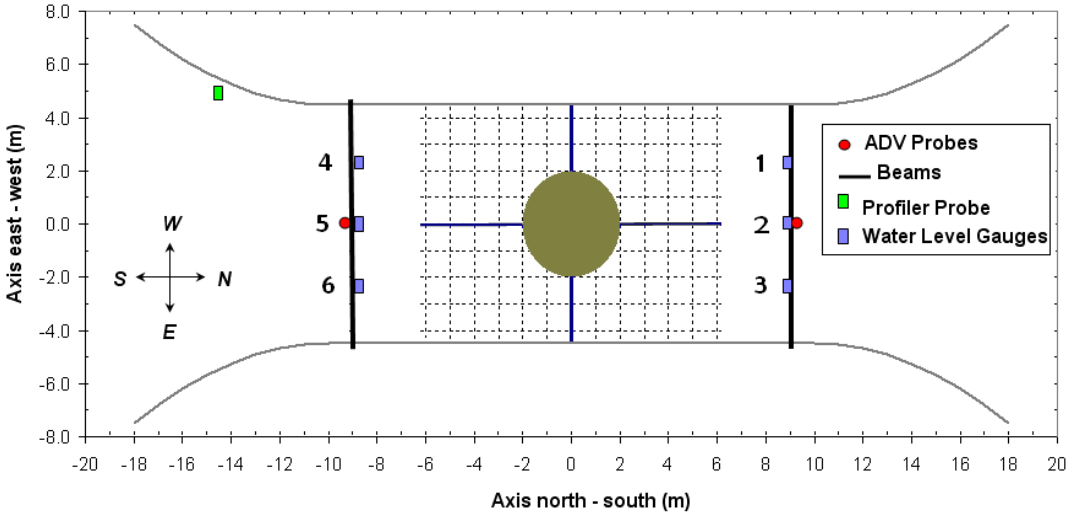


Figure 3.2 Layout of the UKCRF basin (not to scale).

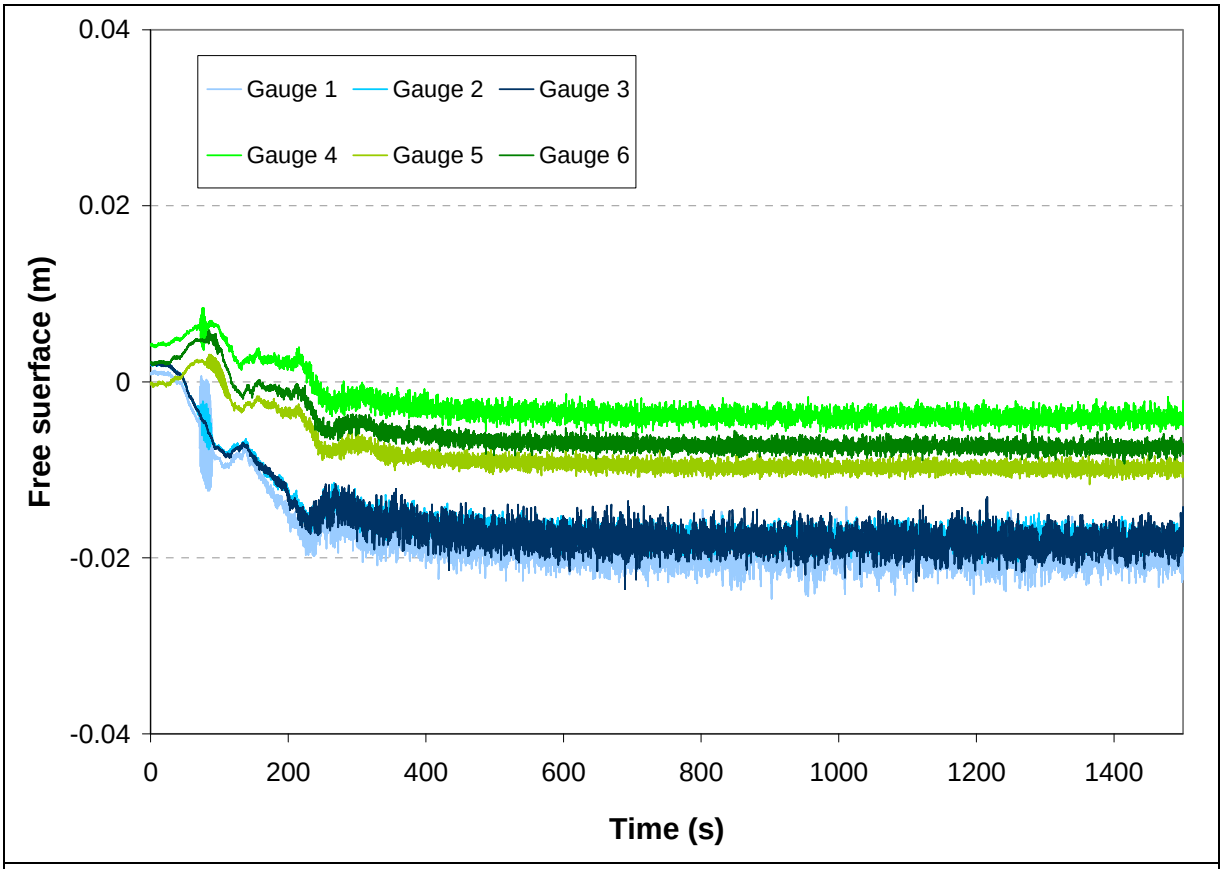


Figure 3.3 Typical free surface time series for a steady flow test (Test 9)

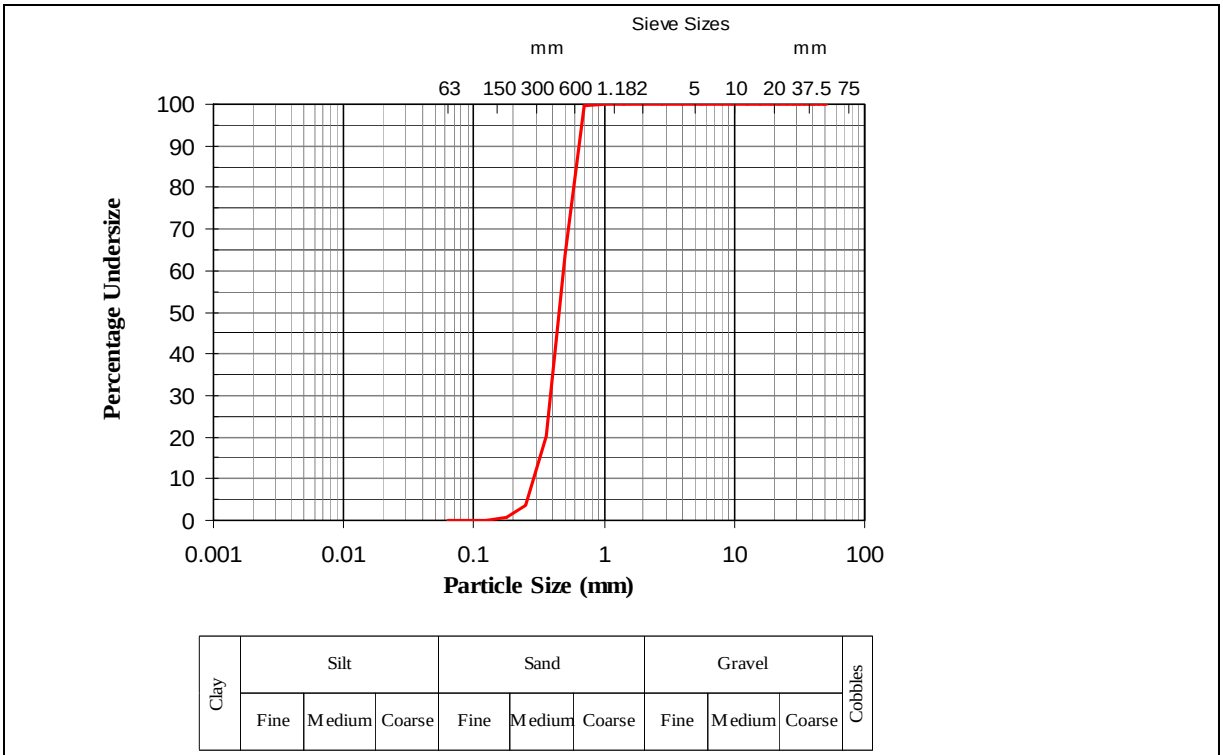


Figure 3.4 Grain size distribution of Garside 21 sand ($d_{50}$ = 0.454 mm).

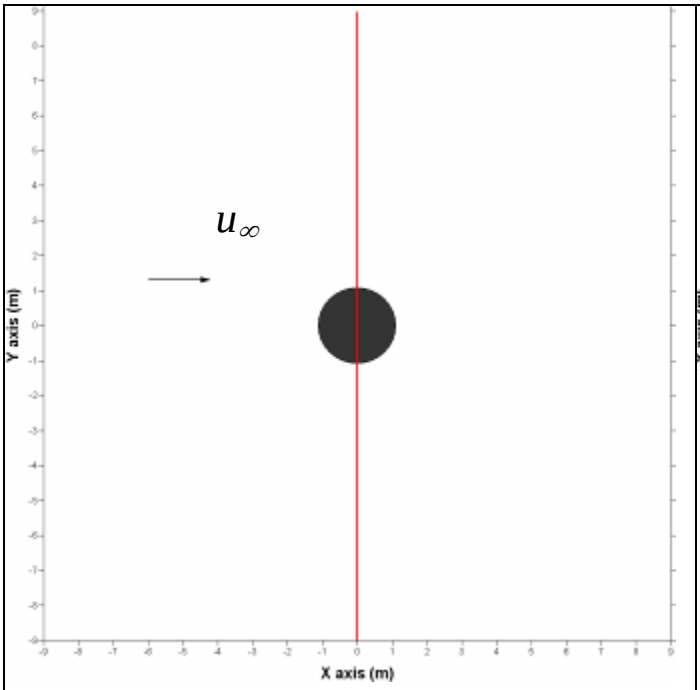


Figure 3.5 Diagram of an infinitely wide basin.

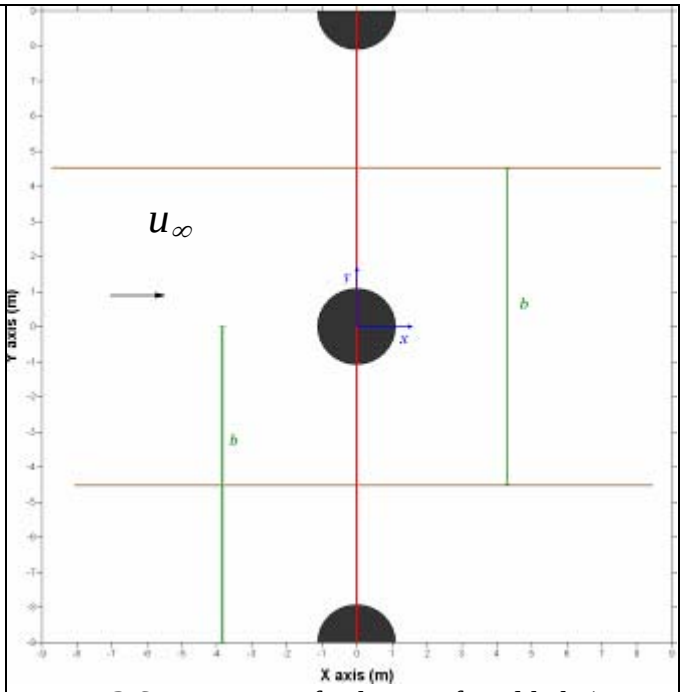


Figure 3.6 Diagram of a basin of width *b* (using the method of images)

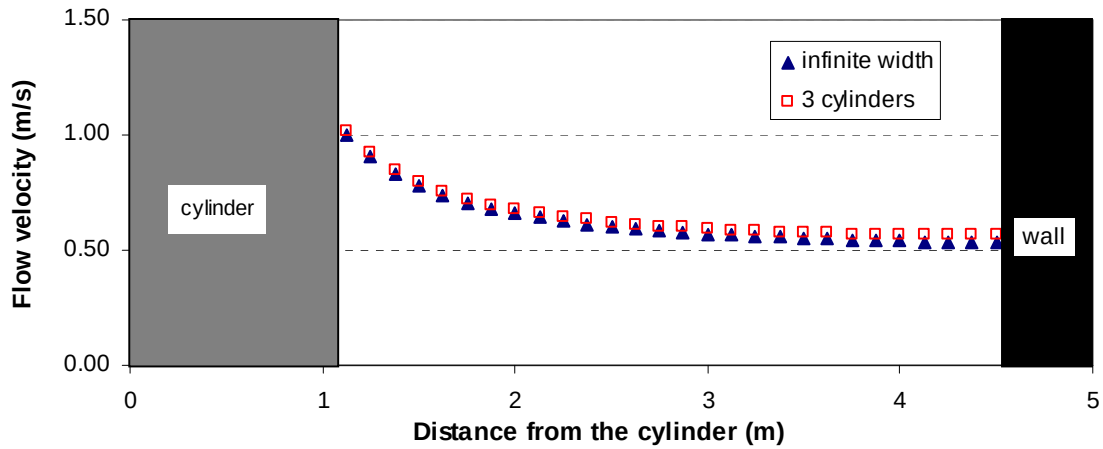


Figure 3.7 Flow velocity profile across the basin.

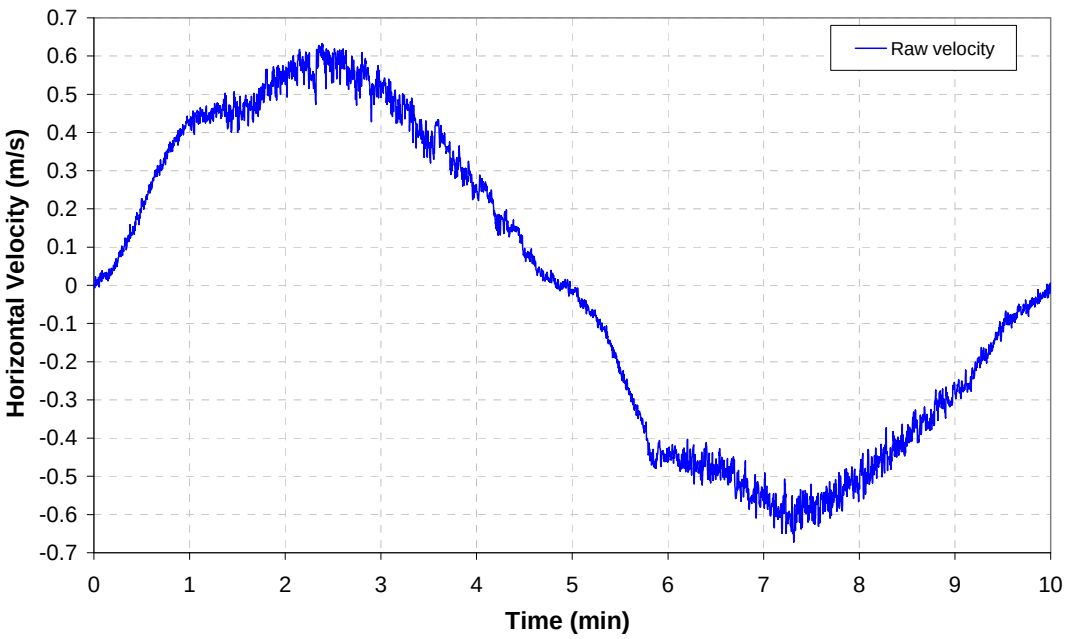


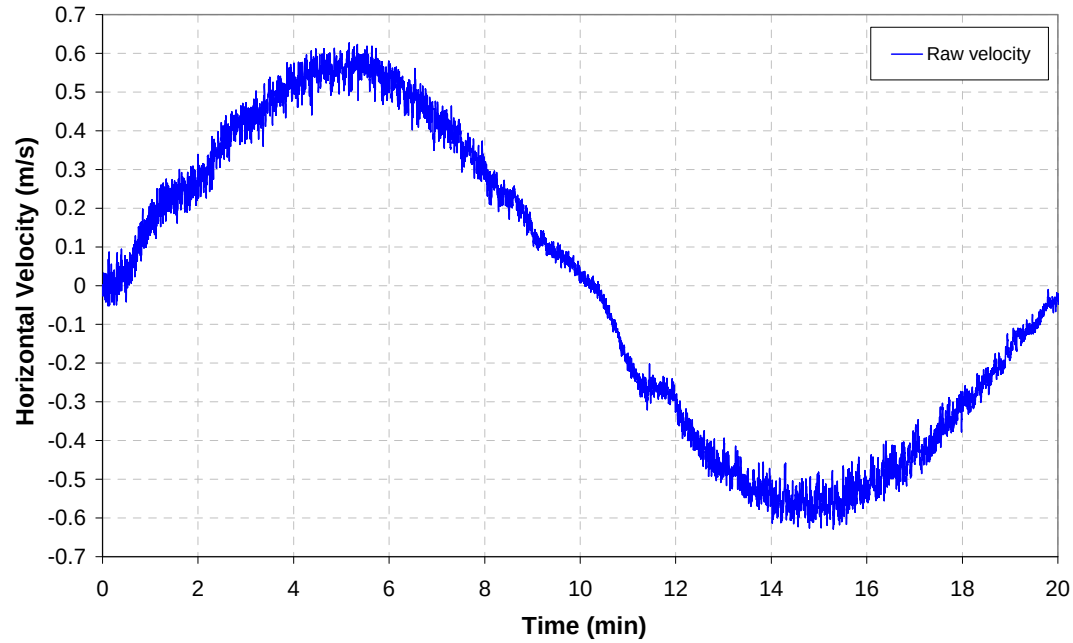


Figure 3.8 Raw velocity plots, comparing oscillation period of 10 min (top) and 20 min (bottom)

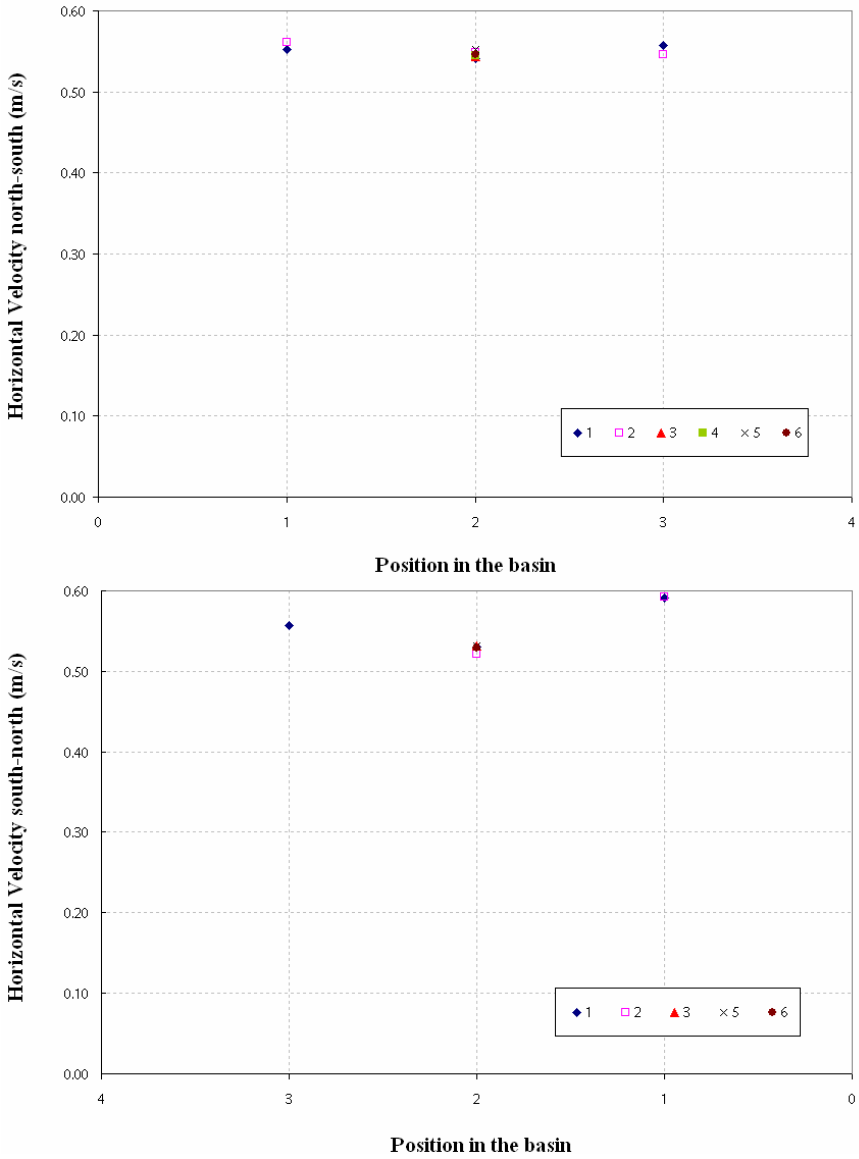


Figure 3.9 Profile of horizontal stream-wise velocity component across the basin positive (top) and negative (bottom) directions.

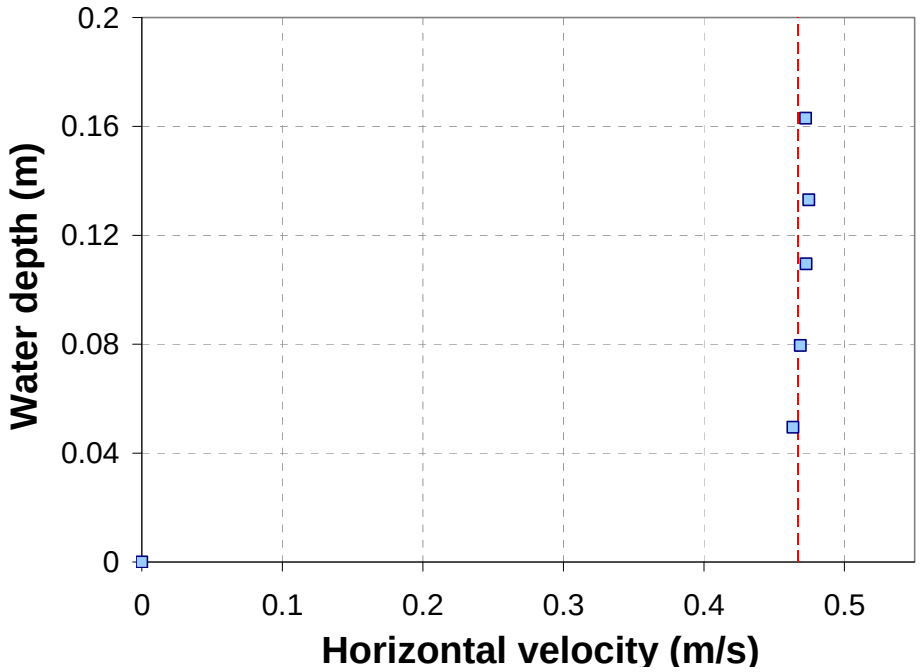


Figure 3.10 Vertical profile of the horizontal water particle velocity component at the North side of the basin of the raised bed. Vertical red line is the calculated depth averaged velocity (method of Soulsby, 1997).

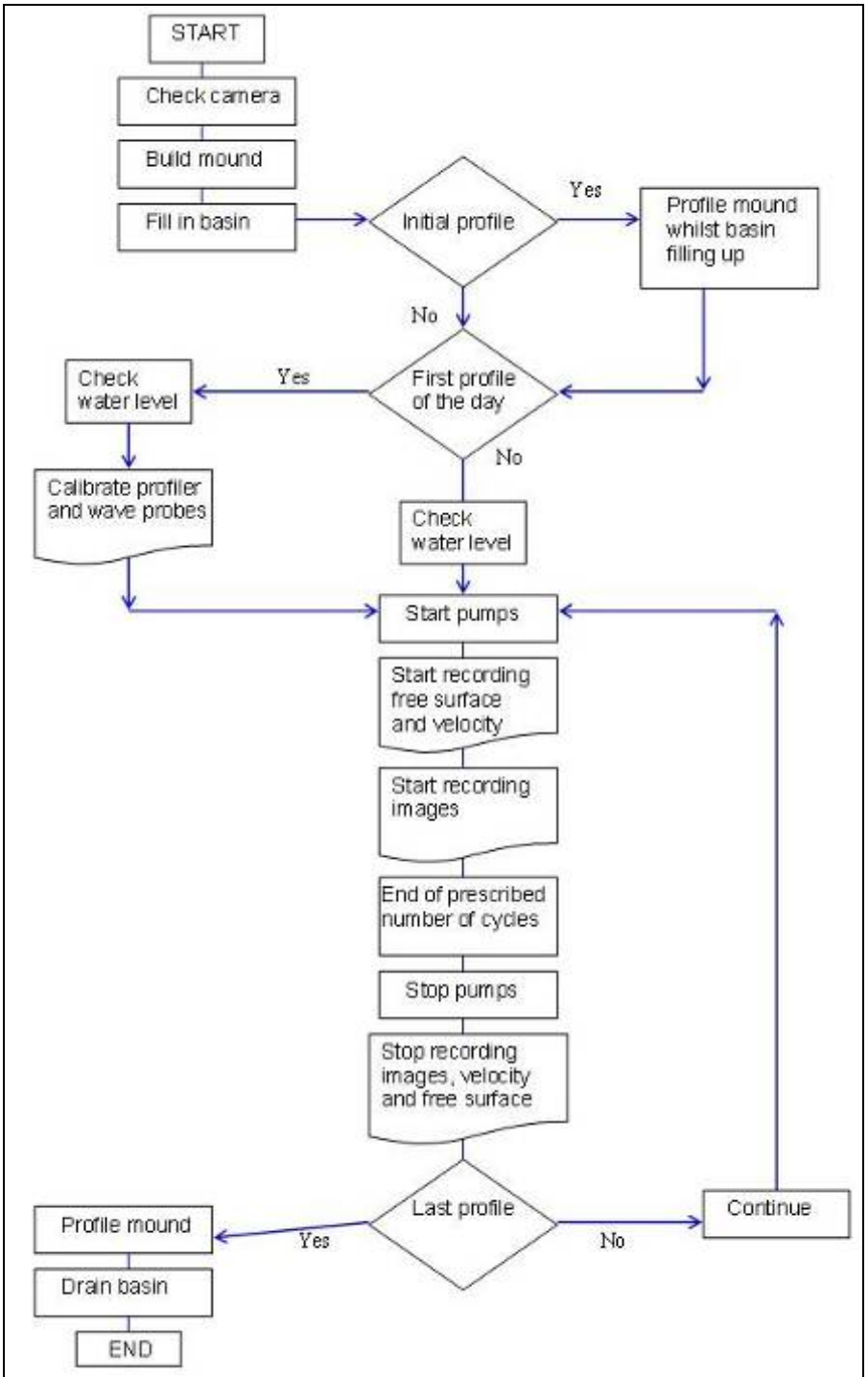


Figure 3.11 Diagram of procedure followed during a typical test

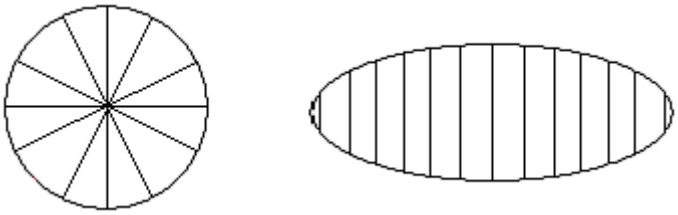

Figure 3.12a Template layout for the Gaussian, circular (left) and elliptical (right) mounds.

Figure 3.12b Gaussian or circular mound

Figure 2.12c Elliptical mound

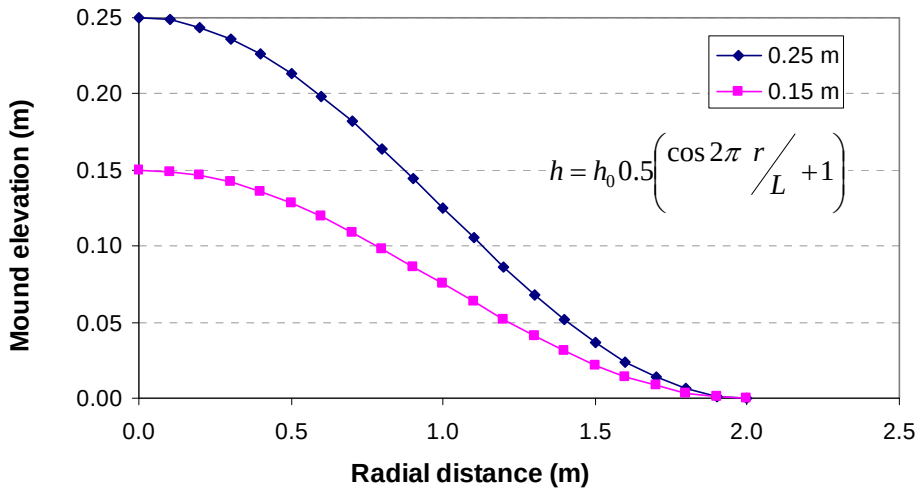


Figure 3.13 Dimensions of the template for the circular mound. Submerged ($h$ = 0.15 m), surface piercing ($h$ = 0.25 m).

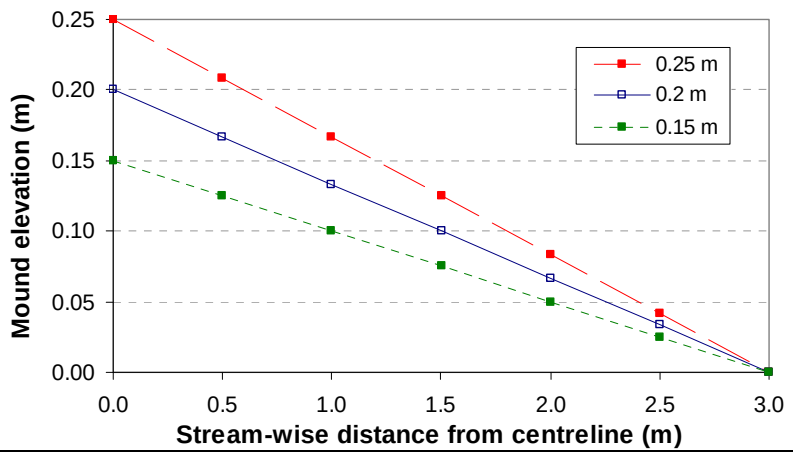


Stream-wise cross-sections

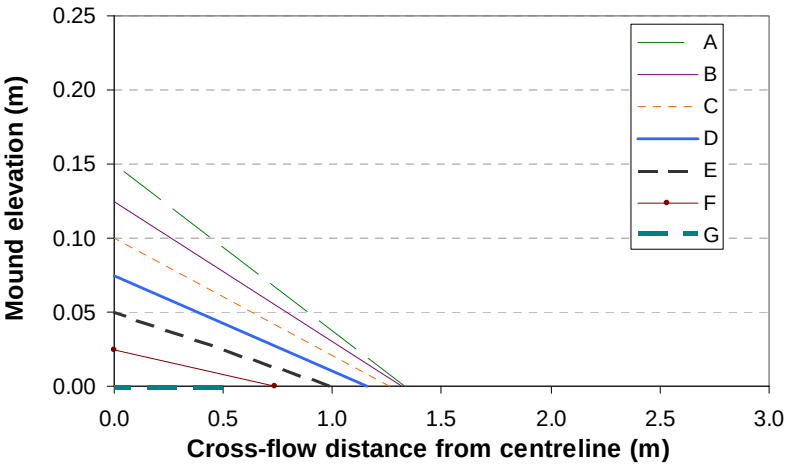


Cross-flow cross-sections

Figure 3.14 Dimensions of the templates for the elliptical mound.
Top figure, submerged mound ($h$ = 0.15 m), surface touching ($h$ = 0.20 m), surface piercing ($h$ = 0.25 m). Bottom figure, submerged mound ($h$ = 0.15 m).

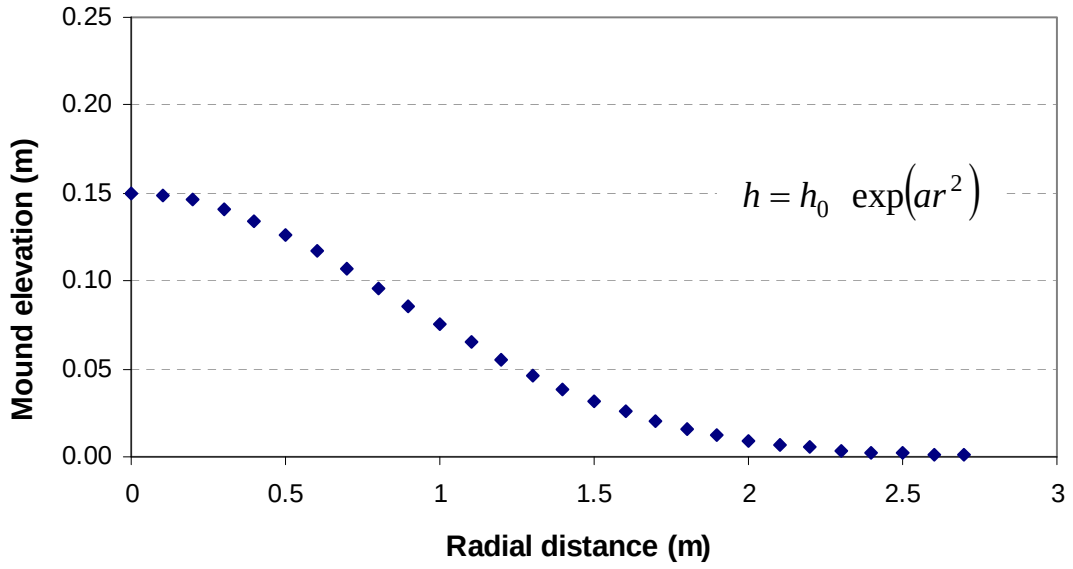


Figure 3.15 Dimensions of the template for the Gaussian mound ($h$ = 0.15 m).

# 4. UKCRF LARGE-SCALE EXPERIMENTAL RESULTS

This chapter presents the interpretation of the large-scale bed mound evolution tests carried out in the UKCRF (a description of the facility and procedure was given in Chapter 3). The pilot experiments carried out in the Reversing Flume (Chapter 2), resulted in the identification of the following main factors that influence the evolution of the bed mound: sediment grain size; flow velocity; water depth; flow oscillation period; flow elapsed time; and relative height of the mound with respect to the water depth.

The experiments carried out in the UKCRF were aimed at understanding the evolution of a bed mound under controlled conditions typical of a sandbank or spoil heap in unidirectional and tidal flow. Answers were sought to the following questions: What are the differences in evolution of a large-scale mound when subject to steady unidirectional or simulated tidal flows? What is the difference in effect of placing the large-scale mound on a mobile or a fixed bed? How does the initial shape of the large-scale mound affect its evolution? How does the mound's initial height with respect to the water depth influence its evolution?

The extensive data collected provided information on:

- Flow velocity time histories from the ADV[1] records and image tracing analysis;
- Velocity deficit downstream of the mound;
- Wake characteristics (width, strength, periodicity, eddy shedding) from the images;
- Integral properties of the mound (height, volume and centroid coordinates);
- Sediment transport rates from analysis of cross-sections of the mound in steady flow conditions; and
- Qualitative visualisation of the morphodynamic processes from the coloured sand tests (see Table 3.4).

This chapter includes a detailed description of the evolution of the mound during the reference cases, Tests 8 and 9 (see Table 3.4). Both mounds were circular in plan shape, and Gaussian in cross section, about 0.15 m in height, and of about 2.5 m radius on a fixed concrete bed. Test 9 was subject to unidirectional steady flow, and Test 8 was performed under oscillating tidal flow conditions. The chapter next evaluates variations in the

[1] Acoustic Doppler Velocitimeter

morphodynamic behaviour from a parameter study. The cases covered steady and tidal flow; mobile and fixed bed; circular Gaussian and triangular elliptical mound shape, and submerged, surface-touching and surface-piercing mounds. The chapter then discusses the evolution of the bed mound volume. It next presents the comparison between experimental sediment transport rates derived through cross-sections and transport rates from well established formulae. Finally the chapter explores the results of a qualitative analysis of the coloured sand images.

## *4.1. Analysis of the morphological evolution of a bed mound*

This section describes the evolution of the bed mound in the analysed test cases, with the aim of providing insight into the morphodynamics of the large-scale bed feature. During the experimental phase, 14 tests were carried out of which 7 cases were fully analysed. Table 3.4 lists the test conditions. The information was gathered from observations: during the testing phase; from image and velocity records; surface float tracks; contour information; mound cross sections; and calculation of transport rates through cross-sections. During the experiments, ripples (laboratory-scale features) were superimposed on the mound and on the fixed bed; these affect the flow conditions and the bed roughness.

### 4.1.1. First reference case: Gaussian Hill with steady flow over a fixed bed (Test 9)

The initial shape was circular in plan view and Gaussian in cross section (2.4 m radius and 0.15 m crest height). Section 3.5 and Table 3.4 give details of the initial conditions for Test 9. Figure 4.1 presents the velocity time history measured by the ADVs upstream and downstream of the mound. Note the flow is from right to left in the Plates.

Figure 4.2 provides a detailed picture of the velocity during the first 20 minutes of the test (the time period denoted $T_1$ in Figure 4.1). Throughout $T_1$ (from 6 to 26 min elapsed time), the velocity upstream remained relatively steady between 0.48 and 0.5 m/s. During $T_1$, the peak downstream velocity was about 0.38 m/s, then it increased gradually throughout the test as illustrated by the black line in Figure 4.1. The changes in downstream velocity are attributed to the presence of the mound and the generation and development of a wake downstream of the mound. These effects will be described further later.

In the initial stages of $T_1$ the water depth at the crest of the mound was at its shallowest and the blockage effect generated strongly sheared secondary flows, which created an area of disturbance at the water surface. The slowing down of the shear fluid layers passing over the mound, and the acceleration of the flow on the sides of the mound initiated flow separation, and generated the wake downstream of the mound. The wake formation process coincided with the dip in downstream velocity observed in Figure 4.2. A wake appeared downstream of the crest (indicated by the lines and ellipse in Figure 4.3, flow from right to left). The crest migrated downstream when the flow velocity rose above the threshold value for sediment motion. As the crest migrated, the wake and water surface disturbance associated with it also travelled downstream. In Figure 4.4, the sand formed a *collapse line* (a structure similar to a large ripple) when the crest of the mound was pushed downstream by the flow, creating a smooth upstream slope and a steep downstream edge. The evolution of the *collapse line* was traced in the images by the migration of the associated surface disturbance. The migration of the crest was associated with the migration of the *collapse line* (as in the Reversing Flume experiments, Chapter 2) (Figure 4.4). When established, the edges limiting the wake were aligned approximately 20º to the stream-wise direction. Figure 4.5 shows the mound began to form a crescentic dune (barchan). As the crest migrated downstream, the top of the mound became flatter and more streamlined. The layer of sand along the radius from 2 m to 2.5 m was thin, and due to the flow velocity exceeding the threshold of motion, the layer formed small ripples that travelled downstream. This made the overall width of the mound decrease. After 11 min elapsed time the floats marking the surface flow trajectories can be seen as white streaks in Figure 4.5. Figure 4.5b shows the velocity over and around the mound as estimated from the float track information. Upstream of the mound, the flow velocity was weaker than on top of the mound and the float trajectories curved around the crest of the mound. Velocities at the front edge of the mound were approximately between 0.44 and 0.48 m/s, in the central mound area were between 0.60 to 0.75 m/s and reached 0.80 m/s or more over the crest of the mound. The *collapse line* ceased to migrate downstream when the mound reached a dynamic equilibrium shape, with a streamlined surface adapted to the flow conditions. The wake stabilised, the surface disturbance became wider and the boundary of the wake less clear (Figure 4.6). The re-circulation bubble at the lee of the mound corresponded to a region of relatively low flow velocity. The effect extended downstream into the far wake, and influenced the record of the downstream ADV located along the centreline. The flow structure in the mound area is shown in Figure 4.6, and can be interpreted as follows: i) yellow ellipse, an area of wavy free

surface associated with the mound crest (very shallow); ii) dark blue ellipse, a region of high turbulence immediately downstream of the crest, including the re-circulation bubble (generated due to flow separation at the crest) where the mean velocity is slower than in the free stream; and iii) light dashed ellipse, the near wake area where the water surface is disturbed. Sand travelling over the crest was entrained into the flow and caught in the re-circulation bubble. These sand particles were deposited gradually on the bed at the lee of the mound forming a layer of short wavelength ripples. The barchan dune appeared fully formed after 20 min elapsed time (Figure 4.7). Strong secondary flows developed due to the blockage effect of the mound on the flow, and generated 'cow horn' eddies over the 'shoulders' of the mound. These flow structures dug pronounced troughs (indicated by black arrows in Figure 4.7) through the mound and dented the sides (marked by ellipses, Figure 4.7). Ripples also developed superimposed on the mound, with their crests aligned approximately perpendicular to the flow direction. Smaller wavelength, straight-crested ripples (classification from Baas, 1993) developed where the water was deeper. Sinuous-crested ripples with greater wavelength occurred at the crest of the mound, where the water was shallower. The smaller, shallower ripples were superimposed on the underlying, larger ripples. At the end of $T_1$ the front and back edge slopes of the mound along the centre-line were about 3° and 27° respectively. The back edge slope was close to the angle of repose (typical value for sand is 32°). The front of the mound migrated approximately 0.5 m downstream. The mound spread in the cross-flow direction although, due to dents on the lateral edges its effective width decreased locally from 5 m to about 4 m.

During $T_2$ (33 to 73 min elapsed time), the mound continued to migrate steadily downstream. This was due to the sand travelling downstream over the ripples as bed-load by means of saltation and rolling. Meanwhile ripples themselves move, with sand particles being carried up the upstream slope to the crest, and from the crest to the next trough by vortices located in the lee of each ripple, the vertical flow structure is shown in Figure 4.8. It should be noted that the sand travelled at different speeds depending on location. Strong secondary flows helped remove sand to the extent that the concrete bed became exposed in places close to the central area of the mound. Sometimes, these exposed areas became covered again as the mound evolved (Figure 4.9). At the end of $T_2$ (after 1 hr total test run time) the bed slope at the front of the mound was about 2°. The bed slope downstream was again approximately equal to the angle of repose (~32°). With time, the shape of the mound became more elongated, narrower upstream and wider downstream; its overall width was

approximately 3.5 m. The front edge of the mound migrated 0.8 m relative to its position at the start of the test. The back edge of the mound migrated 0.85 m. This indicated that the front edge of the mound was migrating at a slightly slower rate than the back edge, so that the length of the mound grew. The trails downstream of the mound were thicker, but they were mostly outside the image frame. A tail-like structure aligned to the stream-wise direction appeared, and was connected to the back step (indicated by a white arrow in Figure 4.7, also present in Figure 4.10). It may have been due to existence of a flow convergence area (between the re-circulation bubble and the flow) where the sediment deposits**.** The smaller wavelength ($L_r$) ripples at the front of the mound travelled faster and grew by combination of small ripples and being absorbed by larger ripples (short $L_r$ ripples travel faster, Baas 2003). These ripples evolved from straight-crested (Figure 4.7) to be sinuously-crested ($L_r$ ~ 0.4 – 0.5 m) (Figure 4.10). The larger wavelength ripples in the central area were sinuous-crested (Figure 4.7) and became linguoid ripples ($L_r$ ~ 0.5 – 1 m) (Figure 4.10). At this time there was evidence of a preferential alignment of the linguoid ripple crests and troughs. The crests seemed to be connected and aligned between 30 and 45 degrees anti-clockwise to the stream-wise direction (indicated by dashed lines in Figure 4.10).

During $T_3$ (81 to 142 min elapsed time), the mound migrated steadily downstream. The overall shape of the mound became narrower and more pointed as the mound decreased in height. The flow over the mound during $T_3$ was not as violent as during $T_1$ and it was steadier than during $T_2$. Whereas the re-circulation bubble was still visible, it was weaker than in $T_1$ and $T_2$ (the loss of strength is connected with the decrease in height of the mound). At the front of the mound the sand layer thinned and stretched as the mound migrated downstream. Intermittently the flow dug holes through the sand to the concrete bed in the central part of the mound (Figure 4.11). At the end of $T_3$ the slopes of the front and back end of the mound were respectively about 3°, and 29°. The front-edge of the mound had migrated about 1.5 m downstream at the end of $T_3$ (black lines in Figure 4.12). The back edge of the mound was outside the image frame (more than 4.2 m downstream from the initial position of the crest). The back edge migrated about 2 m from its position at the start of the test. The width of the mound at the end of $T_3$ was 3.8 m (initial width 4.8 m). It should be noted that only partial information was available from the images, from which to estimate the width of the mound. The mound was overlain with large wavelength ripples, on

top of which were superimposed shallow ripples. The large wavelength ripples appeared flatter.

During $T_4$ (147 to 208 min elapsed time) the front end of the mound became even more pointed and narrower (arrow-like shape, Figure 4.13) as the mound continued to travel downstream. The wake and re-circulation bubble were not visible in $T_4$ as the back of the mound was outside the image frame. There were small saw tooth features on the lateral edges of the mound (Figure 4.13). At the end of $T_4$ (and end of the test) the front slope of the mound was 3°. Overall the mound migrated a total of 2.25 m. The width of the mound within the image frame was 3.5 m. The total decrease of the width of the mound at the end of the test was 1.5 m. The mound was superimposed with linguoid ripples of varying wavelengths ($L_r$ ~ 0.25 – 0.8 m). The ripple wavelengths on the front and sides of the mound were smaller than in the central region.

Figure 4.14 shows the evolution of the crest height and volume of the mound with time. The volume was calculated using the digitised contours (as described in Section 3.5.2). The crest elevation decreased by 56 % after 3 hr run time under steady flow conditions. At the end of the test (208 min elapsed time) sand from the back of the mound was outside the image frame, so the volume calculations at this point underestimated the total volume of the mound. Throughout the test, the volume of sand making up the mound decreased. After 3 hr the total visible volume was about 48 % that of the initial volume. Figure 4.15 shows the time history of the location of the centroid of the mound. The centroid (calculated as per Section 3.5.2) moved 2.5 m downstream in the stream-wise direction by the end of the test (i.e. about 0.84 m/hr, which is 0.05 % of the flow velocity, 1800 m/hr). There was no net migration in the cross-flow direction where the centroid remained within ± 0.1 m of the flume centreline. As the mound spread and decreased in height, the vertical position of the centroid decreased to approximately half its initial value, from 0.04 to 0.018 m.

The velocity deficit between the upstream and downstream ADVs provided information about the effect of the mound on the flow conditions. As the mound changed shape (most critically height) its effect became less pronounced on the downstream velocity. Figure 4.2 presents the detailed horizontal velocity time history for $T_1$. The velocity was ramped up slowly. During this time both the upstream and downstream ADVs recorded the accelerating flow until the flow upstream reached the peak flow velocity. The upstream ADV recorded the unaffected velocity (0.48 and 0.5 m/s). The downstream velocity initially followed the upstream velocity up to 0.35 m/s, then breaks away up to 0.41 m/s. Then it

decreased for about 5 min to a minimum of 0.17 m/s (at this point the maximum velocity deficit was 0.33 m/s), and then recovered after 21 min to about 0.39 m/s. After 25 min elapsed time the ramping down of the flow started. Flow separation occurred in the first 5 min of $T_1$, marked by the dip in the downstream velocity (Figure 4.2). Through this time, a wake started to develop and the crest of the mound travelled downstream. During the ramping up, the flow is uniformly accelerating, the boundary layer is thin; the forces on the mound are inertial; the flow is irrotational; and the favourable pressure gradient suppresses the turbulence. Flow separation did not occur immediately after the velocity became uniform (it would occur when the velocity gradient near the mound was greatest), so it took some time for a wake to form and develop. The sediment started to move only when the velocity exceeded the threshold for motion. The crest travelled downstream and the mound changed shape to adapt to the flow conditions. Once the mound reached a certain height, and the wake became more stable the velocity downstream started to recover. In Figure 4.1 the black line indicates the gradual increase in downstream velocity from about 0.38 m/s at the end of $T_1$ to approximately 0.43 m/s at the end of $T_4$. This trend is confirmed by Figure 4.16, presenting the comparison of the evolution of the crest height and the downstream velocity.

### 4.1.2. Comparison of a Gaussian Hill with steady flow over mobile (Test 13) bed with fixed bed case (Test 9)

The results from Test 13 are compared against those of Test 9 to assess the differences in the evolution of a Gaussian mound on an underlying mobile or fixed bed under steady flow conditions. This discussion will concentrate on differences between the results from Tests 9 and 13. New information will also be included for Test 13, in particular the evolution of the mound on the mobile bed. Further analysis of this test case will be reported in Section 4.4 in relation to the qualitative findings from the coloured sand analysis.

The mound in Test 13 was circular in plan view, and Gaussian in cross section (2.7 m radius and 0.15 m crest height, refer to Section 3.5.1). The mound was composed of red and green sand, as shown in Figure 4.17, with a blue sand circle at the centre. The mound laid on a natural-coloured mobile bed of 0.025 m thickness. The still water depth was 0.20 m above the initial sand bed. There was no mobile sand layer under the ADVs. Note the unidirectional flow was from right to left in the figures. Figure 4.18 exhibits the time history of horizontal velocity during Test 13. The peak upstream horizontal velocity measured at

the ADV was 0.43 m/s. Assuming continuity the estimated flow velocity over the mobile bed for a water depth of 0.20 m was about 0.48 m/s.

The initial behaviour of the mound and the related flow hydrodynamics are similar to those in Test 9: the blockage effect, secondary flows, surface disturbance and formation of a wake and a re-circulation bubble, the migration of the crest, flattening of the mound and the development of a smooth front slope and a sharp lee slope.

Figure 4.19 shows the details of the horizontal velocity history for $T_1$ (4 to 25 min elapsed time). The velocity was ramped up for 4 min to the peak velocity value. Then, during $T_1$, the upstream velocity remained relatively constant at about 0.43 m/s (approximately equivalent to 0.48 m/s over the mobile bed). At the end of the ramping, the downstream velocity decreased for 4 min and reached a minimum after 8 min elapsed time. Small ~ 2 min oscillations were observed in the downstream velocity time history that will be discussed later. Figure 4.20 shows the detailed time history for $T_2$ (33 to 73 min elapsed time), during which the upstream velocity remained constant at about 0.48 m/s over the mobile bed. The downstream velocity trace contained low frequency oscillations (of period ~10 min) about 0.43 m/s. Test 13 was the only test in which the recorded downstream and upstream velocities were so similar.

Figure 4.21 exhibits the initial extent of the thin layer of coloured sand on the skirt of the mound (of thickness varying from 0 to 0.01 m, more detailed information on the cross sectional shapes is given in Section 3.5.1). This surface sediment layer was highly mobile. After 9 min elapsed time (Figure 4.22) the mobile bed became superimposed with short wavelength ripples ($L_r$ ~ 0.05-0.10 m). The crest of the mound formed two ‘shoulders’ (indicated by white arrows, Figure 4.23) approximately 2 m apart in the cross-flow direction. After 14 min elapsed time, most of the thin sand layer (mentioned in Figure 4.21) had travelled downstream, leaving a footprint of coloured sand around the mound (Figure 4.24 onwards).

The float tracks visible as white streaks in Figures 4.25 and 4.26, describe the flow path-lines (given the snapshot was taken over a fraction of a second and the trajectories were fairly straight it can be assumed that the floats followed the streamlines). Near the crest of the mound, the trajectories diverged. Downstream of the crest the trajectories were straight and parallel. The velocities estimated from the tracks varied in the stream-wise direction. After 14 min, the tracks from Figure 4.25 indicate that in the upstream region of the mound the velocity was equal to the free stream velocity. After 16 min, the velocities deduced from the float tracks in Figure 4.26 are shown in Figure 4.27. These show that the velocity

upstream of the mound is similar to the free stream velocity. The flow accelerated over the front area of the mound, and in the central area it reached a magnitude of about 0.75 m/s or greater. Downstream of this central area the flow started to decelerate slightly, and at the lee of the crest (corresponding to the re-circulation bubble) the velocities were much lower than the free stream value (~0.15 – 0.20 m/s). This behaviour was similar to Test 9. Figure 4.25 shows the mobile bed where ripples evolved differently during $T_1$ according to their location relative to the mound and local flow conditions.

The ripples in Area 1 were straight-crested and of short wavelength (~0.10 to 0.15 m). The shortest wavelength ripples occurred in Area 2, corresponding to the re-circulation bubble. Sinuous-crested ripples with longer wavelengths were present in Area 3 where the effects of the secondary flow were greatest. Figure 4.28 shows the mobile bed at the end of $T_1$ (26 min elapsed time). Short wavelength sinuous-crested ripples occur in the area upstream of the mound (Area 1). Short wavelength, straight-crested ripples are present in Area 2. Short wavelength incipient ripples (red sand) form over Area 2a on the mound. Linguoid ripples of intermediate wavelengths occur in Area 3; longer-wavelength linguoid ripples occur in Area 4. In Areas 3 and 4 small regions of the concrete floor are visible through the mobile sand layer. At the end of $T_1$ the mound was sparsely covered with incipient or short-wavelength ripples (Figure 4.28). This was not the case for Test 9, where the mound was superimposed with linguoid ripples (Figure 4.8). The bed disturbance in Area 4 contributed to give the mound the characteristic star-shape pattern (Figure 4.29) described by De Vriend (1987) and Lesser *et al*. (2004). The increase in sand height in this area was not due to cross-flow sand transport (the sand would be coloured), but to a feed-back mechanism comprising the mound, the flow and the free surface disturbance (Figure 4.28). This will be further discussed in Chapter 5. This effect was not so clear in the fixed bed case, due to the lack of excess material available to be eroded or deposited. In this case the sand formed ripples at the back of the mound. The dashed line in Figure 4.8 (including the sand at the back of the mound) shows that the back edge of the mound appeared more curved and the overall shape was more similar to the star-shaped pattern. Note the feature marked by an arrow in Figure 4.29, similar to that observed in Figures 4.7 and 4.10.

In Test 13, sand from the mobile bed travelled downstream; evidence for this was that the small strip of concrete visible at the left hand boundary of Figure 4.17 was almost covered by sand after 26 min elapsed time (Figure 4.28). At the end of $T_1$, the slopes at the front and back edge of the mound were 5° and 26° respectively. These are similar values to

the fixed bed case. At the end of $T_1$ the front of the mound migrated approximately 0.75 m and the crest travelled more than 2 m downstream. The width of the coloured sand portion of the mound along the cross-flow direction was approximately 3.1 m. Figure 4.30 indicates the shape of the coloured part of the mound at the end of $T_1$.

At the start of $T_2$ (33 to 73 min elapsed time) the mound became superimposed with small incipient ripples that grew with time. The concrete bed became visible intermittently at certain locations after 36 min (Figure 4.31). Ripples in the mobile bed at the sides of the mound started growing from 39 min onwards, until their wavelengths were comparable to those on the edges of the coloured part of the mound (Figure 4.32, 42 min). Ripples of longer wavelength (red sand) travelled over the central area of the mound. Natural sand from the mobile bed, upstream from the mound, travelled over the front of the mound (Figures 4.32 to 4.40). From 49 min onwards, deep troughs started to develop on the central area of the mound, with the crests at an angle to the flow direction (indicated by arrows in Figures 4.33 and 4.34). At 52 min (Figure 4.35) the troughs in the central area of the mound deepened. Figures 4.36, 4.37 and 4.38 show the formation of three large ripples superimposed on the mound. The three ripples became clearer after 61 min (Figure 4.39). The troughs of the three ripples were aligned about 120° degrees anti-clockwise from the stream-wise direction. The flow structures dug pronounced troughs through the mound, natural sand was exposed locally (Figure 4.39) and on occasions the concrete bed was also exposed (Figure 4.40). The crests of the ripples migrated downstream at similar rates.

At the end of $T_2$, the volume of red sand at the front of the mound had reduced to a strip about 1 m wide in the stream-wise direction. The dimensions of the mound behind the $x$ = 0 m line increased in length and decreased in width with respect to the initial shape. Figures 4.41 and 4.42 indicate the evolution of the plan shape of the coloured portion of the mound, becoming more elongated with time. At the end of the test (Figure 4.43a) the crest migrated 3.9 m from its initial position. The front and back edges of the mound both migrated about 1.5 m over the duration of the test. For the same time period, the crest migration in the fixed bed test was shorter (3.2 m) than in the mobile bed case. Similarly, the distance travelled by the front and back edges of the mound was smaller (~0.8 m) than in the mobile bed case. In Test 13, the width of the coloured portion of the mound decreased to about 3 m in 1 hr. In this test it was difficult to define the edge of the mound because part of the disturbed mobile bed needed to be taken into account (white line forming the star-shaped pattern, Figure 4.43b). In Test 9, the mound described a similar star-shaped pattern to

Test 13, when the sand downstream of the mound was considered (Figure 4.7 and 4.43b). The slopes of the mound at the end of Test 13 were 7° at the front and about 25° for the back edge. At the end of the test the mobile bed was covered with linguoid ripples of varying wavelengths and the concrete bed was exposed through the layer of natural sand. Mobile bed ripple migration rates were estimated along the stream-wise direction (after 64 and 65 min) and were found to be between 0.29 and 1.1 mm/s. Table 4.1 compares the ripple and centroid migration rates along the stream-wise direction for a mobile bed case (Test 13) and a fixed bed case (Test 9). The average migration of ripples in the mobile bed, along the stream-wise direction was up 2.5 times faster than the centroid of the mound, confirming that small ripples/features migrate faster than large ripples/features. The ripple migration was estimated from images, measuring the distance a number of ripples travelled for a time interval.

Figure 4.44 presents the time evolution of the crest height of the mound for both Test 9 and 13. The crest elevation decreased exponentially by 42 % after 1 hr in the mobile bed case compared to a 38 % decrease in the fixed bed case. The volume of sand making up the mound decreased by 49 % in 1 hr in the mobile bed case, but only 11 % in the fixed bed. It should be noted that the volume of the mound was estimated using bed elevation values above the 0 m contour, corresponding to the elevation of the undisturbed mobile bed in the absence of the mound. This could be related to a feed-back mechanism between the mobile bed layer and the local flow hydrodynamics affecting the sediment transport. Figure 4.45 shows the time history of the location of the centroid of the mound. The centroid migrated 2.05 m downstream in the stream-wise direction. Net migration in the cross-flume direction was almost negligible. The vertical location of the centroid decreased slightly from 0.035 to 0.019 m.

Figure 4.19 presents the detailed horizontal velocity time history for $T_1$ (4 to 25 min elapsed time). During the initial stages of the ramping period (from 0 to about 4 min before the start of $T_1$) the upstream and downstream velocities increased together up to 0.17 m/s, when the two curves started to differ. The upstream velocity increased until it reached the peak flow velocity, about 0.43 m/s and remained relatively uniform during the rest of $T_1$. The downstream velocity reached its maximum value, about 0.32 m/s, after 4 min elapsed time, and reached a minimum of about 0.12 m/s after about 8 min. The maximum velocity deficit occurred at this point, when the downstream velocity was 72 % of the upstream velocity. During this velocity decrease, the downstream ADV recorded some oscillations

due to the formation of the wake downstream of the mound, and the initial downstream migration of the crest of the mound. Once the mound decreased to a certain height the conditions changed and the wake became dynamically stable. After about 9 min, the downstream flow velocity started to recover gradually, reaching 0.40 m/s at the end of $T_1$.

Figure 4.20 shows the detailed time history of the horizontal velocity during $T_2$, during which the upstream and downstream velocities were very similar. The downstream ADV recorded some oscillations of about 10 min period. These oscillations could be connected to the head of water generated upstream by the pumping system. The similarity between the upstream and downstream velocity record was not found in the other tests, where the underlying bed was fixed and the velocity downstream was lower due to the effect of the mound on the flow. The effect of the reduction in height of the mound was not visible in the downstream velocity record. Therefore it is assumed that it was the mobile bed that induced the recorded behaviour. Presumably, the effect of the mobile bed in the downstream velocity suppressed the effect that the decrease in height of the mound and the wake would have on the downstream velocity record. The mound and the mobile bed seemed to be adjusting hydrodynamically, so that the result was a reduced drag effect on the downstream velocity.

Figure 4.46 presents the relationship between the decay in height of the mound and the variation in the velocity deficit.

### 4.1.3. Second reference case: Gaussian Hill with tidal flow over a fixed bed (Test 8)

The initial shape and dimensions of the mound were the same as the first reference case (Test 9, described in Section 4.1.1), i.e. a Gaussian hill in cross-section, 0.15 m height, 2.4 m radius. The oscillation period of the tidal flow was 20 min. Section 3.5 and Table 3.4 give details of the initial conditions. Figures 4.47, 4.48 and 4.49 show the time history of the horizontal velocity component measured by the ADVs upstream and downstream of the mound. Figure 4.50 gives a detailed picture of the measured horizontal velocity components during the first three cycles of Test 8. Flow initially proceeded from right to left in the images (in the images, ADV1 is on the right and ADV0 on the left of the mound).

The mound behaved as a dynamic structure, the bedforms evolved continuously from the moment the flow was above the threshold of sediment motion until it dropped below it. Details on the bedforms were inferred mainly at periods of slack water. Figure 4.51

indicates that flow separation occurred at the crest and shear flows developed at the sides of the mound, causing a wake to evolve behind the mound. The wake consisted of a re-circulation bubble and associated free surface waves. The wake was unsteady and grew to a maximum, reduced and reversed according to the phase of the tidal flow. Figure 4.52 shows the situation at elapsed time ($T_E$ =) 5 min, when the limits of the wake were aligned at about 20 degrees to the stream-wise axis. The crest of the mound travelled downstream (as a *collapse line*) until the flow lost strength forming a barchan dune with a smooth front face and steep step at its rear (Figure 4.53). The flow reversed and the process was repeated, generating strongly three-dimensional flows ('cow-horn' eddies) due to blockage and the development of a wake downstream of the mound. The central area of the crest travelled faster than the sides generating a V-shaped front beyond which the surface slope was limited by the angle of repose of the sand, as can be seen in Figures 4.54 and 4.55. Meanwhile, the wake including the re-circulation bubble travelled downstream. As the crest travelled downstream the top of the mound became flatter. Figures 4.54 and 4.55 illustrate the time-varying extent of the wake over half a cycle. The free surface waves generated at the crest were of larger amplitude when the crest was travelling downstream, than when the crest ceased to migrate.

For the tidal case, it was not clear whether there was sufficient time within each half cycle for the mound to reach a dynamically stable form before flow reversal occurred. The sand was in motion for about 5-6 min of each half cycle, which lasted 10 min. However, in the steady flow case, the crest took about 5-6 min to travel downstream, which would seem to indicate that the crest may have had enough time to migrate downstream in the tidal case. Figures 4.56 and 4.57 compare the wake after 5 and 15 min respectively, the times corresponding to the peak flow velocity. The wake appears weaker after 15 min, in agreement with the recorded velocity time history during the first cycle (Figure 4.50). Figure 4.53 shows the downstream migration of the crest of the mound after 10 min (mid-cycle). Float track information was available after 6 and 16 min (Figures 4.58 and 4.59 respectively). Careful inspection of the float tracks in Figures 4.58 and 4.59 indicates that the streamlines diverge near the mound. Figures 4.60 and 4.61 present the velocity magnitudes at 6 and 16 min elapsed time. The flow speeds up over the mound, whereas the flow in the re-circulation bubble after 6 min (Figure 4.58) is relatively stationary. Horizontal flow speeds over the mound are estimated to be between 0.46 m/s at the leading edge to 0.8 m/s over the crest (Figure 4.60). After 16 min (Figure 4.61) the horizontal flow speed at the leading edge of the mound is approximately the same as the free stream velocity.

Immediately before the crest the flow accelerates to about 0.75 m/s. Over the crest, the flow accelerates further to about 0.85 m/s. Figure 4.62 shows dents developed on the flanks of the mound. Figure 4.63 shows the mound at the end of the first cycle, where no net migration had occurred. The crest line (and the steep step) migrated an equal distance either side of the cross-flume centre line after 10 min (mid-cycle) and 20 min (end of the cycle) as can be seen in Figures 4.53 and 4.63. At the end of the first cycle, the slopes of the front face and the back step of the mound were about 4° and 25° respectively. After one cycle the effective width of the mound decreased to 2.5 m in the central section (indicated by red circles in Figure 4.63) due to the strong shear flows generated by separation from the mound. The transport of sediment over the mound generated trails of sand downstream of the mound. Ripples were superimposed on the mound (Figure 4.63), of short wavelength in deep water and larger wavelength in shallower water. After 20 min the ripple wavelengths superimposed on the mound were shorter than in the corresponding steady flow case described in Section 4.1.1 (Figure 4.8). The ripple characteristics provided qualitative information regarding the flow behaviour. Upstream of the peak of the mound, the ripple wavelengths were shorter and straight-crested. In the peak area, ripples became linguoid (due to 3D flow effects). Figure 4.63 shows ripples curved around at an acute angle, and hugging the central area of the mound that is higher and flatter. Downstream of the peak is a steep step followed by a smooth slope with short wavelength ripples superimposed.

Figures 4.64, 4.65 and 4.67 exhibit the migration of the crest at 23, 24 and 26 min, with its central area travelling faster than its sides. Figures 4.65 and 4.66 demonstrate the time-varying intensity of the wake and re-circulating bubble. Figure 4.67 shows the mound after 29 min (near slack water) when the wake downstream of the mound is still visible. Figures 4.66 and 4.68 show the flow path-lines marked by the float tracks after 26 and 37 min, the flow pattern curving around the mound. Figure 4.69 shows the surface disturbance after 44 min was weaker than earlier and covered a large area. The crest migrating downstream was wider and appeared to be starting to divide into two fronts. After 54 min the surface disturbance generated by the migrating crest was as wide as the mound (Figure 4.70). After one hour elapsed time (Figure 4.71) two crests were identified (indicated by white lines, and shown in more detail in Figures 4.72 and 4.73). At this time, the mound was 2.5 m wide at its narrowest (in the central region). After one hour the front and back slopes were 4° and 25°. The alternating reversing flows drove the sand downstream and re-shaped the mound every half cycle. As the mound evolved, its surface

slopes were smooth before and after the crest, except for new and relict steps (Figures 4.72 and 4.73). The resulting shape comprised an overlapping pair of barchan dunes (Figure 4.74). Ripples were superimposed on the mound, the larger and irregular ones in shallower areas and straight-crested in deeper water where the layer of sand was thinner. Ripple troughs were more pronounced in the central area of the mound (indicated by white lines in Figure 4.71). The ripples may be subject to a feedback mechanism, whereby they grow as the local sediment transport rate increases.

Figure 4.75 shows the mound after 2 hr. The width of the mound in the central area was about 2.5 m. The dents on the sides of the central part have widened (indicated by red ellipses). The trails of sand on the upstream and downstream end of the mound were comparatively symmetrical, the most recent one to the right. The front and back slopes were 4° and 11°. After 2 hr, the mound presented three crests (shown as white lines on Figure 4.75). These crests corresponded to three long wavelength ripples, whose crests were aligned at about 65° to the flow direction. Smaller ripples (indicated by blue circles in Figure 4.75) were superimposed on these long wavelength ripples. Other small ripples covered the front and back slopes.

Figure 4.76 shows the situation after 4 hr elapsed time, with the mound further spread in the stream-wise direction. However, the bulk of the sand volume remained within the confines of the initial footprint (implying that the sand moved along the stream-wise axis and that the mound volume was re-distributed transversely within the footprint area). The front and back step slopes were 6° and 21° respectively. After 4 hr there were multiple crests and troughs in the central area of the mound. The troughs were more pronounced. Due to the decrease in mound height the reversal of the flow did not generate such strong secondary flows as before, and the blockage effect was weaker. A weak wake persisted behind the mound.

Between Cycles 6 and 12 (2 to 4 hr elapsed time) the mechanics of the mound evolution changed from that of a single entity to that of a succession of ripples. Figure 4.77 shows the mound after 5 hr, whose plan shape is similar to the superimposition of two barchan dunes of opposite sense of orientation (Figure 4.74). The rear edges of both dunes spread further in the cross-flow direction (the trails of sand emanating from both sides of the mound formed the back edge of the crescentic dunes). The mound was 2 m wide at its narrowest. The slopes were 9° and 20° at the front and back step of the mound. There was no definite sign of preferential net migration of the mound, however the trail to the right

appeared to be thicker. There were multiple crests in the central area of the mound, with deep troughs between them. The concrete bed underlying the mound was visible at certain points. After 5 hr the mound appeared partially to lose its identity and cohesion. The wake and surface disturbance at the lee of the mound were weaker. In general the images from the mound after 2, 4 and 5 hr are similar to each other in general shape and structure (Figures 4.75, 4.76 and 4.77). With time the flanks of the mound became indented, and increasingly corrugated, until the mound degenerated into multiple intermediate wavelength ripples.

Figure 4.78 presents the final evolved shape of the mound at 20.3 hr. The mound has flattened out and spread longitudinally, while its centroid migrated leftwards due to slight asymmetry in the flow velocity. After 20.3 hr, almost no trace was left of the original mound, it having broken down into large ripples interspersed with the exposed concrete bed. It may be that if the mound were much larger (i.e. a full-scale sandbank), there would be a sufficient internal supply of sand for the sandbank to remain an entity that does not degenerate but become progressively streamlined while having small scale ripples superimposed. The slopes of the final evolved mound were particularly difficult to estimate due to the dominance of the ripples. Rough estimates of the slopes of the back step were about 24 to 29° and the front slopes were about 7 to 13°.

Figure 4.79 and exhibit the evolution of the mound during the test. After 1 hr the mound height decreased by 16 %. At the end of the test (20.3 hr) the height of the mound was 47 % of the initial mound height. The volume of the mound in tidal flow decreased at a slower rate than the steady flow case. At the end of the test the volume of the mound reduced by 32 %. The evolution of the centroid location is presented in Figure 4.80 The net migration of the centroid in the stream-wise direction was noticeable only at the end of the test, and was due to a small flow asymmetry, the centroid migrated 0.96 m to the left of the image (Figure 4.76). There was no significant transverse migration. The initial height of the centroid of the mound was approximately the same in both the steady flow and tidal flow cases. However the centroid height decreased more quickly in the steady flow case (0.018 m after 3 hr) than in the tidal flow case (0.017 m after 20.3 hr).

Figure 4.50 shows the time dependent horizontal velocity components measured by the ADVs either side longitudinally (i.e. in the stream-wise direction) of the mound. Initially the flow accelerated over the mound, and the upstream and downstream velocity components were similar. When the peak upstream velocity was reached, the flow stopped accelerating

over the mound and instead separated from the sides of the mound forming a wake. A velocity deficit then occurred between the upstream and downstream ADVs (depending on the reversing flow direction during the tidal cycle) due to blockage and wake effects. This deficit then decreased with time, from about 0.2 m/s at the end of the first cycle to about 0.05 m/s after 20.3 hr, as the height of the mound (and hence its blockage) reduced (Figures 4.47 to 4.49). Figure 4.81 shows both the reduction in velocity deficit and crest height during the test. A slight asymmetry was evident in the flow velocity. Although the target velocity was 0.5 m/s, the peak velocities measured by ADV 1 and ADV 0 were ~ 0.51 m/s and ~ -0.49 m/s.

**Summary of differences between steady and tidal flow**

The wake was more stable in the steady flow case, as it was allowed to develop and reach a 'dynamic equilibrium' that evolved as the mound changed shape. In the tidal flow case the wake had limited time to develop, and it was an unsteady feature, forming and disappearing every half cycle.

For a comparable period of time, the migration rate of the mound was noticeable under steady flow and practically zero under tidal flow conditions. The flow velocity exceeded the threshold of sediment motion for the duration of the test in the steady flow cases, whilst in the tidal flow cases it only exceeded the threshold about 50 % of the time. During the tidal cases (if suspension occurred) the sediment transport might not reach equilibrium, though most of the transport during our tests was assumed to be bed load transport. For bed load, once the threshold of sediment motion is exceeded, the reaction is near-instantaneous between the flow velocity and the sediment motion.

In steady flow the mound evolved into a barchan dune. In the tidal flow case the mound evolved to form two superimposed barchan dunes migrating through each other in opposing directions (Figure 4.74).

The morphology of the mound in the tidal case registered the morphological history of the previous half cycle. The flow did not act on it for long enough (or was not strong enough from the opposite direction) to erase the steep step from the previous half cycle. In the steady flow case the flow started always from the same direction, and there is no evidence of any residual form.

The form and evolution of the ripples was different in tidal and unidirectional flow cases. Due to the (unsteady conditions) varying velocities, water depth and the reversal of

the flow in the tidal case, there was not enough time for the ripples to reach the predicted equilibrium wavelength and height given the grain size according to Baas (1993) formula.

It is possible that if the mound were much larger (i.e. a full-scale sandbank), there would be a sufficient internal supply of sand for the sandbank to remain an entity that does not degenerate but become progressively streamlined while having small scale ripples superimposed.

### 4.1.4. Comparison of a submerged Gaussian Hill (Test 8) and an elliptical mound (Test 11) under tidal flow

This section considers the effect of the initial shape of the submerged mound on its evolution in a tidal flow. Test 8 involves a Gaussian hill, whereas Test 11 deals with an elliptical mound. The mound in Test 11 was elliptical in plan view, triangular in cross-section (6 m long axis and 2.6 m short axis) and 0.15 min height. The flow past the Gaussian hill started from right to left in the images, and in the elliptical mound case the flow started from left to right. The bed profiles were acquired at the end of a cycle, with the last flow direction from the left in the case of the Gaussian hill and from the right in the elliptical case.

For both the elliptical and Gaussian mounds, the peak upstream horizontal velocity components were similar (about 0.52 m/s and -0.50 m/s, with respect to each half cycle). Figures 4.82 to 4.86 show the time history of the horizontal velocity components measured for the elliptical mound case using the upstream and downstream ADVs (noting of course that upstream and downstream swap over as the flow reverses each tidal cycle).

Table 4.2 lists the angles of the front and back slopes obtained at different elapsed times for the elliptical and Gaussian mound cases. The upstream slope for a given cycle is the front slope, and the back slope is the lee slope for that cycle. These slopes are based on cross sectional information of the interpolated contour data along the centreline of the basin in the stream-wise direction. In general, the front slopes are approximately the same for both cases, noting that the front slope contained a residual step left behind from the previous half cycle. The back slopes were less steep for the elliptical case in accordance with the mound's more streamlined shape, which disturbed the flow less causing a narrower crest front. There may also be memory effects, so that the downstream slope is larger for the Gaussian hill where the flow is more disturbed in its wake.

Figure 4.87 compares the time-dependent behaviour of the crest height and volume for Tests 8 and 11. The crest height of the elliptical mound decreased about 6 % less than

that of the Gaussian hill over the elapsed period of 20.3 hr. The volume of the elliptical and Gaussian mounds decreased by 27.5 % and 32 % over the same period, the difference being about 5 %. Figure 4.88 indicates the evolution of the centroid location with time. In the stream-wise direction the centroid of the elliptical mound migrated 0.2 m further than the Gaussian hill. Although the initial elevation of the centroid of the elliptical mound was slightly lower than that of the Gaussian hill, both centroids decreased in elevation by about the same amount over the duration of the test. Figures 4.89 to 4.93 show the evolution of the elliptical mound after 0.33, 1, 3, 20.3 hr. The width of the elliptical mound was initially about 2.6 m. The width of the mound did not change rapidly through the test, after 3 hr the mound was 2 m wide and after 20.3 hr the remainder of the mound was a slightly less that 2 m wide. However, due to the evolution of the indentations in the sides of the mound, the width of the mound appeared to increase with time (after 20 min ~ 2.9 m, after 1 hr ~ 3.2 m, after 3 hr ~ 3.5 m, at the end of the test ~ 4 m including all the ripples).

No eddy shedding was observed during either Tests 8 or 11. Instead, in both cases, a wake formed as the crest migrated downstream and a large area of free surface disturbance was observable as trailing waves downstream of the crest of each mound. After 5 min the area covered by the free surface disturbance in Test 8 was larger than that in Test 11 (Figure 4.52 and 4.94). After 15 min, the area covered by the free surface disturbance in both cases was similar to that after 5 min though the waves became weaker (Figures 4.55 and 4.95). The wake downstream of the elliptical mound was narrower than that behind the Gaussian hill. The blockage effect of the elliptical mound was weaker than that of the Gaussian hill. Secondary flow had greater effect on the Gaussian hill than the elliptical mound after 1 hr, causing deeper indents to the side of mound (Figures 4.71 and 4.91). At the end of the test, the initially Gaussian hill (Figure 4.78) had dispersed more than the initially elliptical mound (Figure 4.93). The ripples in the central area of the initially Gaussian hill were separated by strips of the exposed concrete floor, where the otherwise overlying sand had been lifted out by eddying motions. By contrast, the initially elliptical mound had retained more of its identity. In the central area of Figure 4.93 there is a portion of the sand not broken down and separated into ripples.

Figures 4.82 to 4.86 show the time history of the horizontal velocity components measured for the elliptical mound case using the upstream and downstream ADVs (noting of course that upstream and downstream swap over as the flow reverses each tidal cycle). During the first cycle, the velocity components behave in a similar manner to that recorded for the Gaussian hill, but with a reduced velocity deficit. This is likely to be due to the more

streamlined shape of the elliptical mound, which helped curtail wake development. However, the long-term rate of decrease in velocity deficit as the mound lost height was less than for the Gaussian hill. After about 3 hr elapsed time, the velocity deficit was similar in the elliptical and Gaussian mound cases. Although the elliptical mound continued to lose height, the velocity deficit remained nearly constant from about 15 hr onward, unlike for the Gaussian hill. This may indicate that the surface of the evolving elliptical mound becomes increasingly rippled (in comparison to the Gaussian hill) as the height reduced, maintaining a nearly constant overall resistance to the flow. Even with the re-shuffling of the (elliptical mound) volume in cross-section (became flatter) the blockage for the Gaussian and elliptical mounds remained similar. The comparison of the decay of crest height and velocity deficit with time in the elliptical mound case is shown in Figure 4.96 (the equivalent plot for the Gaussian hill, Test 8 is shown in Figure 4.81).

### 4.1.5. Evolution submerged (Test 11, SM), surface-touching (Test 4, ST) and surface-piercing (Test 3, SP) elliptical mound in tidal flow

The results from Tests 3, 4 and 11 are compared to assess the effect of the initial mound crest height relative to the water depth with regard to the evolution of a mound under tidal flow conditions. The main differences in the results obtained for the three cases occurred during the first few tidal cycles. In each case, the initial mound was elliptical in plan (6 m long axis, 2.5 m short axis, Section 3.5.1) and triangular in cross-section. The mound crest heights were 0.15 m (SM), 0.20 m (ST) and 0.25 m (SP) for the submerged, surface touching and surface piercing cases.

Figures 4.82, 4.97 and 4.98 show the time histories of the upstream and downstream horizontal velocity components for the first 4 hr of the tests (where the target upstream velocity was the same in each case). In each case, the upstream flow velocity components were slightly asymmetric, where the positive half cycle being 0.02 - 0.03 m/s stronger than the negative half-cycle, due to pumping differences. The plots show that the downstream horizontal velocity components were strongly influenced by the different blockage effects induced by the initial crest height of the mound. Figures 4.86, 4.99 and 4.100 provide a detailed view of the variation in the horizontal velocity components with time over the first hour for Tests SM, ST and SP. A wake formed downstream of the mound in each test. The wake formation was induced by flow separation as the fluid layer slowed over the mound (in the surface piercing case, the complete blockage of the flow over the crest of the mound) and

the deceleration around the sides of the mound. Depending on the relative water depth and the height of the crest of the mound, the wake was composed of a steady re-circulation bubble or shed vortices. The mound behaved as a dynamic feature, with feed-back between the changing morphodynamics and the flow field. In the UKCRF tests, the adaptation of the flow conditions to the changes in the bed morphology happened quasi-instantaneously. Therefore as the morphology of the mound evolved, so the wake characteristics also evolved. The mounds in Tests SP and ST induced vortex shedding whilst the crest was emerged and near the surface. Lloyd and Stansby (1997a) studied the flow around surface-piercing conical islands of small side slopes, and Lloyd and Stansby (1997b) submerged conical islands. In the UKCRF experiments, the main differences appeared in the first few cycles when the crest of the mound was highest, as with the velocity deficit (discussed later). Where possible, the period of vortex shedding was inferred from high quality images captured at high frequency.

The wake stability parameter ($S$) was calculated using:

$$S = C_f \frac{D}{H} \tag{4.1}$$

where $C_f$ is a bottom friction coefficient defined by the shear velocity $u_* = \sqrt{C_f}\, 2\overline{U}$ (calculated according to Eq. 2.7), $H$ is the undisturbed water depth, and $D$ is the characteristic diameter of the mound at mid-depth. Lloyd and Stansby (1997b) suggested the following categories of wakes in oscillatory laminar flows, that depend on the value of the stability parameter for a circular cylindrical body: values of $S < 0.2$ indicated vortex shedding periodically from the island; for values of $S > 0.5$ two steady counter rotating eddies were generated (a steady bubble wake); and when $0.2 < S < 0.5$ an unsteady bubble formed. Lloyd *et al*. (2001) described four categories of wakes in oscillatory laminar flows as: symmetric without vortex pairing; symmetric with pairing; sinuous with pairing; and vortex shedding.

The Strouhal number ($S_t$), gives an idea of the wake characteristics and was calculated using:

$$S_t = f \frac{D}{u_\infty} \tag{4.2}$$

where $f$ is the frequency of vortex shedding, and $u_\infty$ is the free stream velocity. Table 4.3 presents information regarding the wake characteristics. The data collected only permitted an estimate of $f$ from Test ST.

Test SM did not present a wake with eddy shedding properties. Figures 4.101 to 4.109 and 4.110 to 4.116 show images captured during the first cycle of Tests SP and ST. At the start of the first cycle in ST, and during the first three cycles in SP, an eddy shedding wake formed and developed downstream of the mound. The overhead images captured only the frame in the vicinity of the mound (about 4 m either side of the initial position of the crest of the mound): the far wake behaviour can only be inferred. Figures 4.110 and 4.104 show the mound after about 4 min elapsed time for Tests SP and ST, the wake and the vortex (eddy) shedding were more marked in Tests SP than in ST. In Test SP the frequency of image capture was insufficient to calculate the frequency of vortex shedding. There was no image information available for Cycle 2. During Cycle 3 the mound still presented an eddy shedding wake, where eddies were less marked (weaker) than at the start. Figures 4.95, 4.117, 4.115, and Figures 4.118, 4.119, 4.116 compare the wake strength in each test (SM, ST and SP) after about 15 and 17 min during the first cycle. The wake downstream of the mound in Test SM appeared weaker than in Test SP where the wake appeared stronger and was shedding eddies. Figures 4.120 and 4.121 show the mound after 86 min (Cycle 5), in Test SP the free surface disturbance on the wake area and over the mound covered a larger area than in Test ST.

Figures 4.89, 4.122 and 4.123 show the initial conditions of Tests SM, ST and SP. Figures 4.90, 4.124 and 4.125 show the mound after the first cycle (20 min) in each test. After 20 min elapsed time, the width of the mound hardly changed in each case. The strong secondary flows dented the sides of the central area of the mound, and the lateral dents appeared deeper in Test SP and smaller in Tests ST and SM. Figures 4.91, 4.126 and 4.127 present the mound after 1 hr, the lateral dents in each case deepened, the previously emerged volume of the crest was re-distributed in the stream-wise and cross-flow directions. The central area of the mound became flatter in each case. In each case after 2 hr, the width of the mound decreased locally due to the dents deepening, and in other areas became slightly wider due to the spread of sand in the cross-flow direction. Figures 4.128 and 4.129 present the mound after 2 hr for Tests ST and SP. For Test ST the width of the mound was about 2.2 m at its narrowest on the central area. The SM mound after 3 hr was 2 m wide in the central area, and its width increased to about 2.7 m elsewhere (Figure 4.92). The lateral dents in Test SM deepened further than in the two other tests, as the mound ‘stored’ a smaller volume of sand, and was more vulnerable to the erosive action of the flows. Figure 4.130 shows the SP mound after 3 hr, the width was about 2.5 m at its narrowest and slightly larger than 3 m in other areas. The width of the ST and SP mound after 4 hr varied

locally as before (Figures 4.131 and 4.132). At the end of Test SM after 20.3 hr (Figure 4.93) the mound was 1.75 m wide at its narrowest. Figure 4.133 shows the mound at the end of Test SP (19.3 hr), where the mound retained its identity, though there were a number of ripples superimposed on the mound, and the concrete floor was not exposed in the central area. The width of the SP mound was narrower (2.25 m) in the central area, and it was 3.5 m at its widest. At the end of the Test the SM mound ceased to act as a single entity and was more degraded than in Test SP. The sand mound had degenerated largely into ripples with the concrete floor exposed in various locations in the central area.

The evolution of the crest height, and percentage of the initial crest height are shown in Figure 4.134. The percentage of the initial crest height provides comparative information on each test independent of the initial height. The decay in crest height in each test was rapid in the first few cycles before becoming moderate. The crest height decreased by 42 % in 20.3 hr for Test SM and by 57 % in 19.3 hr in Test SP. The crest height in Test ST decreased by 29 % in 4 hr (total duration of the test). The rates of decrease in crest height between the last two measurements in Tests SM, ST and SP are 0.0015, 0.002 and 0.002 m/hr respectively. Figure 4.135 shows the time history of the volume and percentage of the initial volume for Tests SM, ST and SP. The volume of the mound in Test SM decreased by about 28 % after 20.3 hr. In Test ST the mound volume decreased by 4.4 % after 12 hr (end of the test). The volume decrease in Test SP was about 41 % after 19.3 hr. The percentage difference of volume at the end of the test (20.3 hr and 19.3 hr respectively) between Tests SM and SP was about 12 %. By the end of Test SP the volume had decreased further than in Test SM, probably due to the enhanced flow velocities due to the increased blockage in Test SP that enhanced the sand transport (further discussion in the summary). The time history of the location of the centroid for Tests SM, ST and SP is shown in Figure 4.136 . The migration rate of the centroid in the stream-wise direction was 0.06 m/hr (after 20.3 hr) for Test SM and 0.08 m/hr in Test SP (after 19.3 hr). The migration rate for Test ST was the smallest at 0.04 m/hr (it run for 4 hr). Test ST exhibited an intermediate behaviour between Test SM and Test SP, corresponding to an intermediate initial crest height.

The evolution of the front and back slopes through Tests SM, ST and SP is shown in Tables 4.2 and 4.14. These slopes are based on cross sectional information of the interpolated contour data along the centreline of the basin in the stream-wise direction.. Overall the slopes were similar to the initial slope (between 2° and 6°). The central area of the mound typically became flatter in the first few cycles of Tests SP and ST, when the crest

became submerged. During each test, a steep slope developed downstream of the crest, and the process was repeated in the opposite direction when the flow reversed. A relic 'former' step was found in most cases in the upstream slope, though it presented a gentler slope. Typically, the slopes in Table 4.4 became slightly steeper with time. The initial side slopes of Test SP were steeper than in the other two tests, and this affected the evolution of the slopes.

Overall, ripple wavelengths were of similar dimensions in Tests SM and ST, where small wavelength ripples were found on the upstream and downstream areas of the mound (Figures 4.90, 4.91, 4.92 and Figures 4.124, 4.126, 4.128). Also in these figures, the central area of the mound exhibited longer wavelength ripples and deep troughs. Figures 4.91 and 4.92 show the mound in Test SM, where ripple wavelengths were smaller in the area behind the crest of the mound (on the left in the figures) than in the front. Figures 4.126, 4.128 and 4.131 show Test ST, where ripples on the lee side of the mound (on the right of the figures) exhibited longer wavelengths than those on the front side. Figure 4.125 presents the mound after the first cycle in Test SP, complicated ripple patterns developed on the surface of the mound, induced by the strong surface disturbance and the wake. Eddies shed in the wake of the mound swept the downstream end of the mound flattening it (the strong flows in shallow waters washed over the mound), hence the atypical ripple pattern downstream of the crest (aligned to the free-stream flow direction). In Test SP the crest of the mound remained above the water until the middle of the third cycle. Ripple wavelengths grew with time and the ripple crests became more irregular. The ripples in the central area of the mound were linguoid-crested. At the end of Test SP the ripple crests superimposed on the mound were fairly parallel to each other (Figure 4.133).

Figures 4.86, 4.99 and 4.100 provide a detailed view of the variation in the horizontal velocity components with time over the first hour for Tests SM, ST and SP. The velocity deficit, determined as the difference between the free stream (upstream) and downstream horizontal velocity components, indicates the feedback effect between the mound topography and the flow field. Figure 4.137 shows a period of 3 hr from the start of Test SM. The velocity deficit (in SM) varied slightly in the first two cycles (0.12-0.13 m/s), then was slightly reduced in the negative flow and remained similar for the positive flow (Table 4.5). The effect of the mound on the flow velocity was less important in the submerged case than in the other two (shorter mound, and smaller volume of sand, shallower slopes). In Test ST (Figure 4.99) the velocity deficit in the first half cycle was about 0.08 m/s (Table 4.6a). Figure 4.138 shows the 3 hr period after the crest became submerged,

when the velocity deficit reached the maximum. After 3 hours the negative velocity deficit decreased, and hardly changed in the positive flow (Table 4.6a). In the first two cycles of Test SP the velocity deficit was about 0.06-0.10 m/s (positive and negative flows) (Figure 4.100, Table 4.6b). In the second half of Cycle 3 (Figure 4.139), when the crest became submerged, the velocity deficit reached a maximum greater than in SM or ST, due to pronounced flow blockage caused by the surface-piercing crest (Table 4.6b). During the following 3 hr period the velocity deficit decreased progressively with time, as the mound spread out and lost height. Once the crest became submerged, ST and SP exhibited higher velocity deficits that SM. In the first two cycles the velocity deficit varied slightly and for the rest of the 3 hr hardly varied. The values of velocity deficit after 3 hr from the submersion of the crest in Tests ST and SP are similar (Tables 4.6a and 4.6b). The comparison between the decrease in crest height and the decrease in velocity deficit with time for Tests SM, ST, SP are presented Figures 4.140 and 4.141.

**Summary**

The main differences in the results obtained for the three cases occurred during the first few tidal cycles.

When the mound was surface piercing or touching, the velocity deficit was lower than when the crest became submerged. This could be due to the shape of the mound being more streamlined, or due to the increased acceleration of the flow around the crest. The probe measured the velocity 8 m, *downstream* from the centre of the mound, so the ADV recorded the velocities in the area of influence of the wake downstream of the mound. When the crest became submerged the velocity deficit increased. The velocity downstream of the mound was more similar to the upstream velocity when the mound was surface piercing/touching, and when the mound became submerged the velocity downstream decelerated. The reason was not self-evident, perhaps once the crest became submerged there was a larger volume blocking the flow (the volume previously above the water surface was re-distributed) hence the flow decelerated; or as the crest of the mound travelled downstream, the wake disturbance also travelled downstream and reached the ADV, which recorded the decelerated flow velocity in the vicinity of the ADV.

In the SP case there are two factors with opposing effects on the long-term evolution of the mound: the emerging crest and the initial volume. The larger initial volume allows the mound to retain its identity for longer. The surface piercing mound induces a large blockage effect, accelerates the flows further around the crest, and induces strong secondary flow that

dents the mound, and more violent flows in the wake, increasing the sediment carrying capacity of the flows. The surface piercing crest has the effect of decreasing the volume of the mound and accelerating the destruction mechanism. The mound is surface piercing for a short part of the total test duration, and after that the initial volume plays an important role in the long term evolution of the mound. For smaller volume mound and crest height the blockage effect reduces, and the acceleration effect of the flow velocities over and around the mound diminishes, though it may disperse in a shorter timescale. Hence these factors affected the general 'long-term' evolution of the mound.

### 4.1.6. Comparison of flow velocity recorded during two tests with submerged elliptical mounds (Test 11 and 12) in tidal flow

To assess the repeatability of the evolution of the mound and the flow velocity records, Tests 11 and 12 were compared. In Test 11 the flow started from the left in the images and in Test 12 from the right. Both tests were run for a long time (~19 hr) but in the case of Test 12 there is a record of the evolution of the mound after 0.33, 1 and 3 hr, but there was no record of the last stage of the mound evolution from the overhead camera. The general pattern of mound evolution is relatively similar in both tests. The footprint shape is very similar in both tests after 0.3, 1 and 3 hr. Dents developed on the sides of both mounds, and the difference in the direction of the flow did not appear to have an impact in the short term (further discussion of Tests 11 and 12 is available in Section 4.4, where colour figures will be discussed).

There was a slight difference in the velocity deficit between the first two cycles and the following cycles. In the first two cycles in Test 11 the velocity deficit was slightly smaller than from the third cycle onwards (Figures 4.142 and 4.143), this effect was not noticeable in the first two cycles in Test 12. However in both tests the positive downstream velocities fluctuate throughout the test more than the negative downstream velocity. The velocity deficit variation for both tests in Cycles 3, 4, 5 and 6 are of similar order of magnitude (0.04 m/s in the positive velocity and 0.02 m/s in the negative velocity) as shown in Table 4.7. The flow conditions were relatively repeatable and the blockage effect of the mound on the flows was considered repeatable too.

## *4.2. Evolution of the volume of the bed mound*

This section describes the results of the investigation on the volume changes throughout the tests.

### 4.2.1. Apparent sand volume expansion measured after 20 min.

During the analysis of certain tests (Tests 4, 8 and 9, Table 4.8) it was found that the mound volume increased by as much as 6 % after the first 20 minutes. This behaviour is counter-intuitive as the expectation was for the volume to reduce with time, and explanation was sought as reported here. These were the first tests to be analysed and it was thought the volume increase would be found in all tests. However, when the analysis of other tests continued it was discovered that this effect only occurs in these three tests. The construction of the mound was carried out with damp sand. The building process involved compacting the sand to the template shape (details of the experimental procedure are given in Section 3.5). After the sand was under water for some time and the cycle was run, the sand appeared to 'swell'; i.e. the pore volume expanded even if the amount of sand remained fairly constant.

*A priori* the causes were thought to be either due to changes in compaction of the sand and hence the changes in pore volumes, or due to errors in the analytical procedure (i.e. the digitising technique and the accuracy in the representation of ripples whilst digitising). The first of the potential causes was investigated experimentally.

In the initial hypothesis the increase in volume could be explained by a re-structuring of the grain matrix of the sand in the mound as the water level rose during the filling of the basin, resulting in a looser grain packing. The porosity of well-sorted sand varies from 40 % to 46 % (Table 4.9) depending on the degree of compaction.

Assuming the volume of sand ($V_s$) is constant and the proportion of the pore volume changes from $P_0$ to $P_1$, the total volume change from initial ($V_i$) to final ($V_f$) is given by:

$$V_s = V_i(1-P_0) = V_f(1-P_1) \quad (4.3)$$

$$V_f = V_i(1-P_0)/(1-P_1) \quad (4.4)$$

Example Test 8:
$P_0 = 0.4$

Observed $V_i = 0.682$ m$^3$
Observed $V_f = 0.723$ m$^3$

averaged packed, $P_1 = 0.42$

$$V_f = \frac{V_i(1-P_0)}{(1-P_1)} = V_i\frac{(1-0.4)}{(1-0.42)} =$$

loosely packed, $P_1 = 0.46$

$$V_f = \frac{V_i(1-P_0)}{(1-P_1)} = V_i\frac{(1-0.4)}{(1-0.46)} =$$

$$= 0.682 \frac{0.6}{0.58} = 0.71 \text{ m}^3 \qquad = 0.682 \frac{0.6}{0.54} = 0.76 \text{ m}^3$$

The change in volume due to the change in porosity can be of the order of 0.05 $m^3$. This could explain a change in volume up to 6.9 %. These results show that in principle the hypothesis of the change in pore volume could explain the observed increase in volume.

Exploratory tests were carried out to study the increase in volume using a measuring cylinder of 2 litres capacity, and sand of the same grain size characteristics as the one used during the experiments (Garside 21).

1) The measuring cylinder was filled with sand, which was manually compacted and the volume was measured (620 ml). Water was added slowly from above and bubbles appeared through the sand surface whilst the water filled up inter-grain spaces. There was no noticeable change in volume after adding the water.

2) The sand was placed in the measuring cylinder along with a small diameter tube inserted down the measuring cylinder, to help fill the cylinder with water from below (similar to the situation as the basin was filled up). The sand was compacted around the tube. The sediment volume after being compacted and the sediment surface flattened by hand was 600 ml. There were problems with the tube being narrow. In the end the measuring cylinder had to be filled using a syringe, very gently and so the sediment surface was not greatly disturbed. The final volume was between 1 and 1.5 % larger than the initial volume.

The results from the experiments were not entirely conclusive. In general, no volume increase was observed. The observed increase in volume of 0 to 1.5 % was not sufficient to explain the large increases in volume in the UKCRF tests where the expansion was observed. An alternative explanation is that the apparent increases in volume in Tests 4, 8 and 9 were associated with errors in the contour digitisation procedure, possibly associated with the treatment of ripples. A cautious interpretation, taking account of all the analysed tests, is that the measurement of volume is subject to random errors up to 6 %.

### 4.2.2. Decay of volume throughout the test after 1st cycle

After the first cycle, the volume of the mound decreased gradually with time, and the volume spread over the model area in *x*- and *y*-direction.

For the steady flow case there was a greater decay of height and volume than for the tidal flow case. This was expected in the steady unidirectional cases due to the sustained

peak flow velocity for the duration of the testing interval. In the tidal case the sediment was transported only when the flow velocity exceeded the threshold of particle motion. This happened approximately 50 % of the time in each cycle. In the tidal case the sand travelled first in one direction and when the flow reversed in the opposite one. In the tidal case most of the sand is spread by the flow in a slow and gradual manner (diffusion-like) to the sides of the mound, whereas in a steady flow the motion of the sand was dominated by advection of sand and migration of the mound in the main flow direction.

In an idealised symmetric tidal flow, a particle trajectory is closed and after one cycle the particle returns to the initial position, independently of the particle excursion. The maximum water particle excursion in the tidal flow case was calculated as:

$$(V\,T_o)/\pi = (0.5*1200)/3.1415 = 191 \text{ m} \quad (4.5)$$

Hence, half the excursion is 95.5 m, where $V$ is the peak velocity and $T_o$ is the oscillation period in seconds. The water particle excursion thus greatly exceeded the length of the UKCRF. However, the excursion of the sand grains as bed load was very much smaller – typically a few metres. Entrained grains would travel only a small fraction of the water excursion, as they are picked up and set down in discrete hops. During the experiments the floor in the central part of the UKCRF was elevated above the floor on the sides, where the water was deeper. Particles entrained in the flow during a tidal cycle became deposited in the areas where the velocity decreased. This occurred typically due to the increase in depth outside of the central area of the UKCRF or at the turn of the 'tide'. In the experiments a small portion of sediment was lost outside the image frame. This percentage was typically small in comparison to the total volume of the mound.

In the steady flow case the particles always had an 'open trajectory' (i.e. unidirectional flow). In these cases, the sand deposited when the velocity decreased below the threshold of motion at the end of the testing interval or when the depth of water increased. This is an important factor in the evolution of the centroid, referred to in Section 4.1.

## *4.3. Analysis of change of volume through cross-sections and estimate of experimental sediment transport rates*

Sediment transport rates were estimated analysing volumetric changes spatially through cross-sections of the mound along the basin, and temporally. These rates were compared to

predictions carried out using existing bedload formulae. Two steady flow tests were analysed, Test 9 (fixed underlying concrete bed) and Test 13 (mobile underlying sand bed). Details regarding the characteristics of the tests are described in Section 3.5.2 and Table 3.4. In Test 9 the still water depth was 0.2 m; in Test 13 it was 0.225 m. It should be noted that this analysis could only be applied to the steady flow tests, as the alternating flow directions in tidal cases would complicate the interpretation.

The experimental transport rates for Tests 9 and 13 were compared to predictions from the bedload formulae developed by Meyer-Peter-Müller (1948) (MPM) and Van Rijn (1984). These formulae were developed for steady flows in rivers based partially on laboratory experiments. The formulae have been applied in this analysis although field water depths typically are deeper than in the laboratory.

Two sets of predictions were obtained by applying the two sediment transport formulae using: a) water depth and velocity values computed by numerical simulations (discussed further in Chapter 6); and b) flow speed information estimated from surface float tracks from Test 13 (after 16 min) along with water depth information from the cross sections of the mound's profile after 20 min (Figure 4.146b). These predictions are understood to be instantaneous sediment transport. The calculations (in MATLAB) followed relevant formulae from Soulsby (1997).

The contoured mound was split by a number of cross-sections at fixed locations along the *x*-axis, separated by 1 m in the stream-wise direction (Figure 4.144). The sections started upstream from the edge of the mound at $t_0$ up to where the mound was present at the end of the tests. The volume between each pair of cross-sections was calculated. The transport rates through a cross-section were calculated as the change in volume upstream of a given cross-section at consecutive times i.e. for cross-section *n* was calculated as:

$$\Delta volume = volume\text{-}up_n\,(t_i) - volume\text{-}up_n\,(t_{i-1})) \tag{4.6}$$

where volume $up_n$ is the summation of all the volume upstream of section *n* (located on the *x*-axis).

The experimental transport rates were estimated in Test 9 at four time intervals (from 0 to 20 min; 20 to 60 min; 60 to 120 min; and from 120 to 180 min, denoted P20, P60, P120 and P180 respectively). In Test 13 the transport rates were estimated at two time intervals (from 0 to 20 min; and 20 to 60 min, P20 and P60 respectively). The transport rates were calculated where data were available, using the width of the mound at each of the cross-

sections to calculate sediment transport rates (Tables 4.10 and 4.11). The experimental sediment transport rate was calculated as:

$$q_b = \left( \frac{\Delta volume \ (1-\varepsilon) \ \rho_s}{L \ \Delta t} \right) \tag{4.7}$$

where $L$ is the width of the sediment at the cross-section, $\Delta t = t_i - t_{i-1}$ is the time interval, $\varepsilon$ is the sediment porosity (typically 0.40) and $\rho_s$ is the sediment density (typically 2650 kg/m$^3$ for sand).

Figures 4.145a and 4.146a show curves that represent the spatial distribution of the mean sediment transport rate over the preceding time interval (as described above). In each curve the sediment transport was greatest near the crest of the mound and decreased towards the upstream and downstream edges. The crest of the mound migrated downstream with time and so did the maximum transport rate. The flow diverged near the mound, the crest height and mound volume decreased with time, and the velocity (and hence transport rates) increased near the crest of the mound due to continuity. Initially ($t$ = 0 min) the mound occupied ¾ of the water depth at the crest, causing an acceleration of the flow near the mound which enhanced the sediment transport. As the crest height and the volume of the mound decreased, the velocities over and around the mound reduced due to the increase in water depth, resulted in an overall reduction in sediment transport. The observed transport rates estimated from Test 13 (mobile bed) are shown in Table 4.10 and Figure 4.145a. The cross sections of the mound during the test are shown in Figure 4.145b. Unlike in the fixed bed case, the transport through the cross-sections downstream of the crest remained high (P20) in Figure 4.145a, possibly due to the background transport due to the mobile bed. The same effect was observed in P60, though the values were about half of the P20 values. The experimental transport rates for Test 9 are shown in Figure 4.146a and Table 4.11 for each time period. The stream-wise cross-sections of the mound through the basin centre-line for the corresponding times are given in Figure 4.146b. During Test 9, typical transport for P120 was reduced to less than half of that for P60. At the end of the test (after 180 min) the front of the mound had travelled 1.5 m downstream. The downstream end of the mound travelled partially outside of the image frame and a portion of the volume of the mound was lost downstream during the test (it was more than 50 % of the initial volume after 3 hr, according to Figure 4.15). If the transport rates had been calculated at smaller intervals ($x$ < 1m); the error in calculation due to the variation in mound height between point would be smaller, and the calculations would represent the local sediment transport.

### 4.3.1. Methods for predicting the sediment transport rates through the sections

The results from the two formulae show variability, such behaviour has been previously described by other authors (e.g. Soulsby 1997). Depending on the formula used the results can differ by factors between 0.7 to 1.23 for the MPM and Van Rijn's formulae produce. The predictions using Van Rijn's bedload method gave the lowest rates. In broad terms, the experimental (Tables 4.10 and 4.11) and predicted bedload transport rates were found to be of similar order of magnitude. When making more detailed comparisons, it must be borne in mind that the experimental values represent the transport averaged across all the depths and velocities within the cross-section. Also, the experimental transport rates were calculated as variations in upstream volume between $t_1$ and $t_2$, so the resulting transport rate corresponded to the accumulated transport for the $\Delta t$ (that varied and was 20, 40 or 60 min). On the other hand, the transport rates estimated from the model water depth and velocity, or from surface float tracks were a measure of the instantaneous transport rate for the conditions at that point in space and time. The predicted transport rates presented a time lag with respect to the experimental rates, which corresponded to an intermediate stage between $t_1$ and $t_2$, whilst the predicted rates were the measure of the transport rates at that instant.

### 4.3.2. Transport rates calculated using water depth and velocities from modelling predictions

To compare experimental and predicted transport rates for Tests 13 and 9, velocity and water depth values were computed in numerical simulations (model discussed in Chapter 6). Each cross-section was divided into twelve segments of 0.5 m, and the values of water depth and velocity were extracted from the middle point of each segment (so that, the values of water depth and velocity were representative of each segment). To ease the understanding of the figures the results for Test 13 will be presented before Test 9, (Test 13 was analysed for two time intervals). The transport rate predictions estimated from numerical simulations are shown in Figures 4.147 to 4.148 for 20 and 60 min in Test 13, and Figures 4.149 and 4.150 for 20, 60, 120 and 180 min in Test 9.

The MPM method (Figure 4.147) over-estimates the transport rates at P20 and P60 by a factor of 2. The shape of the curves in Figure 4.147 seems to fit well the experimental value upstream of the peak transport rate, downstream of the peak the prediction drops. The

peak rate shows a spatial and temporal lag between the predictions and the experimental transport rates. Van Rijn's method (Figure 4.158) provides values very similar to the MPM formula, and the behaviour is similar throughout. A lag is present in all the formulae due to the conceptual differences between the experimental and predicted transport rates. The drop in the predicted transport rate seems representative of the instantaneous transport rate, as the experimental rate is accumulated over a $\Delta t$.

The predictions from MPM (Figure 4.159) over-predicts P20 by 0.5, and P60, P120 and P180 provide satisfactory fits to the experimental rates, even if they slightly under-estimate the rates. The method from Van Rijn (Figure 4.150) produces similar results to MPM. The peak of P60 is slightly under-estimated. P120 and P180 are in agreement with the experiments.

### 4.3.3. Transport rates calculated from velocity estimated from float tracks and cross sectional data

A comparison of the experimental transport rates from Test 13 and rates predicted using estimated velocities from surface float tracks and water depths from cross section results are given in Figure 4.151 and Table 4.12. The float tracks correspond to Test 13, after 16 min elapsed time and the cross sections correspond to the profile after 28 min elapsed time. All methods predict either very small or zero transport rates downstream of Cross-section 6 ($x$ = -3 m) whilst the experimental rates remain relatively high. The methods from MPM and Van Rijn give relatively similar predictions, both methods slightly underestimate the transport rates. The experimental rates consider the transport of sand from the mobile bed and the mound, the predictions are instantaneous rates.

***Summary***

The two bedload methods generally over-predict the peak sand transport rates measured in the UKCRF. Both the experimental and predicted transport rates were larger for Test 13 than Test 9. Probably the mobile bed has an impact in the transport, adding a consistent amount to the transport rate. MPM over-predicts the transport rates for Test 13 although shows a better fit in Test 9. Van Rijn's shows over-prediction in Test 13 for all cross-sections, but slightly better overall agreement in Test 9.

The aim during the experiments was for the transport to be mostly by bedload mechanisms, hence the formulae used for the prediction of the sediment transport rates were based on bedload transport only. The transport measured in the UKCRF was total transport,

i.e. the combination of both bed and suspended load. Sediment transport, by definition, is strongly dependent on the variation in water depth and flow velocity. The mound behaved as a bluff body due its blockage effect, this led to flow acceleration and separation in the proximity of the crest of the mound. The flow separation generated a pressure deficit area downstream of the mound and a wake formed. The turbulence due to the wake enhanced the velocity locally and may have led to some suspended transport, even if for a short time and distance. When the depth gradient over the crest of the mound was sharpest (at the initial stages of the test) the blockage was larger. Hence, the flow velocity and the enhancement of the sediment transport were stronger. In the latter stages of the test the transport rates through the cross-sections became more similar. The height of the mound changed less with time, and the supply of sediment in the front cross-sections was decreasing. This suggested that the mound was reaching a streamlined shape that was in relative equilibrium with the flow conditions. However, in Test 9 there was no input of sediment so complete equilibrium could not be reached as the sand continued to travel downstream.

Ripples were identified in the cross section (of Test 9) corresponding to P120 and P180, as they became more important during the test (Figure 4.146b). The experimental results at P120 and P180 show that the rates were lower than before and more similar to each other. Ripples and bedforms in general have an effect on the sediment transport. Energy is spent by the flow in generating the ripples, which increase the bed drag due to flow separation and the formation of eddies downstream of the crest. Sediment transport is modified over a rippled bed because only part of the shear stress is effectively acting on the sediment grains (McDowell and O'Connor, 1977) (minimum energy loss).

## *4.4. Qualitative information from coloured sand analysis*

This section provides qualitative information from tests on the evolution of mounds initially composed of sections from different coloured sands. The coloured sand helped visualise the boundary layer flow close to the surface of the sand heap and relate the transport process to the migration and evolving shape of the mound. Four tests were carried out with coloured sand during the UKCRF experiments, three of which are discussed here (Tests 11, 12 and 13). Section 3.5 and Table 3.4 give details of the initial conditions.

Figure 4.17 illustrates the initial shape of the submerged mound in Test 13 (steady flow, right to left), which was constructed from red (up-crest) and green (down-crest) sand, with a central circular region of blue sand. A more detailed description of the mound can be

found in Section 4.1.2., whilst Section 3.5 and Table 3.4 provide details of test conditions. A step formed on the lee face of the mound as sand travelled downstream from the crest of the mound to form a dynamically stable shape in quasi-steady equilibrium with the steady flow conditions. Initially, the red sand travelled as a front, and later as small ripples. The step/crest area formed from red sand that overlaid the green sand (Figure 4.23, for example). Mixing occurred during the downstream migration of the crest of the mound, as the red sand travelled over the green sand. This mixing process intensified when the mound reached a dynamically stable shape. The thin green layer of sand downstream of the mound changed shape in the same way as the crest of the mound (see Figures 4.23 to 4.26). The surface layer of sand was very mobile, and after 26 min the only evidence left behind of this layer was its relict footprint (Figure 4.28). The transverse movement of the blue sand indicated the strength of the cross-flow transport. Figure 4.29 shows that some of the blue sand also travelled downstream over the underlying mound by 26 min elapsed time. The transverse extent of the blue sand trace increased slightly with distance downstream, indicating that the cross-flow transport was quite small there. Two trails formed downstream of the mound over the natural coloured sand layer (Figures 4.22, 4.24 and 4.26). With time the trails become less clear. The trails were closely related to the 'shoulders' of the mound (black arrows in Figure 4.24), following the lines from the double peaked crest-line. After 26 min elapsed time there was a deposit of mixed red and green sand in the area of the re-circulation bubble behind the crest (Figure 4.28). The sand that travelled over the crest of the mound became entrained in the flow and entered the wake re-circulation bubble. Not all of this sand settled in the re-circulation zone; some remained entrained and settled further downstream. Short wavelength red ripples could be observed travelling over the mound at a migration speed faster than that of the underlying mound.

The area covered by red sand upstream of the underlying mound crest decreased during the first period of steady flow, which lasted $T_1$ = 20 minutes, as indicated in Figures 4.25 and 4.28. By the end of $T_1$, (Figure 4.28) the plan area of the upstream portion of the mound had reduced visibly. The green portion of the mound increased in plan area, and was partially covered with a layer of mixed red and green sand. On the lateral sides of the downstream part of the mound, the natural sand layer was disturbed, and accreted in places (Figure 4.29). The increase in height was not due to the cross-flow transport of sand; instead it was generated by the pressure gradient induced by the free surface disturbance due to the mound. The increase in bed height is interpreted in Chapter 5 with reference to the analytical solution. Figures 4.31 to 4.33 show that the mound became more elongated and

narrow with time. Strong secondary flows dug troughs on the sides of the mound and at the crest; these troughs deepened and migrated downstream with time. A feedback mechanism exists between the flow and the troughs. The flow deepened the troughs resulting in the formation of large ripples superimposed on the mound. In the troughs, the flow removed the surface layer of mixed sand and uncovered bright undisturbed sand (Figure 4.35). During the second period of steady flow, which lasted for $T_2$ = 41 min, secondary flows dug holes in the red and green sand in the central area of the mound, uncovering patches of bright green sand below. In some places, the underlying layer of natural sand was exposed (Figures 4.32 and 4.33). The secondary flows also affected the sides of the mound (Figures 4.32), which became progressively dented with undisturbed sand from below the exposed mixed layer. In the central area of the mound, troughs were created that reached into the natural sand layer (Figure 4.37) which then became available for transport. During $T_2$, natural sand travelled over red and green sand, red sand travelled over green sand, and green over red. The layers of mixed sand overlaid each other as the sand was transported over the ripples downstream. A simple schematisation of the cross-sectional evolution of the mound under steady flow is presented in Figure 4.152.

Test 11 involved a submerged elliptical mound of triangular cross section located on the fixed concrete bed, and subjected to a tidal flow. The mound was built in six cross sectional 1 m segments of different coloured sand. From left to right in Figure 4.89, the sand is blue, red, natural, green, natural (2) and blue (2). At the start of the test, the flow speed at the crest speeded up as the depth shallowed. After 2 min elapsed time, sand near the crest began to travel downstream (i.e. from left to right) (Figure 4.153). The sand migrating downstream (visible in the images over a different colour sand, Figure 4.154) travelled mostly as bed load forming small amplitude ripples. The bed ripples ahead of and behind the crest were of shorter wavelength than those in the central area of the mound. After 10 min, sand near the crest travelled faster downstream due to the more rapid flow over the crest, while sand further to the lateral edge of the mound moved more slowly (indicated by lines in Figure 4.155). However, the sand stripes appear to curve in an opposite direction to what would be expected. This may be because the sand near the crest may have entered suspension and been dispersed downstream (and not be sufficiently concentrated to be visible as covering the mound). The edges of the red stripe remained well-defined, whereas the boundary between the natural and green stripes were disturbed and started to mix as the flow passed the crest changing its shape. In the recirculation bubble area downstream of the step, the flow velocity reduced while remaining turbulent causing the central green and

natural sand stripes to extend further laterally. Trails of green sand were evident downstream of the crest after 10 min (Figure 4.155). When the flow reversed, the sequence of events repeated in the opposite direction. At the point of flow reversal it was possible to visualize the change of orientation of the ripples (Figures 4.156, 4.157, 4.158 and 4.159) and see the effect of secondary flow in the vicinity of the crest (Figures 4.160 and 4.161) where the greatest mixing took place. However, there was no evidence of secondary flow acting on the lateral sides of the mound, until the second flow cycle. The largest ripples and sharp dents also caused other vortical flow structures to develop, which encouraged feedback between the bed morphology and flow dynamics.

As the mound evolved, dents to the side of the mound (formed from Cycle 2 onwards) became deeper and wider as the sand travelled to and fro in the reversing flow. Sand spread in both cross-flow and stream-wise directions as the width and length of the mound increased and its height decreased. By Cycle 10, Figure 4.162, the ripple crests run almost unbroken across the width of the mound, even in the central area where the ripple wavelength was longer. This encouraged the spread of sand across and along the flume. Every time the flow reversed, the sand continued to be re-distributed. Further troughs and holes developed in the sand, at times exposing the concrete bed. After 4 hours, the visible, mobile sand layer started to mix, and this process continued until the end of the test. After about six hours, five large ($\geq$ 0.5 m) ripples could be seen in the central area of the mound (Figure 4.163). Degradation of the mound continued, and more of the undisturbed sand from under the layer of mixed coloured sand became exposed (Figure 4.164). This process continued until the end of the test, indicating that undisturbed sand had lain under mobile layers of mixed sand (which varied in thickness). The number of large ripples ($\geq$ 0.5 m) increased, and after 9 hr there were six ripples (Figure 4.165). At certain times during the test, the ripple crests were relatively parallel to each other and fairly straight; at other times the crests were very irregular (Figure 4.166). This may be related to the flow asymmetry. After 13 hr, (Figure 4.167) the mound was superimposed with seven fairly large ripples (about 0.5 m in wavelength).

The scouring process by which holes were dug in the mound contributed to its disintegration by removing the underlying reserve of otherwise undisturbed sand. A mound structure nevertheless persisted. The coloured sand helped visualise the symmetric development of the shape of the mound with respect to the stream-wise axis.

Test 12 repeated the conditions of Test 11, and was also a coloured sand test. The mound was submerged and elliptical in plan with triangular cross section, and located on a fixed concrete bed; the flow was tidal. The mound was built using sand of four different colours. It was divided in two along the major and minor axis, forming four quadrants (Figure 4.168). Overhead images were taken at the same time as the contouring profiles, except at the end of the test. Video footage was captured at the end of the test from within the basin, which provided information on the fate of the mound.

As in Test 11, the sand on the crest area was first to enter motion. A pattern of overlying structures emerged in the mobile sand layer due to the opposing directions of sand transport during the two half cycles. The white line in Figure 4.169 is drawn over the front left behind after the first half cycle that then persists throughout the second half cycle. The blue line shows the front after the second half cycle. The pattern at the end of the cycle was more complicated than that at the end of the first half cycle, due to mixing in the central area of the mound. Cross-flow transport over the mound was inferred from the intensity of the cross-flow sand mixing. During the first cycle the cross-flow mixing was localised mostly near the crest. Figure 4.174 presents the mound after Cycle 3 (1 hour elapsed time), where two or three dents can be seen in the lateral sides of the mound due to secondary flow effects. A fine layer of blue sand covered part of the green sand quadrant, and green sand covered part of the blue quadrant. The same happened on the half of the mound composed of natural and red sand. The grey line in Figure 4.170 indicates the variation in cross-flow mixing in the stream-wise direction, and is pushed about 0.25 m sideways near the crest. At this time, there was no evidence that large ripples had travelled over sand of a different colour. Nevertheless the surface of the mound was superimposed with ripples, and a thin layer of sand from the front quadrants covered part of the back quadrants (i.e. the blue/natural sand quadrants were partially covered with green/red sand, and vice versa). Ripples had longer wavelengths in the central area than on the front and back of the mound.

Figure 4.171 illustrates the plan-form shape of the mound after Cycle 9 (3 hr elapsed time). Four dents can be seen on the flanks of the mound (arrows, Figure 4.171) corresponding to the troughs of four long-wavelength ripples in the central area of the mound (blue lines, Figure 4.171). The extent of the cross-flow mixing (indicating cross-flow sand transport) is marked approximately by white lines, and is again greatest in the central area of the mound, and about the same order of magnitude as in Figure 4.170. Figures 4.172 to 176 show the mound at the end of the test (20.3 hr and 61 cycles). It can be seen that the final state of the mound in Test 12 was very similar to that in Tests 11 and 8.

As previously described in Sections 4.1.3 and 4.1.4, the mound spread both in the stream-wise and cross-flow directions, and with time broke down into ripples of varying wavelength. The sand from the mobile layer was partially mixed; the amount of mixture of coloured sand was larger ahead of and behind the mound (perhaps due to sand becoming entrained in the flow and carried downstream into the recirculation bubble, and then settling far from the central area of the mound). Figures 4.172 and 4.173 are basin-wide images, showing the shape of the sand footprint. Ripple beds formed upstream and downstream of the mound (at both ends of the basin), which indicated a degree of stream-wise mixing (i.e. mixed red and natural sand in one half, and green and blue sand in the other half). Figures 4.174 to 176 illustrate the mound evolution in the central area of the basin from three different points of view (block arrows in Figure 4.171). The extent of the cross-flow transport is indicated by arrows in the close-up Figures 4.174 and 4.175, and ranges from about 0.5 to 0.75 m either side of the centreline. Figure 4.176 shows the central area of the mound, where the net displacement of the mound towards one side (the right in the figure) can be discerned. This is also noticeable from Figure 4.173, where most of the sand was located towards the far side of the basin's transverse centreline (indicated by a white line). Figure 4.177 shows a simple schematisation of the evolution of the mound under tidal flow after one cycle (equivalent to that for steady flow).

***Summary***

Coloured sand helped to visualise the evolution of the surface sediment, and to relate the transport processes to the migration and evolving shape of the mound. In particular, coloured sand: (i) showed the extent of the effect of the secondary flows digging troughs on the mound and how these evolved; (ii) helped visualise changes in orientation of ripples (due to reversing flow), provided information on ripple migration, and gave an indication of migration speeds of ripples of different sizes; (iii) showed how large ripples formed over the mound, parallel to each other; (iv) gave certain quantitative information on the extent of the cross-flow transport over the crest of the mound; (v) demonstrated how the surface layer of sand became mixed with time, and how after many hours after the start of the test, there were portions of undisturbed sediment underlying the ripples; (vi) provided insight on the hydrodynamic processes taking place associated with the recirculation bubble (in Test 13, the deposition of highly mixed coloured sand), and with flows further downstream (in Test 13, a faint trail of red sand, aligned to the flow direction, was overlying the mobile bed); (vii) helped visualise the effects of the interaction of the mound and the free surface, i.e. the

star shaped pattern did not appear due to cross flow transport but due to this mechanism; (viii) provided an indication of how symmetric was the development of the mound in the cross-flow direction; and (ix) hinted at the mechanism by which sand spread in the cross-flow direction, secondary flows denting the mound and gravity.

| Maximum ripple migration rate (mobile bed) m/hr | Minimum ripple migration rate (mobile bed) m/hr | Centroid migration in stream-wise direction (mobile bed) m/hr | Centroid migration in stream-wise direction (fixed bed) m/hr |
|---|---|---|---|
| 3.979 | 1.042 | 0.935 | 0.637 |

Note: average ripple migration (mobile bed) = 2.5 m/hr

**Table 4.1 Comparison of ripple migration rates with the centroid migration rate of the mobile bed and fixed bed case.**

| Time (hr) | Test 8 | | Test 11 | |
|---|---|---|---|---|
| | Front slope (deg) | Back slope (deg) | Front slope (deg) | Back slope (deg) |
| **0** | 4 | 4 | 3 | 3 |
| **0.3** | 3, 4 | 1.5, 3 (***25***) | 3, 6 | 3 (***8*** & ***11***) |
| **1** | 4 | 3 (***25***) | 4, 7 | 3 (***13***) |
| **2** | 3, 5 | 4 (***11***) | - | - |
| **3** | - | - | 4, 7 | 3 (***13***) |
| **4** | 4, 8 | 21 r | - | - |
| **5** | 7, 11 | 20 r | - | - |
| **20.3** | 7 - 13 | 24 – 29 r | 11, 10 r | 10, 16 and 18 r |

r: slope of ripples; ***bold and italics*** slope of the steep step

**Table 4.2 Comparison of mound front and back slopes with time for Tests 8 and 11**

| | Ellipse Submerged | Ellipse Touching | Ellipse Piercing | Gaussian Submerged |
|---|---|---|---|---|
| **S** | 0.407 | 0.597 | 0.723 | 0.678 |
| **St** | | 0.110 | | |

**Table 4.3 Wake characteristic for a range of initial bed mounds**

| Time (hr) | Test 3 (SP) | | Test 4 (ST) | |
|---|---|---|---|---|
| | Front slope (deg) | Back slope (deg) | Front slope (deg) | Back slope (deg) |
| **0** | 5 | 6 | 2 | 4 |
| **0.33** | 4/3 (***23***) | 5/2/23 | 4/3 | 4 (***10***) |
| **1** | 3/2 (***23***) | 4/5 | 3 (***7***) | 4 (***8***) |
| **2** | 2 (***10***) | 3 (***30***) | 4 (***8***) | 3 (***12***) |
| **3** | 3/4 (***11***) | 4/3 (***18***) | | |
| **4** | 4/3 (***10***) | 3 (***9***) | 4 (***9***) | 4 (***22***) |
| **19.3** | 4 | 2 | | |
| | 13, 21 r | r 17/22 - 10/9 | | |

r: slope of ripples; ***bold and italics*** slope of the steep step

**Table 4.4 Comparison of mound front and back slopes with time for Tests 4 and 3**

| Test SM | Positive-velocity deficit (m/s) | Negative- velocity deficit (m/s) |
|---|---|---|
| **1st cycle** | 0.13 | 0.12 |
| **2nd cycle** | 0.12 | 0.08 |
| **3rd cycle** | 0.15 | 0.11 |
| **After 3 hr** | 0.13 | 0.10 |

**Table 4.5 Variation of the velocity deficit for the submerged mound (SM=Test 11)**

| Test ST | Positive-velocity deficit (m/s) | Negative- velocity deficit (m/s) |
|---|---|---|
| **1st cycle** | 0.08 | 0.19(*) |
| **2nd cycle** | 0.23(*) | 0.17 |
| **3rd cycle** | 0.22 | 0.19 |
| **After 3 hr** | 0.23 | 0.15 |

*After crest submerged (10 min).

**Table 4.6a Variation of the velocity deficit for the surface-touching mound (ST=Test 4)**

| Test SP | Positive-velocity deficit (m/s) | Negative- velocity deficit (m/s) |
|---|---|---|
| **1st cycle** | 0.06 | 0.10 |
| **2nd cycle** | 0.05 | 0.10 |
| **3rd cycle** | 0.07 | 0.21(*) |
| **After 3 hr** | 0.23 | 0.17 |

*After crest submerged (30 min )

**Table 4.6b Variation of the velocity deficit for the surface-piercing mound (SP=Test 3)**

| Test Number | Positive velocity deficit (m/s) | Negative velocity deficit (m/s) |
|---|---|---|
| **11** | 0.18, 0.14, 0.17, 0.15, 0.15, 0.14 | 0.13, 0.11, 0.12, 0.12, 0.10, 0.11 |
| **12** | 0.13, 0.11, 0.15, 0.13, 0.11, 0.14 | 0.11, 0.12, 0.11, 0.10, 0.12, 0.11 |

**Table 4.7 Comparison of velocity deficit between Test 11 and 12 (repeatability) for Cycles 1 to 6.**

| Time (hr) | Initial volume (%) | | |
|---|---|---|---|
| | **Test 4** | **Test 8** | **Test 9** |
| **0** | 100.0 | 100.0 | 100.0 |
| **0.33** | 104.4 | 106.2 | 105.1 |
| **1** | 103.3 | 92.3 | 89.0 |
| **2** | 98.4 | 86.8 | 74.2 |
| **3** | - | - | 52.1 |
| **4** | 95.6 | 86.3 | - |
| **5** | - | 87.5 | - |
| **20.33** | - | 67.9 | - |

**Table 4.8 Evolution of the percentage of the initial volume with time, showing the increase in volume at 0.33 hr.**

| Porosity of well-sorted sand | (%) |
|---|---|
| Densely packed | 40 |
| Averagely packed | 42 |
| Loosely packed | 46 |

**Table 4.9 Porosity of well-sorted sand (Soulsby, 1997) p35**

| Time period | Distance from centre of grid | | | | | | |
|---|---|---|---|---|---|---|---|
| | Section 7 $x = -4$ | Section 6 $x = -3$ | Section 5 $x = -2$ | Section 4 $x = -1$ | Section 3 $x = 0$ | Section 2 $x = 1$ | Section 1 $x = 2$ |
| **P20** | 0.0862 | 0.0777 | 0.0785 | 0.0924 | 0.0659 | 0.0296 | 0.0112 |
| **P60** | 0.0328 | 0.0413 | 0.0439 | 0.0305 | 0.0171 | 0.0072 | 0.0039 |

**Table 4.10 Transport rates estimated through sections from Test 13 (kg/ $m^3$ s)**

| Time period | Distance from centre of grid | | | | | | |
|---|---|---|---|---|---|---|---|
| | Section 7 $x = -4$ | Section 6 $x = -3$ | Section 5 $x = -2$ | Section 4 $x = -1$ | Section 3 $x = 0$ | Section 2 $x = 1$ | Section 1 $x = 2$ |
| **P20** | - | - | 0.0113 | 0.0594 | 0.0437 | 0.0097 | - |
| **P60** | 0.0166 | 0.0384 | 0.0564 | 0.0397 | 0.0237 | 0.0131 | - |
| **P120** | 0.0147 | 0.0226 | 0.0198 | 0.0159 | 0.0113 | - | - |
| **P180** | 0.0172 | 0.0154 | 0.0154 | 0.0099 | 0.0066 | - | - |

**Table 4.11 Transport rates estimated through slices from Test 9 (kg/ $m^3$ s)**

| Section No. | Distance (m) | Average velocity (m/s) | Water depth at $y = 0$ (m) | Sediment transport rate (kg/ $m^3$ s) | |
|---|---|---|---|---|---|
| | | | | MPM | VR |
| **1** | 2 | 0.506 | 0.200 | 0.0093 | 0.0076 |
| **2** | 1 | 0.582 | 0.150 | 0.0230 | 0.0215 |
| **3** | 0 | 0.645 | 0.122 | 0.0404 | 0.0416 |
| **4** | -1 | 0.751 | 0.113 | 0.0757 | 0.0917 |
| **5** | -2 | 0.665 | 0.118 | 0.0465 | 0.0494 |
| **6** | -3 | 0.511 | 0.200 | 0.0098 | 0.0081 |
| **7** | -4 | 0.388 | 0.200 | 0.0008 | 0.0008 |

**Table 4.12 Sediment transport rates (kg/ $m^3$ s) for every cross-section in Test 13, velocities estimated from float tracks (16 min), water depths from cross-sections after 20 min (P20).**

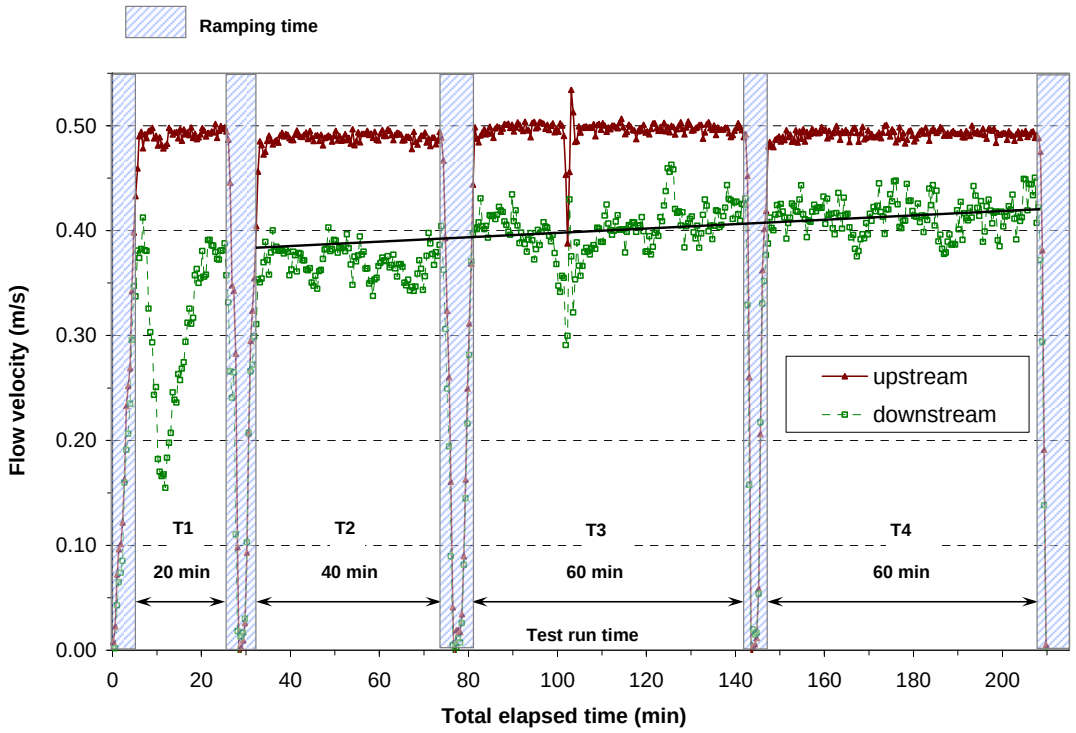


Figure 4.1 Time series of velocity upstream and downstream from the mound during the test

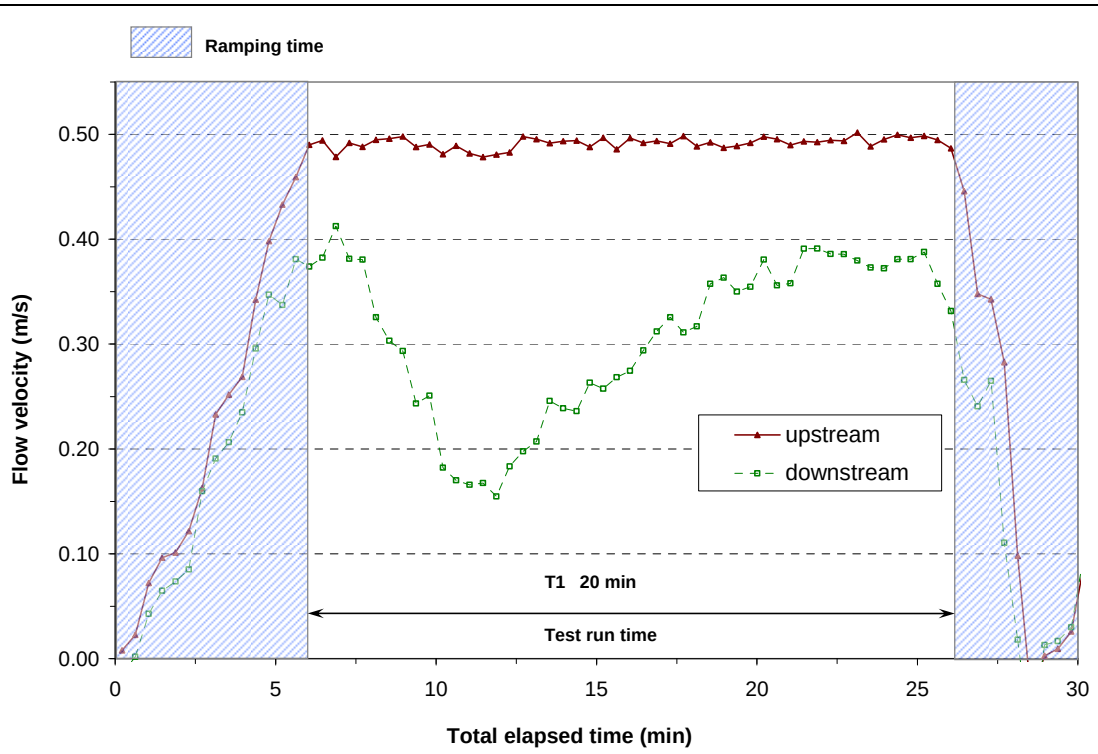


Figure 4.2 Detail of velocity during T1, the first 20 minutes of test run time.

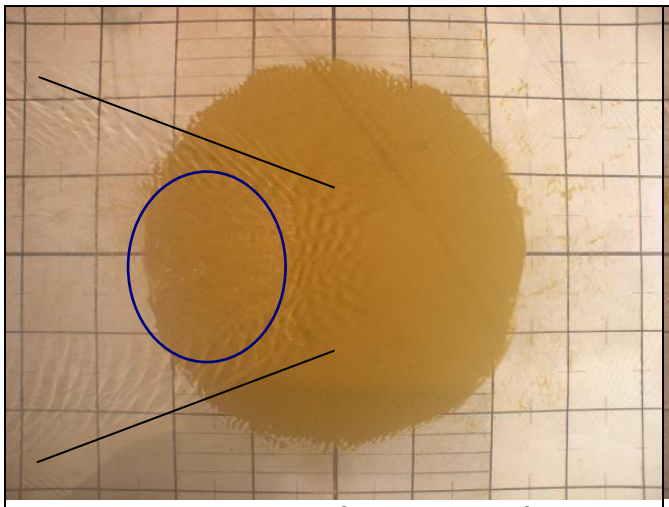

Figure 4.3 Evolution of the mound after 7 min ($T_E$). Ellipse marks the approximate extent of the re-circulation bubble; lines mark the lateral extent of the wake

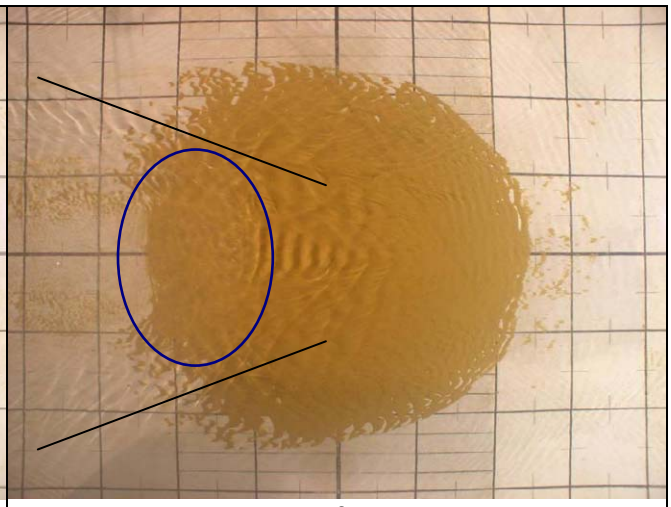

Figure 4.4 Evolution of the mound at 10 min ($T_E$).

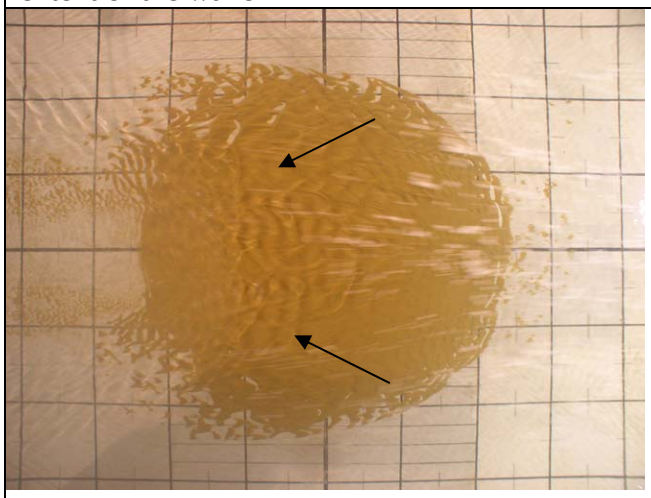

Figure 4.5 Evolution of the mound after 11 min ($T_E$). Arrows point at 'shoulders'

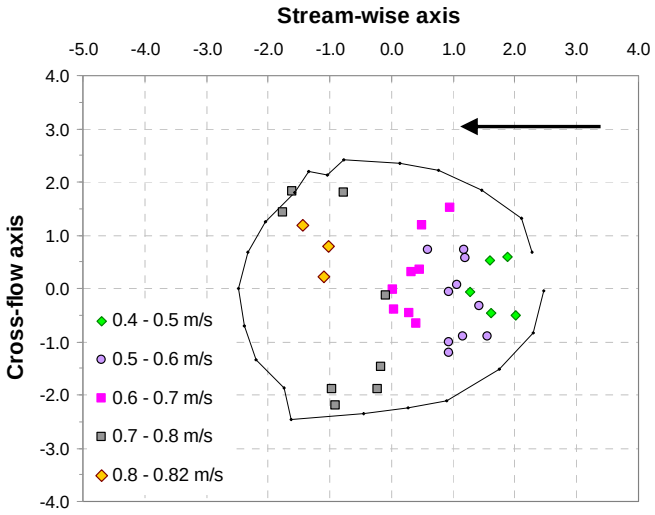


Figure 4.5b Velocity estimates at $T_E$= 11 min from float tracks and approximate position of the mound.

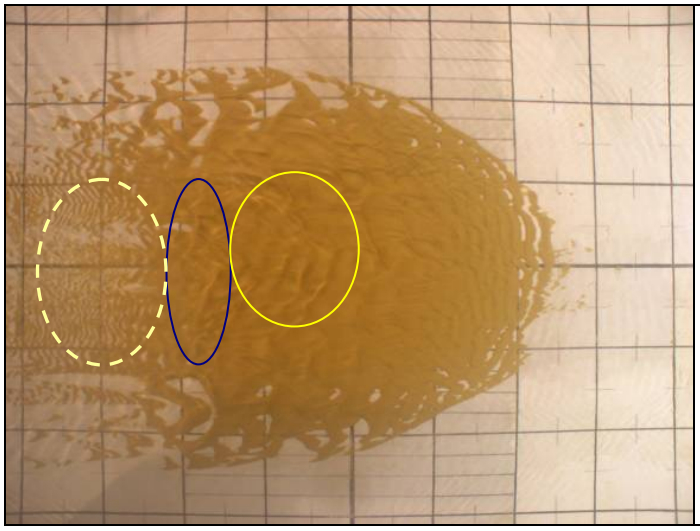

Figure 4.6 Evolution of the mound at $T_E$=18 min.

Ellipses
Dashed light: generalised surface disturbance.
Dark blue: intense disturbance.
Yellow: disturbance associated with crest migration.

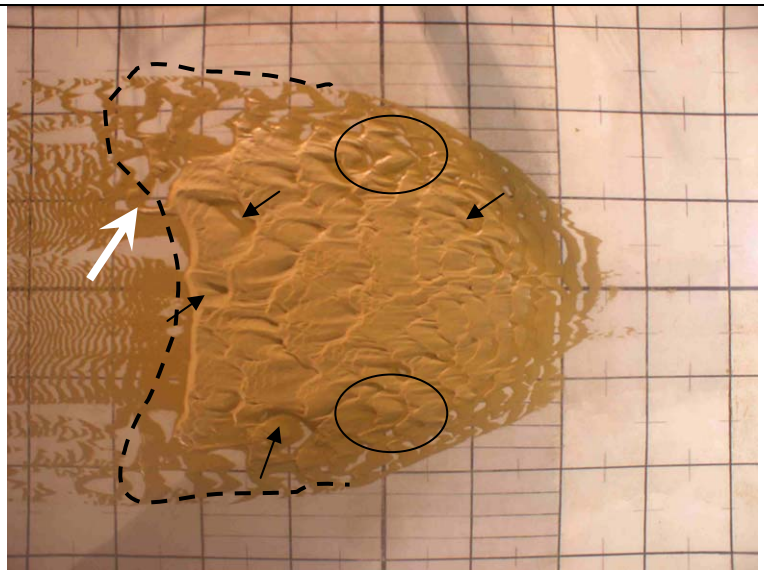

Figure 4.7 Overhead image of mound after 20 min run time. Arrows show pronounced ripple troughs. Circles show areas where the mound is dented. Dashed line shows contour of barchan shape. The white arrow points to an appendix of sand (occuring also in Figures 4.10 and 4.29).

The figure originally presented here cannot be made available via ORA for copyright reasons. It can be found at http://www.bangor.ac.uk/~oss40d/download/Baas%20(Encycl%202003).pdf

Figure 4.8 Diagram of flow over a rippled bed from Allen (1968), Reineck and Singh (1980) as cited by Bass (2003).

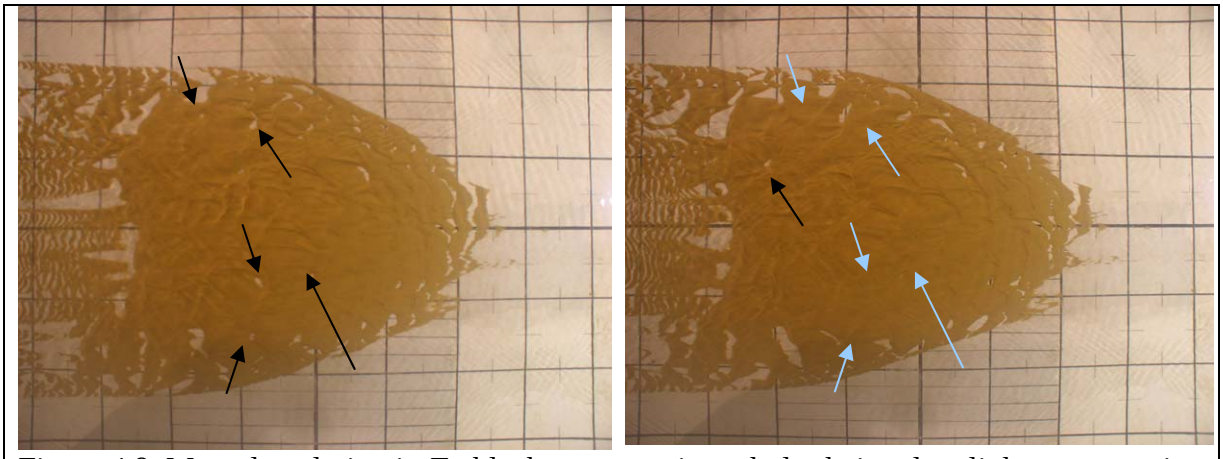

Figure 4.9 Mound evolution in $T_2$, black arrows point at holes being dug, light arrows point at holes covered.

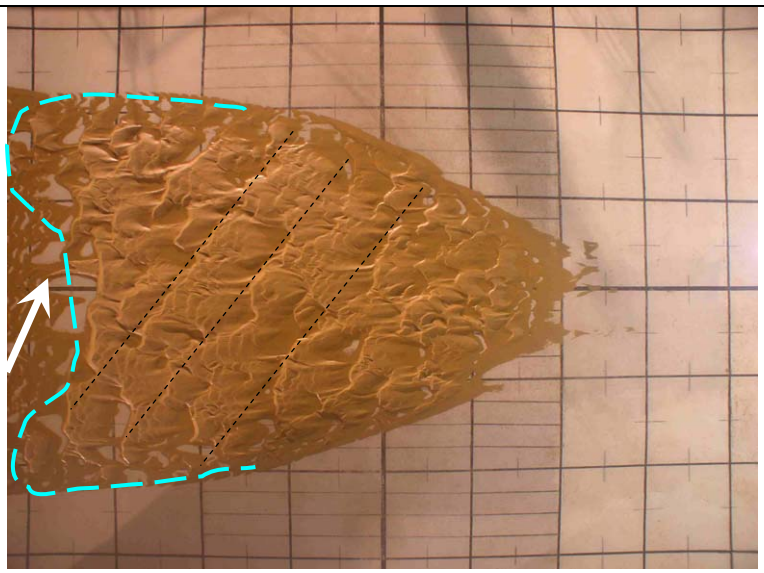

Figure 4.10 Overhead image of mound evolution after 1 hr run time. Straight dashed black lines exhibit some preferential alignment of the ripple troughs. Blue dashed line outlines the near-star-shape pattern of the mound. White arrow points to an appendix of sand (occuring in Figures 4.7 and 4.29).

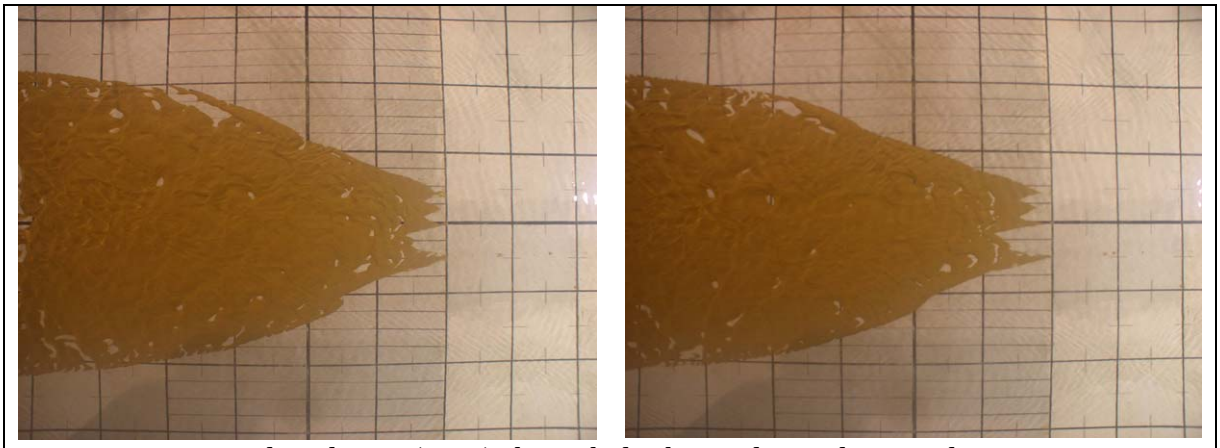

Figure 4.11 Mound evolution (in $T_3$) shows holes being dug and covered.

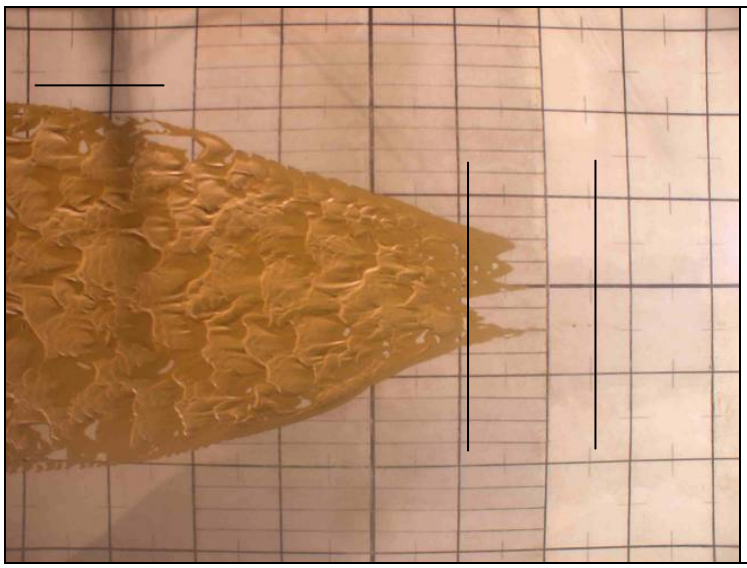

Figure 4.12 Overhead image of mound evolution after 2 hr run time.

Vertical lines mark an approximate extent of the stream-wise migration of the mound. Horizontal line marks the initial width of the mound.

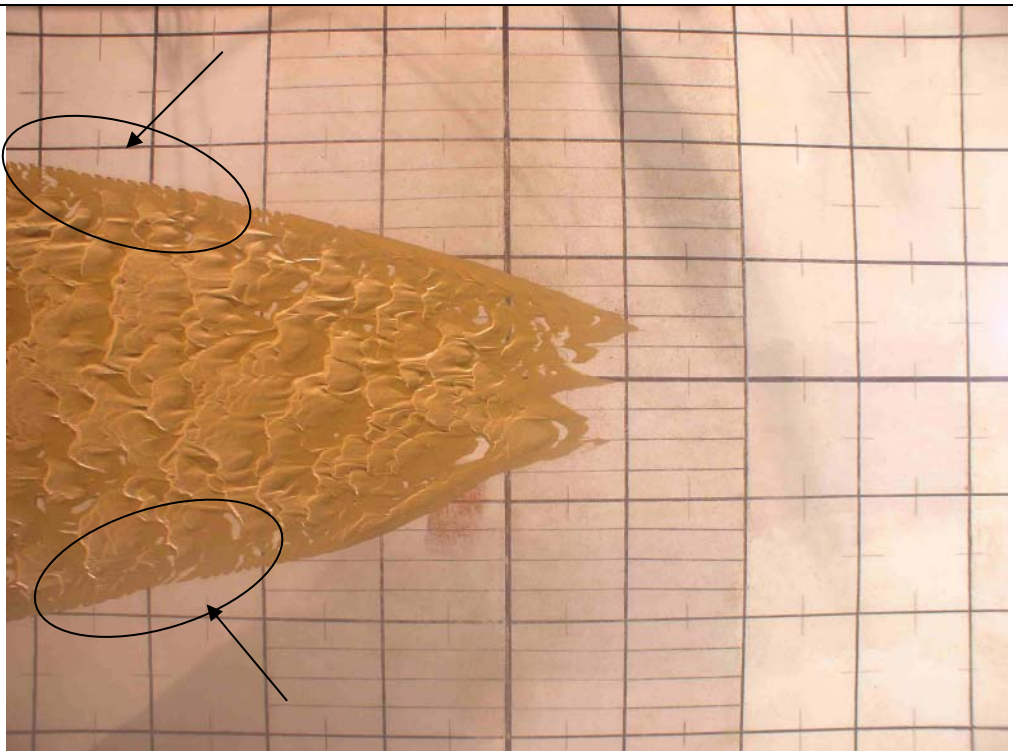

Figure 4.13 Overhead image of mound evolution after 3 hr run time. Arrows point at saw-tooth features.

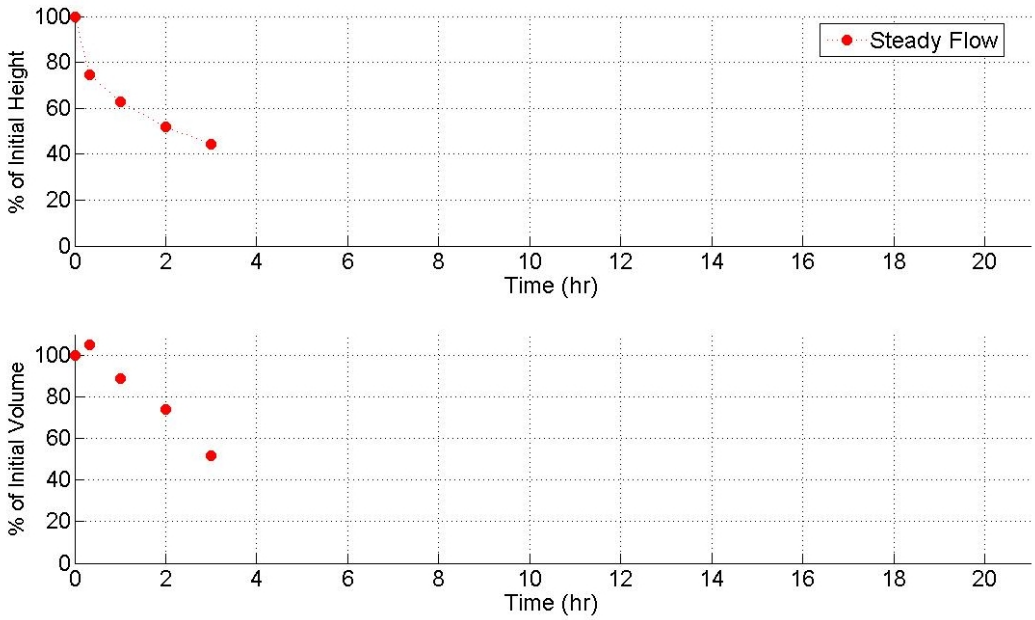


Figure 4.14 Time evolution of the percentage of initial crest height (top), and volume (bottom).

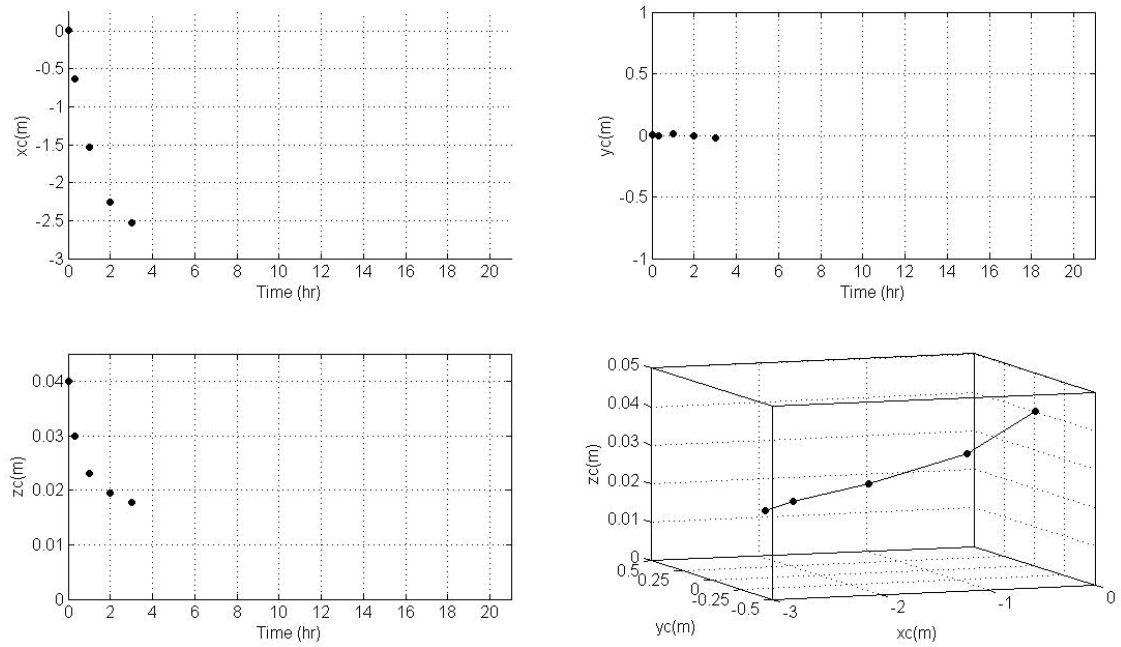


Figure 4.15 Time evolution of the location of the mound's centroid during the test

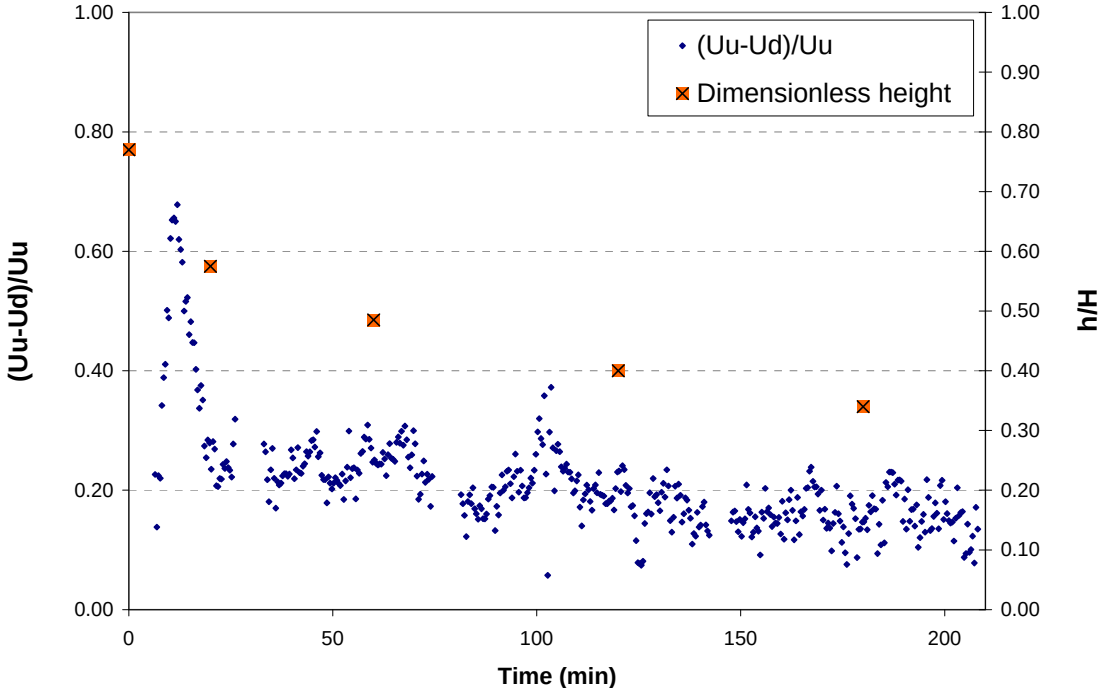


Figure 4.16 Time evolution of dimensionless parameters for the velocity deficit and mound crest height.

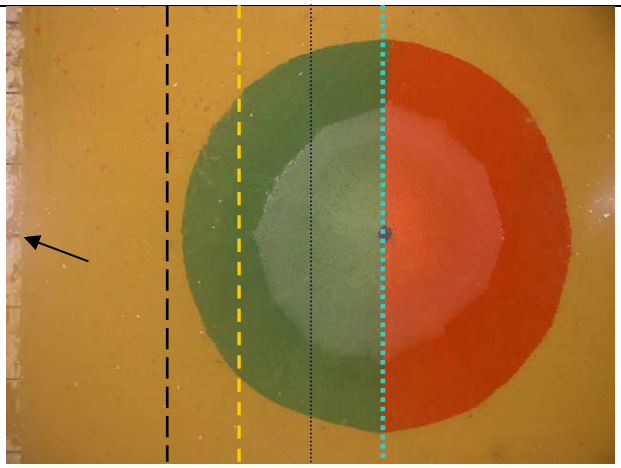

Figure 4.17 Initial state of the mound.
Lines: Light blue-dotted $x$ = 0 m; dark blue $x$ = 1 m; yellow-dashed $x$ = 2 m; black-dashed $x$ = 3 m. Arrow points at the extent of the mobile bed

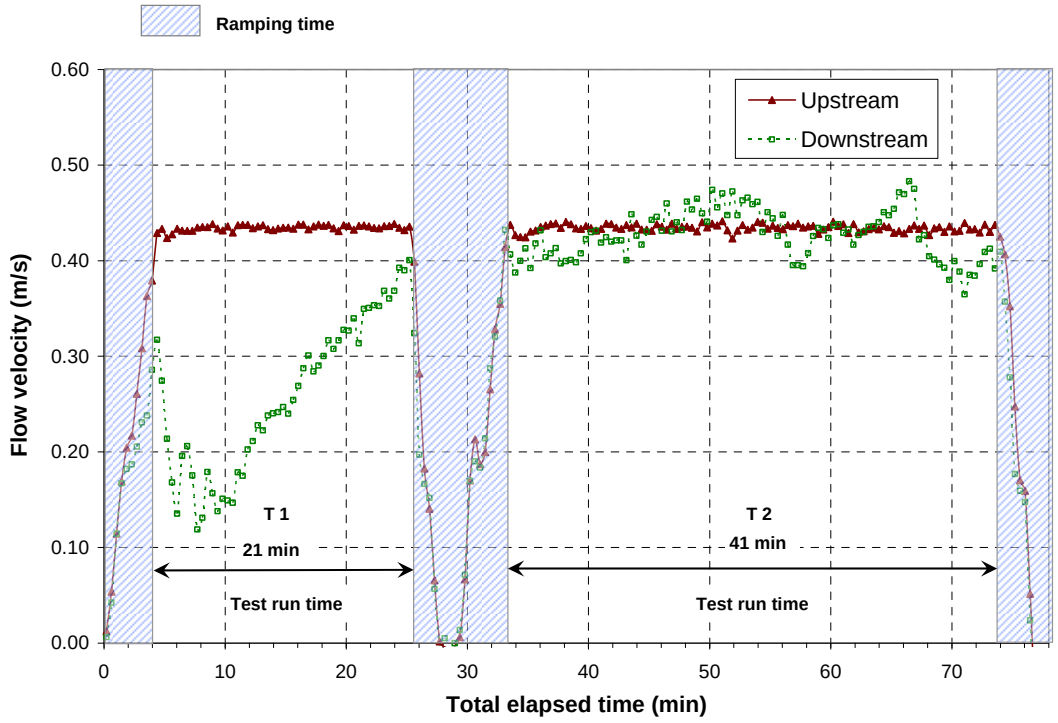


Figure 4.18 Time series of velocity upstream and downstream from the mound during the test.

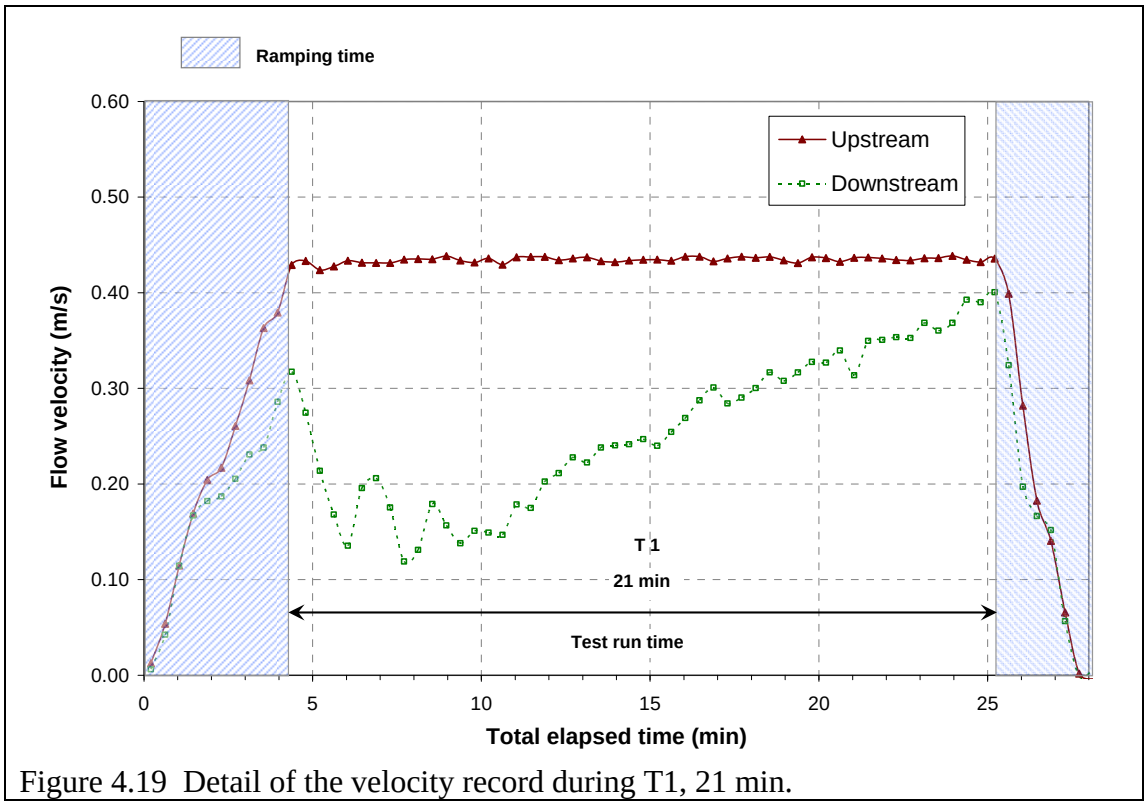


Figure 4.19 Detail of the velocity record during T1, 21 min.

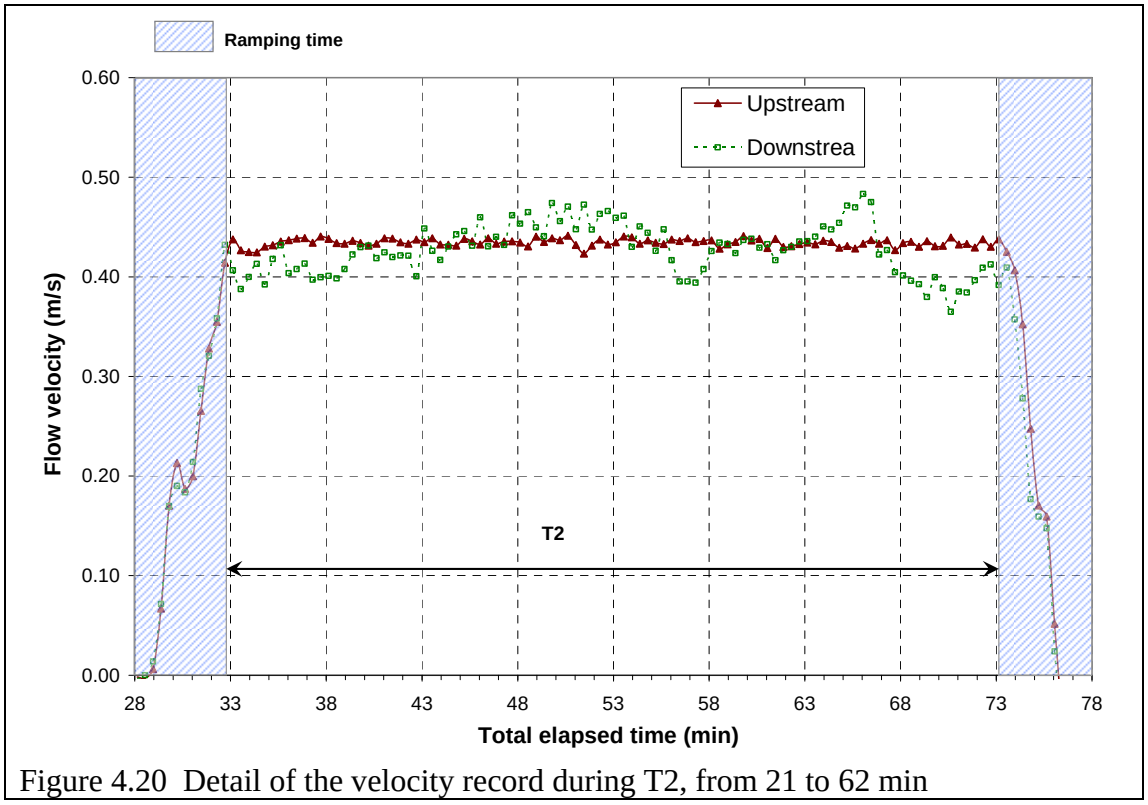


Figure 4.20 Detail of the velocity record during T2, from 21 to 62 min

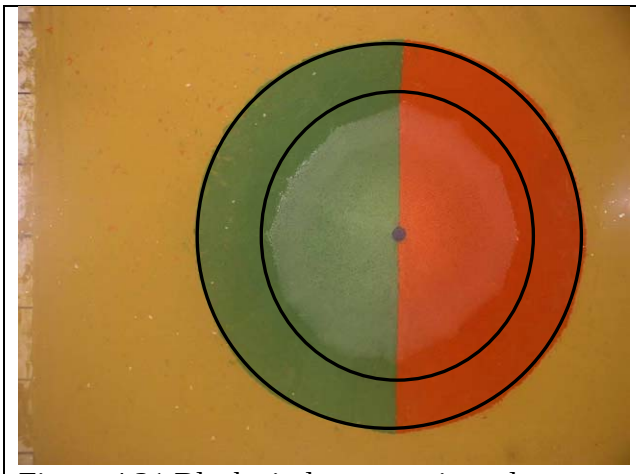

Figure 4.21 Black circles approximately indicate the outer area of the radius, where the thickness of the colour sand layer is ≤ 0.005 m.

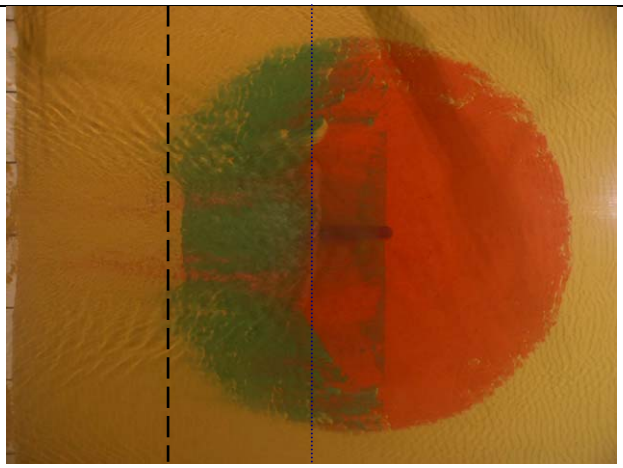

Figure 4.22 – Evolution at $T_E$ = 9 min. Green sand on the mobile bed mimics red sand at the crest. Lines as per Figure 4.17.

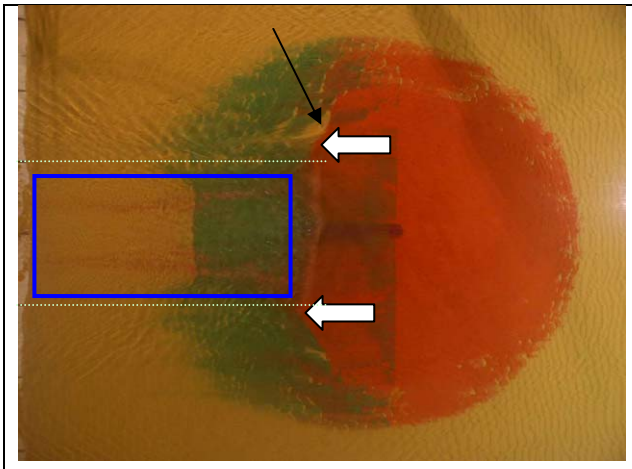

Figure 4.23 Evolution at $T_E$ = 10 min. White arrows point at mound's shoulders, and lines show their separation. Black arrow points at affect of strong secondary flow. Blue box delineates red trails.

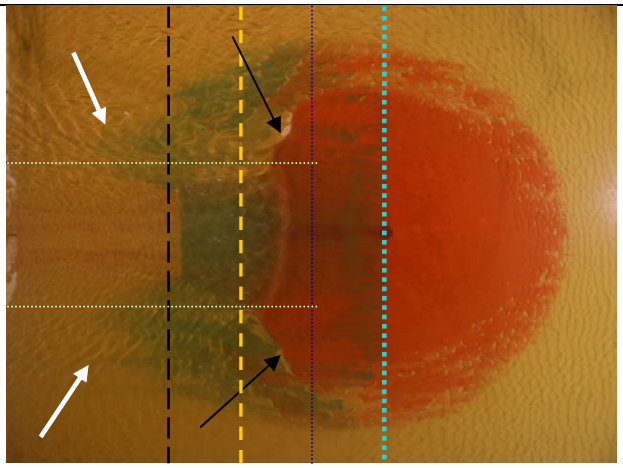

Figure 4.24 Mound evolution at $T_E$ =14 min. Arrows point at the shape of sand later (white, green sand; black red sand). Lines as per Figures 4.17 and 4.23.

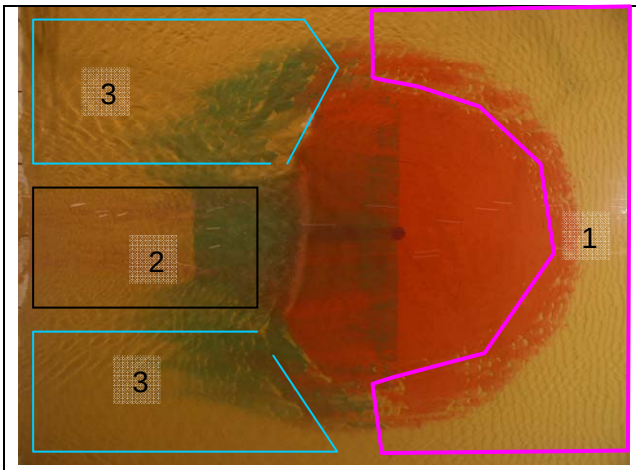


Figure 4.25 $T_E$=14 min. Areas of different ripple morphology described in Section 4.1.2

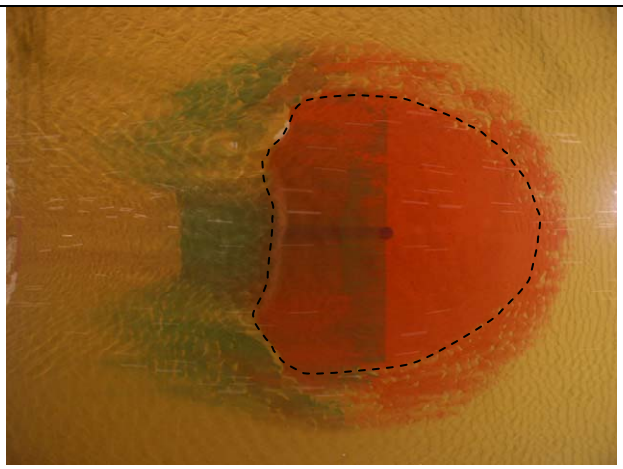

Figure 4.26 Mound evolution at $T_E$= 16 min. Faint white lines mark float tracks.

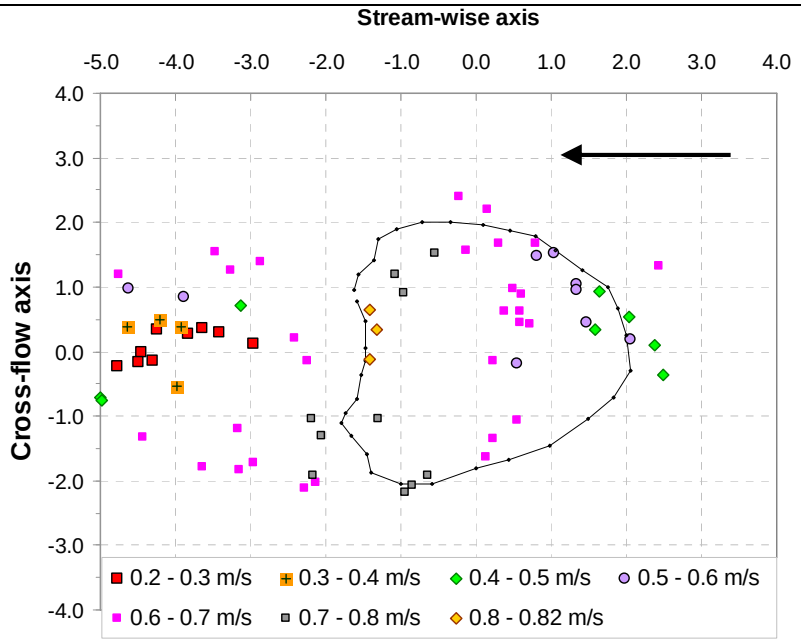


Figure 4.27 Velocity estimates at $T_E$= 16 min from float tracks and approximate position of the mound.

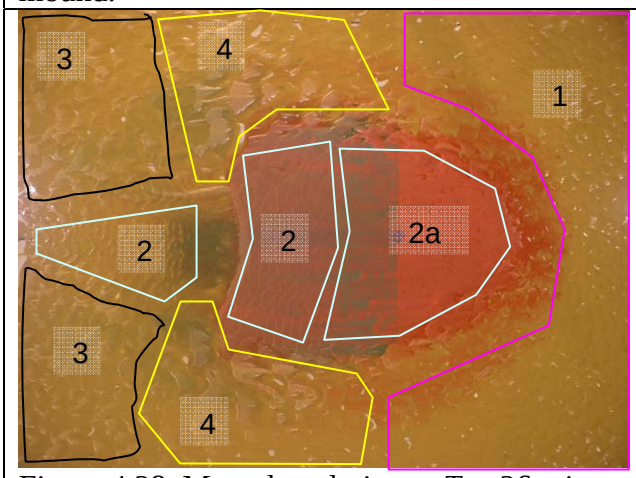


Figure 4.28 Mound evolution at $T_E$= 26 min (end of $T_1$). Areas of different ripple morphology.

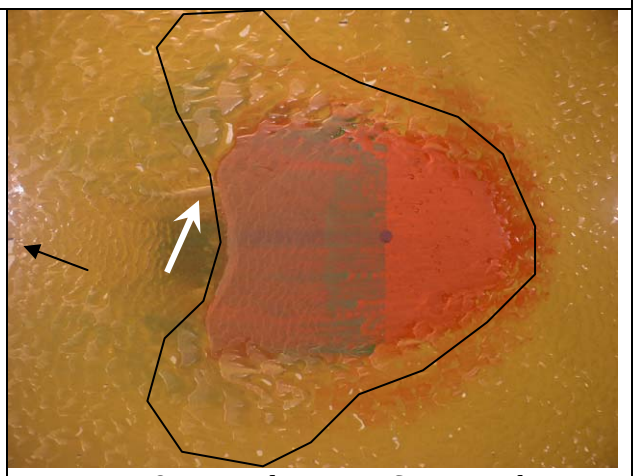

Figure 4.29 Mound at $T_E$= 26 min. White arrow shows a small appendix of sand similar to one in Figures 4.7 and 4.10.

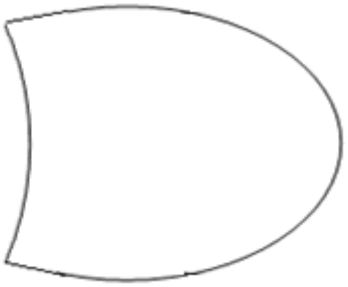

Figure 4.30 Diagram of shape of the coloured part of the mound at $T_E$= 26 min.

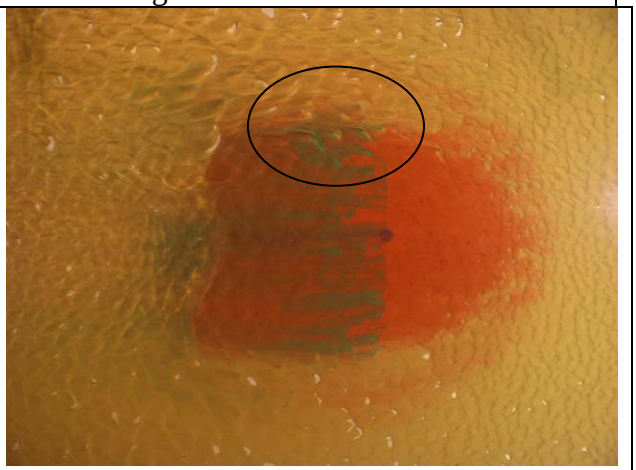

Figure 4.31 Mound evolution at $T_E$= 36 min. Ellipse marks dented area.

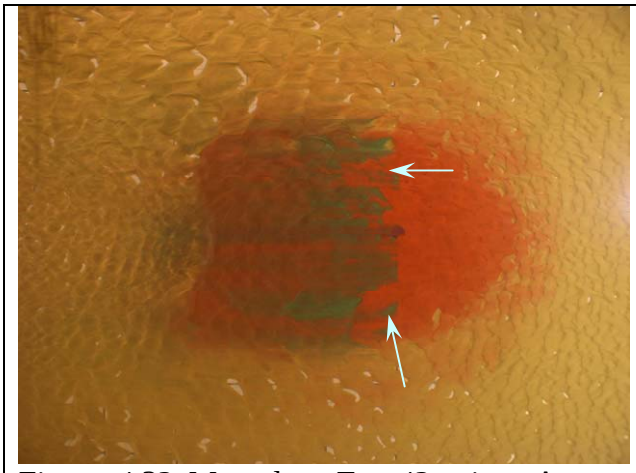

Figure 4.32 Mound at $T_E$= 42 min. Arrows point to large ripples travelling over the mound.

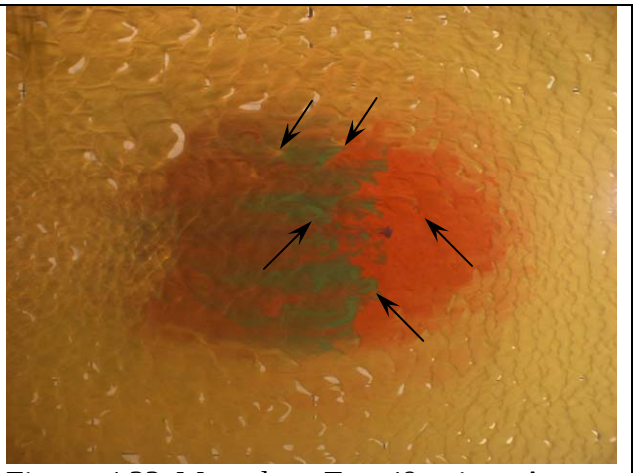

Figure 4.33 Mound at $T_E$= 49 min. Arrows point to deep troughs developing.

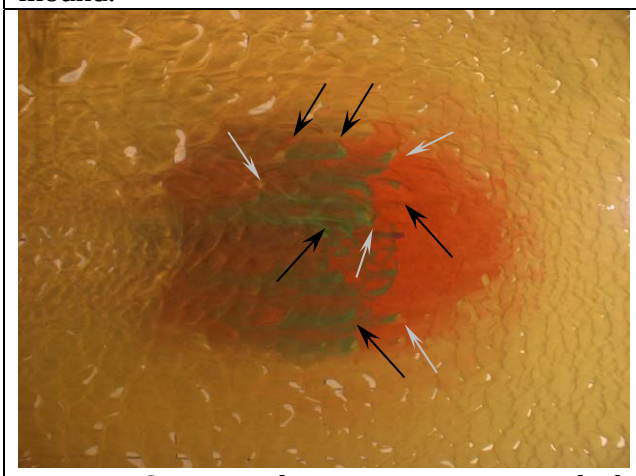

Figure 4.34 Mound at $T_E$= 51 min. Black arrows as per Figure 4.33, light arrows point at deeper troughs.

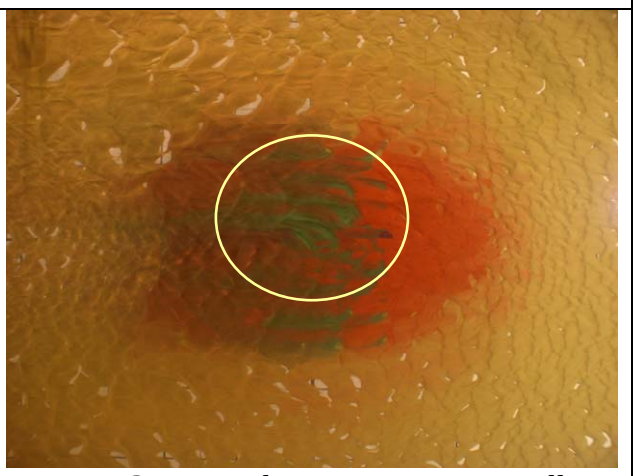

Figure 4.35 Mound at $T_E$= 52 min. Ellipse shows deep troughs in the central area of the mound.

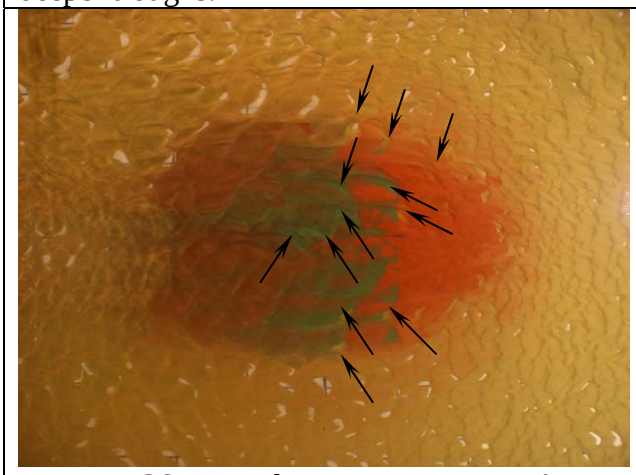

Figure 4.36 Mound at $T_E$= 54 min. Arrows point at deep troughs.

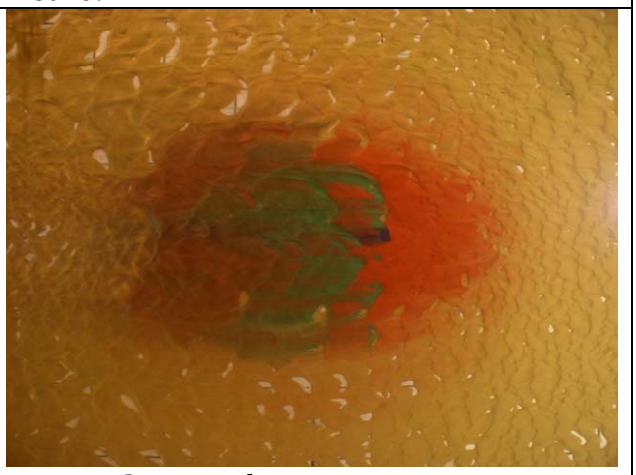

Figure 4.37 Mound at $T_E$= 55 min

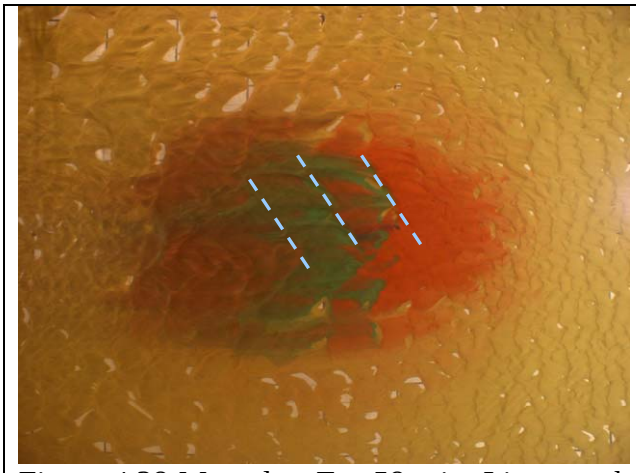

Figure 4.38 Mound at $T_E$= 58 min. Lines mark position of large ripples' troughs.

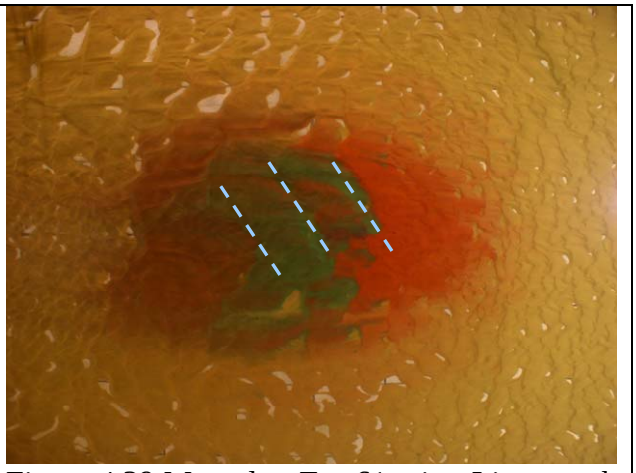

Figure 4.39 Mound at $T_E$= 61 min. Lines mark alignment of the ripples.

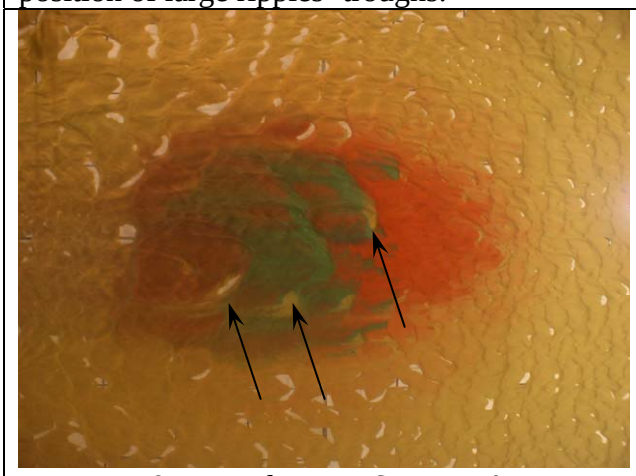

Figure 4.40 Mound at $T_E$= 64 min. Arrows point at deep troughs.

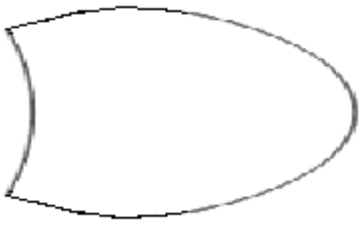

Figure 4.41 Diagram of shape of the coloured part of the mound at an intermediate stage in $T_2$.

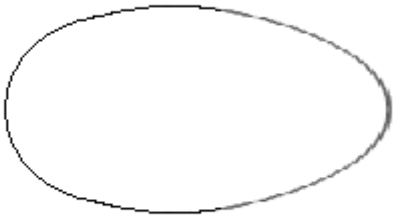

Figure 4.42 Diagram of shape of the coloured part of the mound at the end of $T_2$.

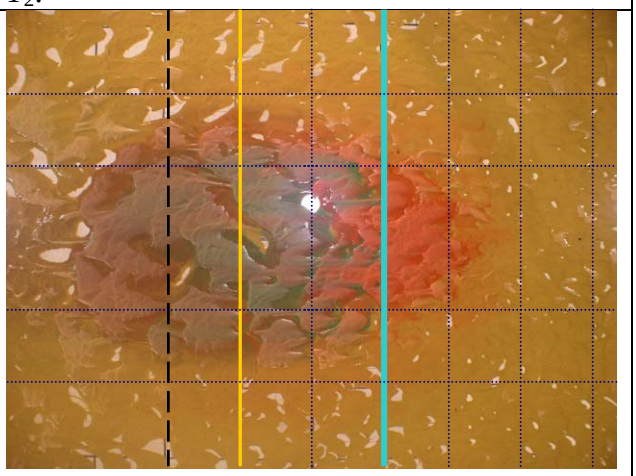

Figure 4.43a Mound at $T_E$= 1 hr. Grid shown for ease of assessment of migration and shape change.

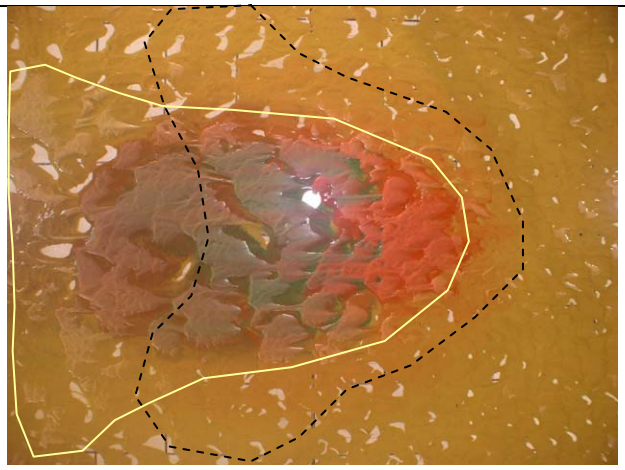

Figure 4.43b – Mound at $T_E$= 62 min. Dashed line shows star shape at $T_E$= 26 min. White line shows star shape at $T_E$= 62 min

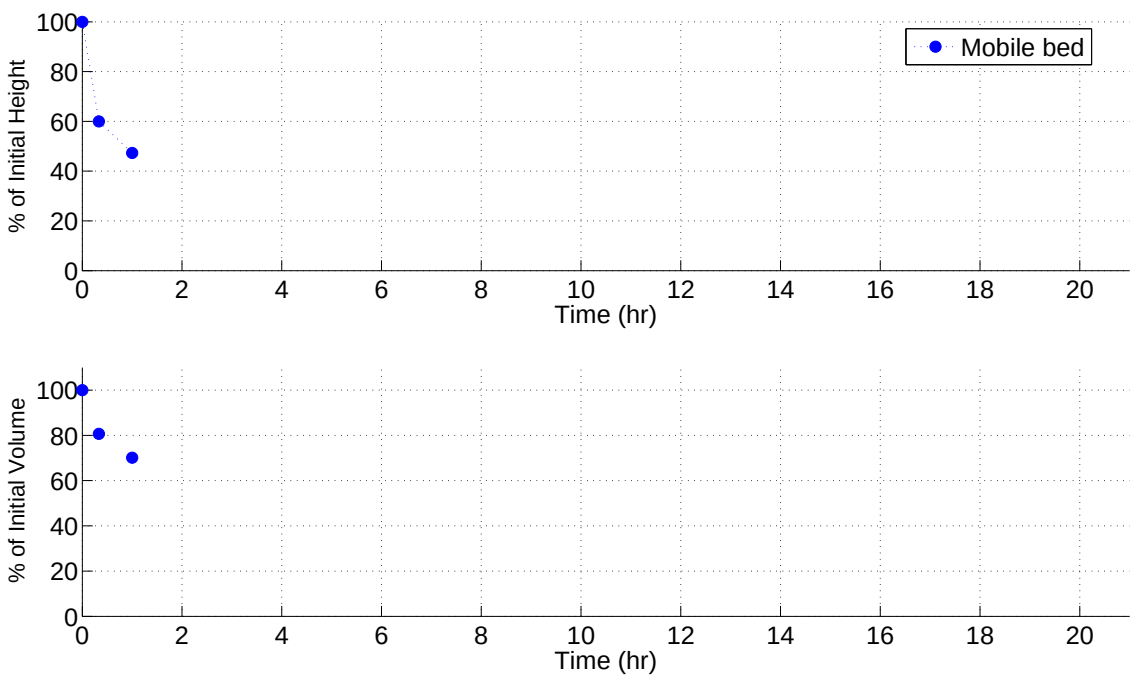


Figure 4.44 Time evolution of the percentage of initial crest height (top), and volume (bottom), Test 13.

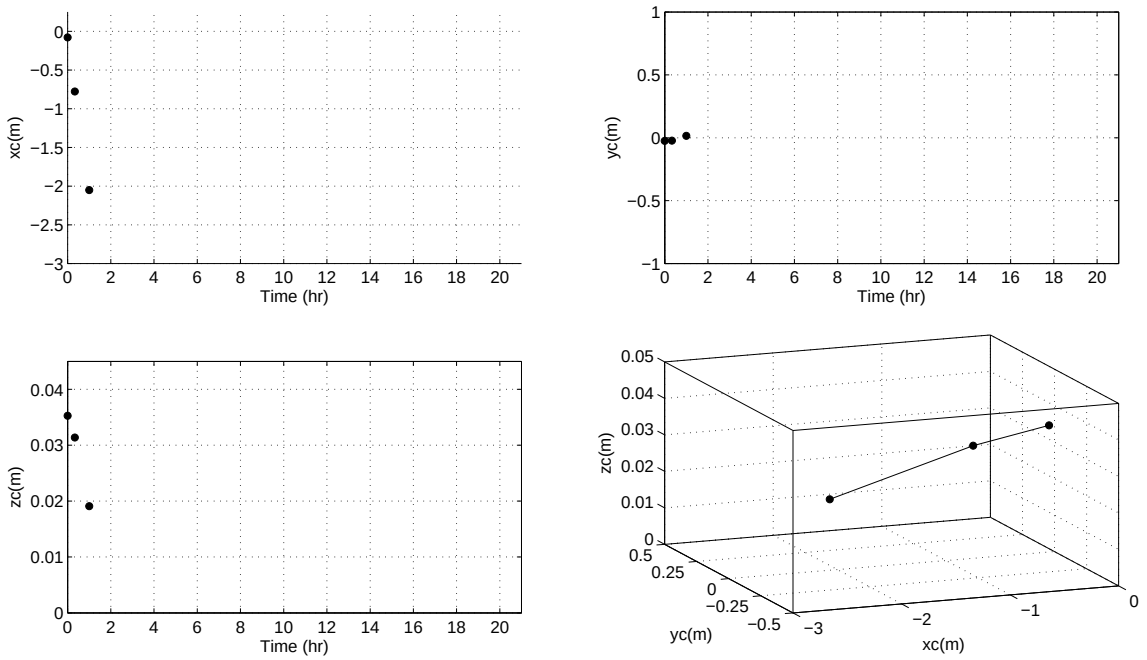


Figure 4.45 Time evolution of the location of the mound's centroid during the test.

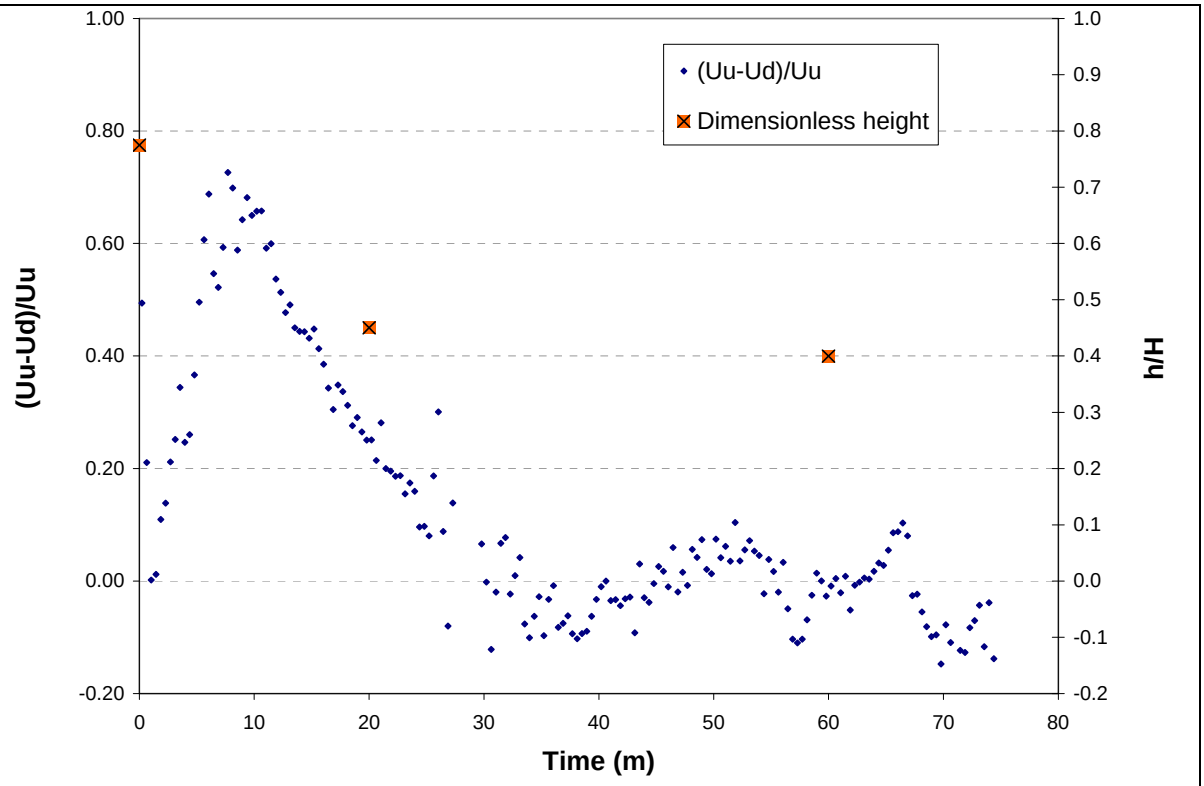


Figure 4.46 Time evolution of dimensionless parameters for the velocity deficit and mound crest height.

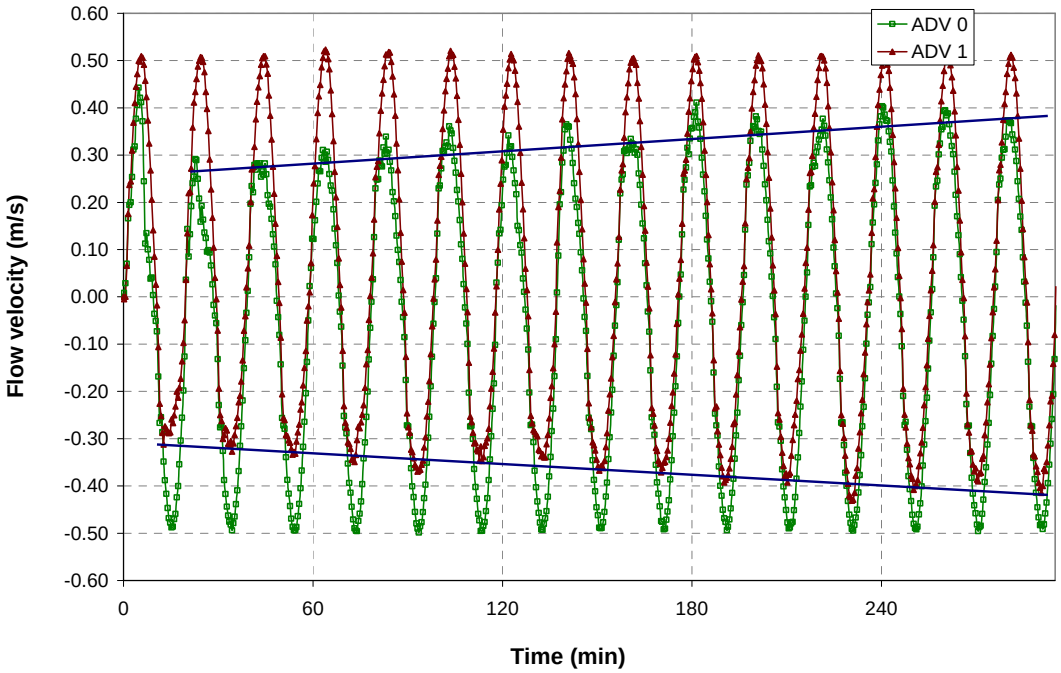


Figure 4.47 Time history of flow velocity for the first 15 cycles (5 hr).

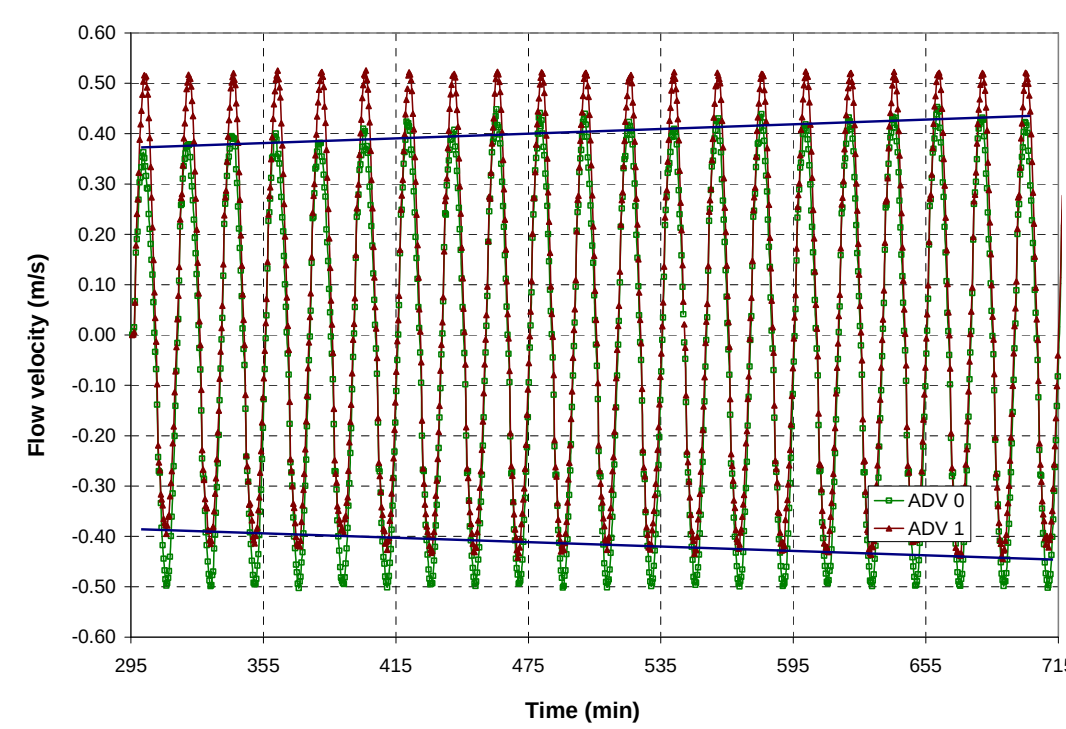


Figure 4.48 Time history of flow velocity from cycle 16 to 36 (7 hr).

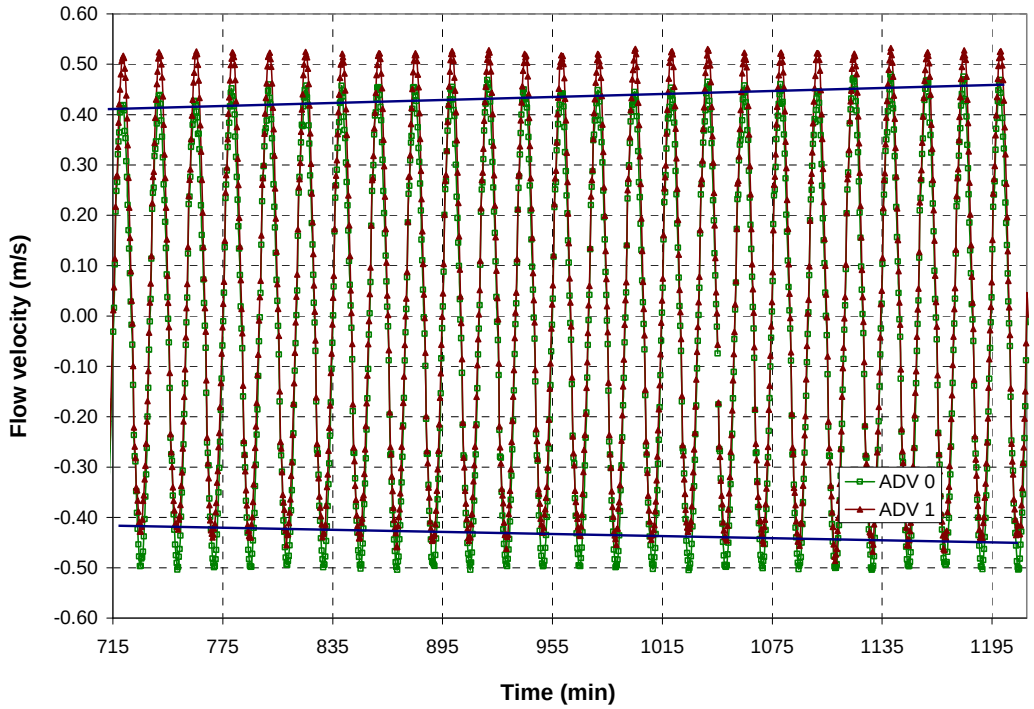


Figure 4.49 Time history of flow velocity from cycle 37 to 61 (8.3 hr)

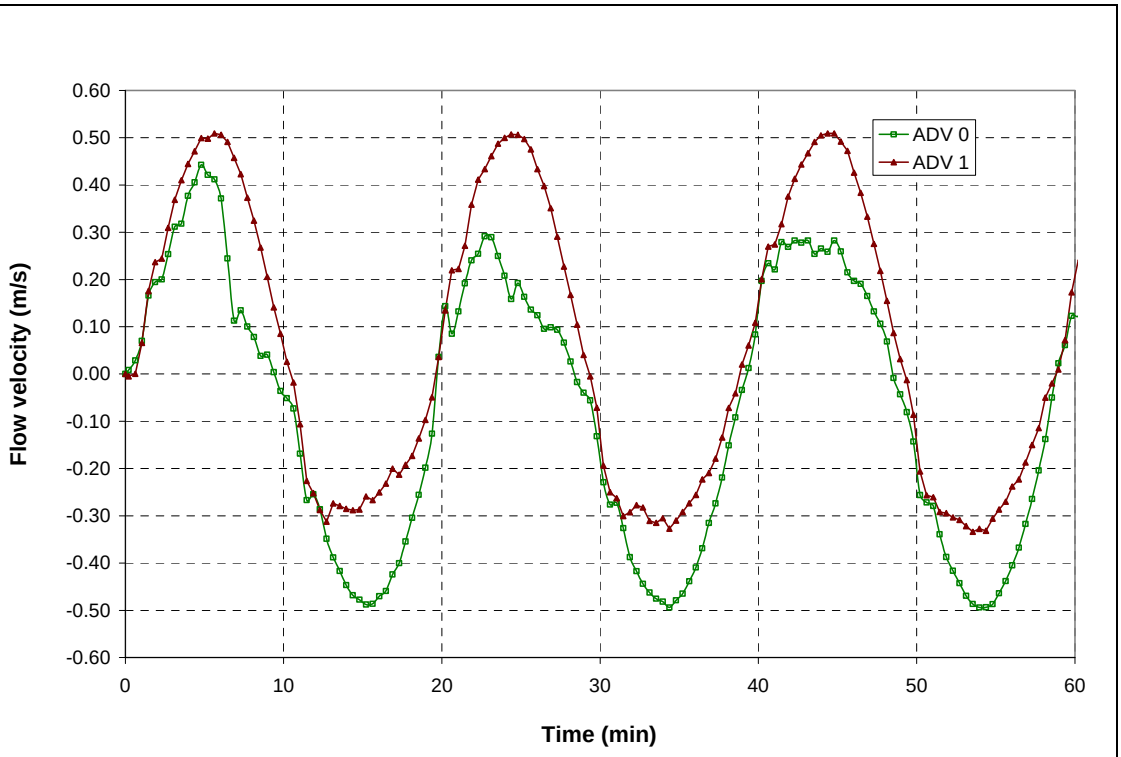


Figure 4.50 Detail of flow velocity time history during the first 3 cycles (1 hr)

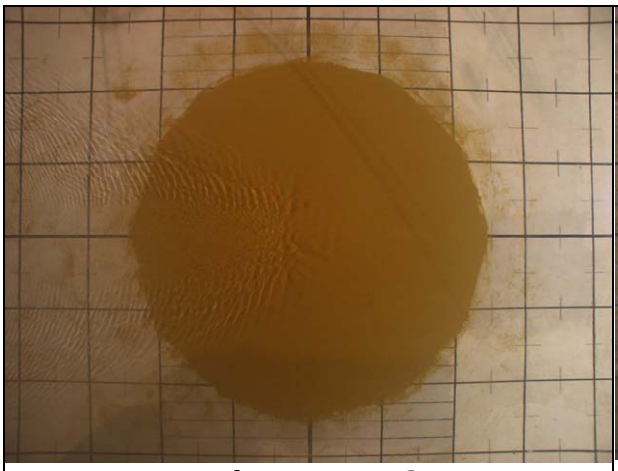

Figure 4.51 Evolution at $T_E$= 3 min

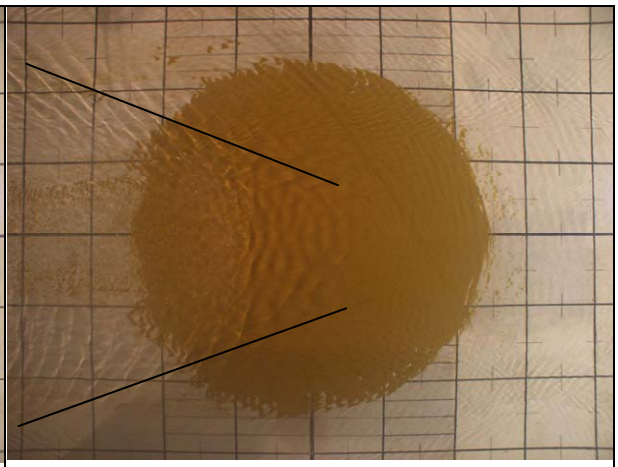

Figure 4.52 Evolution at $T_E$= 5 min. Lines mark approx. extent of wake.

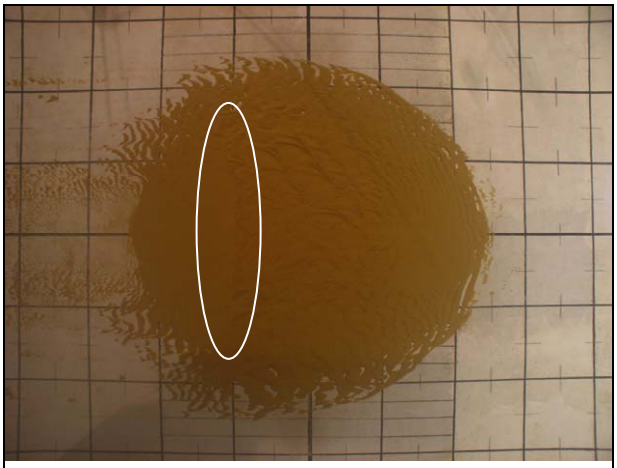

Figure 4.53 Evolution at $T_E$= 10 min. Steep step marked by ellipsoid

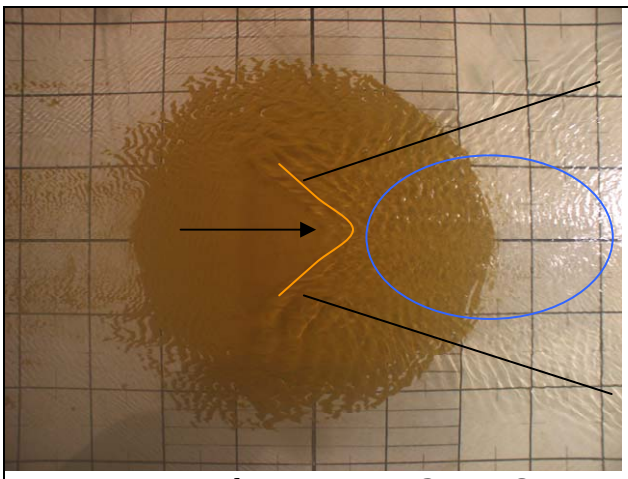

Figure 4.54 Evolution at $T_E$= 13 min. Orange line and arrow point effect of flow reversal on crest. Black lines as per Figure 4.52. Ellipse marks strong wake.

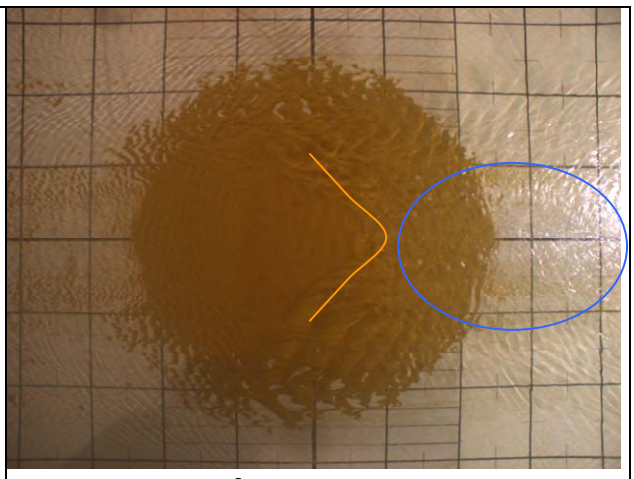

Figure 4.55 Evolution at $T_E$= 15 min. Line and ellipse as per Figure 4.54. Slightly weaker flow and wake.

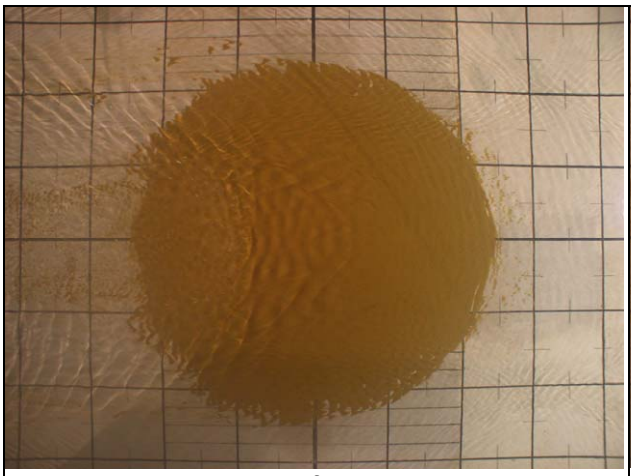

Figure 4.56 Strength of the wake at $T_E$= 5 min

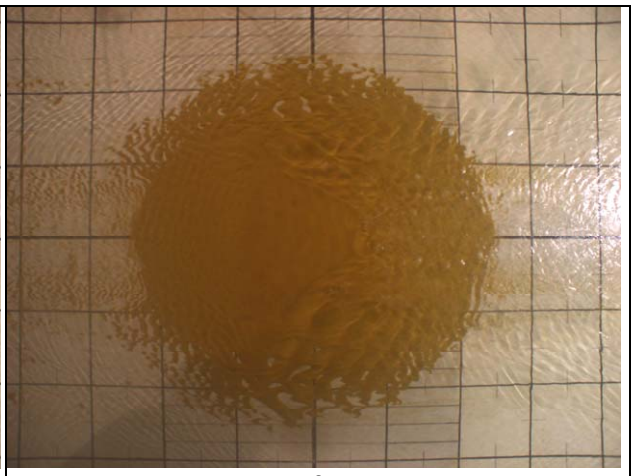

Figure 4.57 Strength of the wake at $T_E$= 15 min

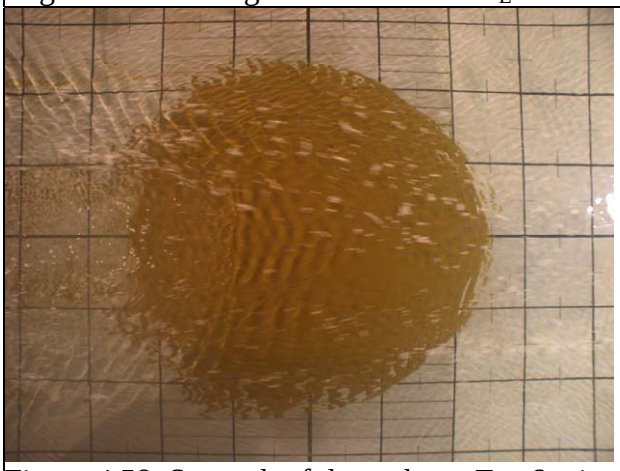

Figure 4.58 Strength of the wake at $T_E$= 6 min. Faint white lines mark float tracks.

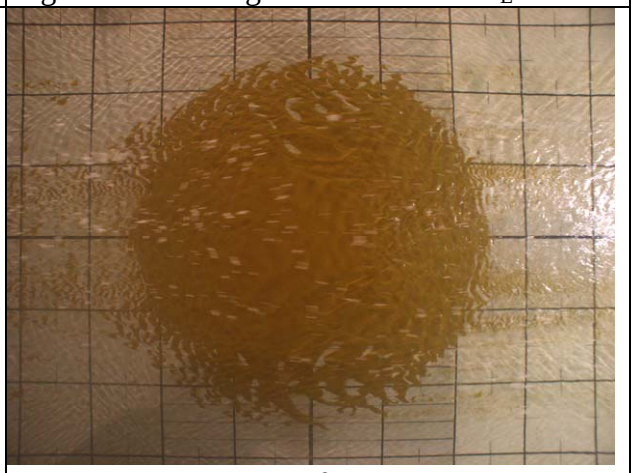

Figure 4.59 Strength of the wake at $T_E$= 16 min. Faint white lines mark float tracks.

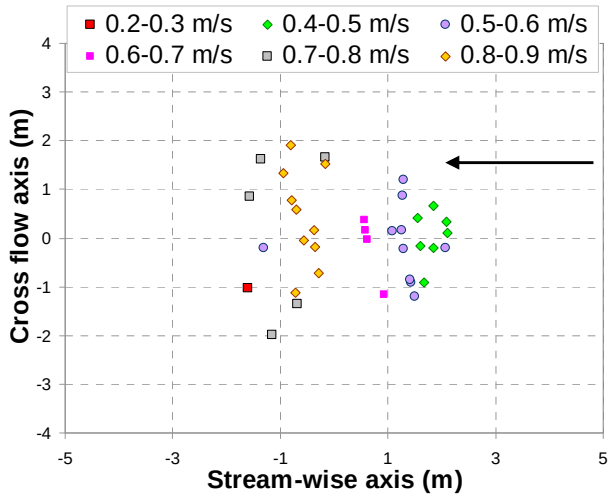


Figure 4.60 Surface velocity estimated at $T_E$= 6 min from float tracks.

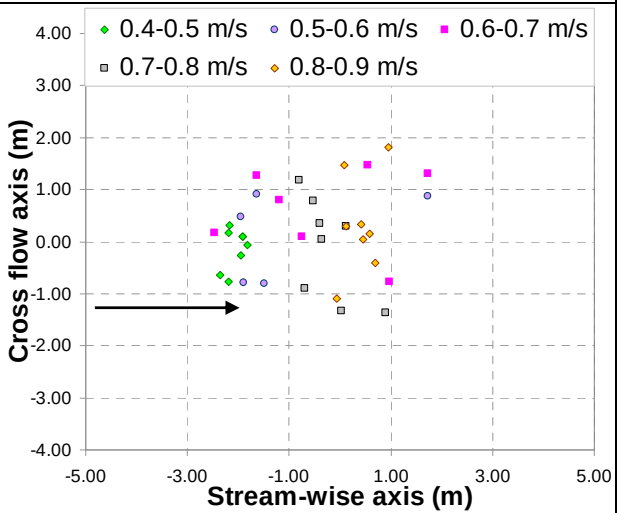


Figure 4.61 Surface velocity estimated at $T_E$= 16 min from float tracks.

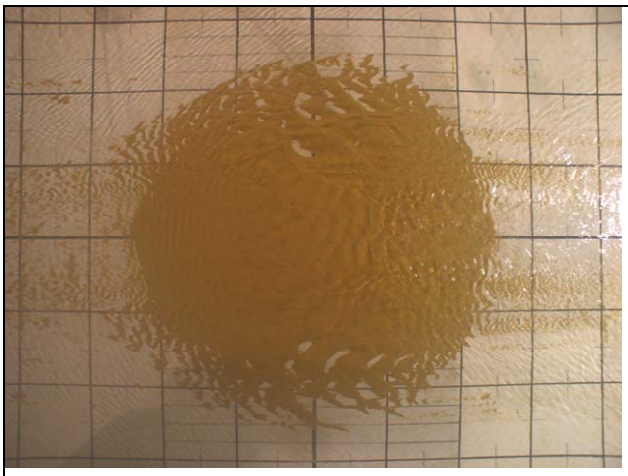

Figure 4.62 Evolution at $T_E$= 18 min

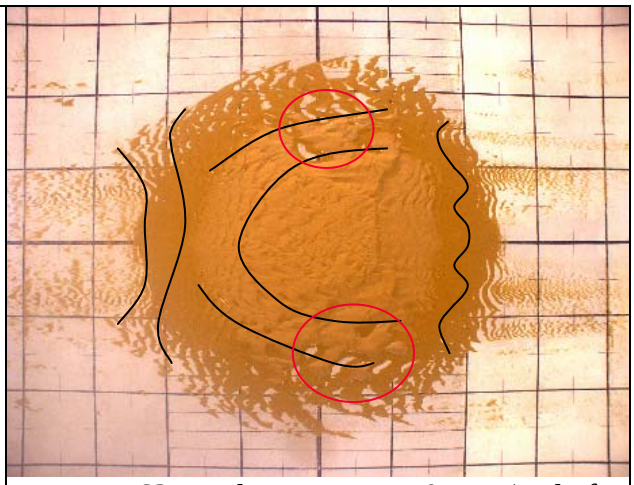

Figure 4.63 Evolution at $T_E$= 20 min (end of cycle)

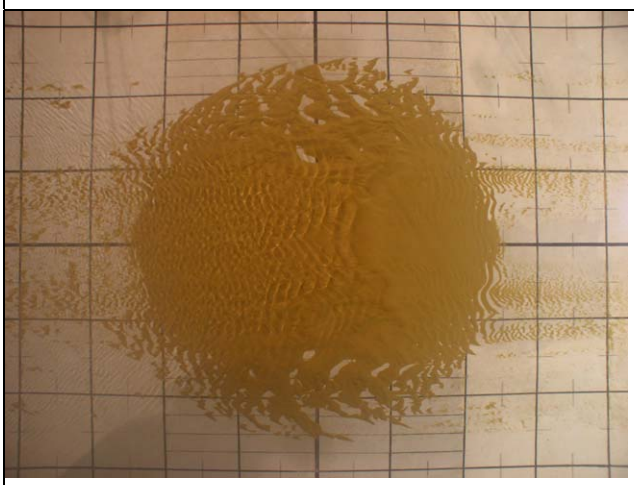

Figure 4.64 Evolution at $T_E$= 23 min (second cycle).

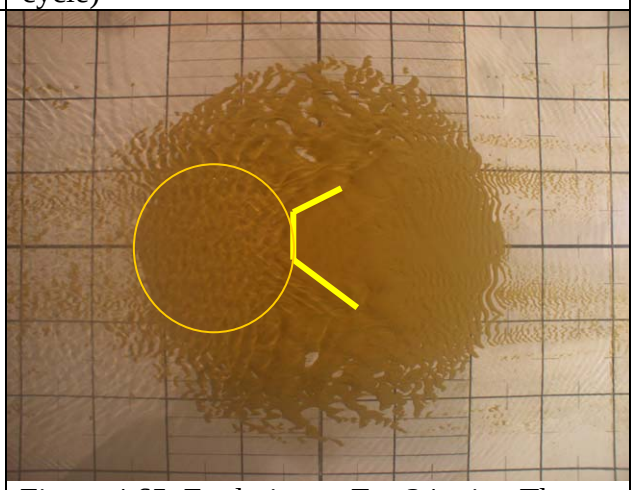

Figure 4.65 Evolution at $T_E$= 24 min. The crest travels faster on the centre than on the sides

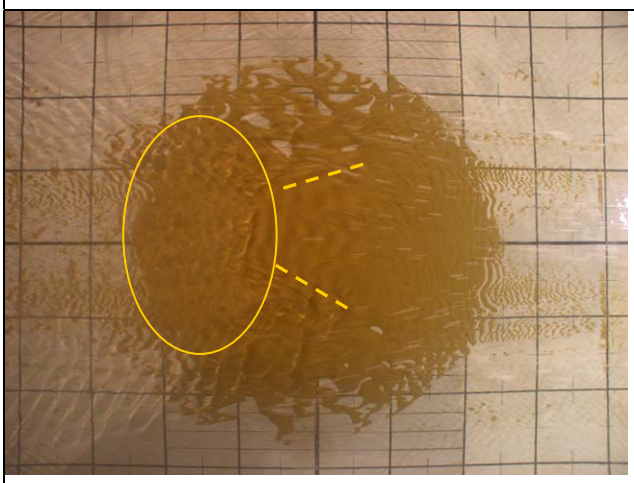

Figure 4.66 Evolution at $T_E$= 26 min. ellipse and lines as per Figure 4.65.

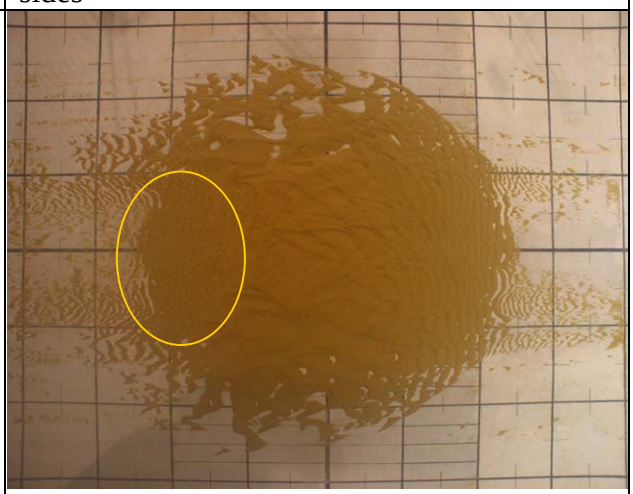

Figure 4.67 Evolution at $T_E$= 29 min. Weaker flow, visible surface disturbance in the lee of th emound.

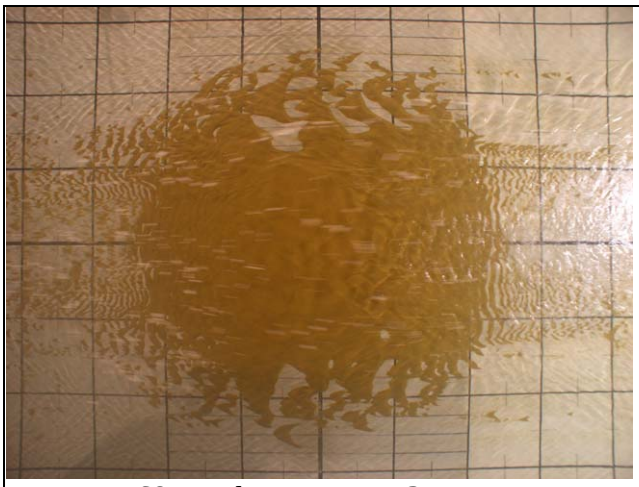

Figure 4.68 Evolution at $T_E$= 37 min. Faint white lines mark float tracks.

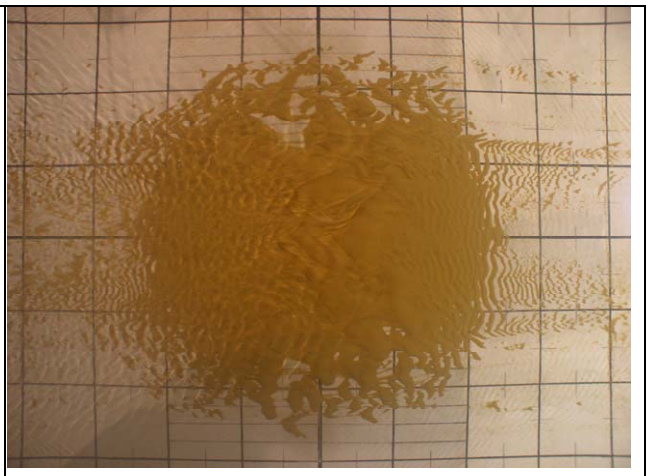

Figure 4.69 Surface disturbance at $T_E$= 44 min

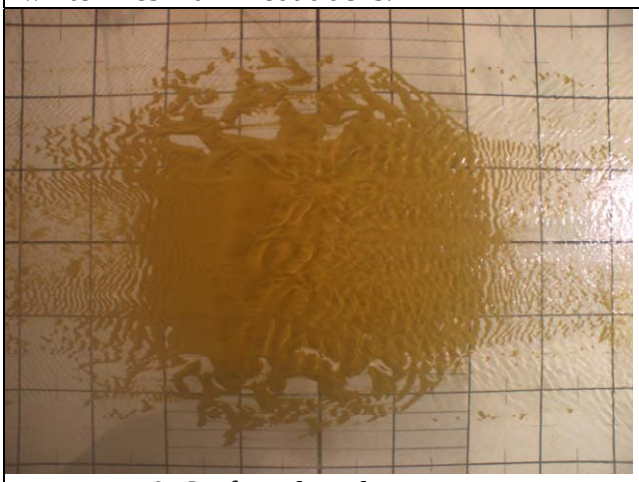

Figure 4.70 Surface disturbance at $T_E$= 54 min

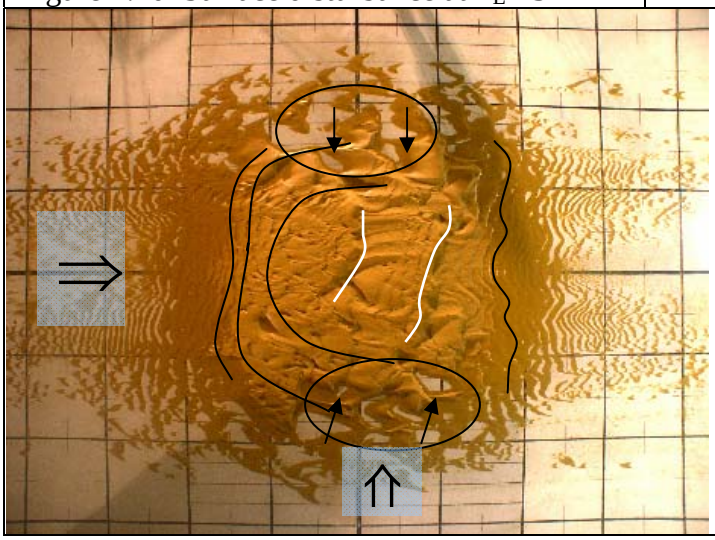

Figure 4.71 Mound at $T_E$= 1 hr (3 cycles).

White lines mark the two crests.
Black lines mark the alignment of the ripples.
Ellipses and small arrows point at areas where the secondary flows scour the sides of the mound.
Big arrows indicate where the 3D views are taken from

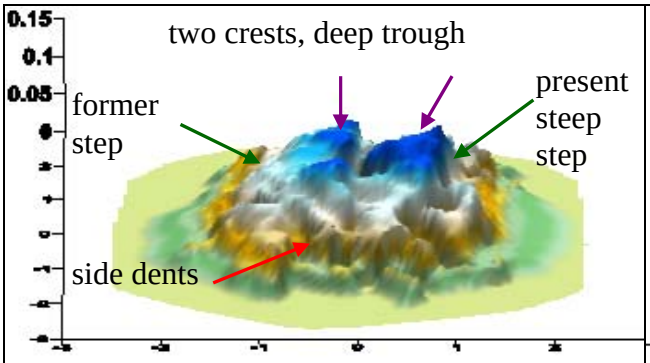


Figure 4.72 3-D view from interpolated contours. Side view of the mound min after 1 hr (from the bottom of images).
Note exaggerated z-axis scale

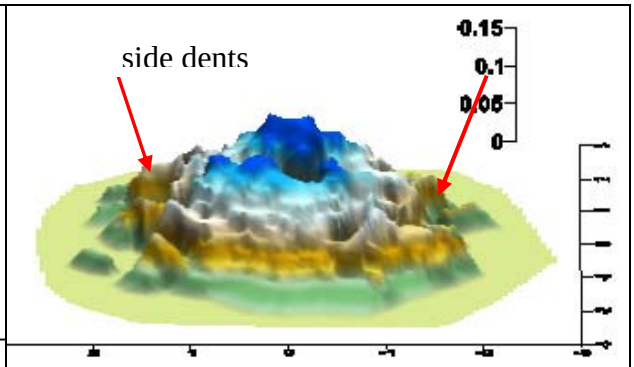


Figure 4.73 3-D view from interpolated contours. Front view (from the left in images) arrows point at lateral dents.
Note exaggerated z-axis scale

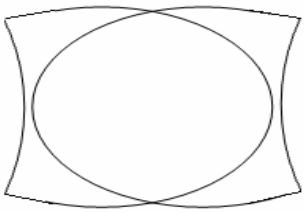

Figure 4.74- Diagram interpreting the shape of the mound

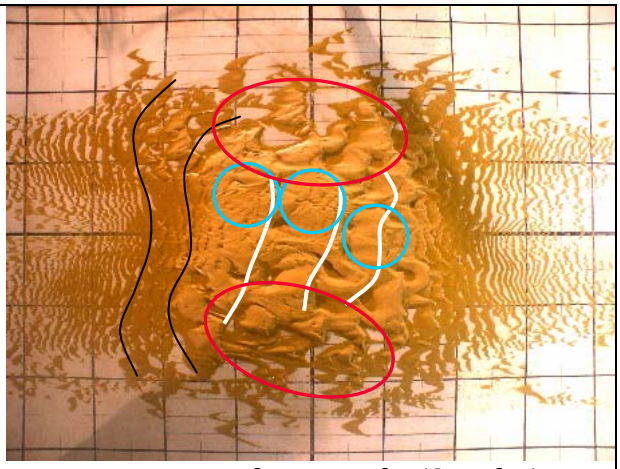

Figure 4.75 Mound at $T_E$= 2 hr (6 cycles)

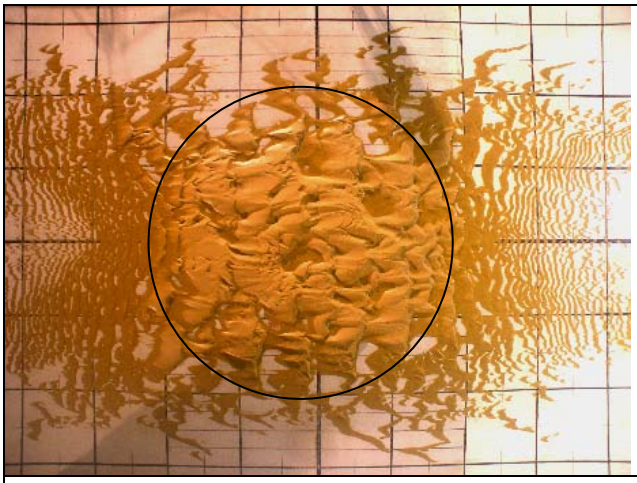

Figure 4.76 Mound at $T_E$= 4 hr (12 cycles)

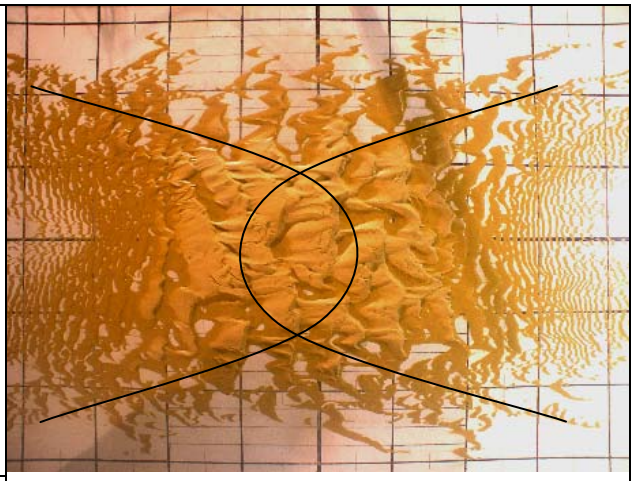

Figure 4.77 Mound at $T_E$= 5 hr (15 cycles)

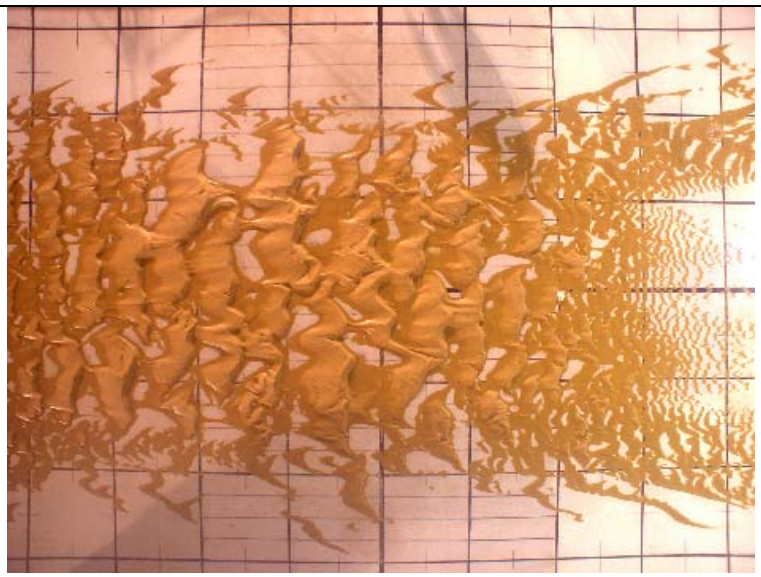

Figure 4.78 Mound at $T_E$= 20.3 hr (61 cycles).

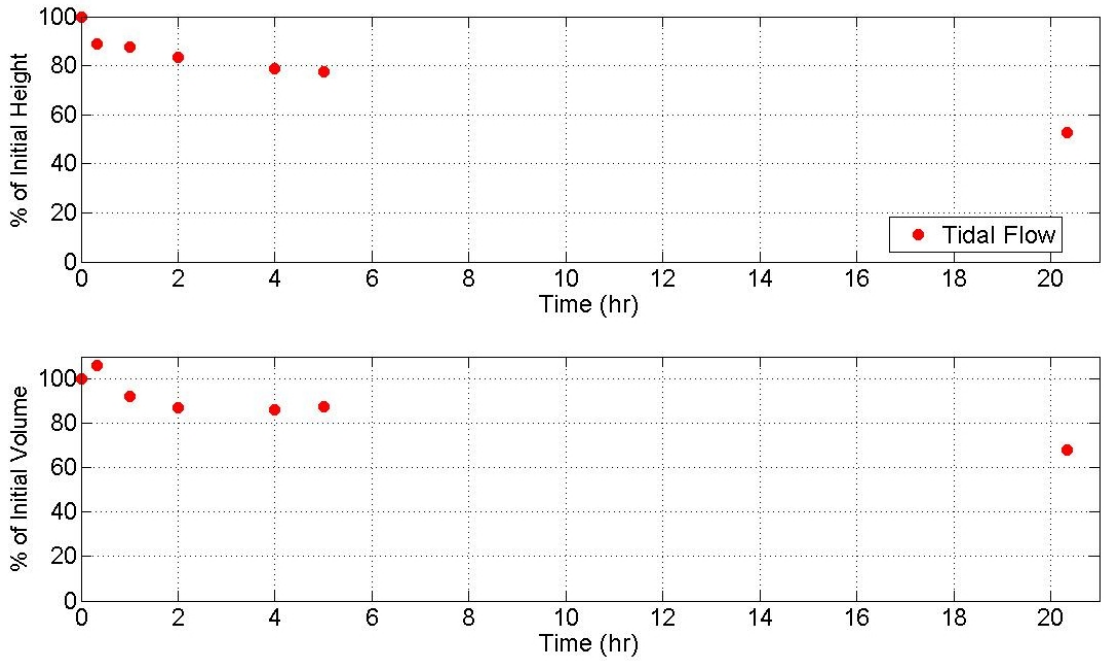


Figure 4.79 Time evolution of the percentage of initial crest height (top), and volume (bottom), Test 8.

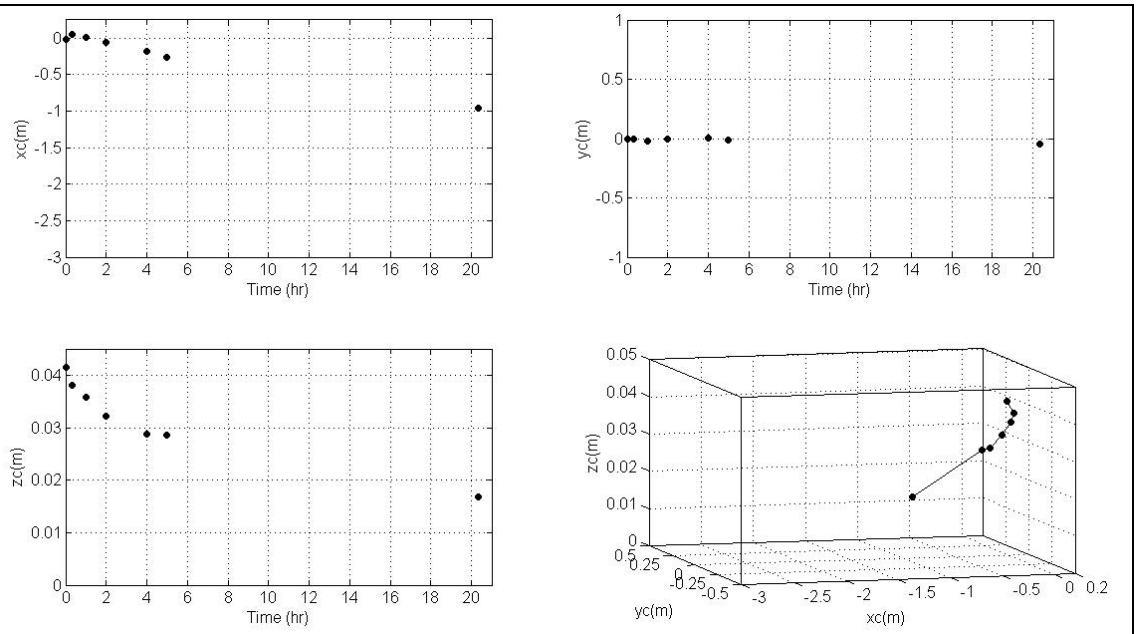


Figure 4.80 Time evolution of the location of the mound's centroid during the test.

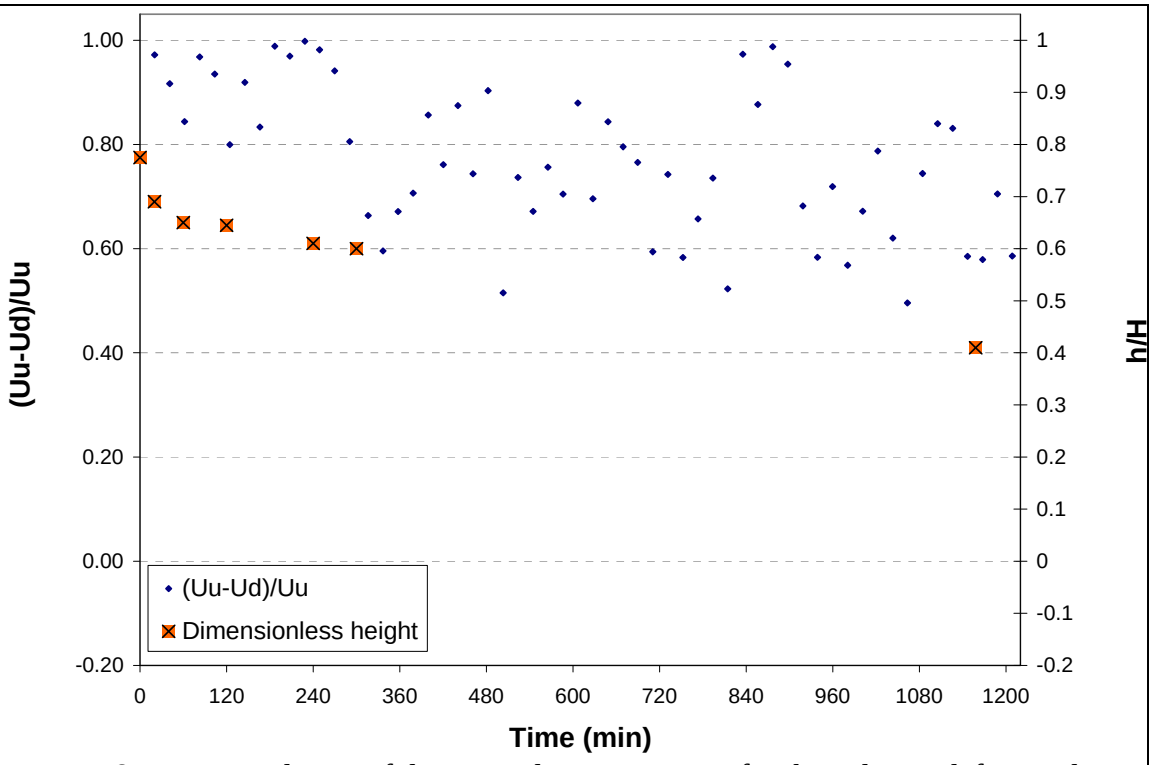


Figure 4.81 Time evolution of dimensionless parameters for the velocity deficit and mound crest height.

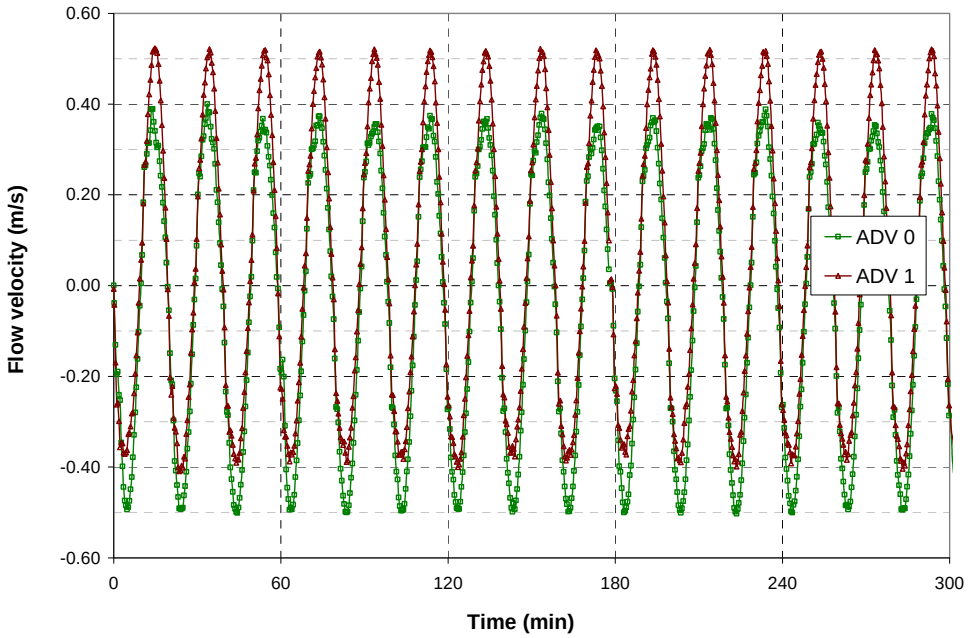


Figure 4.82 Time history of velocity from the start of the test until 5 hr

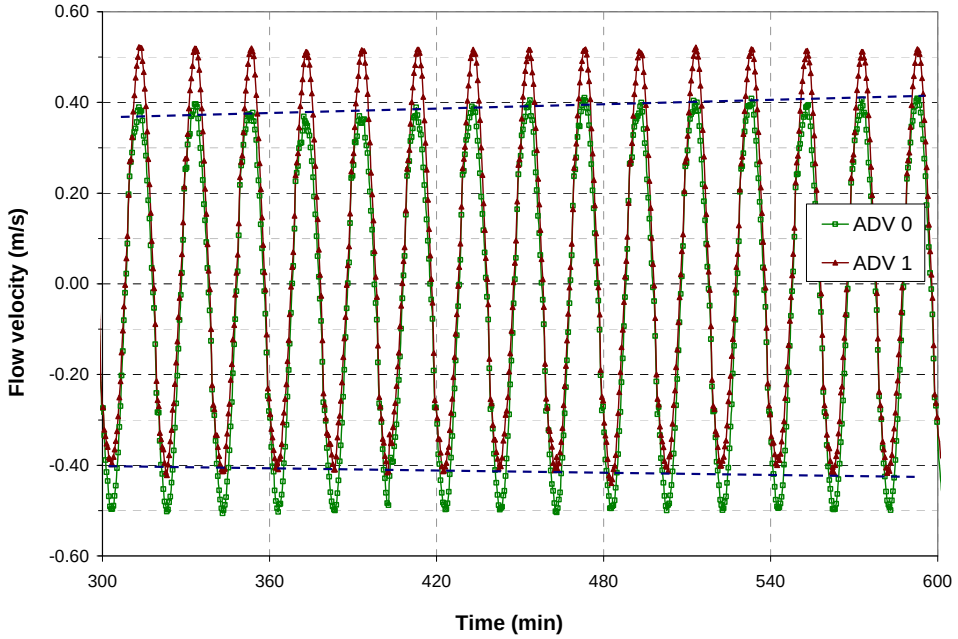


From 4.83 Time history of velocity from5 hr until 10 hr

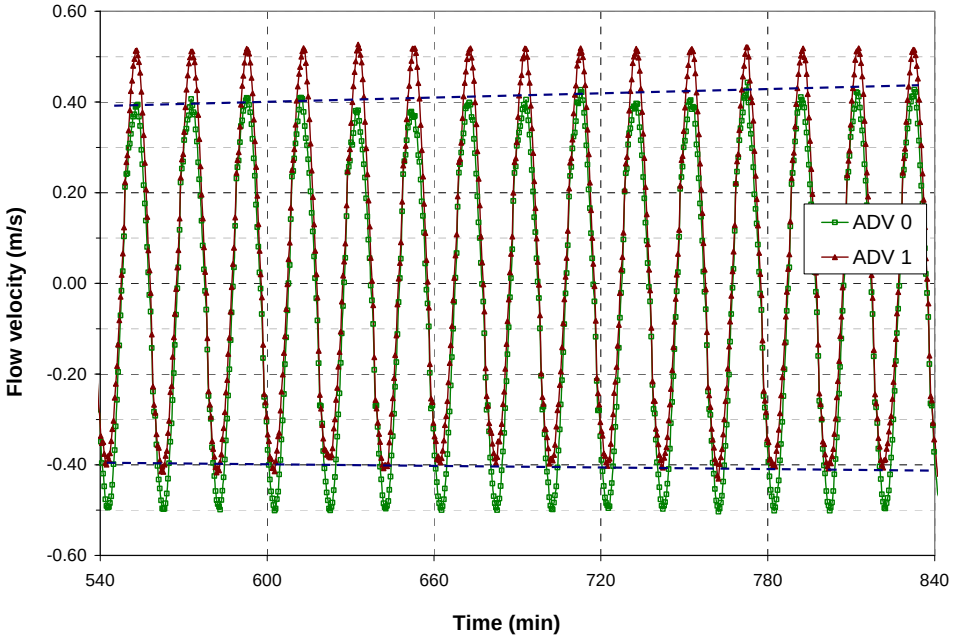


From 4. 84 Time history of velocity from10 hr until 15 hr

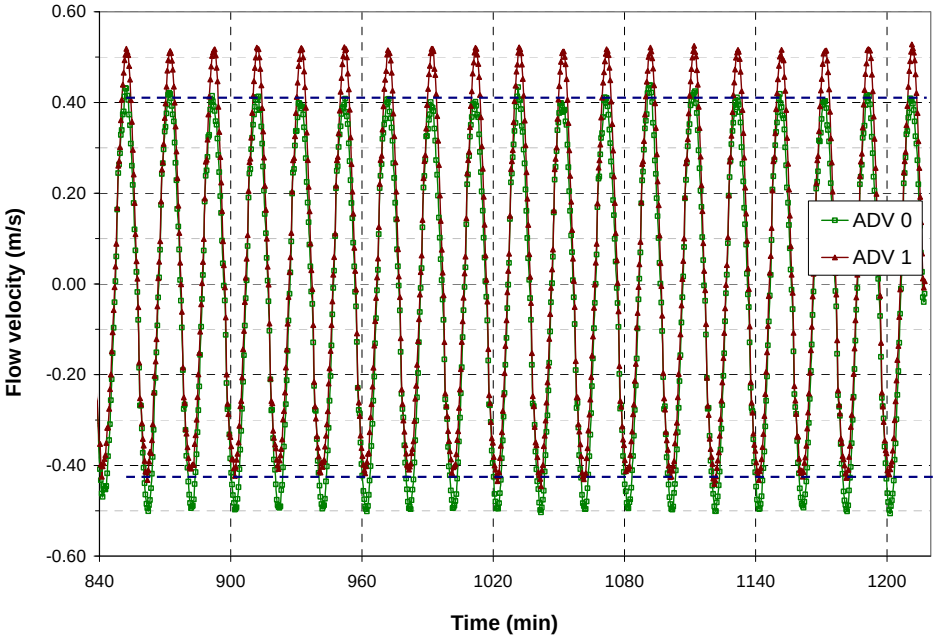


From 4.85 Time history of velocity from15 hr until the end of the test at 20.3 hr

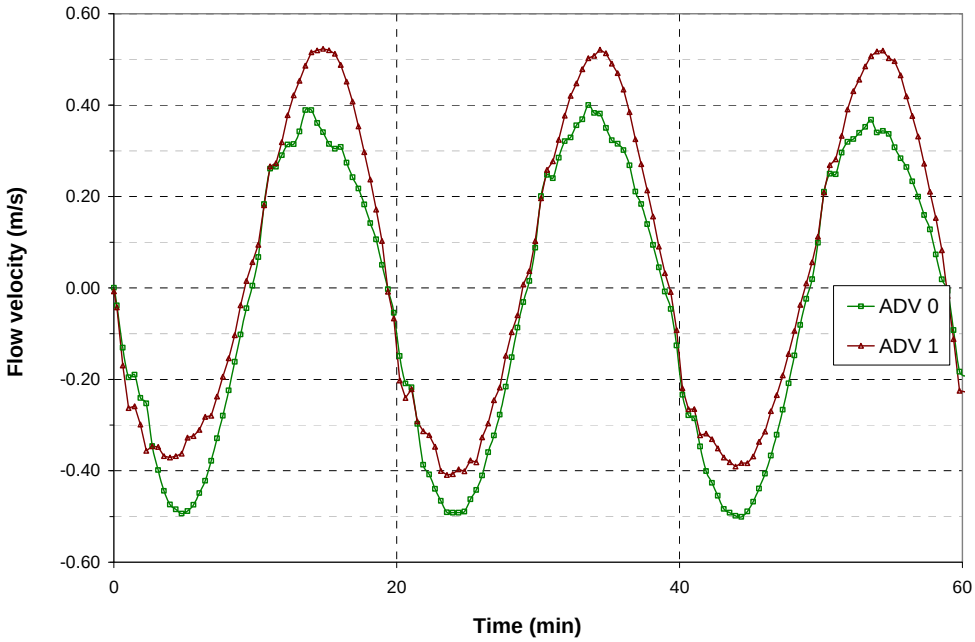


From 4.86 Time history of velocity, detail of the first hour.

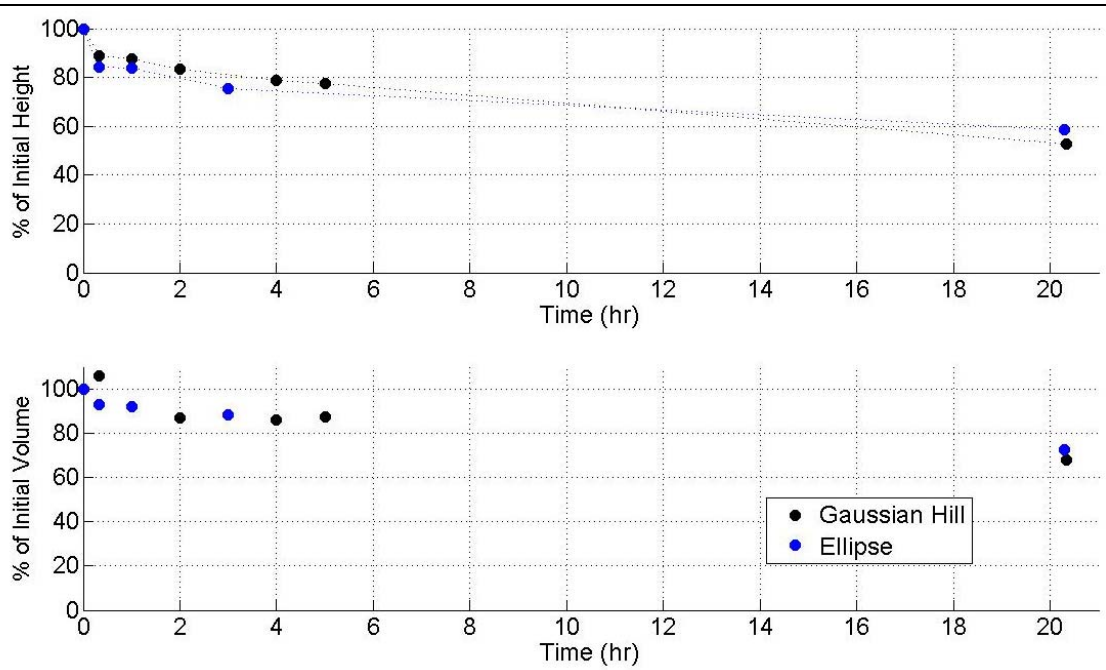


Figure 4.87 Time evolution of the percentage of initial crest height (top), and volume (bottom) for Tests 8 (Gaussian hill, black) and 11 (ellipse, blue).

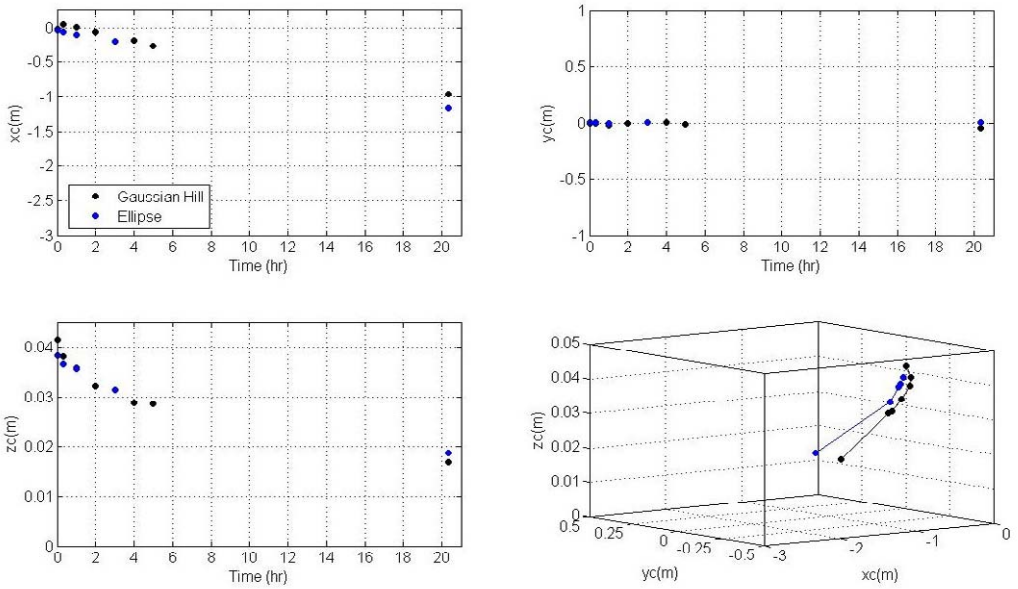


Figure 4.88 Time evolution of the location of the mound's centroid, Tests 8 (black) and 11 (blue)

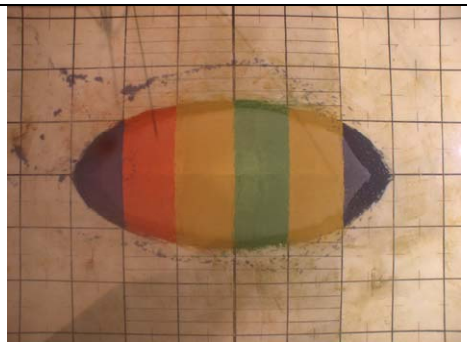

Figure 4.89 Initial profile

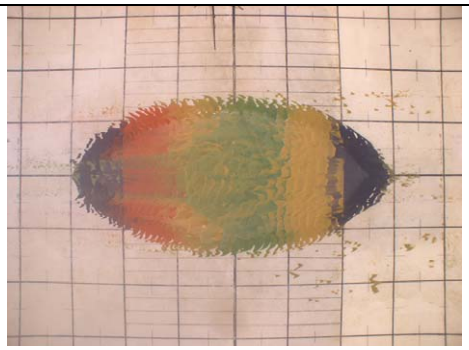

Figure 4.90 Mound at $T_E$= 20 min

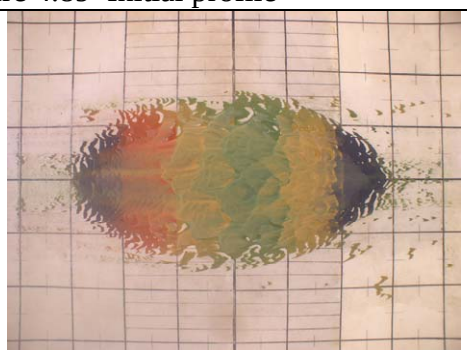

Figure 4.91 Mound at $T_E$= 1 hr

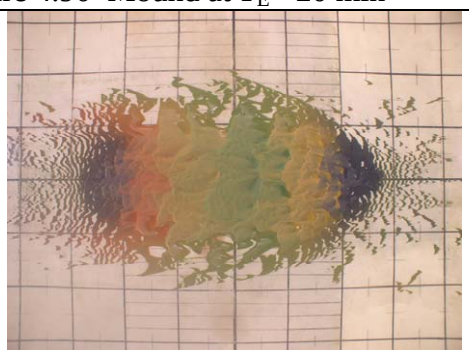

Figure 4.92 Mound at $T_E$= 3 hr

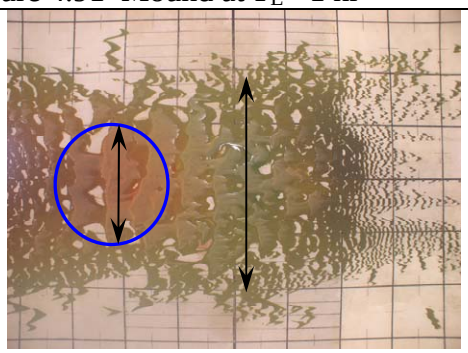

Figure 4.93 Mound at $T_E$= 20.3 hr

Test 11

| **Test 8** | Test 11 |
|---|---|
| 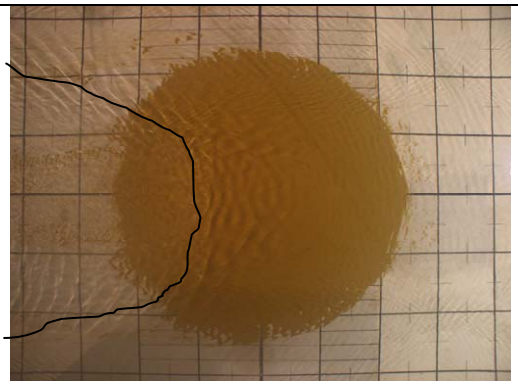 | 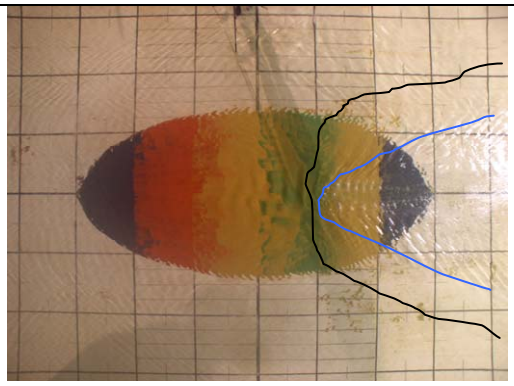 |
| **Figure 4.52** Test 8, mound at $T_E$= 5 min. Line marks the extent of the wake | Figure 4.94 Test 11, mound at $T_E$= 5 min. Line marks the extent of the wake |
| 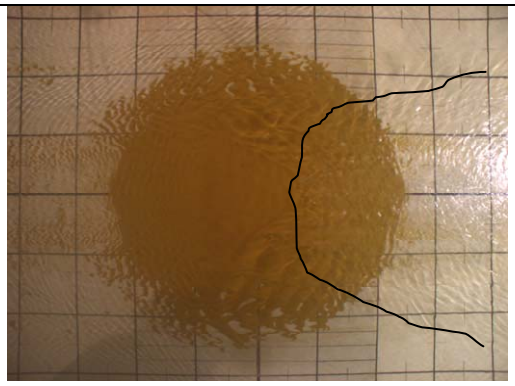 | 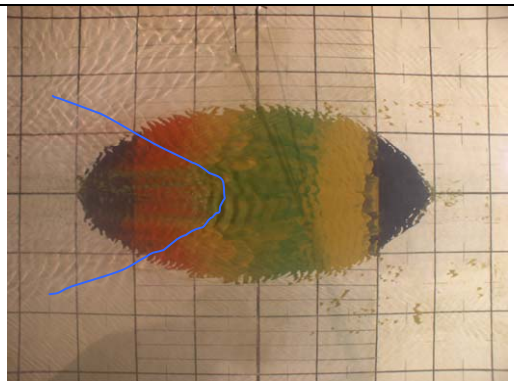 |
| **Figure 4.55** Test 8, mound at $T_E$= 15min. Line marks the extent of the wake | Figure 4.95 Test 11, mound at $T_E$= 15 min. Line marks the extent of the wake |

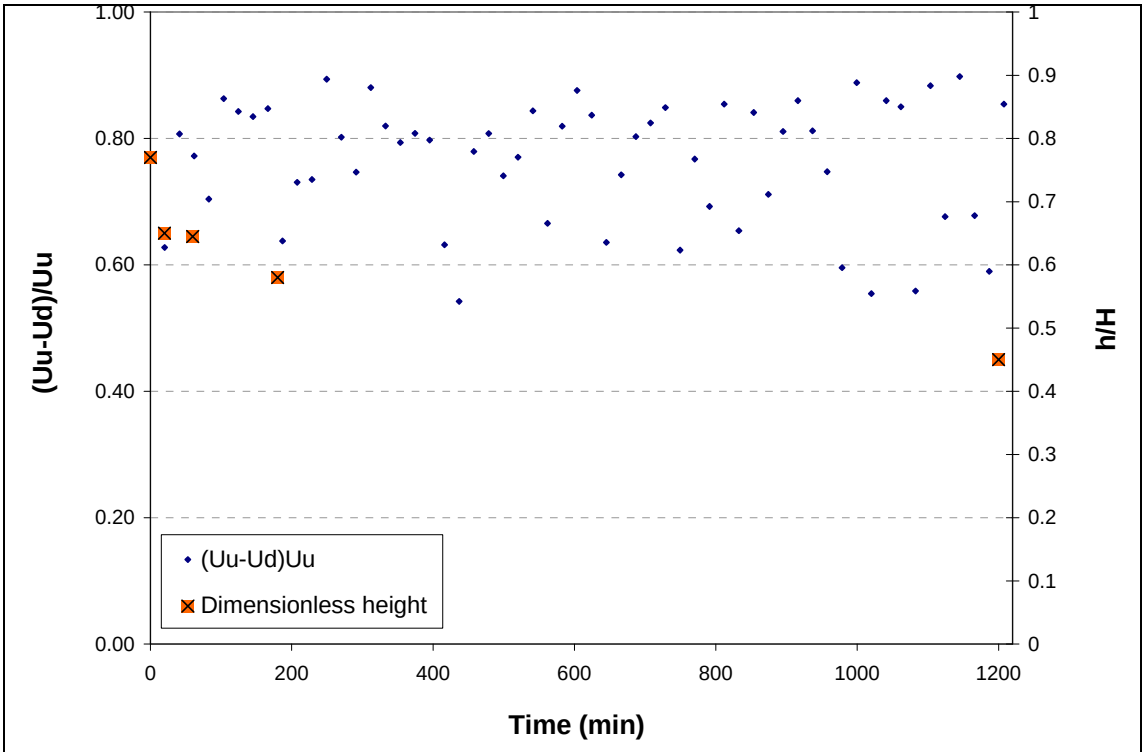


Figure 4.96 Time evolution of crest height and velocity deficit.

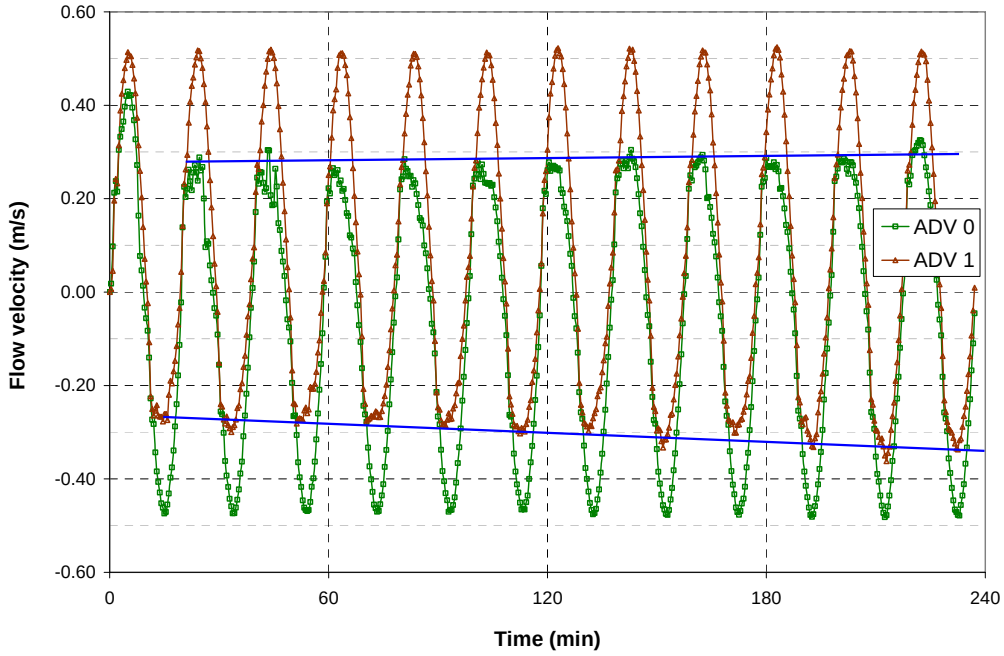


Figure 4.97 Time history of velocity for Test 4, from the start to 4 hr.

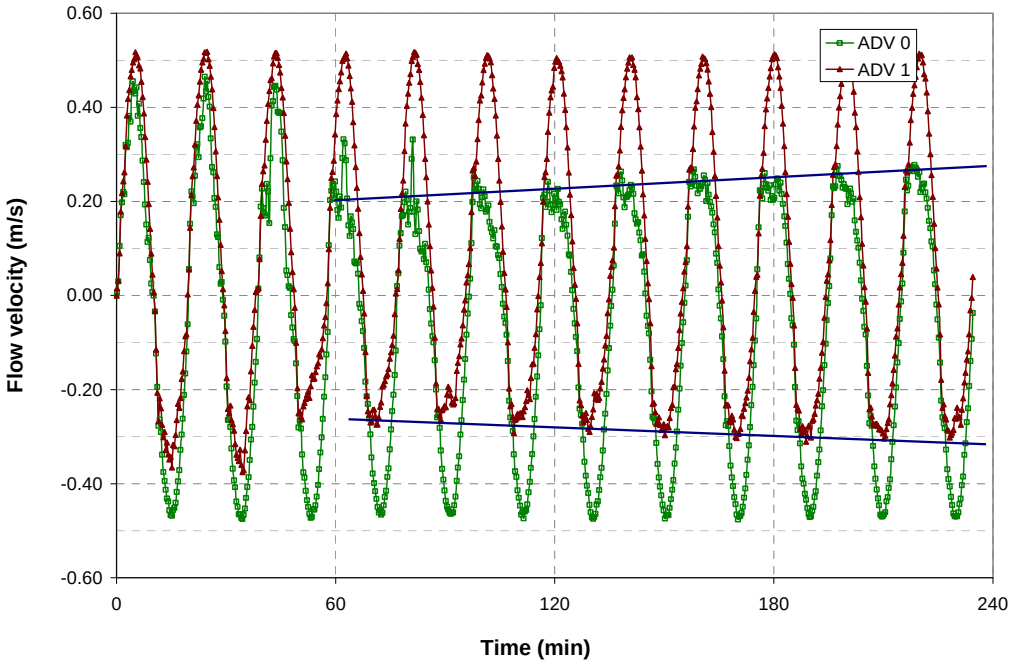


Figure 4. 98 Time history of velocity for Test 3, from the start to 4 hr.

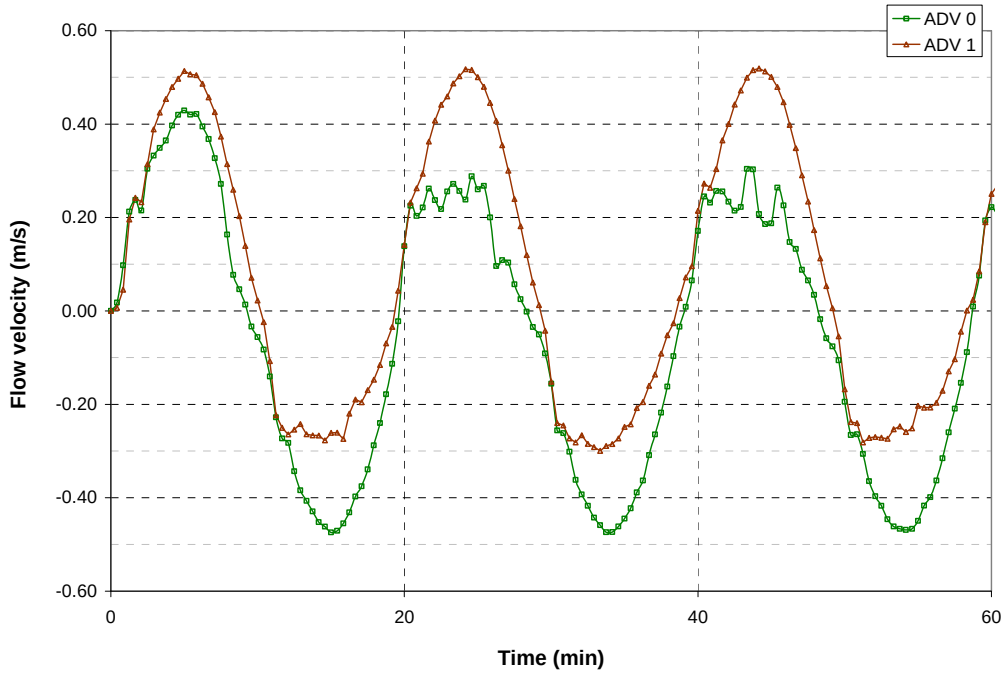


Figure 4.99 Time history of velocity Test 4, detail of the first hour.

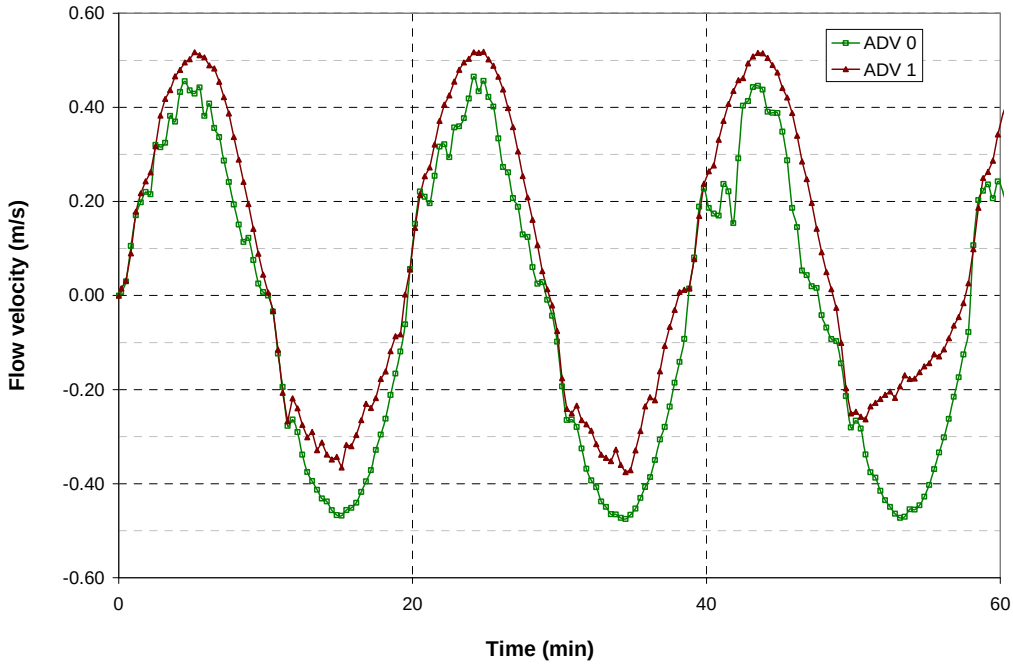


Figure 4.100 Time history of velocity Test 3, detail of the first hour.

Test 4, Surface touching mound (ST)

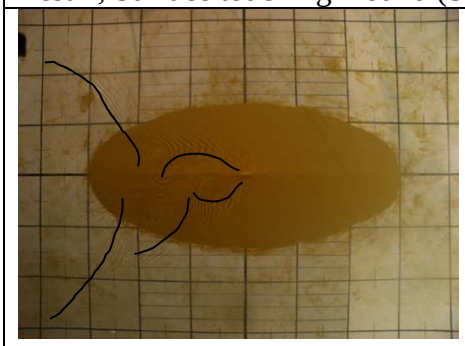

Figure 4.101 $T_E$= 2’ 10’’.
Lines mark wake

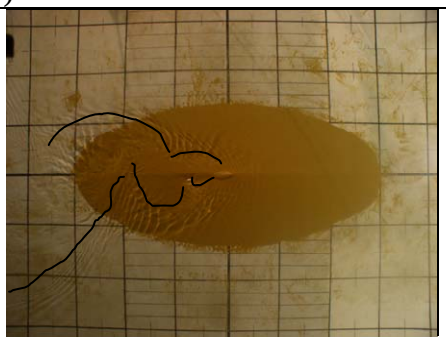

Figure 4.102 $T_E$= 2’ 54’’

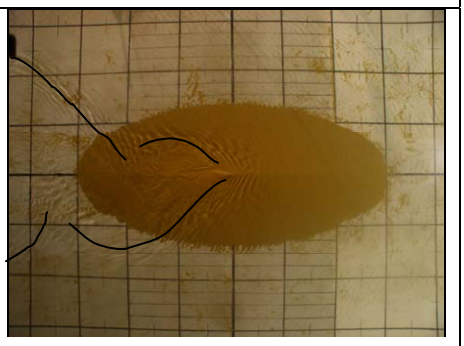

Figure 4.103 $T_E$=3’ 38’’

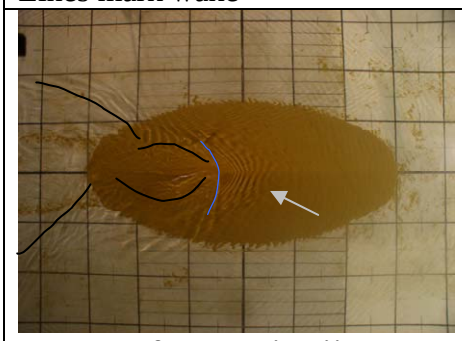

Figure 4.104 $T_E$= 4’ 44’’
Lines mark wake. Arrow points at backwater effect (supercritical flow).

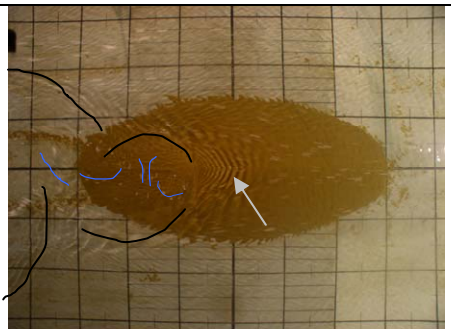

Figure 4.105 $T_E$= 5’ 6’’

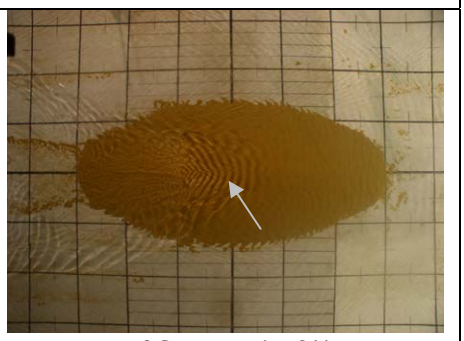

Figure 4.106 $T_E$= 5’ 50’’

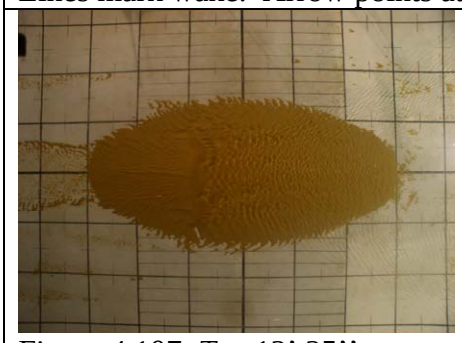

Figure 4.107 $T_E$= 12’ 25’’
Reversed flow, evolution of crest – similar to submerged cases, may be a bit stronger flows

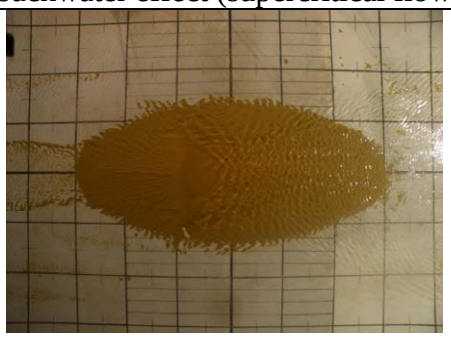

Figure 4.108 $T_E$= 13’ 9’’

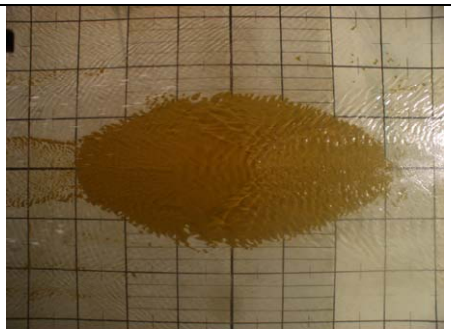

Figure 4.109 $T_E$= 14’ 36’’

Test 3, Surface piercing mound (SP)

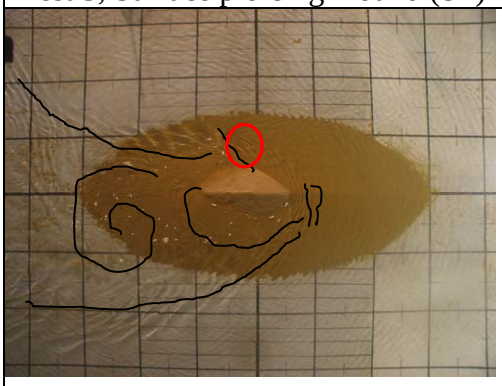

Figure 4.110 $T_E$= 4’ 16’’

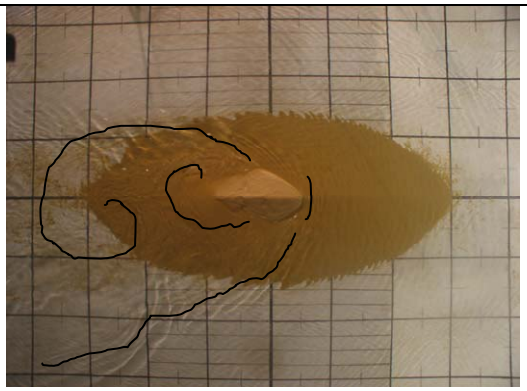

Figure 4.111 $T_E$= 4’ 50’’

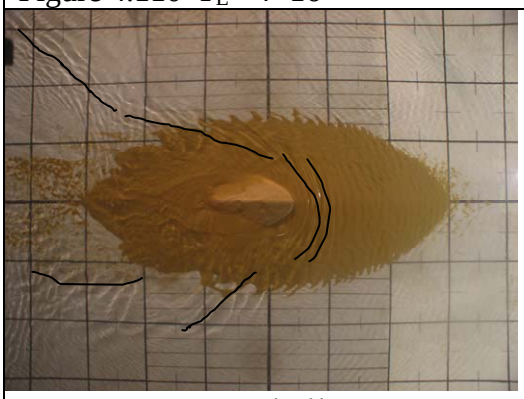

Figure 4.112 $T_E$= 7’ 2’’

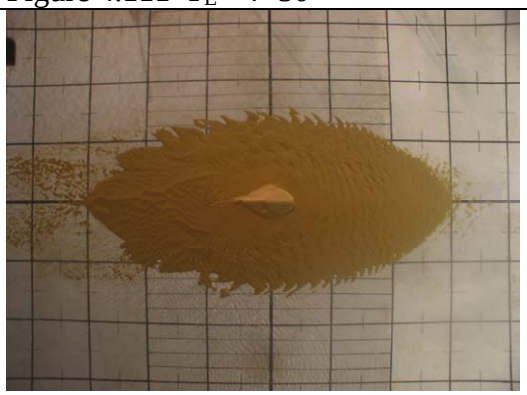

Figure 4.113 $T_E$= 9’ 16’’

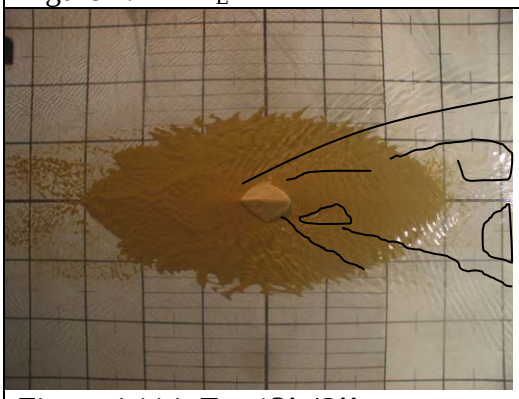

Figure 4.114 $T_E$= 13’ 42’’

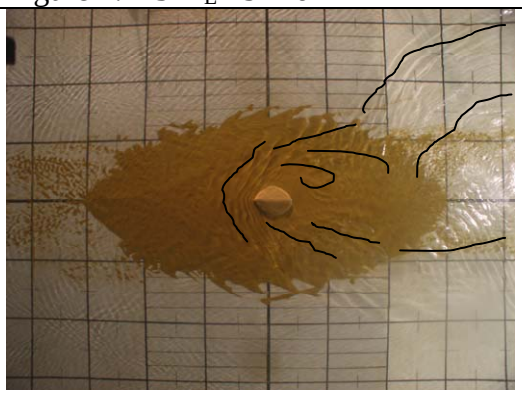

Figure 4.115 $T_E$= 15’ 56’’

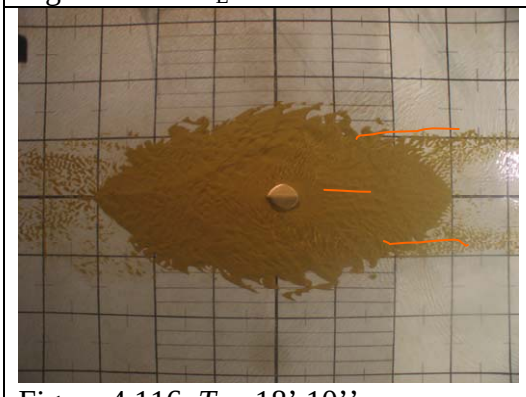

Figure 4.116 $T_E$= 18’ 10’’

Lines mark the wake

| **Test 11**, Submerged (SM) | Test 4, ST | Test 3, SP |
|---|---|---|
| 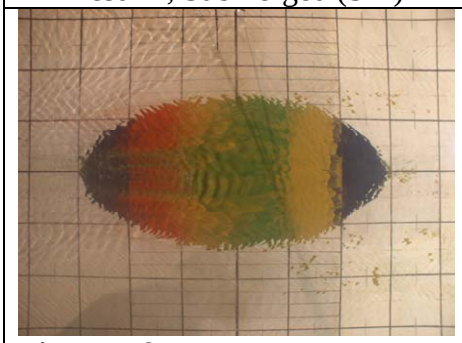 | 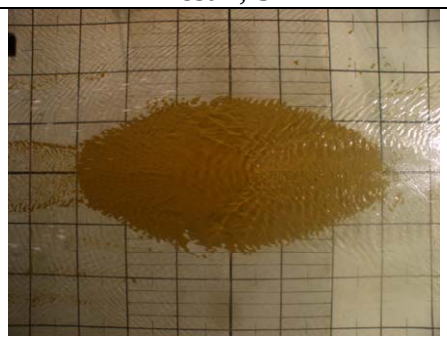 | 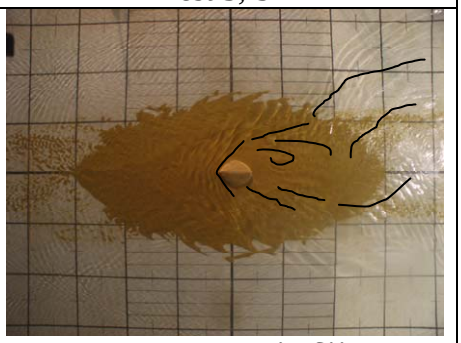 |
| **Figure 4.95** $T_E$= 15 min | Figure 4.117 $T_E$= 15 min | Figure 4.115 $T_E$= 15’ 56’’ |
| 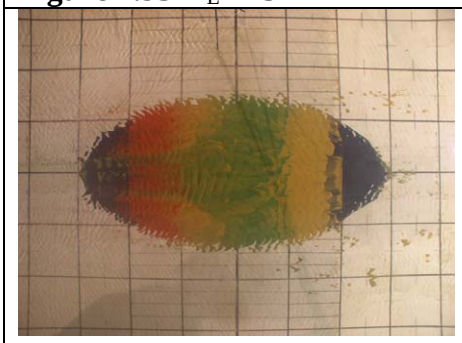 | 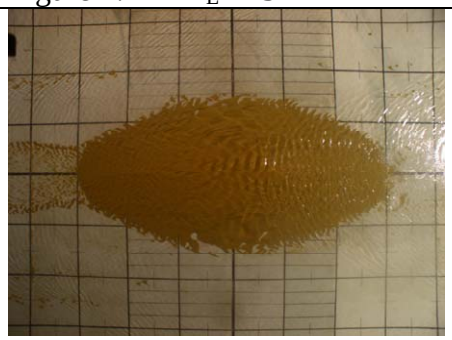 | 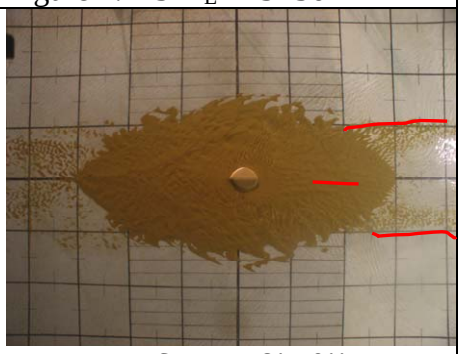 |
| Figure 4.118 $T_E$= 17 min | Figure 4.119 $T_E$= 17 min | Figure 4.116 $T_E$= 18’ 10’’ |
| Comparison of wake strength for submerged (left), surface touching (centre) and surface piercing (right) mounds | | |

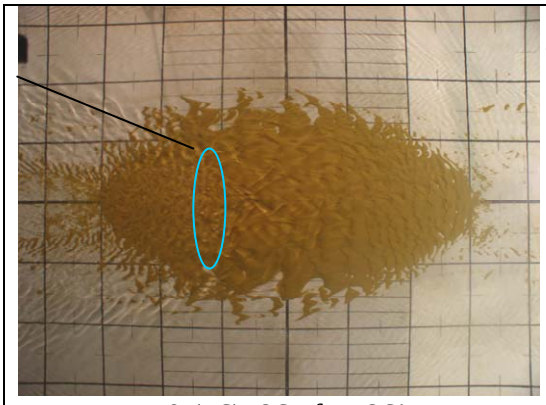

Figure 4.120 (26)c86 after 86’ T4

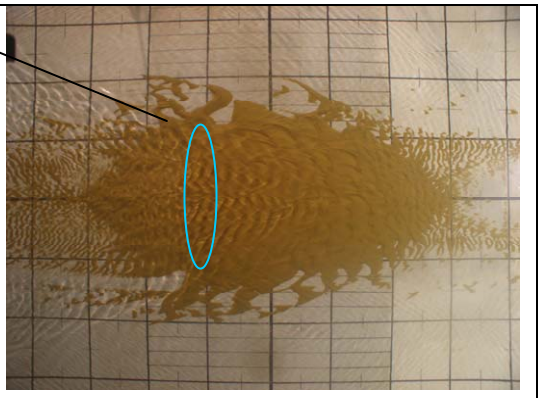

Figure 4.121 (S11) after 86’ Test 3

| Test 11, SM | Test 4, ST | Test 3, SP |
|---|---|---|
| 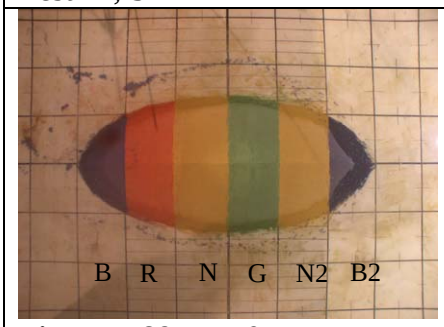  | 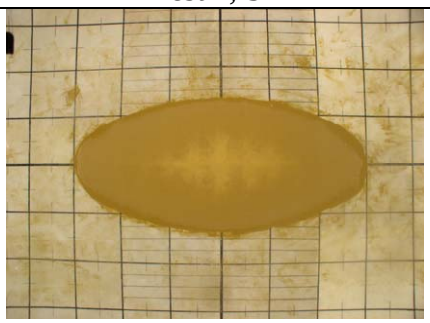 | 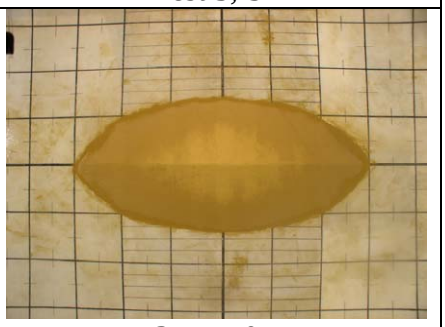 |
| **Figure 4.89** $T_E$= 0 | Figure 4.122 $T_E$= 0 | Figure 4.123 $T_E$= 0 |

These images are shown to present the initial stage of the mounds in Tests 3, 4 and 11
(continues…)

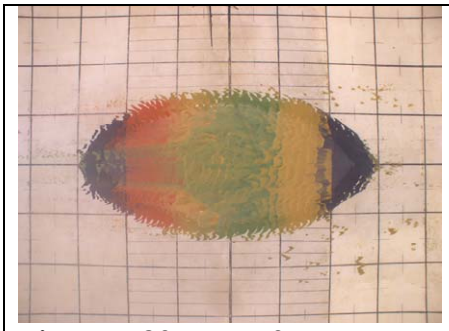

**Figure 4.90** $T_E$= 20 min

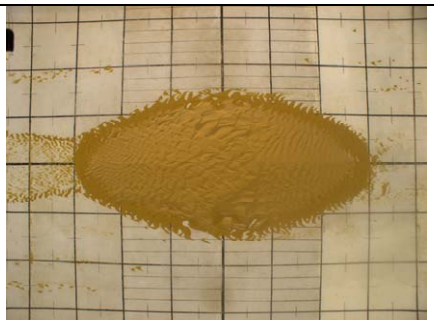

Figure 4.124 $T_E$= 20 min

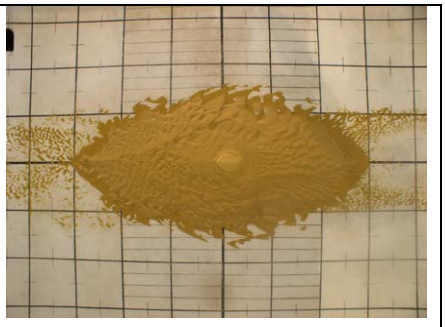

Figure 4.125 $T_E$= 20 min

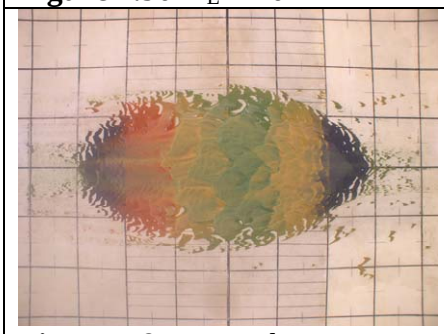

**Figure 4.91** $T_E$= 1 hr

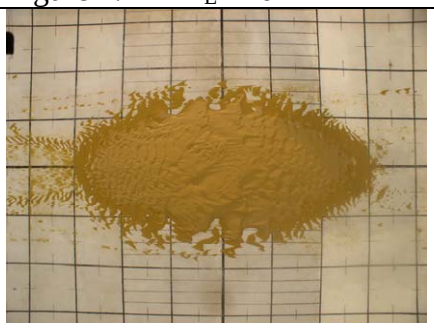

Figure 4.126 $T_E$= 1 hr

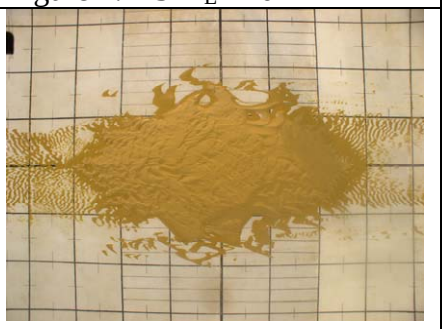

Figure 4.127 $T_E$= 1 hr

Cycle 6

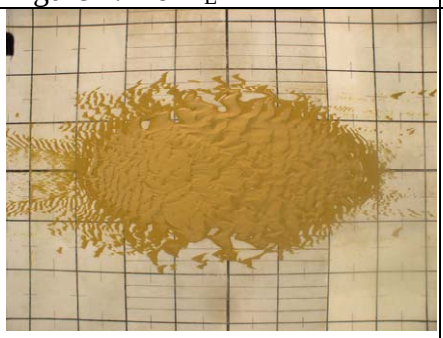

Figure 4.128 $T_E$= 2 hr

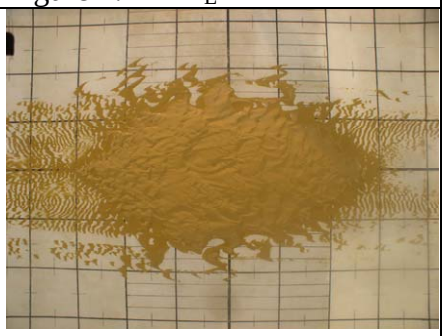

Figure 4.129 $T_E$= 2 hr

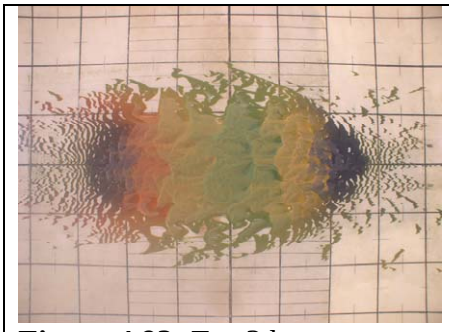

**Figure 4.92** $T_E$= 3 hr

Cycle 9

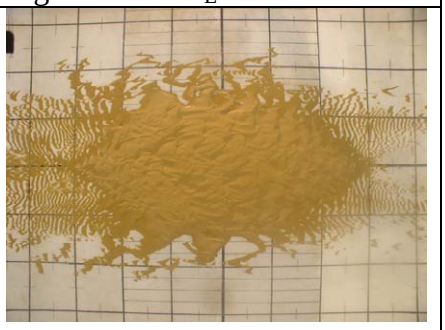

Figure 4.130 $T_E$= 3 hr

Cycle 12

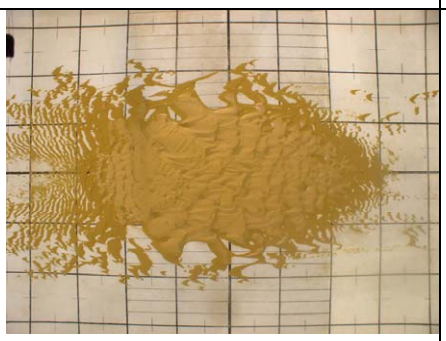

Figure 4.131 $T_E$= 4 hr

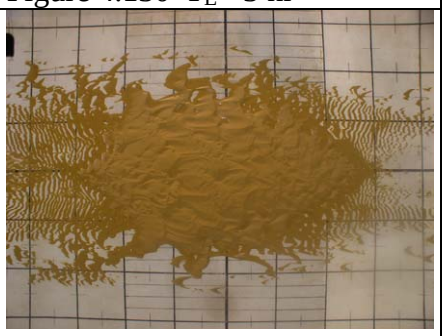

Figure 4.132 $T_E$= 4 hr

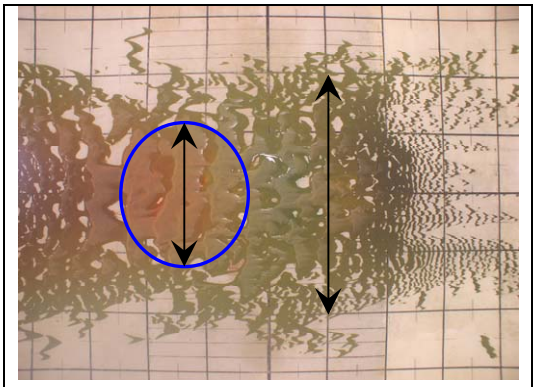

**Figure 4.93** $T_E$= 20.3 hr

Last cycle

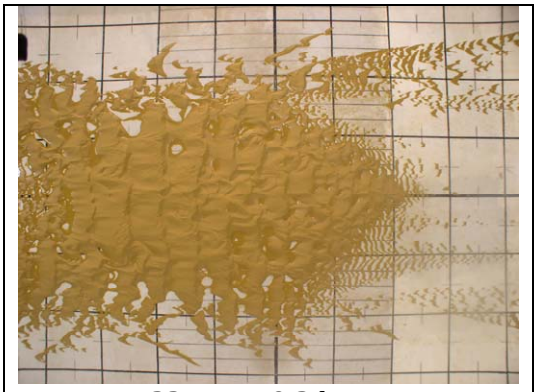

Figure 4.133 $T_E$= 19.3 hr

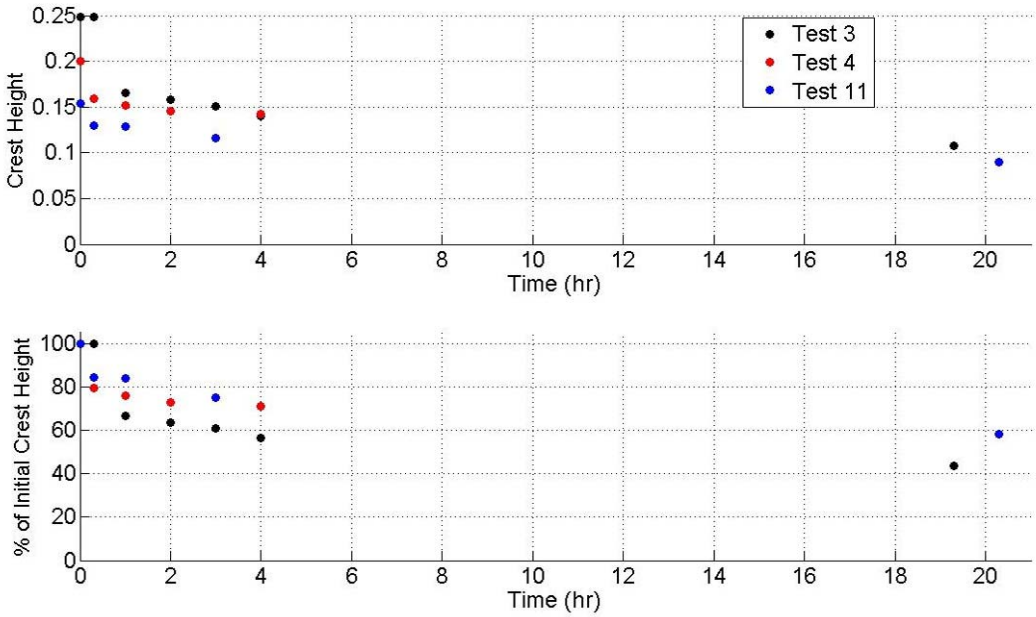


Figure 4.134 Time evolution of the crest height (top), and percentage of initial crest height (bottom). Test 3 (SP), Test 4 (ST) and Test 11 (SM)

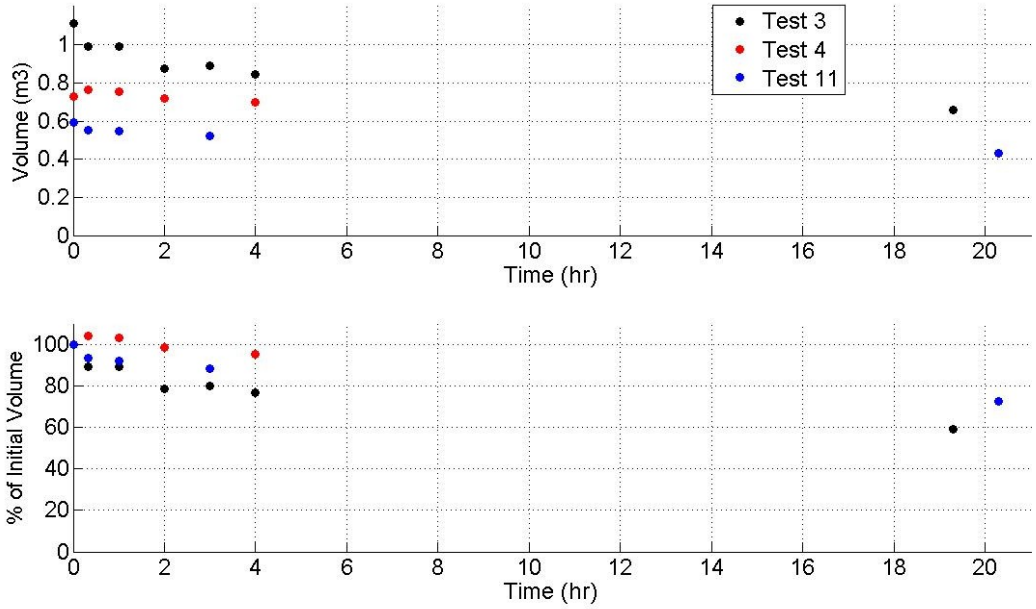


Figure 4.135 Time evolution of the volume (top) and % of initial volume (bottom).

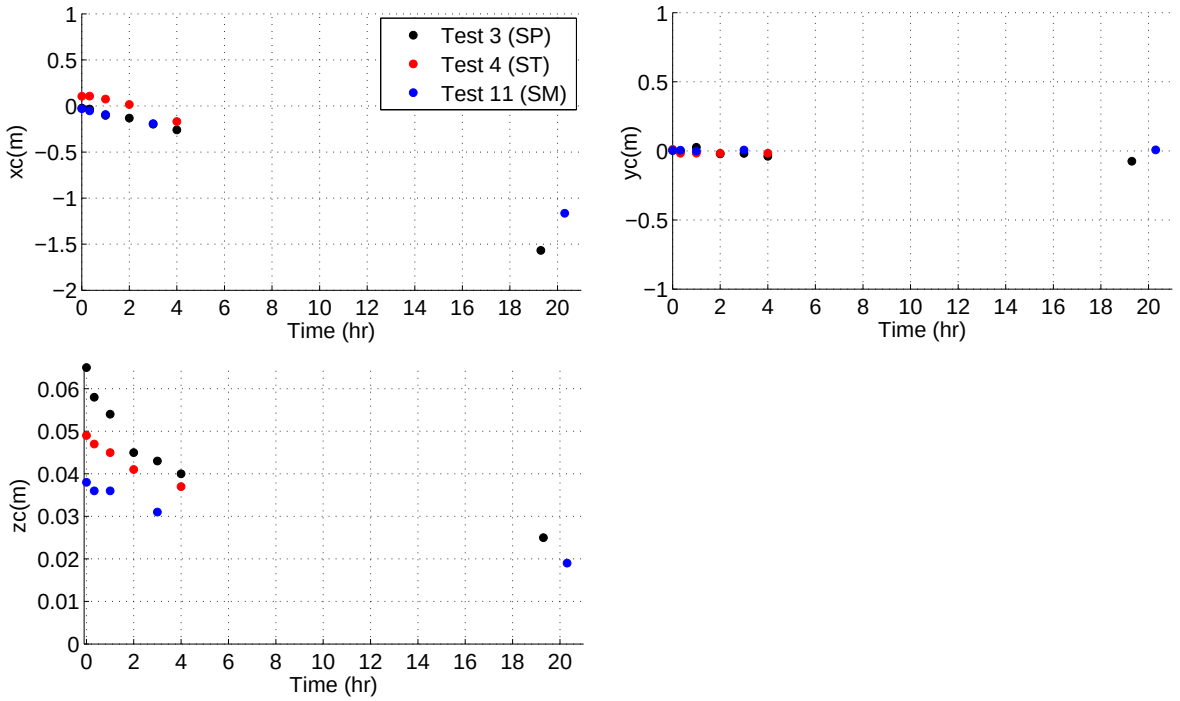


Figure 4.136 Time evolution of the location of the mound's centroid during Tests 3, 4 and 11

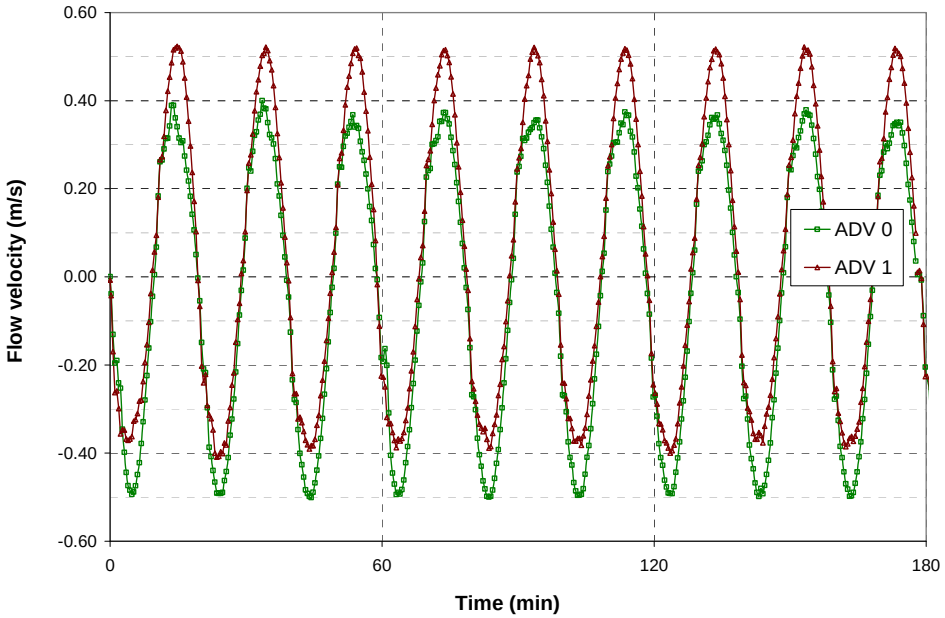


Figure 4.137 Time history of velocity for Test 11 (0 to 3 hr).

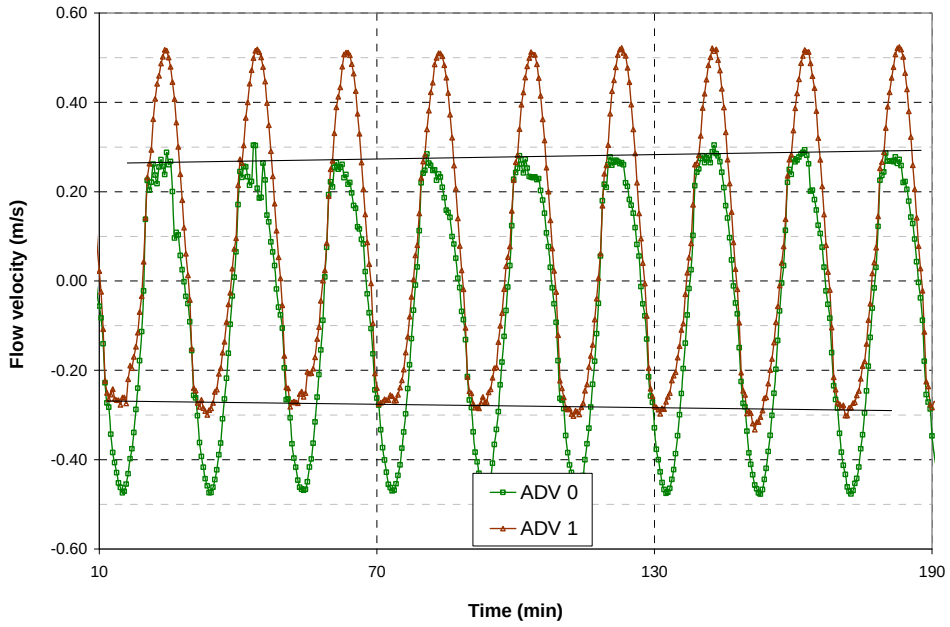


Figure 4.138 Time history of velocity for Test 4 (ST), 3 hours from the time the crest became submerged

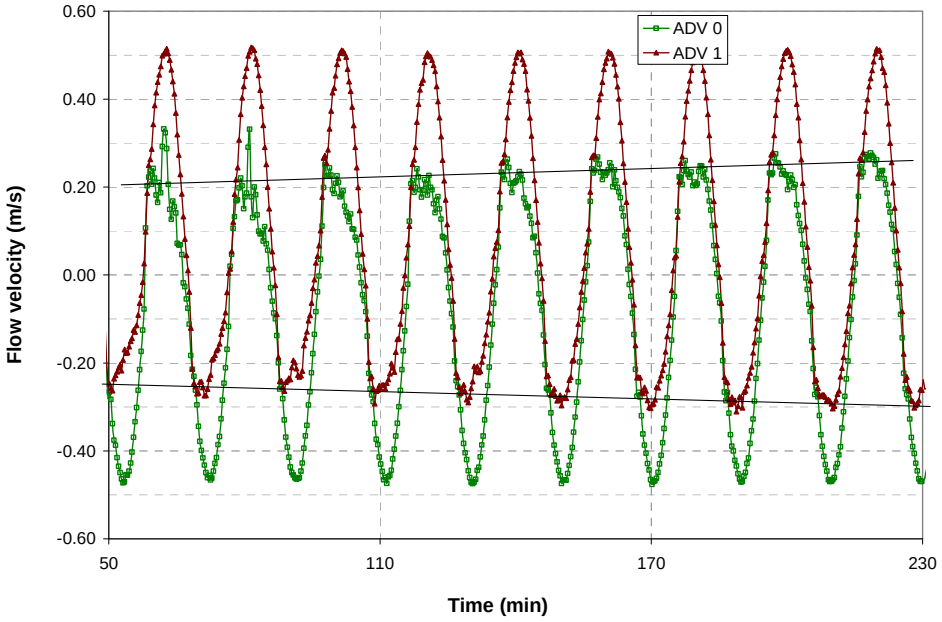


Figure 4.139 Time history of velocity for Test 3 (SP) the 3 hours from the time the crest became submerged

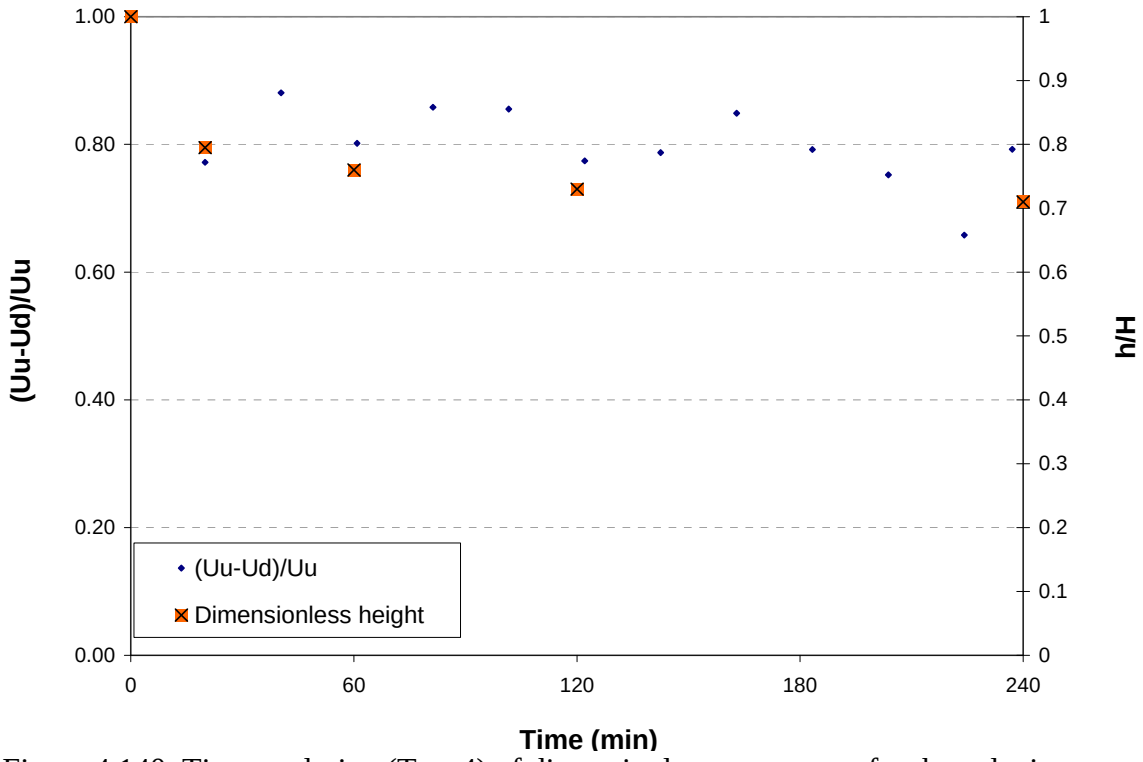


Figure 4.140 Time evolution (Test 4) of dimensionless parameters for the velocity deficit and mound crest height

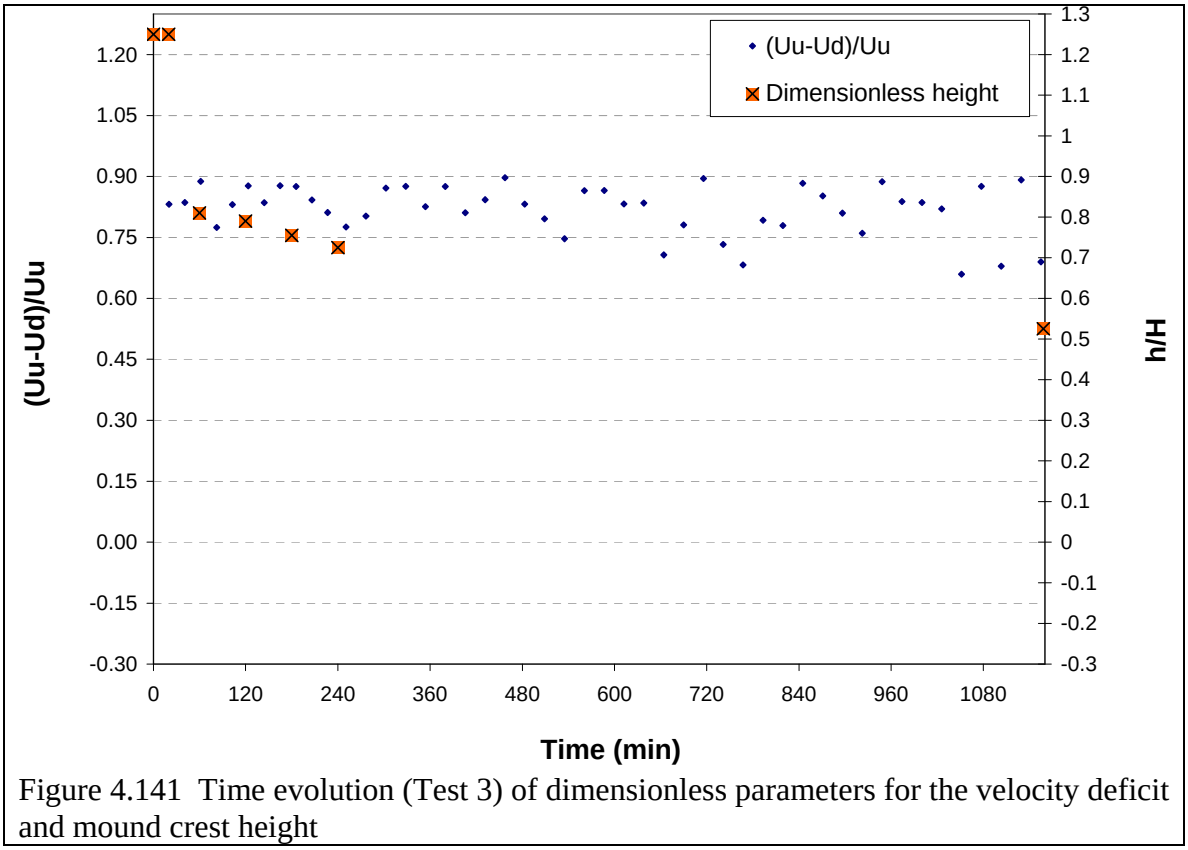


Figure 4.141 Time evolution (Test 3) of dimensionless parameters for the velocity deficit and mound crest height

.

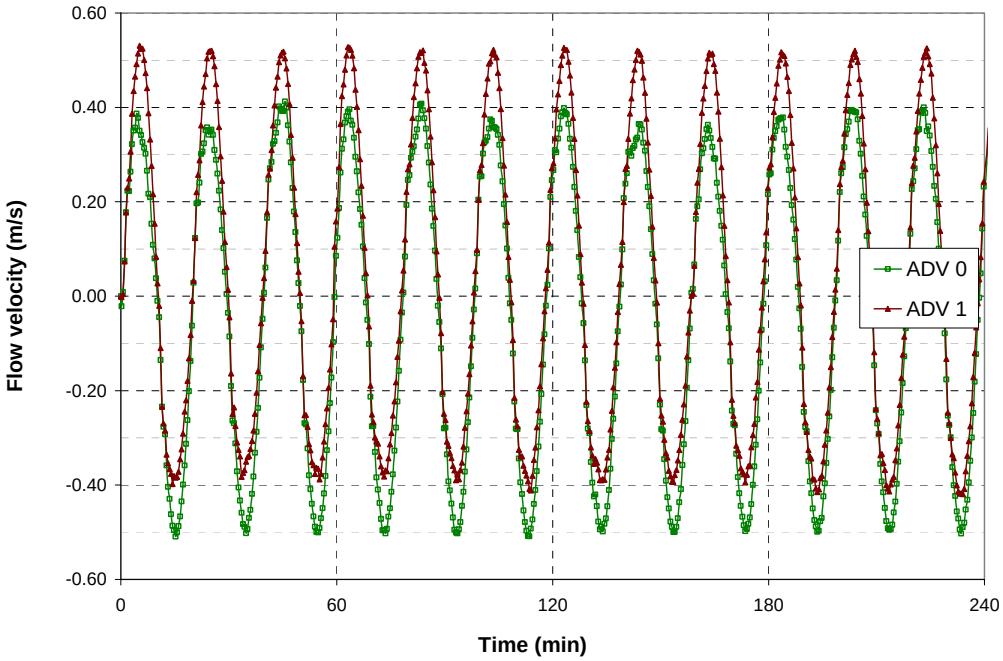


Figure 4.142 Time history of flow velocity during the first 4 hr of Test 12

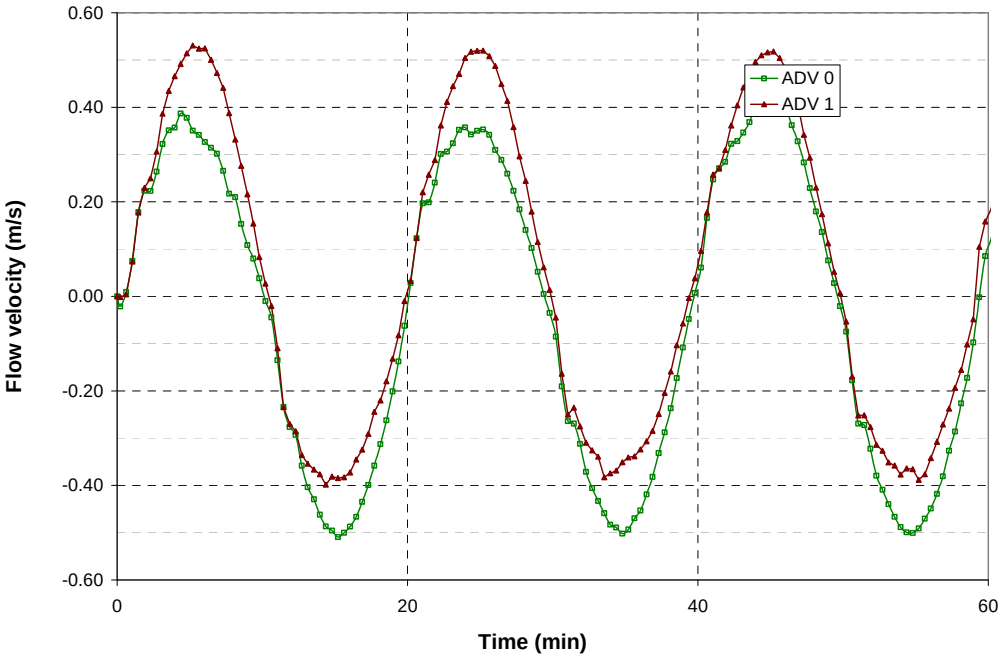


Figure 4.143 Detail of the flow velocity time history for the 1st hour of Test 12

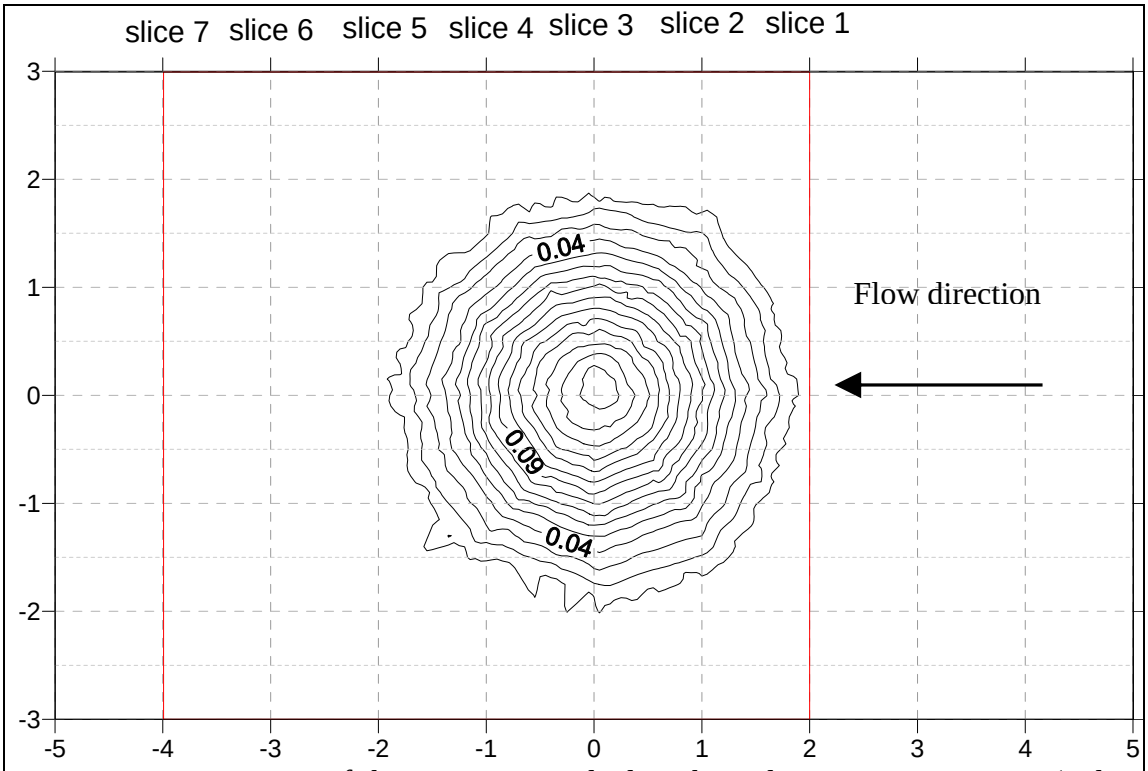


Figure 4.144 Diagram of the sections to calculate the sediment transport rates (red – Slices 1 and 7 – marked as horizontal grid lines, the 0.5 m segments of the slices for extraction of model results).

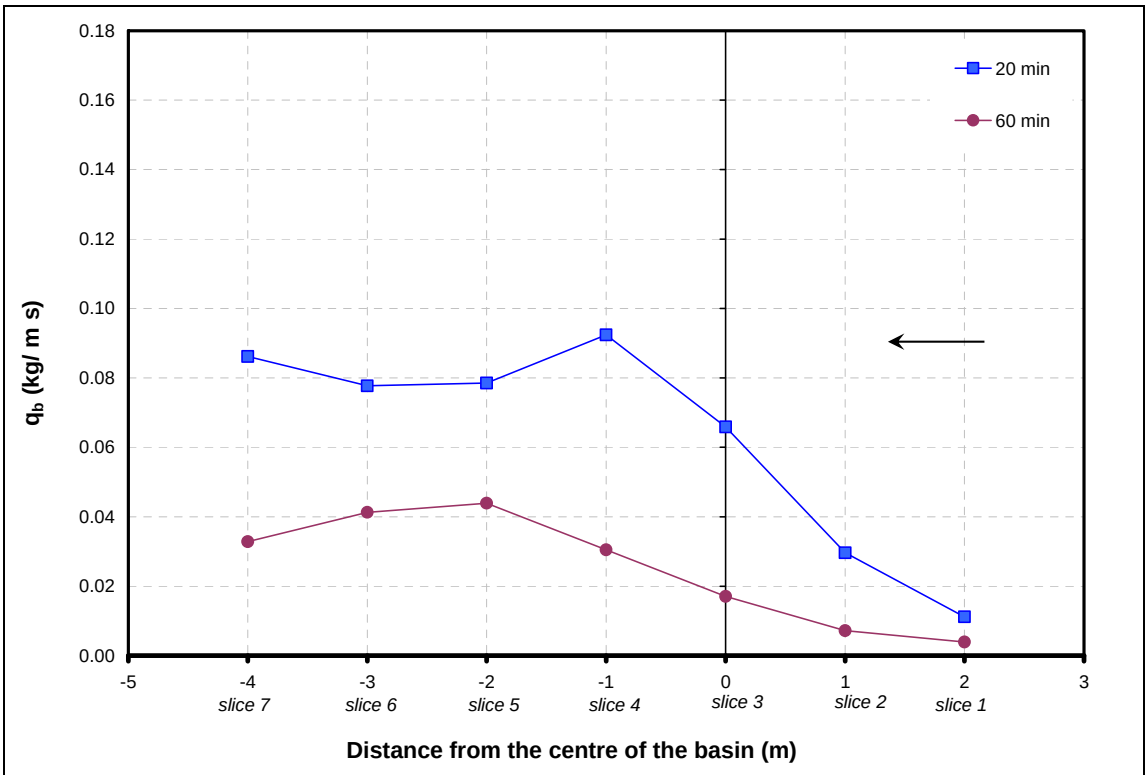


Figure 4.145a Sediment transport rates estimated through slices in Test 13.

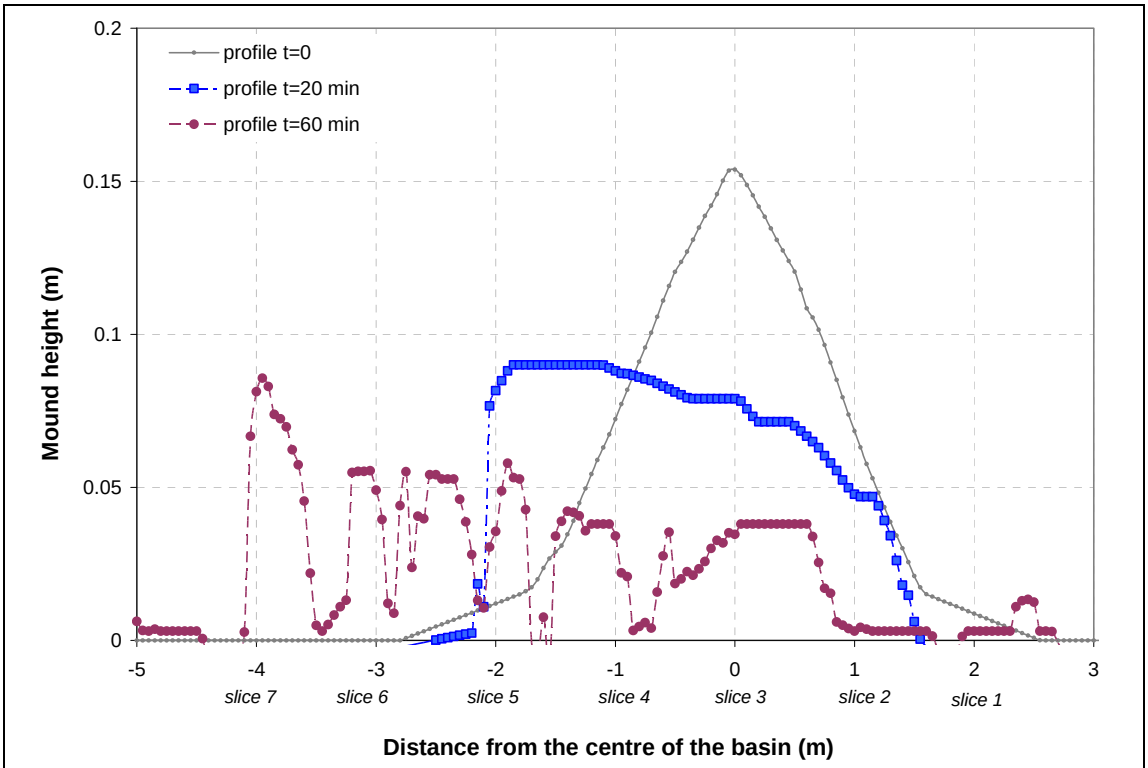


Figure 4.145b Evolution of longitudinal cross sections of Test 13.

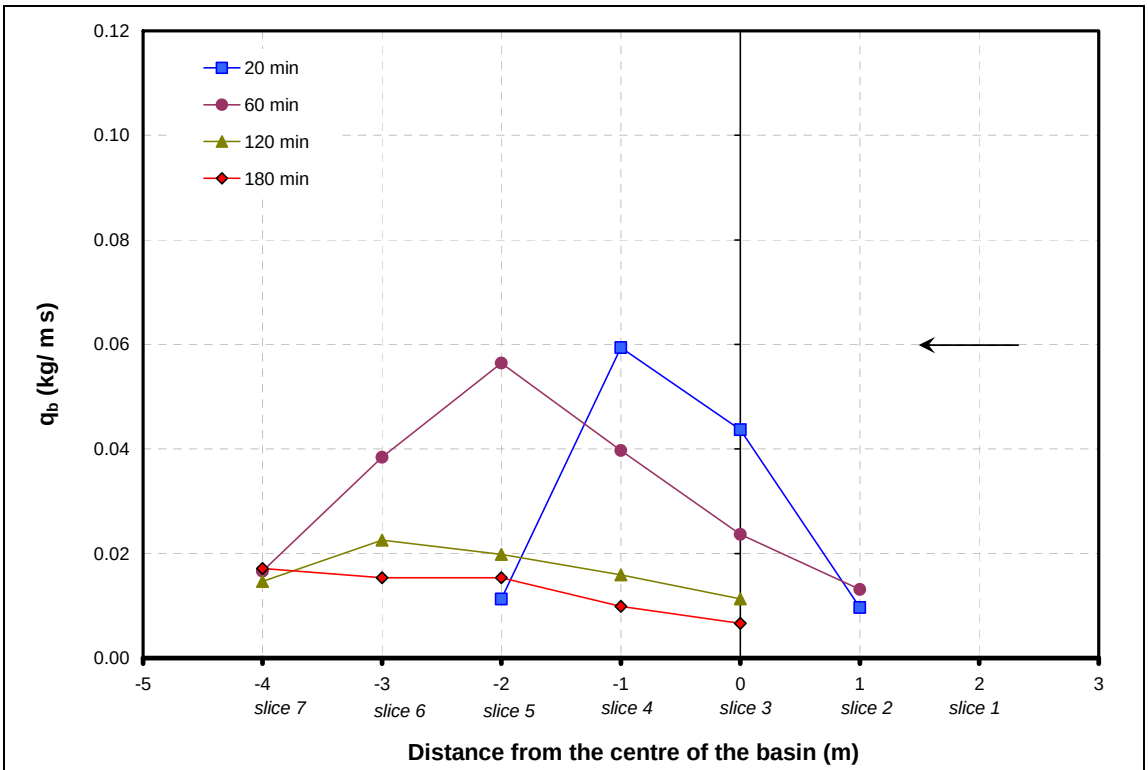


Figure 4.146a Sediment transport rates estimated through slices in Test 9.

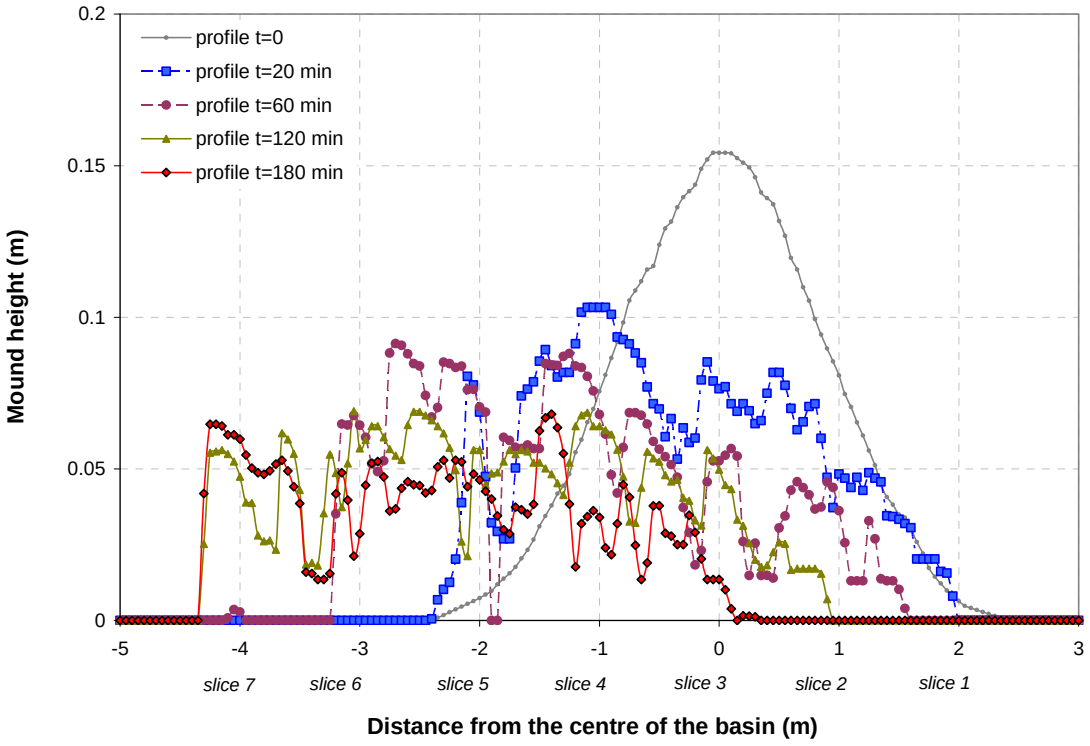


Figure 4.146b Evolution of longitudinal cross sections of Test 9.

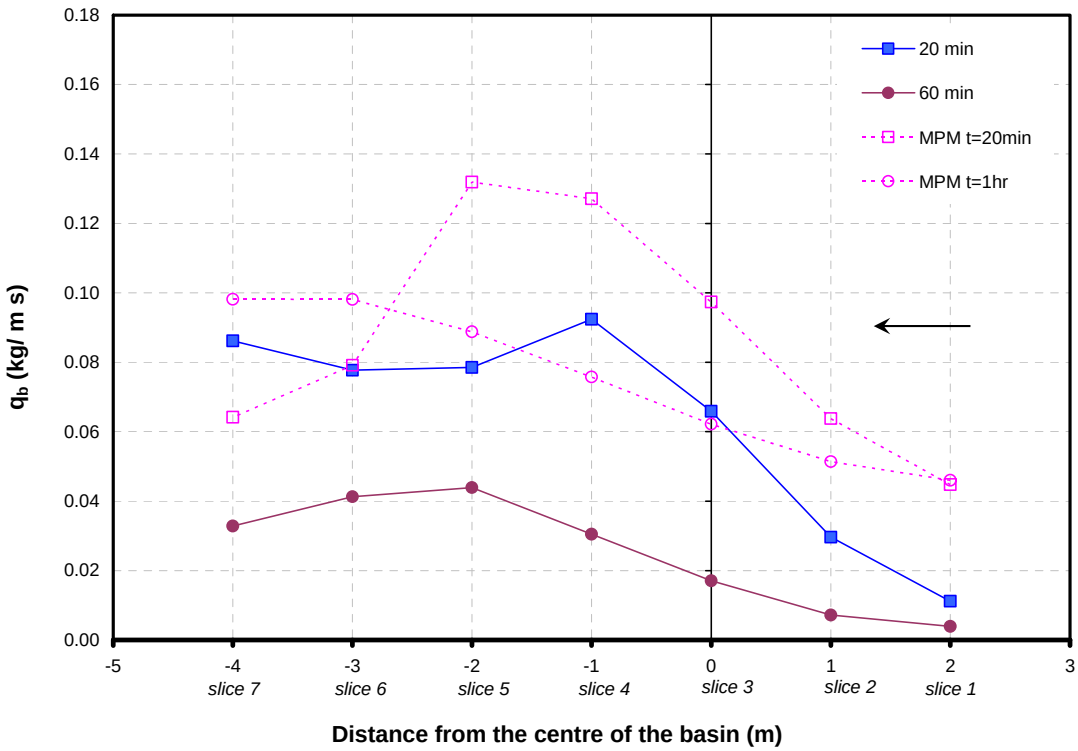


Figure 4.147 Calculated sediment transport rates from Test 13 and predictions using Meyer-Peter-Müller's method.

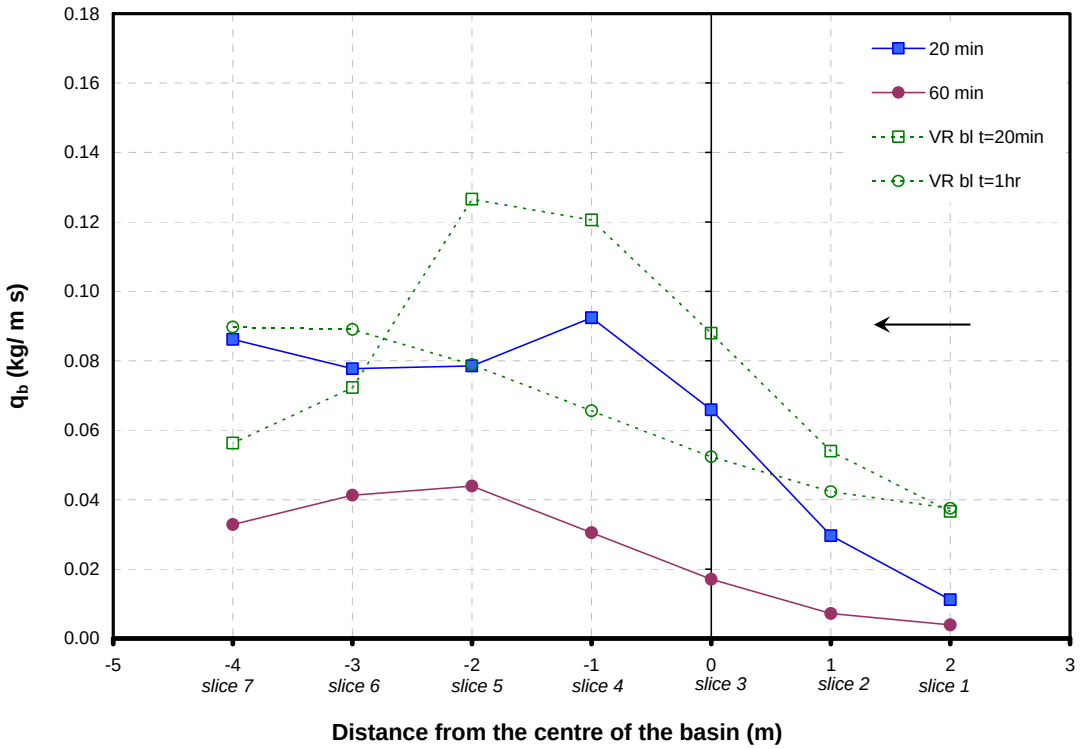


Figure 4.148 Calculated sediment transport rates from Test 13 and predictions using Van Rijn's method.

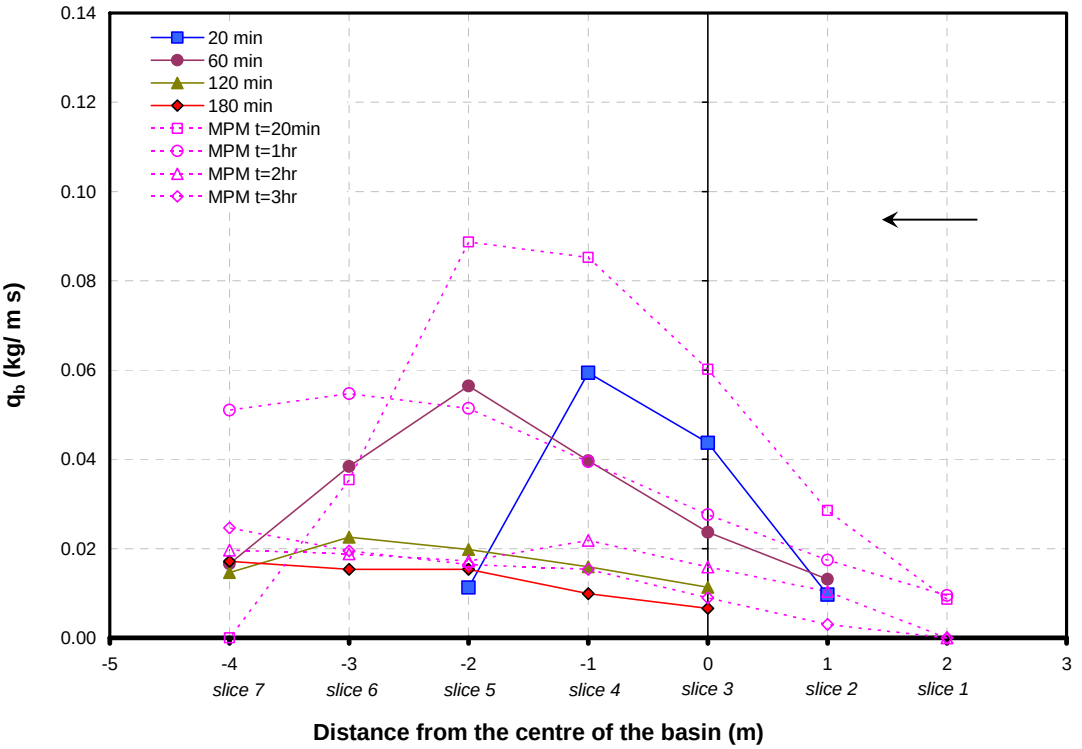


Figure 4.149 Calculated sediment transport rates from Test 9 and predictions using Meyer-Peter-Müller's method.

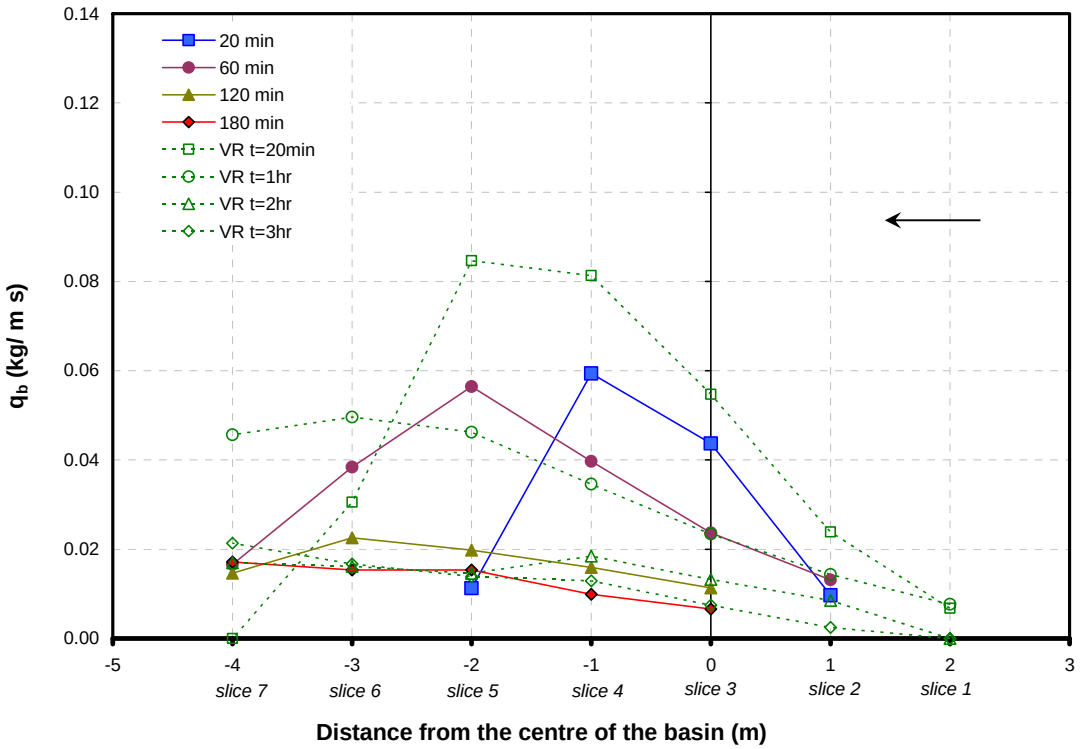


Figure 4.150 Calculated sediment transport rates from Test 9 and predictions using Van Rijn's method.

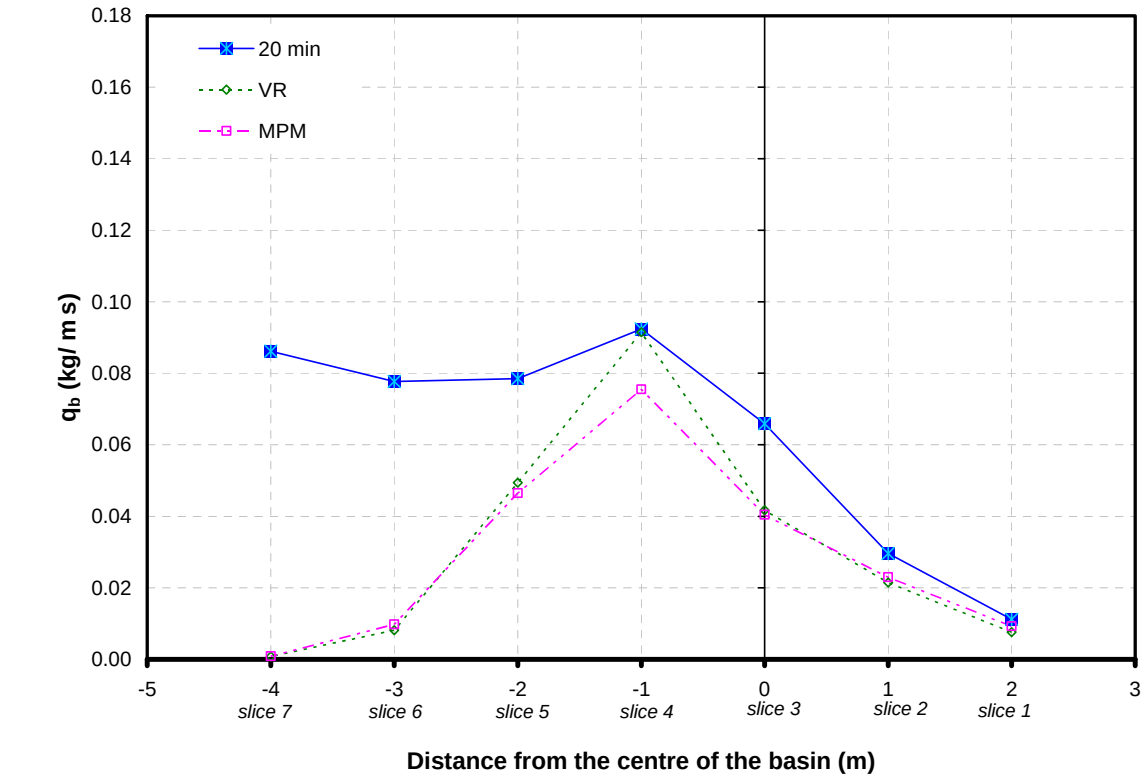


Figure 4.151 Calculated sediment transport rates from Test 13 and predictions using velocity estimated from float tracks (16 min) and water depths from cross sections after 20 min. Note scale in *y*-axis.

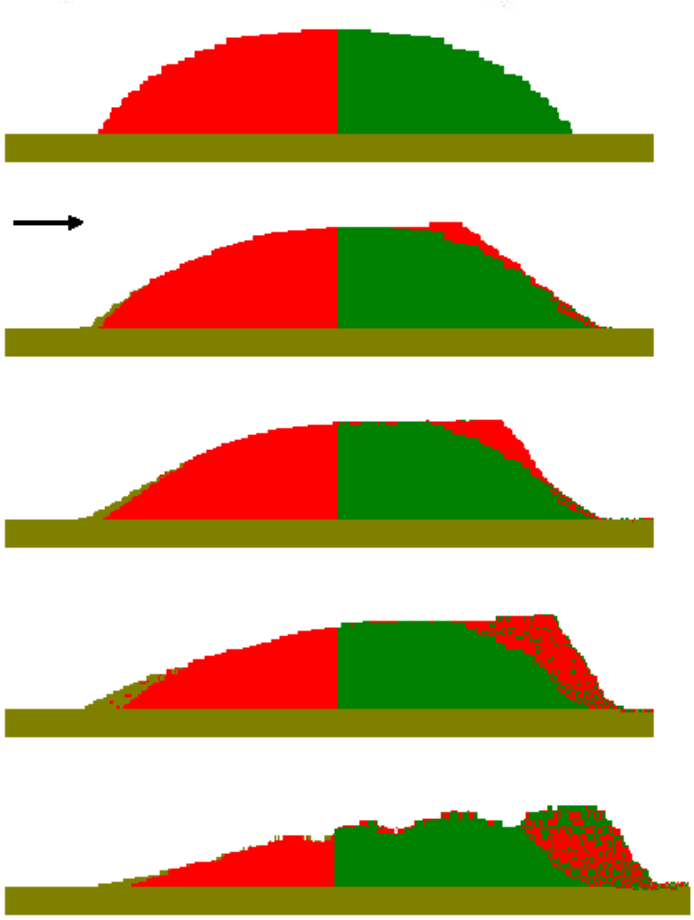

Figure 4.152 Schematic of sand movement in steady flow, initial mound (top), flow from the left (similar evolution to Test 13, mound over a mobile bed).

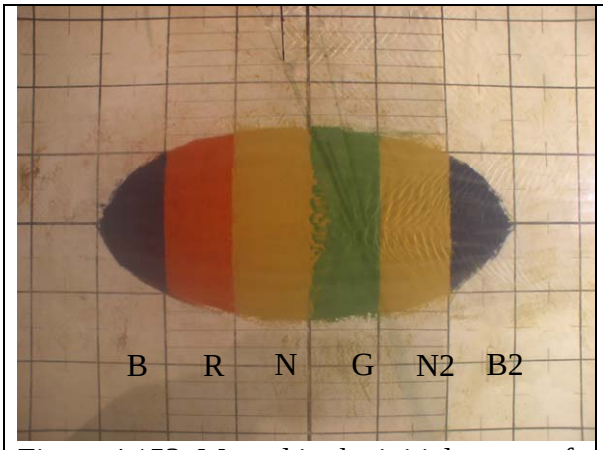


Figure 4.153 Mound in the initial stages of the Test 11

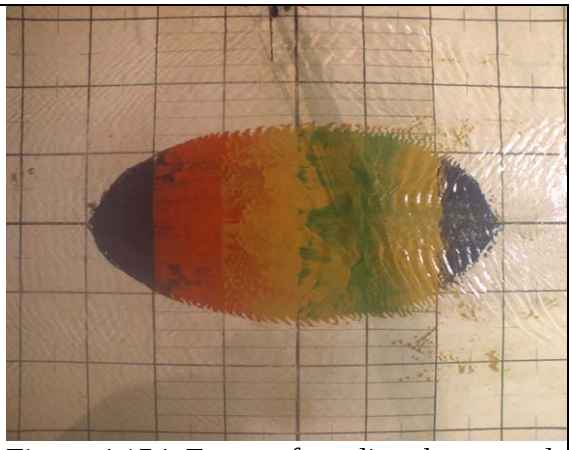

Figure 4.154 Free surface disturbance and wake generation (T 11)

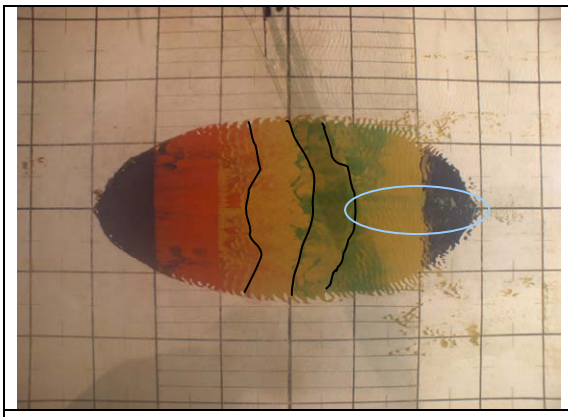

Test 11

Figure 4.155 Black lines mark migration of coloured sand. Arrows show the extent of the migration of the sand over the downstream layer. Blue ellipse shows trails of the sand from the crest.

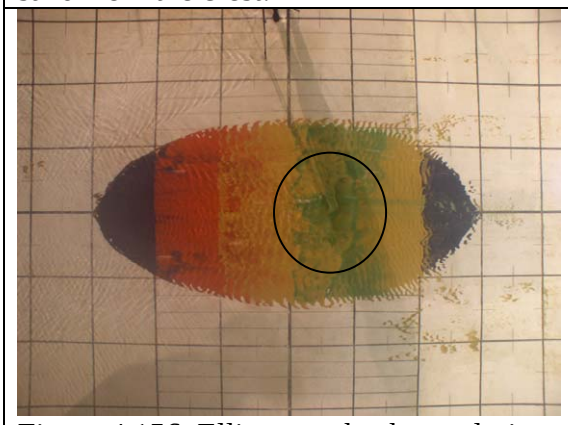

Figure 4.156 Ellipse marks the evolution of the wake as the flow reverses. Reversal of the ripple crests.

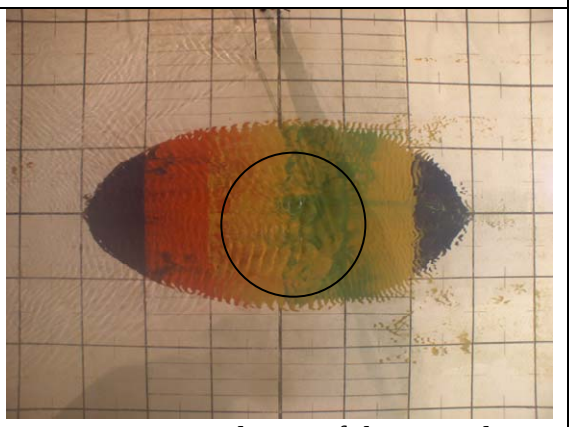

Figure 4.157 Evolution of the mound as the wake forms. Ellipse: refer to Fig. 4.160

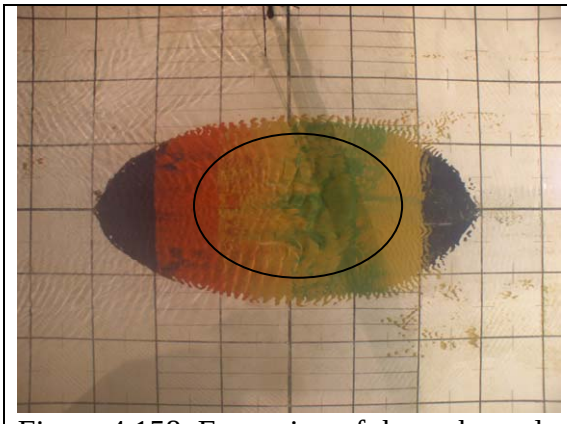

Figure 4.158 Formation of the wake and reversal of ripples in the ellipse

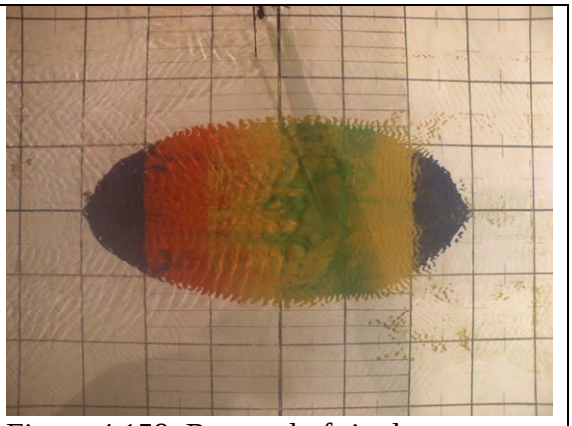

Figure 4.159 Reversal of ripple crests with the flow reversal

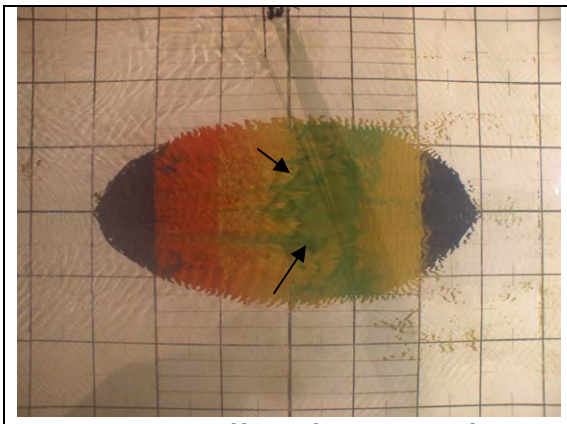

Figure 4.160 Effect of secondary flows on the crest area

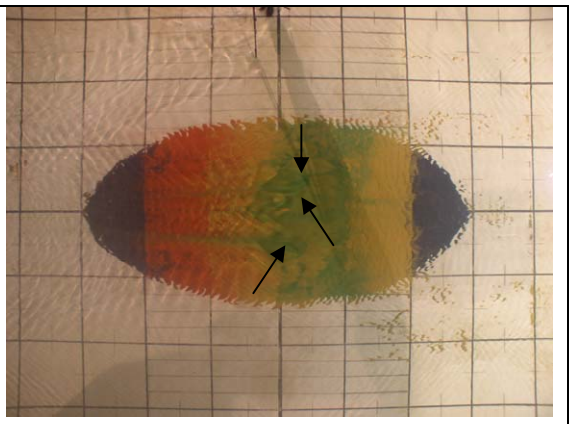

Figure 4.161 Arrows point at crest area

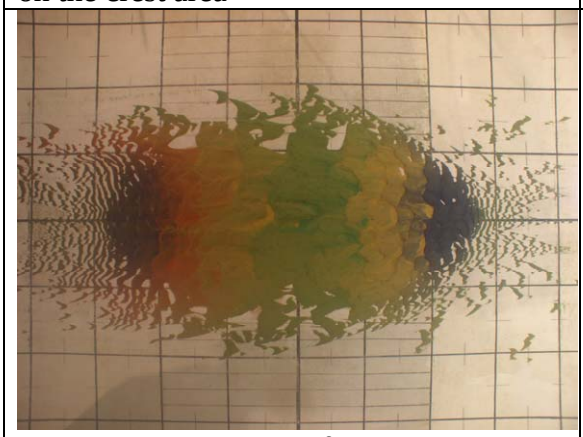

Figure 4.162 Mound after tidal 10 cycles

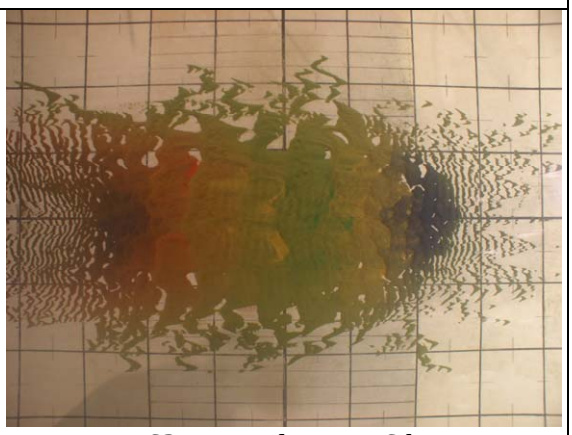

Figure 4.163 Mound at $T_E$= 6 hr

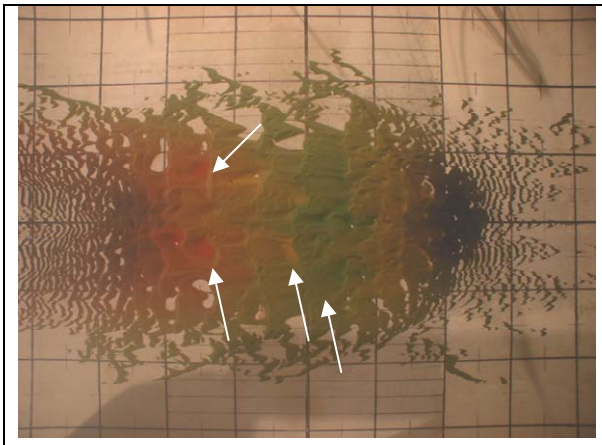

Figure 4.164 Mound evolution Undisturbed sand becomes exposed (arrows)

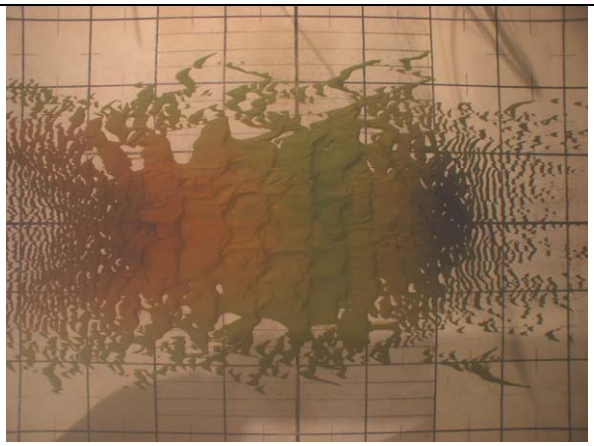

Figure 4.165 Mound at $T_E$=9 hr

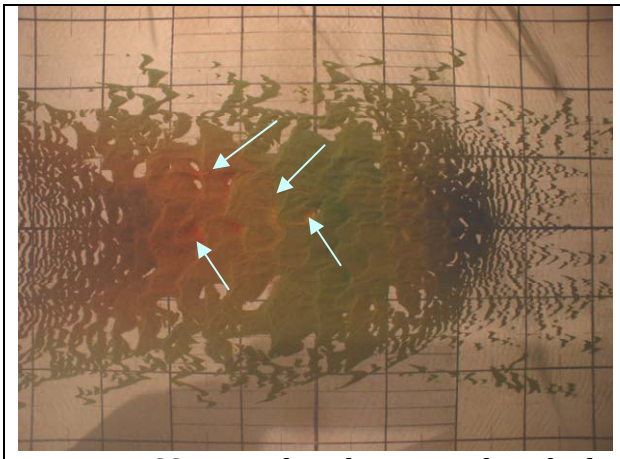

Figure 4.166 Mound evolution. Undisturbed sand becomes exposed (arrows). T 11

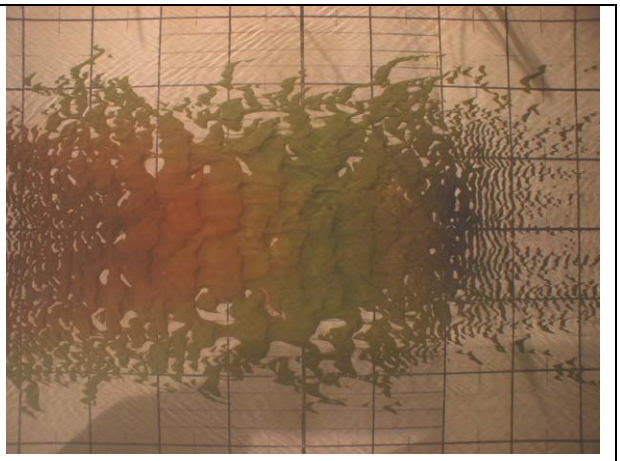

Figure 4.167 Mound at $T_E$= 13 hr
T 11

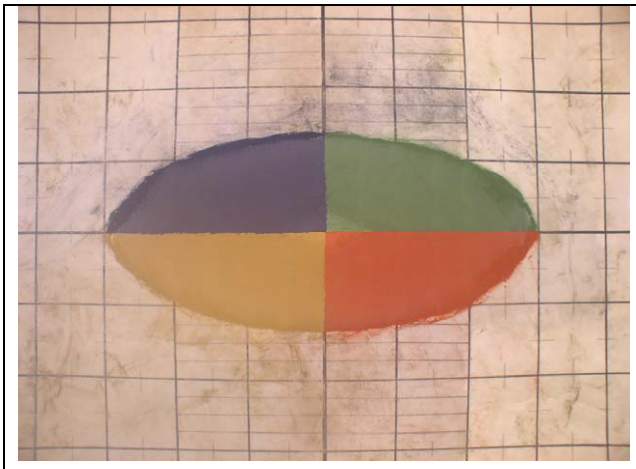

Figure 4.168 Overhead image of the mound at the start of Test 12.

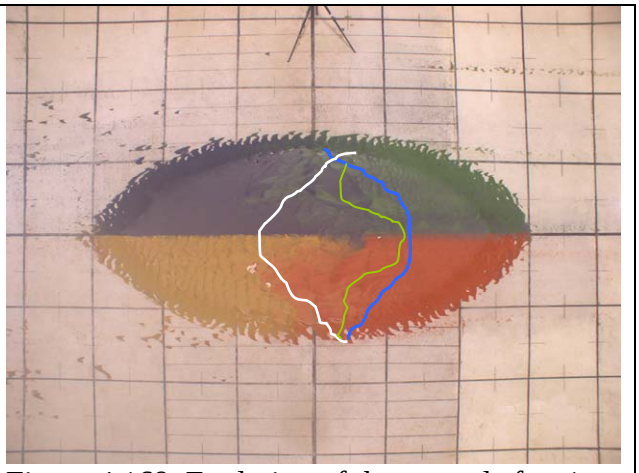

Figure 4.169 Evolution of the mound after 1 tidal cycle (20 min). Lines: refer to text

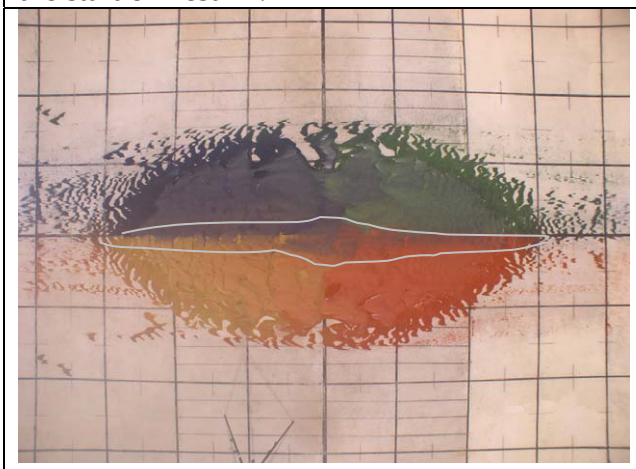

Figure 4.170 Mound after 3 tidal cycles (1 hr). grey lines mark cross-flow transport.

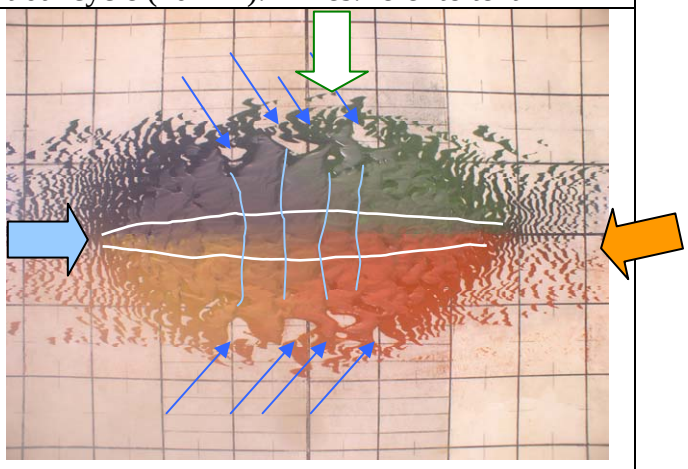

Figure 4.171 Mound after 9 tidal cycle (3 hr). Block arrows show the points of view of Figures 4.178 to 4.182. White line marks cross flow transport

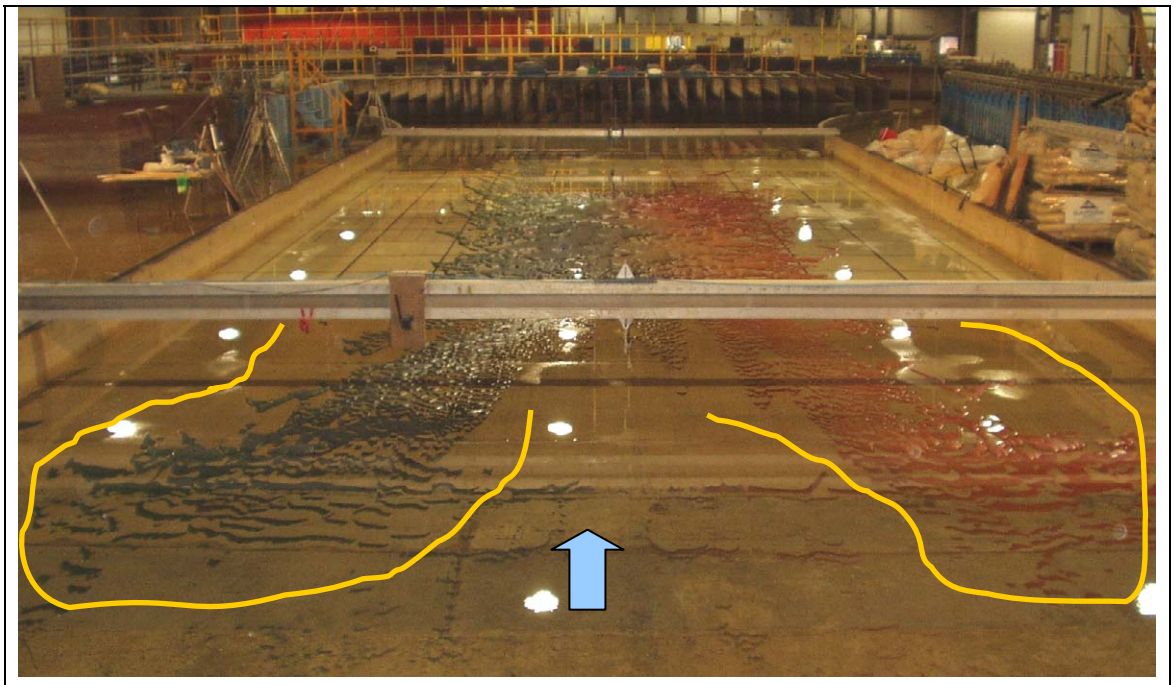

Figure 4.172 Mound after 61 cycles ($T_E$= 20.3 hr) view from the left Figure 4.177

Figure 4.173 Mound after 61 cycles ($T_E$= 20.3 hr) view from the left in Figure 4.177. The white line indicates the cross-flow centre-line

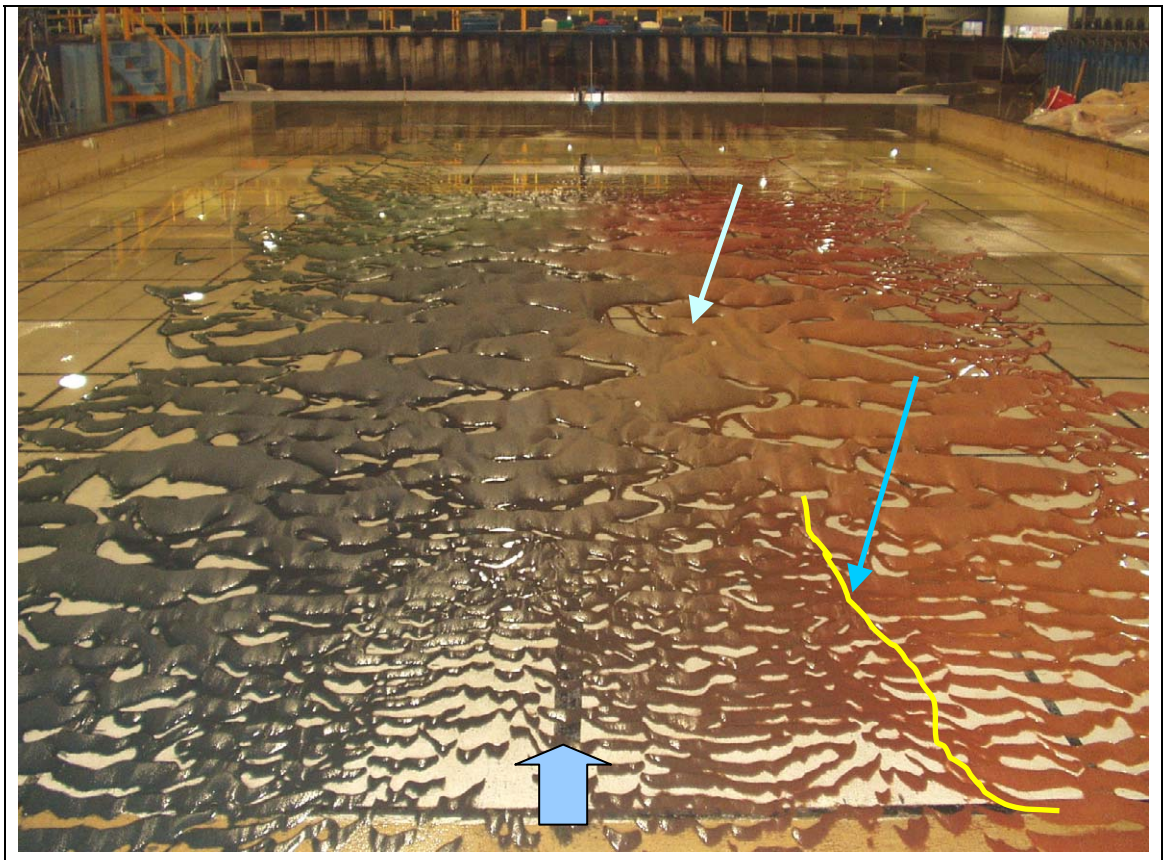

Figure 4.174 Mound after 61 cycles ($T_E$= 20.3 hr) view from the left in Figure 4.177

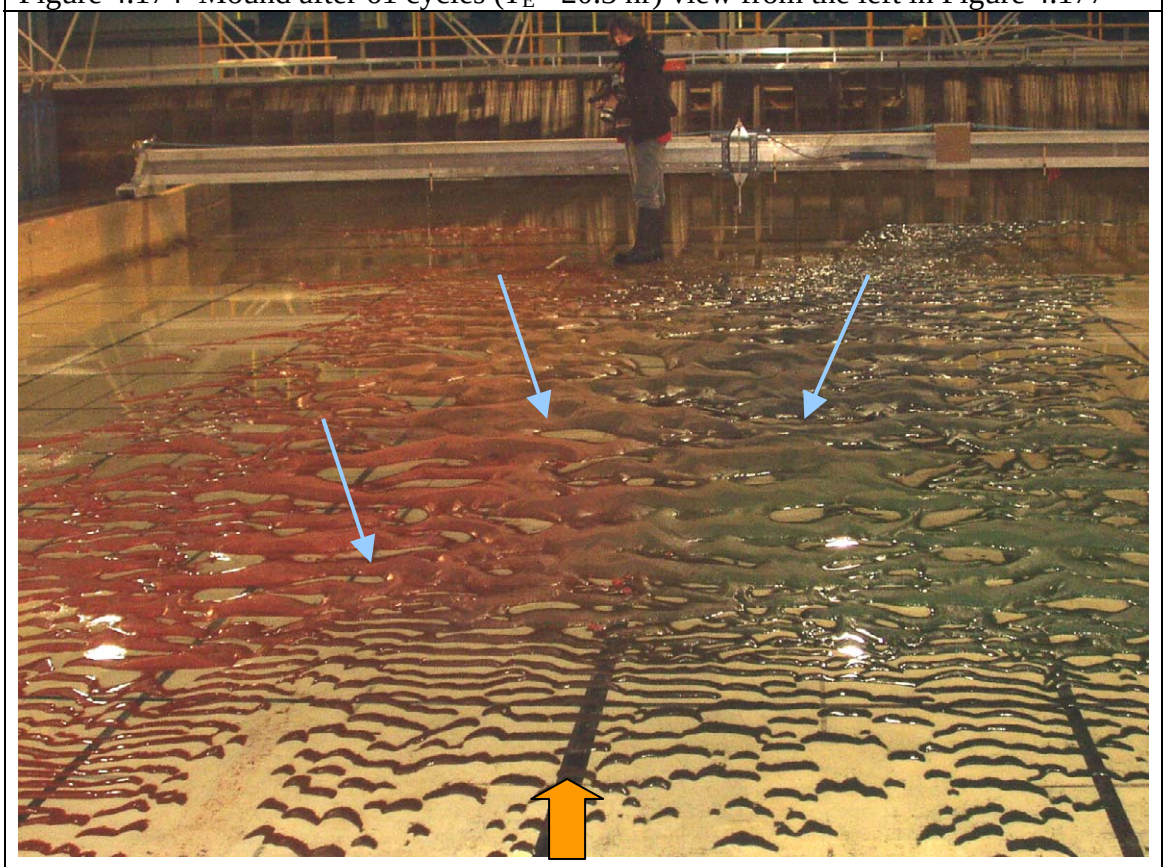

Figure 4.175 Mound after 61 cycles ($T_E$= 20.3 hr) view from the right of the overhead image frame

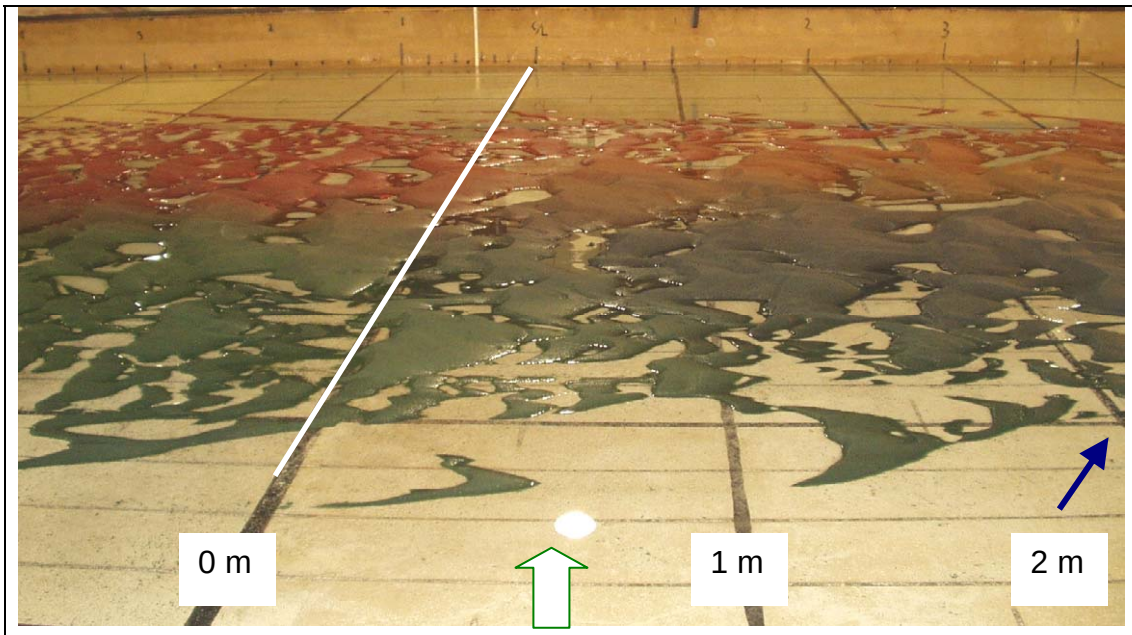


Figure 4.176 Mound evolution after 61 cycles ($T_E$= 20.3 hr) view from the top side of the overhead image frame. White line marks the basin cross-flow centre line

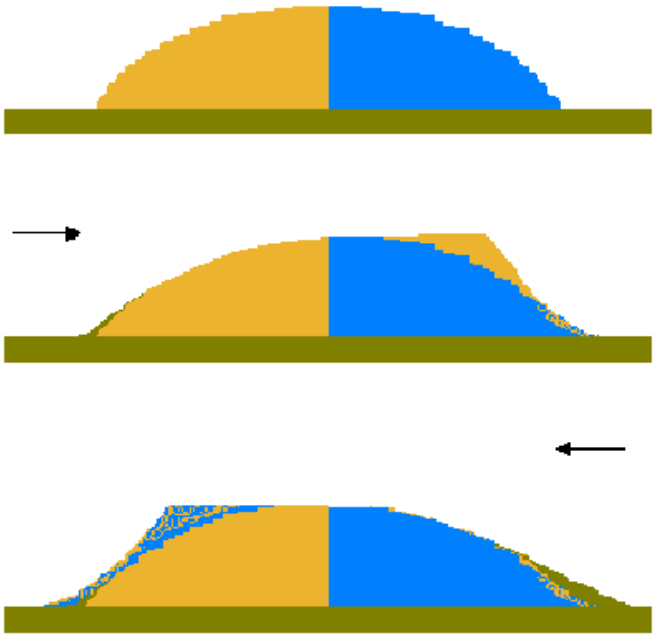

Figure 4.177 Schematic of sand movement in tidal flow, initial mound (top), after half cycle (middle), after one full cycle (bottom)

# 5. COMPARISON OF EXPERIMENTAL RESULTS WITH ANALYTICAL AND EMPIRICAL SOLUTIONS

This chapter presents i) the analytical solution describing the evolution of a bottom disturbance; ii) an approximate solution for the crest migration of a bottom disturbance; and iii) an analytic expression of the decay of volume of a mound. These solutions are compared to the corresponding measurements collected in the UKCRF.

## *5.1 De Vriend solution*

De Vriend (1987) derived an analytical solution for the evolution of a bottom disturbance by applying the method of characteristics to the depth-averaged shallow-water equations coupled with the sediment continuity equation. Figure 5.1 illustrates the star-shaped evolution of an elementary bottom disturbance according to the method of characteristics. Following De Vriend (1987), the analytical solution offers a means of assessing the morphodynamic evolution of a bottom disturbance (by providing expressions to calculate the migration of back edge, spread in the cross flow direction, and angle of spread). The solution obtained with the method of characteristics consists of the following stream-wise and normal components of the celerity for the elementary bottom disturbance:

$$\frac{ds}{dt} = c_0 + c_1\ \xi \qquad \text{and} \qquad \frac{dn}{dt} = c_1\ \eta \tag{5.1}$$

where $s$ and $n$ define the co-ordinate system, parameters $\xi$ and $\eta$ are the co-ordinates that describe the star-shaped pattern according to the method of characteristics (Figure 5.1), $c_1$ is the celerity of the lateral spreading and $c_0$ the migration celerity of the downstream edge. Eq.5.2 defines $c_1$, and $c_0$ as follows:

$$c_1 = T_u \frac{S_{tot}}{H}\ ,\ \ c_0 = (T_u - T_h)\frac{S_{tot}}{H}\ \text{and}\ \tan\alpha = \frac{3\ T_u\ \sqrt{3}}{9\ T_u - 8\ T_h} \tag{5.2}$$

where $S_{tot}$ is the total sediment transport rate, $H$ is the water depth, $\alpha$ is the spread angle, and $T_u$ and $T_h$ (include the porosity of the bed) are dimensionless quantities:

$$T_u = \frac{\overline{U}}{S_{tot}}\frac{\partial S_{tot}}{\partial \overline{U}} - 1 \quad \text{and} \quad T_h = \frac{H}{S_{tot}}\frac{\partial S_{tot}}{\partial H} - 1 \tag{5.3}$$

where $\overline{U}$ is the depth-averaged velocity. The relationship between $\xi$ and $\eta$ from Eq. 5.1 is described by:

$$\eta^4 + \left(2\xi^2 - 5\xi - \tfrac{1}{4}\right)\eta^2 + \xi(\xi+1)^3 = 0 \tag{5.4}$$

where the $\xi$-axis corresponds to the stream-wise direction and the $\eta$-axis to the cross-flow direction. Letting $\varphi = \eta^2$ then Eq. 5.4 becomes:

$$\varphi^2 + \left(2\xi^2 - 5\xi - \tfrac{1}{4}\right)\varphi + \xi(\xi+1)^3 = 0 \tag{5.5}$$

which is a quadratic equation, with solution:

$$\varphi = \frac{-\left(2\xi^2 - 5\xi - \tfrac{1}{4}\right) \pm \sqrt{\left(2\xi^2 - 5\xi - \tfrac{1}{4}\right)^2 - 4\xi(\xi+1)^3}}{2}. \tag{5.6}$$

Noting that $\eta = \pm\sqrt{\varphi}$, Eq. 5.6 gives four, two or zero solutions for $\eta$ for each value of $\xi$. As seen in Figure 5.1, there are no solutions for $\xi < -1$ or $\xi > ½$, two solutions for $-1 \leq \xi < 0$, and four solutions for $0 < \xi < ½$. The solutions are symmetrical about the flow axis, $\eta = 0$.

### 5.1.1. Analytical solution applied to the UKCRF

To test De Vriend's solution against measurements collected from the large-scale experiments, two widely used bed-load sediment transport formulae due to Nielsen (1992) and Meyer-Peter Müller (1948) are considered as part of the solution process. Two expressions for the drag (friction velocity) are applied; a power-law and a logarithmic profile.

Tables 5.1 and 5.2 compare the analytical solution with two sediment transport formulae. The analytical solution obtained by applying the bedload transport formula of Nielsen (1992), described by Eq. 2.4 in Section 2.6.3, to Eqs. (5.2) and (5.3) is presented in Table 5.1. The corresponding solution applying the bedload transport formula by Meyer-Peter Müller (1948), as Eq. 2.5 in Section 2.6.3, to Eqs. (5.2) and (5.3) is shown in Table 5.2.

In these formulae, and those presented in Tables 5.1 and 5.2, $\Phi$ is the dimensionless sediment transport rate, $\theta$ is the Shields parameter and $\theta_{cr}$ is its threshold value, $u_*$ is the friction velocity, $\overline{U}$ is the depth-averaged velocity and $\overline{U}_{cr}$ is its critical value, $d$ is the grain size, $z_0$ is the bed roughness length, $\kappa$ is the von Kármán constant, $A_N$ is the coefficient of the Nielsen formula, $A_{MPM}$ is the coefficient for the Meyer-Peter-Müller formula, and $\varepsilon$ is the bed porosity.

The expression for $T_u$ depends on the transport formula, and is the same for both friction velocity profiles. $T_h$ depends on the friction velocity profile and therefore the expressions are identical when derived from the two different sediment transport formulae.

In the Nielsen formula, $\overline{U}_{cr}$ is calculated with Sandcalc (with Soulsby's 1997 approach), whilst in the Meyer-Peter-Müller formula the value of $\overline{U}_{cr}$ is derived using:

$$\theta_{cr} = \frac{u_*^2}{g(s-1)d} \text{ and } \theta_{cr} = 0.047, \tag{5.7}$$

with either a log- or power-law profile for $u_*$ to calculate $\overline{U}_{cr}$. Note that in all the above formulae, $\Phi = S_{tot} = c_0 = c_1 = 0$ if $\theta \le \theta_{cr}$ or $\overline{U} \le \overline{U}_{cr}$.

### 5.1.2. Calculations from the UKCRF data

Analytical results of the downstream edge migration, lateral spreading and angle of spreading are compared to those derived from the experimental data from the UKCRF. The calculation of the experimental migration, spreading rate and the angle of spread of the mound were done using both the original overhead photographs of the mound's evolution and the digitised contours. The experimental results from the UKCRF tests used in this analysis ran with steady flow conditions, a submerged circular Gaussian mound on a fixed bed (Test 9), and mobile bed (Test 13), and the surface piercing ellipse with triangular cross-sections (Test 10). The main limitations of the methodology used were: (i) the inability to capture the full extent of the basin with the overhead camera, and (ii) the difficulty in determining $c_1$ from the images. During the experiments the overhead camera captured only the central portion of the basin (approximately 8.5 m in the stream wise direction and 6.5 m in the cross-flow direction). Hence, there was a sizeable portion of the basin, outside of the image frame, where data were only recorded in a qualitative manner (from images taken with a hand held camera) and typically at the end of the test. When obtaining $c_1$ from the images (i.e. spread of the mound across flume) it was difficult to choose a suitable point in the contours, using information from the overhead images. This procedure was followed for all the tests analysed in this chapter.

### 5.1.3. Comparison of the back edge migration, lateral spread and angle of spread

The experimental results for the migration of the downstream edge of the mound and the predicted migration using the analytical solution are shown in Figure 5.2 and Table 5.3.

The predictions of downstream edge migration from both sediment transport formulae using power and logarithmic profile, provided an envelope for the solution that was

in broad agreement with the experimental results (Figure 5.2). The well-defined case of Test 9 gave especially good agreement with the predicted migration rates from the log-profile and Nielsen combination. However, it should be noted that the theory is based on an assumed infinite bed of mobile sand, so Test 9 on a fixed bed did not fully conform to the assumption. Test 13 however, was carried out with a mobile bed of 0.025 m depth and covered a surface of approximately 6.0 by 6.5 m. Test 10 was a surface-piercing mound over a fixed concrete bed, so it did not conform to the theoretical assumption of a small-amplitude disturbance.

The experimental and predicted values for the lateral spreading are shown in Figure 5.3, Tables 5.4a and 5.4b (for orientation refer to Figure 5.4). Predictions using both Nielsen and Meyer-Peter-Müller overestimate the width of the mound. The lateral spread calculated from the experimental data was obtained from the overhead image information and contours derived from it. Experimental values of $c_1$ for Test 9 and 13 were very low, and on occasions showed no spread. However, results calculated for Test 10 with the information available were, in the first hour, in the proximity of the envelope provided by the four methods (Figure 5.3). The disagreement could be due to the interpretation of the width of the mound as mentioned earlier: digitised images may not have provided all the information necessary to represent the lateral spread correctly. It should be noted that during the experiments the mound travelled downstream and a portion of the sand spread downstream outside the frame of the overhead image. The image information may therefore be incomplete when calculating the lateral spread of the mound. As seen in Figure 5.4, after 3 hours a portion of sand had travelled downstream, out of the overhead image frame, and an increase in width can be appreciated.

The migration rate of the downstream edge of the mound was greater than the lateral spreading rate. The star-shaped pattern developed in the experiments as outlined in Figure 5.4. The image was taken from the downstream end of the basin after 3 hours run time. A thin layer of sand (ripple field) covered a large area outside of the image frame captured by the overhead camera.

The experimental and predicted values for the spreading angles are shown in Tables 5.5a and 5.5b. Acquisition of the angles from the contours was tricky: after 2 hours run time, part of the mound was outside of the image frame. Hence, the downstream area of the mound was not captured by the contours, nor by the colour photographs. Results of $\alpha$ are presented in Table 5.5a and 5.5b show great variability, ranging from 11º to 31º. In

general the experimental $\alpha$ were close to the predicted values. According to Figure 5.1 the predicted angle should increase as the feature spread laterally and travelled downstream. However, the experimental lateral spreading did not increase as it was predicted to do, and in fact caused the experimental angle of spread to decrease.

### 5.1.4. Assumptions and discussion

The research benefited from valuable comments from Professor H. J. de Vriend, which stimulated the following discussion. As mentioned above, the analysis developed by De Vriend is intended for an infinitesimal bed disturbance on a bed of mobile sand of infinite horizontal extent in a uniform steady flow. The experiments differed from this idealised situation in that:

- The experimental mound initially covered ¾ of the water depth (in Tests 9 and 13) or pierced the surface (in Test 10), hence the bed disturbance cannot be considered infinitesimal;
- Only the mound comprised mobile sand (in Tests 9 and 10), which was placed on a fixed concrete bed;
- The flow was confined to a flume of limited horizontal extent;
- The mound exerted an effect on the flow velocity and on the free surface (as is evident from the overhead images and the velocity record) and hence the flow was non-uniform.

Despite these departures of the experimental conditions from the theoretical assumptions, the predicted migration speeds are in remarkably close agreement with the observed speeds. It is reassuring to have experimental evidence to support the analytical solution used for the validation of morphodynamic models. The analytical solution provides a simple way to calculate the migration rates of the downstream edge and the lateral spreading of the mound without the need for numerical modelling. Hence, if a numerical model is going to be used, it should provide added value, such as information on the evolution of the shape of the bed form.

De Vriend (1987) and Chesher (1993) argued that the bed disturbance on the sides of the mound was not due to the motion of the sand sideways, but to a disturbance of the free surface due to the interaction of the bed feature and the flow. The experimental results for Test 13 corroborate this; Figures 4.29 and 4.43b (Chapter 4) show overhead views of the evolution of a Gaussian mound after 26 min and 62 min elapsed time, and Figures 5.5a and

5.5b show the contoured data corresponding to the same times. The mound was built from coloured sand and the mobile bed was of natural colour (unidirectional flow from the right). The figures show the bed is disturbed on the downstream sides of the mound (see arrows), though this disturbance does not involve any coloured sand. The sand moves downstream along with the velocity iso-lines.

Using the mathematical derivation of the analytical solution of an infinitesimal bed disturbance under steady flow conditions as a starting point, and based on experimental and modelling results, an empirical interpretative shape for tidal flows can be proposed as two superimposed barchan dunes (Figures 4.74 and 4.77). This is a quasi-equilibrium shape, due to the inherent variability of the tidal flow conditions: the shape is not stationary, it varies as the flow intensity varies and the flow reverses. The general shape is like an X, with longer arms in the direction of the strongest flow at the time.

**Discussion**

In interpreting the results it is assumed that the experimental mound is composed of many small initial disturbances located at different heights and water depths. The interpretation of the star shape in this context is that every point in the mound will evolve following the shape of the analytical solution. From an experimental point of view this implies that the crest and the flanks of the disturbance travel downstream evolving into a flatter and streamlined shape that adapts to the flow conditions. This process is a highly turbulent one, with the development of strong secondary flows, a wake and a re-circulating bubble. The disturbances of the free surface can be observed i) over the crest of the mound as it travels downstream; ii) in the re-circulation bubble area, just downstream of the crest; and iii) in the wake area at the lee of the mound. It is not clear whether the crest travels faster than the flanks of the mound, but this is not so relevant to this analysis.

The processes are dominated by the relationship of the water depth and the flow velocity enhancing the sediment transport capacity. The star shape (in Figure 5.1) describes the evolution of the initial disturbance. The star-shape (barchan dune) appeared early on in the test, and the bottom disturbance evolved to the streamlined quasi-equilibrium shape for the given steady flow conditions. In certain cases the star/barchan shape was maintained (Test 9); in others the mound evolved slightly differently, depending on whether the disturbed bed around the mound was considered as part of the mound or not (Test 13, the shape was more like an ellipse Figures 4.30 and 4.41).

The spread in the cross flume direction predicted from the analysis is larger than in the experiments. This may be due to the limited width of the flume having an influence which might have restricted the streamline divergence due to the obstruction of the flow by the mound. However, from overhead images it can be seen that the streamlines do curve around the mound during the test (evidence in float track images, e.g. Figures 4.5 and 4.26). It should be noted that the size of the mound had been chosen to minimise the wall effects.

An important point brought up by Professor de Vriend (in email correspondence) was related to previous experiments (LNH, 1970s). These were unsuccessful due to the ripple scale being very similar to the mound scale. During the UKCRF experiments ripple dimensions were smaller than the mound. In certain long tests, somewhere between 5 hr run time and the end of the test, the mound had lost part of its integrity and was mostly formed by 'fully developed' ripples (for unsteady conditions). This could indicate a qualitative regime change (morphodynamic behaviour, from mound-dominated to ripple-dominated) where the effect of the ripples on the flow and the morphodynamics could become more dominant than that of the mound.

## *5.2 Morphodynamic Timescales*

Morphodynamic timescales are used as tools for prediction of timescales of the migration/decay of a sediment feature or a sediment volume. In this section three formulations of morphodynamic timescale are compared against the experimental results.

Two types of morphodynamic timescale are described here. One type is derived from the characteristic migration of the mound under steady flow conditions, such as Hudson *et al*. (2005) and Huang *et al*. (2008). The second type is derived from the decay of volume in the mound (typically under steady flow conditions, although modified to account for tidal flow conditions). The processes of removal of sediment are similar and are compared to morphodynamic timescales derived from the experiments. Theoretical approaches have conservation of volume (migration of the crest), hence the definition of the 'volume of sand' is important. Through the interpretation of the results in this thesis the decay of volume is taken as the volume of sand that makes up the mound.

### 5.2.1. Timescales based on crest migration

Two approximate analytical formulae were calculate the morphodynamic timescale to predict the migration of the crest of a mound relative to the initial bed topography. The

expressions used are those proposed by Hudson *et al*. (2005) and Huang *et al*. (2008), which were compared to the experimental timescales derived from certain UKCRF tests. These morphodynamic timescales were developed for unidirectional flow, considering only bedload sediment transport.

Hudson *et al*. (2005) described the morphodynamic timescale ($T_{m1}$) as:

$$T_{m1} = \frac{h_{\max}(1-\varepsilon)[H - h_{\max}]^{m+1}}{A\ m\ q_0^m} \tag{5.8}$$

where $H$ is the inflow water depth, $A$ is the bedload transport coefficient, $m$ is the power index in the bedload formula $q_b = A\ u_0^m$, $q_0$ is the flow discharge, $\varepsilon$ is the porosity of the bed, $h_{max}$ is the initial maximum height of the mound and $T_{\mathrm{m1}}$ is defined as the time it takes for the top of the mound to travel a distance $h_{max}$. $T_{\mathrm{m1}}$ depends on the initial height of the mound. The crest of the mound migrates faster than the base, and with time the mound will deform and adapt to the flow conditions, creating a shock at the front after a certain time (Hudson *et al.*, 2005).

The morphodynamic timescale ($T_{\mathrm{m2}}$) proposed by Huang *et al*. (2008) is defined as:

$$T_{m2} = \frac{(1-\varepsilon)H^{m+2}}{A\ m\ q_0^m} = \frac{(1-\varepsilon)H^2}{A\ m\ u_0^m} \tag{5.9}$$

where $u_0$ is the free stream velocity and $T_{\mathrm{m2}}$ is related to the time it takes the crest to travel downstream, creating a shock on the flow, until the mound reaches a shape adapted to the flow conditions, where $T_{\mathrm{m2}}$ is uniform over the whole flow domain and constant with time, hence it is independent of the mound dimensions. The solution is valid until the crest of the mound (*collapse line*, refer to Chapter 4) is vertically above the foot of the mound. At that point the sand travelling over the mound reaching the *collapse line* will avalanche down the back edge of the mound (which would be expected to be of a slope similar to the angle of repose of the sediment).

Both morphodynamic timescales relate to the rate of change of the shape of the mound (Huang *et al*., 2008). The taller the mound, the faster it migrates (larger value of $T_{\mathrm{m1}}$ or $T_{\mathrm{m2}}$).

The relationship between $T_{\mathrm{m1}}$ and $T_{\mathrm{m2}}$ timescales can be expressed as:

$$T_{m1} \Big/ T_{m2} = \frac{h_{\max}(H - h_{\max})^{m+1}}{H^{m+2}} \tag{5.10}$$

If $h_{\max}$ = 0.15 m and $H$ = 0.2 m then $T_{\mathrm{m1}} = 0.003\ T_{\mathrm{m2}}$

In this section, $T_{m1}$ and $T_{m2}$ were calculated with four variations: using two different expressions of the bed shear velocity (a power-law and logarithmic profile) and two well known sediment transport formulae (adapted without considering the critical velocity, as described by Eq. 5.11 by Meyer-Peter-Müller (1948) (MPM) and Nielsen (1992) as in Section 5.1.1. Following the general formula:

$$q_{bN} = A_N \; u_0^m \quad \text{or} \quad q_{bMPM} = A_{MPM} \; u_0^m \tag{5.11}$$

The derived expressions for $A_N$ and $A_{MPM}$, taking the constants in the formulae as $H$ = 0.2 m, $h_{max}$= *0.15* m, $u_0$ = 0.5 m/s, g = 9.81 m/s$^2$, $\varepsilon$ = 0.4, $\kappa$ = 0.4, $z_0 = d_{50}/12$, $s = \rho_s/\rho$ and $m$ = 3 are as follows (the derivation for one case is presented in an appendix as an example):

The bedload coefficients derived for the adapted MPM and Nielsen sediment transport equations assuming a logarithmic profile are:

$$A_N = \frac{12}{g(s-1)}\left(\frac{\kappa}{\ln(H/z_0)-1}\right)^3 \quad \text{and} \quad A_{MPM} = \frac{8}{g(s-1)}\left(\frac{\kappa}{\ln(H/z_0)-1}\right)^3 \tag{5.12}$$

The bedload coefficients derived for the adapted MPM and Nielsen sediment transport equations assuming a power-law profile are:

$$A_N = \frac{12}{g(s-1)7^3}\left(\frac{d_{50}}{H}\right)^{3/7} \quad A_{MPM} = \frac{8}{g(s-1)7^3}\left(\frac{d_{50}}{H}\right)^{3/7} \tag{5.13}$$

Note that the two formulae differ only in the numerical coefficient (12 or 8), because the threshold velocity was omitted in Eq. 5.11. The morphodynamic timescale predictions using the methods of Hudson *et al* and Huang *et al*. are listed in Tables 5.6 and 5.7.

Hudson *et al*. (Table 5.6) predicted very short timescales (< 1 min). The time should relate to the time it takes the crest of the mound to travel downstream a distance equal to its initial height (i.e. 0.15 m). The timescale predictions seemed a bit short, although the actual time was very difficult to assess from the experimental images (the capture interval was typically > 1 min).

The method from Huang *et al*. predicts a characteristic timescale that refers to the mound as an entity. The timescale from Hudson *et al*. is a function of the position relative to the mound and to time. During Test 9 (Gaussian mound in steady flow) the time taken by the crest of the mound to travel relative to the front of the mound, was about 5-7 min from the initiation of motion. The predictions of $T_{m2}$ in Table 5.7 are directly comparable to the experimental measured timescales. The prediction of the crest migration closest to the

observations was achieved using the combination of Nielsen's transport formula and a power-law for the friction velocity. The other three predictions using the method of Huang *et al*. were of the right order of magnitude (Table 5.7) although greater than the measured time for crest migration.

The range of validity of both formulae implies that the mound should occupy ≤ 10 % of the total water depth. This assumption was not met in the experiments, where the mound occupied 75 % of the water column, therefore the experiments were outside the range of application of both methods. The formula from Hudson *et al*. is more sophisticated than Huang *et al*., in that it accounts for the relationship between the height of the mound ($h_{max}$) and the water depth ($H$). However, Hudson *et al*. seems more strict and sensitive to the range of validity where it can be applied successfully (enhancing the importance of the assumption that the mound should be ≤ 10 % of the water depth). Huang *et al*. being simpler can provide reasonable predictions for the UKCRF test conditions, even when these conditions may be outside of the range of application of the expression.

### 5.2.2. Decay of mound volume with time

The volume of the mound decreased with time in the UKCRF tests. The decay of volume was fitted by a simple negative exponential function:

$$Vol(t) = V_0 \ \exp^{-t/T_v} \tag{5.14}$$

where $V_0$ is the initial volume of the mound, $t$ is time and $T_v$ (volumetric morphodynamic timescale) gives an indication of the rate of decrease of the volume with time. A large value of $T_v$ indicates a slow rate of decrease in volume of the mound, and small values correspond to a fast decrease rate. Table 5.8 shows the experimental $T_v$ calculated from the curves fitting the experimental volume data in Figure 5.6. Table 5.8 shows that the dominant factor that influences $T_v$ is the test flow condition. The tests can be divided into two groups, steady flow (with $T_v \leq 6$) and tidal flow ($T_v \geq 43$). The most resilient mound is the submerged ellipse in tidal flow (Test 11) that presents the highest $T_v$ (72.5 hr). The most easily erodible is the Gaussian hill on a mobile bed under steady flow (Test 13) which exhibits the lowest $T_v$ (3 hr). A second important trend is associated with the initial height of the mound in relation to the still water depth. The higher the mound, the faster the volume decreases (true for tidal flow Tests 3, 4 and 11, but not for steady flow Tests 9 and 10). This implies that the exponential decay given by Eq. 5.14 is not fully applicable to the data, since a mound that is initially surface-touching or -piercing, eventually becomes equal in height to a submerged

mound. The rate of decay (measured by $T_v$) appears to be faster when the mound is taller (taking a large fraction of the water depth), and reduces once the mound has became lower (Figure 5.6).

In the case of the decay of the volume of a bed mound there is no analytical solution, although a simple analytic expression considering the volume of the mound (length x width x height = *abc*) and the rate at which the sand is moved away from it can provide a means of obtaining one:

$$Timescale = T_{va} = \frac{abc(1-\varepsilon)}{q_b b} = \frac{ac(1-\varepsilon)}{q_b} = \frac{ac(1-\varepsilon)}{A\overline{U}^3} = ac \ \frac{1}{S_{tot}} \qquad (5.15)$$

where for the elliptical mound $a$ = 6 m; for the Gaussian mound $a$ = 5 m, and for the submerged mound $c$ = 0.15 m; for the surface-touching mound $c$ = 0.2 m and for the surface-piercing mound $c$ = 0.25 m. The calculations using this formula can be compared to the experimental $T_v$. As in Section 5.1, two well-known sediment transport formulae (Nielsen and Meyer-Peter-Müller) were used with a log and power-law friction velocity profile to obtain an envelope of analytical values. The expressions for $A_N$ and $A_{MPM}$ are taken from Section 5.2.1. The undisturbed upstream velocity ($\overline{U}$) and undisturbed water depth ($H$) were 0.5 m/s and 0.2 m respectively. Table 5.9 shows the values of the morphodynamic timescale calculated using Eq. 5.14.

The predictions of the analytical formula agree broadly with the morphodynamic timescales for tests with steady flow conditions. However, it greatly underestimates the tidal flow timescales. This is because it does not take into account the flow reversal, the slack water periods and the time when the velocity is below the threshold of motion. To apply this formula to the tidal flow cases, a representative mean velocity for the whole cycle was used. With this change the formula provides a better representation of the tidal conditions for the experimental data (Table 5.10). The predicted morphodynamic timescales (Tables 5.9 and 5.10) increase with the height and length of the mound (that would correspond to an increase in volume). From the experiments and analytical formula, the mound volume was conserved better when the mound was longer ($a$), and the crest was higher ($c$). The formula combining the adapted Nielsen expression with a power-law produced the largest timescale, and the combination of the adapted MPM expression with a log-profile produced the smallest timescales. Until submergence, the surface-piercing mounds decayed more rapidly than the submerged ones. In the experiments (Table 5.8) the volume was conserved better in

larger mounds (i.e. elliptical shape rather than Gaussian). The flow conditions were very important in the evolution of the mound. In the elliptical plan shape cases with tidal flow, the submerged mound had a longer timescale than the surface piercing. In steady flow the difference was not so clear: the surface-piercing mound had the longest timescale, but it was not obvious whether this was due to its planar shape (elliptical) or its height (larger initial volume).

There was a limitation in using an exponential formula to represent the decay of the emerged or surface mounds with time. The curve describing the decay of the volume had two distinct parts (two slopes); one of rapid decay (at the beginning) and another that had a slower rate of decay (later in the test). The point of change could be interpreted as the time when the mound reached a certain equilibrium shape, in equilibrium with the present flow conditions.

**Summary**

The experimental results and the predictions using De Vriend's analytical expression agreed overall, albeit the experiments were outside of the range of application. The predictions for lateral spreading and angle of spreading were near the range of variation provided by the four expressions. This is probably due to the limitation in the experimental data capture (the area of the basin covered by the overhead image) and the effect of limited data in the calculation of the lateral spreading, which relates to the derivation of the angle of spreading.

Huang *et al.*'s method provided a prediction in reasonable agreement with the observed morphodynamic timescale related to the migration of the crest. The morphodynamic timescale prediction from Hudson *et al.* (the time it takes the crest to move a distance of 0.15 m in the experimental case) gave a very small value (< 1 min), but could not be compared to the experimental data due to the image capture frequency being large in comparison to the timescale of crest evolution.

The predictions of morphodynamic timescale, using an empirical expression for the decay of mound volume, were very sensitive to the sediment transport formula and profile type used. The combinations of the four formulae provided an envelope of predictions. The predictions using a velocity value representative of steady flow were acceptably similar to the corresponding experimental values (Table 5.11). When the velocity value was modified to represent tidal flows (using an average value to represent the velocity throughout the tidal cycle) the predictions were closer to the experimental values.

| Power law (Soulsby, 1997, Eq. 34) | Logarithmic (Soulsby, 1997, Eq. 22) |
|---|---|
| $u_* = \frac{1}{7}\left(\frac{d}{H}\right)^{1/7}\overline{U}$ | $u_* = \frac{\overline{U}\ \kappa}{\left[\ln(H/z_0)-1\right]}$ |
| $S_{tot} = A_N \overline{U}\left(\overline{U}^2 - \overline{U}_{cr}^2\right)$ | $S_{tot} = A_N \overline{U}\left(\overline{U}^2 - \overline{U}_{cr}^2\right)$ |
| $A_N = \frac{12}{g(s-1)(1-\varepsilon)}\frac{1}{7^3}\left(\frac{d}{H}\right)^{3/7}$ | $A_N = \frac{12}{g(s-1)(1-\varepsilon)}\left(\frac{\kappa}{\ln(H/z_0)-1}\right)^3$ |
| $T_u = \frac{2\overline{U}^2}{\overline{U}^2 - \overline{U}_{cr}^2}$ | $T_u = \frac{2\overline{U}^2}{\overline{U}^2 - \overline{U}_{cr}^2}$ |
| $T_h = \frac{-10}{7}$ | $T_h = -\frac{\ln(H/z_0)+2}{\ln(H/z_0)-1}$ |
| $c_0 = \left(\frac{2\overline{U}^2}{\overline{U}^2 - \overline{U}_{cr}^2} + \frac{10}{7}\right)\frac{S_{tot}}{H}$ | $c_0 = \left(\frac{2\overline{U}^2}{\overline{U}^2 - \overline{U}_{cr}^2} + \frac{\ln(H/z_0)+2}{\ln(H/z_0)-1}\right)\frac{S_{tot}}{H}$ |
| $c_1 = \frac{2A_N\overline{U}^3}{H}$ | $c_1 = \frac{2A_N\overline{U}^3}{H}$ |
| Angle of spread: $\tan\alpha = \frac{3\ T_u\sqrt{3}}{9T_u - 8T_h}$ | |

**Table 5.1 Analytical solution from De Vriend (1987) derived using Nielsen's bedload transport formula and a power law (left) and logarithmic (right) friction velocity profile**

| Power law (Soulsby, 1997, Eq. 34) | Logarithmic (Soulsby, 1997, Eq. 22) |
|---|---|
| $u_* = \frac{1}{7}\left(\frac{d}{H}\right)^{1/7}\overline{U}$ | $u_* = \frac{\overline{U}\ \kappa}{\left[\ln(H/z_0)-1\right]}$ |
| $S_{tot} = A_{MPM}\left(\overline{U}^2 - \overline{U}_{cr}^2\right)^{3/2}$ | $S_{tot} = A_{MPM}\left(\overline{U}^2 - \overline{U}_{cr}^2\right)^{3/2}$ |
| $A_{MPM} = \frac{8}{7^3}\frac{1}{g(s-1)(1-\varepsilon)}\left(\frac{d}{H}\right)^{3/7}$ | $A_{MPM} = \frac{8}{g(s-1)(1-\varepsilon)}\left(\frac{\kappa}{\ln(H/z_0)-1}\right)^3$ |
| $T_u = \frac{2\overline{U}^2 + \overline{U}_{cr}^2}{\overline{U}^2 - \overline{U}_{cr}^2}$ | $T_u = \frac{2\overline{U}^2 + \overline{U}_{cr}^2}{\overline{U}^2 - \overline{U}_{cr}^2}$ |
| $T_h = \frac{-10}{7}$ | $T_h = -\frac{\ln(H/z_0)+2}{\ln(H/z_0)-1}$ |
| $c_0 = \left(\frac{2\overline{U}^2 + \overline{U}_{cr}^2}{\overline{U}^2 - \overline{U}_{cr}^2} + \frac{10}{7}\right)\frac{S_{tot}}{H}$ | $c_0 = \left(\frac{2\overline{U}^2 + \overline{U}_{cr}^2}{\overline{U}^2 - \overline{U}_{cr}^2} + \frac{\ln(H/z_0)+2}{\ln(H/z_0)-1}\right)\frac{S_{tot}}{H}$ |
| $c_1 = \left(2\overline{U}^2 + \overline{U}_{cr}^2\right)\frac{A_{MPM}}{H}\sqrt{\overline{U}^2 - \overline{U}_{cr}^2}$ | $c_1 = \left(2\overline{U}^2 + \overline{U}_{cr}^2\right)\frac{A_{MPM}}{H}\sqrt{\overline{U}^2 - \overline{U}_{cr}^2}$ |
| Angle of spread: $\tan\alpha = \frac{3\ T_u\sqrt{3}}{9T_u - 8T_h}$ | |

**Table 5.2 Analytical solution from De Vriend (1987) derived using MPM's bedload transport formula and a power law (left) and logarithmic (right) friction velocity profile**

| Time (s) | Experimental $c_0$ | | | Predicted $c_0$ power-law | | log-profile | |
|---|---|---|---|---|---|---|---|
| | T9 | T10 | T13 | Nielsen | MPM | Nielsen | MPM |
| **0** | 0.00 | 0.00 | 0.00 | 0.00 | 0.00 | 0.00 | 0.00 |
| **1200** | 0.40 | 0.00 | 0.20 | 0.60 | 0.34 | 0.41 | 0.23 |
| **3600** | 1.35 | 0.45 | 2.00 | 1.81 | 1.02 | 1.23 | 0.69 |
| **7200** | 2.45 | 1.45 | - | 3.62 | 2.04 | 2.47 | 1.39 |

**Table 5.3 Results for experimental and predicted stream wise migration celerity of the downstream edge of the mound c0**

**Experimental $c_1$**

| Time (s) | T9 | | T10 | | T13 | |
|---|---|---|---|---|---|---|
| | E | W | E | W | E | W |
| **0** | 0.00 | 0.00 | 0.00 | 0.00 | 0.00 | 0.00 |
| **1200** | -0.10 | -0.20 | 0.30 | 0.45 | -0.25 | 0.15 |
| **3600** | 0.15 | 0.10 | 0.45 | 0.40 | 0.20 | 0.20 |
| **7200** | no data | no data | 0.50 | 0.60 | no data | no data |

**Table 5.4a Results for experimental lateral spreading of the mound c1**

| Time (s) | Predicted $c_1$ power-law | | log profile | |
|---|---|---|---|---|
| | Nielsen | MPM | Nielsen | MPM |
| **0** | 0.00 | 0.00 | 0.00 | 0.00 |
| **1200** | 0.40 | 0.25 | 0.27 | 0.17 |
| **3600** | 1.19 | 0.74 | 0.82 | 0.51 |
| **7200** | 2.39 | 1.49 | 1.64 | 1.02 |

**Table 5.4b Results for predicted lateral spreading of the mound c1**

| Time (s) | T9 | | T10 | | T13 | |
|---|---|---|---|---|---|---|
| | W | E | W | E | W | E |
| **1200** | 31 | 32 | 16 | 17.5 | 17 | 18.5 |
| **3600** | 18 | 17 | 13 | 14 | 15 | 11 |
| **7200** | 16 | 14 | 13 | 12.5 | x | x |

**Table 5.5a Results for predicted angle of spreading of the bed feature α (W and E correspond respectively to the western flank and E eastern flank of the mound, refer to Figure 5.4).**

| power law | | log profile | |
|---|---|---|---|
| Nielsen | MPM | Nielsen | MPM |
| 21.6 | 23.5 | 21.7 | 23.6 |

**Table 5.5b Predicted angle of spreading of the bed mound.**

| **Log profile, Nielsen** | | **Log profile, MPM** | |
|---|---|---|---|
| $A_N$ = 0.000109 $s^2$/m | $T_{m1}$ = 0.028 min | $A_{MPM}$ = 0.000073 $s^2$/m | $T_{m1}$ = 0.043 min |
| **Power law, Nielsen** | | **Power law, MPM** | |
| $A_N$ = 0.000159 $s^2$/m | $T_{m1}$ = 0.020 min | $A_{MPM}$ = 0.000106 $s^2$/m | $T_{m1}$ = 0.030 min |

**Table 5.6 Predictions of the bedload coefficient and $T_{m1}$ (Hudson *et al*., 2005)**

| **Log profile, Nielsen** | | **Log profile, MPM** | |
|---|---|---|---|
| $A_N$ = 0.000109 $s^2$/m | $T_{m2}$ = 9.8 min | $A_{MPM}$ = 0.000073 $s^2$/m | $T_{m2}$ = 14.7 min |
| **Power law, Nielsen** | | **Power law, MPM** | |
| $A_N$ = 0.000159 $s^2$/m | $T_{m2}$ = 6.7 min | $A_{MPM}$ = 0.000106 $s^2$/m | $T_{m2}$ = 10.1 min |

**Table 5.7 Predictions of the bedload coefficient and $T_{m2}$ (Huang *et al*., 2008)**

| **Test No** | **Plan shape** | **Height** | **Flow conditions** | **$V_0$ ($m^3$) measured** | **$V_0$ ($m^3$) from regression** | **$T_v$ (hr)** |
|---|---|---|---|---|---|---|
| **3** | Ellipse | SP | tidal | 1.112 | 0.990 | 43.1 |
| **4** | Ellipse | ST | tidal | 0.730 | 0.752 | 55.9 |
| **8** | Gaussian Hill | S | tidal | 0.682 | 0.630 | 57.1 |
| **9** | Gaussian Hill | S | steady | 0.655 | 0.707 | 4.4 |
| **10** | Ellipse | SP | steady | 0.991 | 1.018 | 6.0 |
| **11** | Ellipse | S | tidal | 0.592 | 0.567 | 72.5 |
| **13** | Gaussian Hill **§** | S | steady | 0.625 | 0.600 | 3.0 |

**§**: Mobile bed mound; S: submerged; ST: surface touching; SP: surface piercing

**Table 5.8 Morphodynamic timescale from UKCRF experiments**

| **$T_{va}$ → Formulae** | **Gaussian SM (hr)** | **ellipse SM (hr)** | **ellipse ST (hr)** | **ellipse SP (hr)** |
|---|---|---|---|---|
| **Log+Nielsen** | 9.15 | 10.98 | 14.65 | 18.31 |
| **Power+Nielsen** | 13.73 | 16.48 | 21.97 | 27.46 |
| **log+MPM** | 6.29 | 7.54 | 10.06 | 12.57 |
| **Power+MPM** | 9.43 | 11.32 | 15.09 | 18.86 |

S: submerged; ST: surface touching; SP: surface piercing

**Table 5.9 Morphological timescales for the decay of volume of the mound ($T_{va}$)**

| $T_{va}$ → Formulae | Gaussian SM (hr) | ellipse SM (hr) | ellipse ST (hr) | ellipse SP (hr) |
|---|---|---|---|---|
| **log+Nielsen** | 26.69 | 32.02 | 42.70 | 53.37 |
| **power+Nielsen** | 40.03 | 48.03 | 64.05 | 80.06 |
| **log+MPM** | 18.33 | 21.99 | 29.32 | 36.66 |
| **power+MPM** | 27.49 | 32.99 | 43.99 | 54.98 |

**Table 5.10 Morphodynamic timescales for the decay of volume of the mound ($T_{va}$) taking to account tidal flow cases**

| Test No | Plan shape | Height | Flow conditions | $T_v$ (hr) | Range of $T_{va}$ for steady flow (hr) | Range of $T_{va}$ for tidal flow (hr) |
|---|---|---|---|---|---|---|
| **3** | Ellipse | SP | tidal | 43.1 | | 36-80 |
| **4** | Ellipse | ST | tidal | 55.9 | | 29-64 |
| **8** | Gaussian Hill | S | tidal | 57.1 | | 18-40 |
| **9** | Gaussian Hill | S | steady | 4.4 | 6-14 | |
| **10** | Ellipse | SP | steady | 6.0 | 12-27 | |
| **11** | Ellipse | S | tidal | 72.5 | | 22-48 |
| **13** | Gaussian Hill § | S | steady | 3.0 | 6-14 | |

**Table 5.11 Experimental $T_v$ from Table 5.9 including results of $T_{va}$ for steady and tidal flow (from Tables 5.10 and 5.11)**

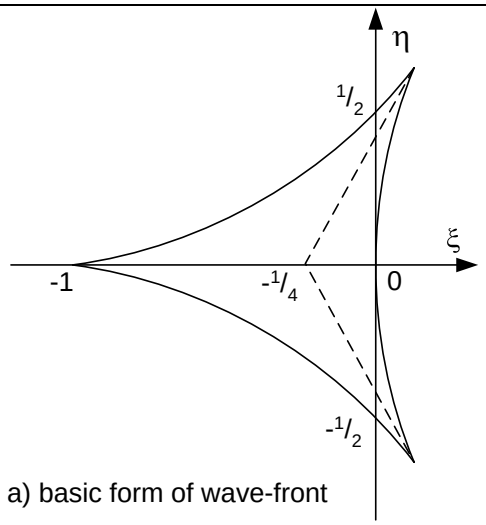


a) basic form of wave-front

$$c_0 = (T_u - T_h)\frac{S_{tot}}{h};\ \tan\ \alpha = \frac{3\ T_u\sqrt{3}}{9T_u - 8T_h}$$

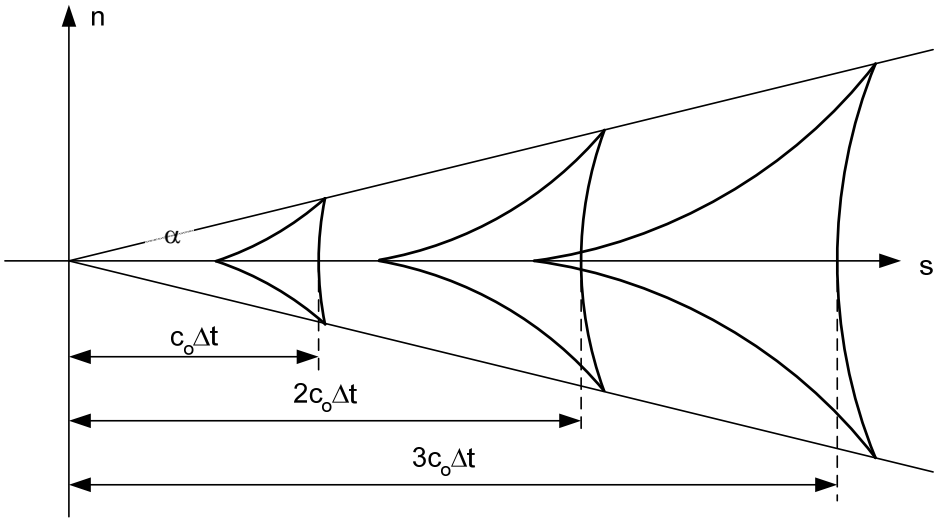


b) evolution of disturbed area from point disturbance

Figure 5.1 Evolution of an elementary bottom disturbance according to method of characteristics (from De Vriend, 1987).

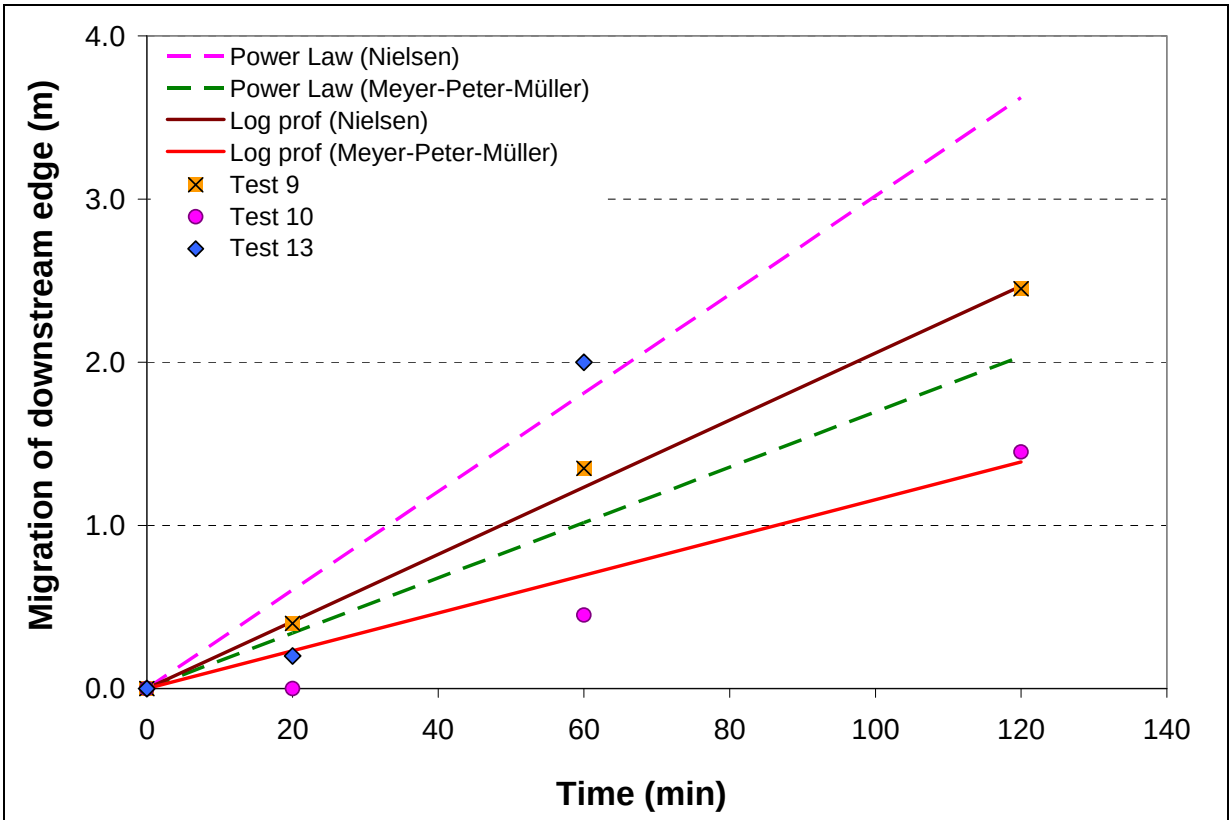


Figure 5.2 Experimental and predicted migration of the downstream end of the mound.

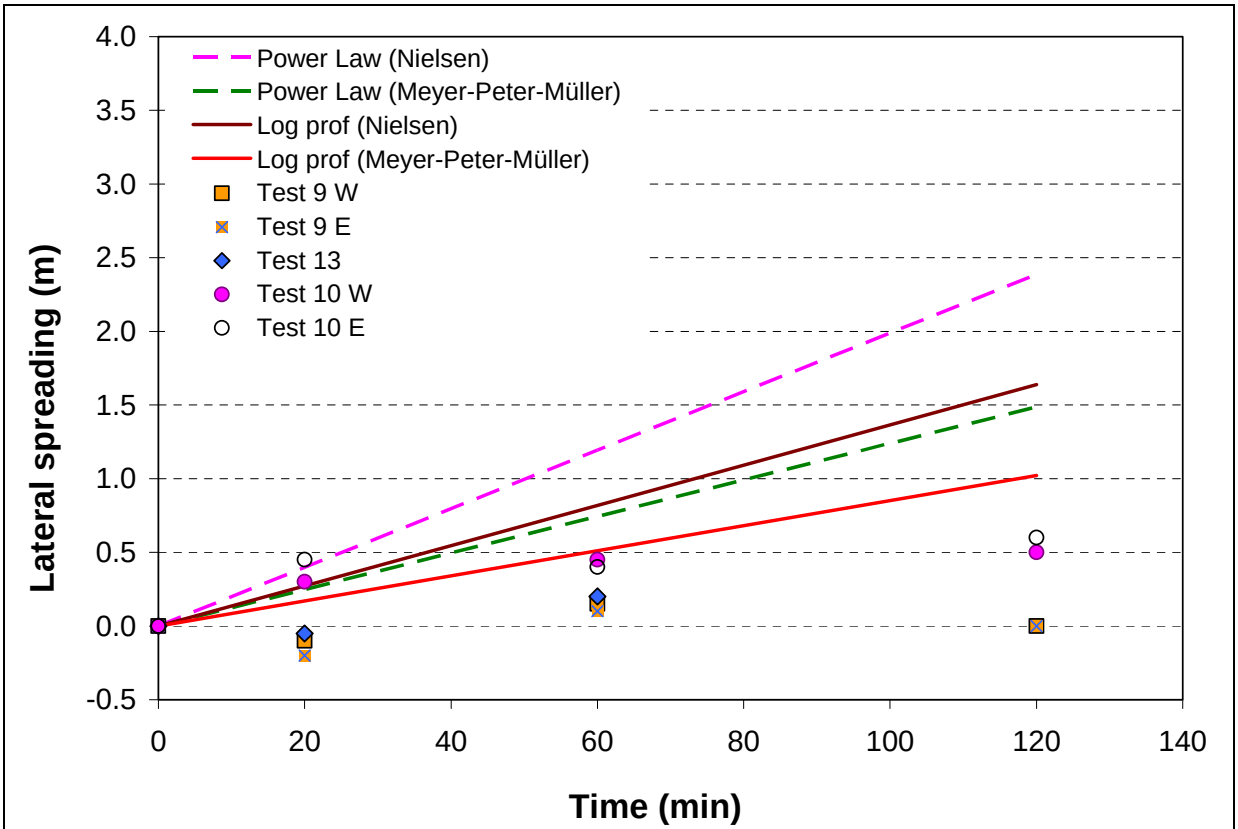


Figure 5.3 Experimental and predicted lateral spreading of the mound. For orientation (W, E) refer to Figure 5.4

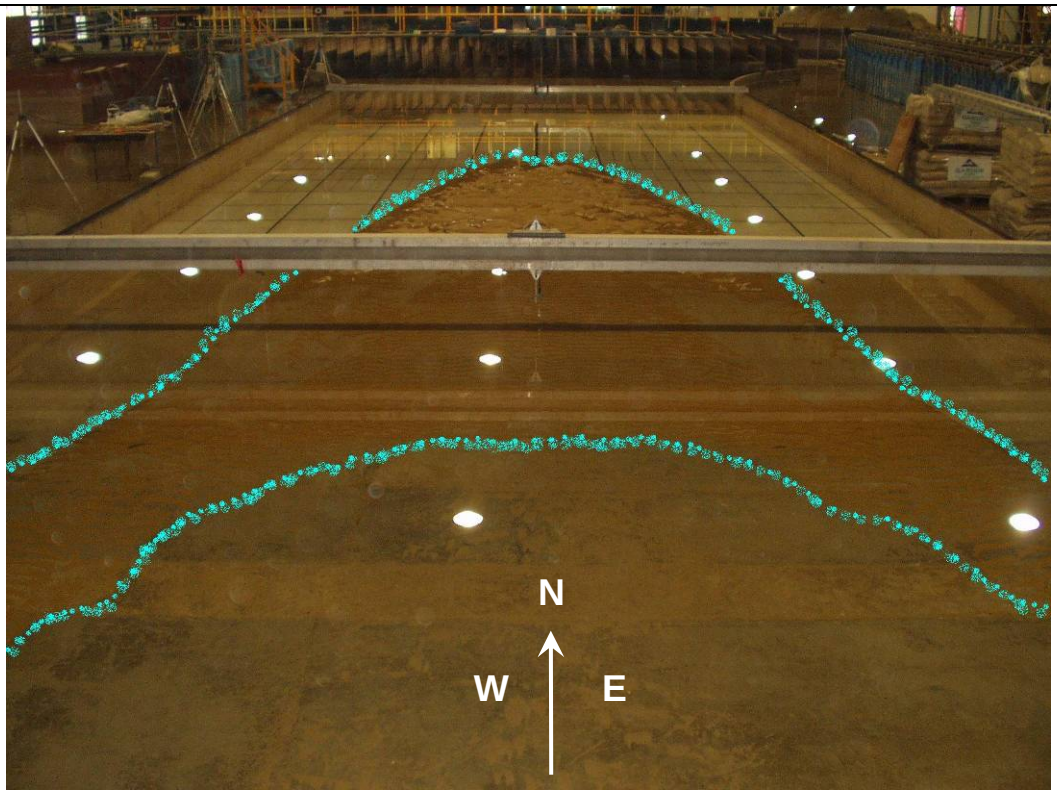


Figure 5.4 Image from Test 9 (Gaussian mound over a fixed bed under steady flow) after 3 hrs. Taken from the South end of the UKCRF. Highlighted in light blue the outline of the sediment footprint. (Incoming flow direction from top of the image)

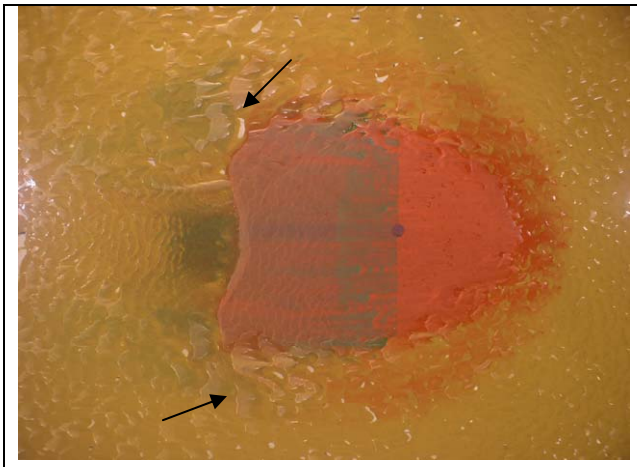

**Figure 4.29** Mound Test 13, $T_E$= 26 min (from Chapter 4)

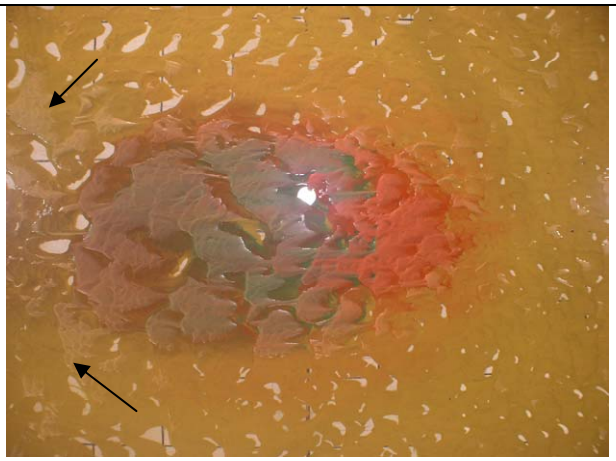

**Figure 4.43b** Mound Test 13, $T_E$= 62 min (from Chapter 4)

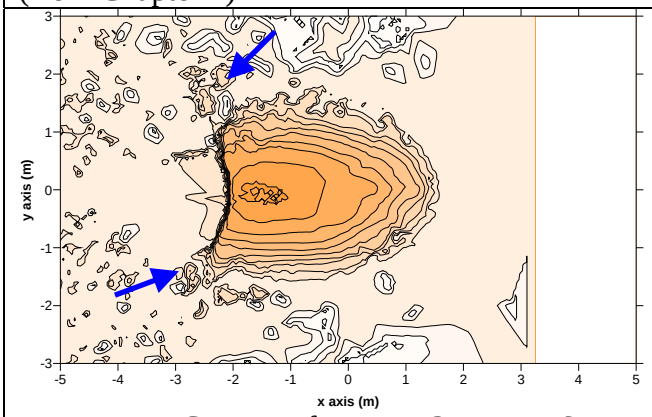


Figure 5.5a Contours for Test 13 at $T_E$= 26 min

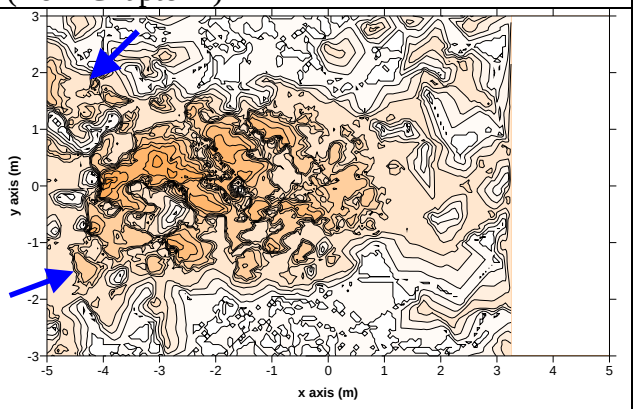


Figure 5.5b Contours for Test 13 at $T_E$=62 min

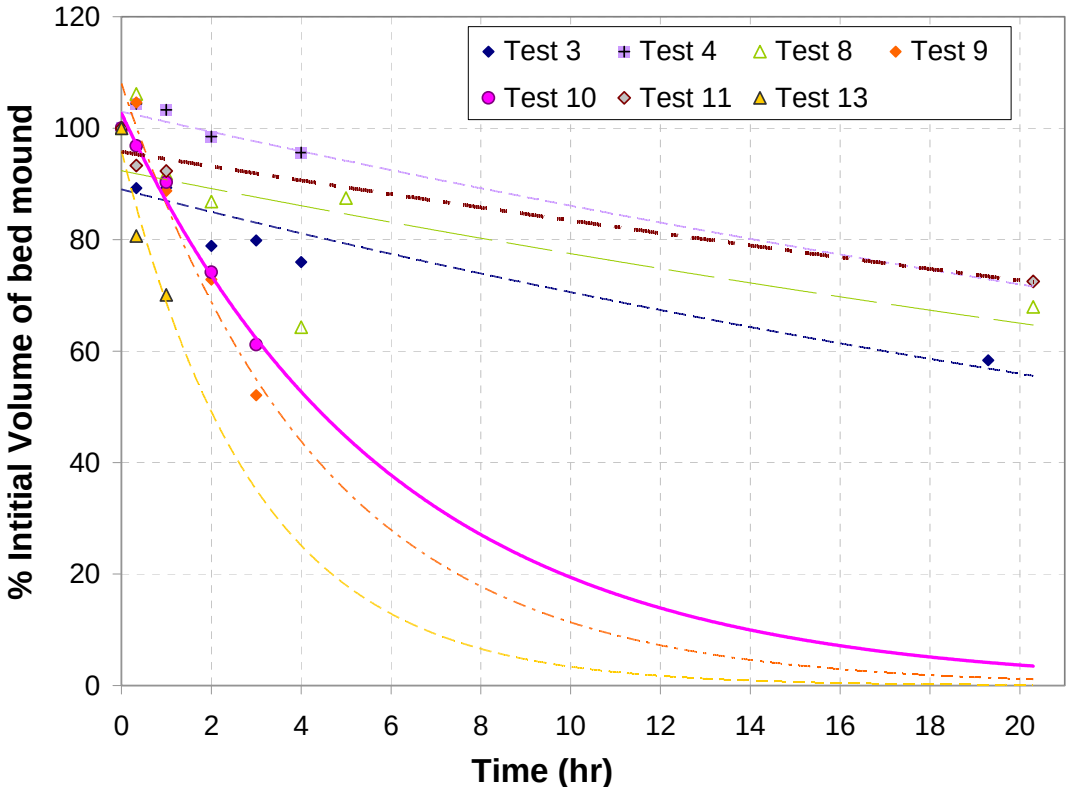


Figure 5.6 Volume decay and fitted exponential decay function of the UKCRF tests analysed.

# 6. NUMERICAL MODELLING

This chapter provides a short description of the numerical model (PISCES) used to predict the morphodynamic evolution of a bed mound. It presents an evaluation of the model results in comparison to the experimental results, and a description of the large scale fit (LSF): a purpose-built tool to pre-process and analyse the experimental and numerical results.

The aim is to use the benchmark experimental data to provide a standard test by which to investigate the performance of a commercial 2-DH morphodynamic model. A secondary aim is to assess what are the benefits and compromises of using a 2-DH numerical model for the problem of the evolution of a bed mound; and whether the predictions are sufficient, and in what context.

Three experimental cases were simulated using PISCES (Chesher *et al*., 1993): a Gaussian mound in steady flow on a fixed bed (Test 9, GS), a Gaussian mound in steady flow on a mobile bed (Test 13, GSM) and a Gaussian mound in tidal flow on a fixed bed (GT, equivalent to Test 8). For convenience, in the present chapter, Test 9 will be referred to as GS, Test 13 will be GSM and Test 8 will be GT.

## *6.1. PISCES – [Telemac2D + Sandflow + Telemorph]*

PISCES is a fully interactive coastal area modelling framework. PISCES is able to simulate the complex flow interaction with the coast and the subsequent changes in bed morphology. The package (whose flowchart is in Figure 6.1), includes a 2D flow model (Telemac2D) coupled with a sand transport model (Sandflow) and a bed update routine (Telemorph).

### TELEMAC 2D (Hervouet, 2003)

Telemac 2D is a finite-element commercial software developed by Laboratoire Nationale d'Hydraulique and Electricité de France (EDF-LNH). It solves the depth-averaged form of the shallow-water equations These equations are used to study flows in rivers, estuaries and seas. The model can simulate depth integrated tidal flows in estuaries and seas including the presence of drying banks. The 2D depth-integrated shallow-water equations are applied to an unstructured grid based on triangular elements, the variables are defined at the nodes (vertices of

the triangles) and a linear variation is assumed within the triangles. There is no particular limit on the time-step for a stable computation but it is best to ensure that the Courant number based on propagation speed is less than about 10. It is found that if the solution is nearly steady then few computational iterations are required at each step to achieve the required level of accuracy, which in TELEMAC is computed according to the actual divergence from the accurate solution. The computation at each time-step is split into two stages, an advective step and a propagation-diffusion step. More details of the development, capabilities and validation tests can be found in (Hervouet, 2003), and URL (www.telemacsystems.com).

### SANDFLOW (Wild, 1988)

The model was developed by HR Wallingford Ltd, and is being developed (Lopez de San Roman Blanco, 2008). The finite-difference sediment transport model uses a total load formula (Van Rijn, 1984) that is the combination of bed load and suspended load transport. A reference/saturated sediment concentration is calculated and compared to the sediment concentration in each grid-cell, the excess or deficit between them will yield the sediment fluxes and whether the sediment will be either eroded or deposited [in $kg/m^2$]. The two modes of transport go into the advection-diffusion subroutine and into the comparison of the saturation and actual concentrations.

### TELEMORPH (Chesher et al., 1993)

The bed update model, takes the deposit information resulting from the Sandflow and converts the weight of sediment per unit area into a thickness of the sediment layer [m].

## *6.2. Large scale Fit, 2-D data pre-processing*

Contour data gathered from the UKCRF experiments indicated the evolution of a bed mound with time. A mixture of scales were present in the contours, small-scale ripple-like features or other small non-scaleable sand features superimposed on the large-scale feature, the bed mound. In order to assess the evolution of the mound (large-scale), it was necessary to separate the two-dimensional Gaussian-like bed mound from the small-scale features. A novel methodology described in detail by Taylor *et al.* (2008) was developed to separate the two coexisting scales

present in the experimental profiles prior to the analysis, providing a better comparison with numerical predictions which do not take these sub-grid scale features into account.

The large scale fit methodology uses a Gaussian function and its first six derivatives (modified to be orthogonal) that are fitted to the experimental data, which separates the large-scale bed mound from the smaller-scale laboratory features and noise. A Gaussian function was chosen because it captures shape, height and width of the original mound. In addition, the mound in the UKCRF experiments had a symmetrical cross-sectional Gaussian shape. The first coefficient (directly from the Gaussian function) $V_{00}$ provides a fit to most of the volume of the mound, and the rest of the coefficients fit small portions of the volume and provide a closer fit to the shape. The Gaussian function and its even derivatives are symmetric with respect to the central axes and provide information about the distribution of the volume along both axes (whether it is spread or not). The odd derivatives provide information about the asymmetry of the distribution of the mound volume along the central axis. If a larger number of derivatives were used, the fit would be more exact. This method is similar in concept to signal analysis using a Fourier transform, where the signal is analysed, its components identified and their contribution quantified.

Once the two scales were separated, two different analyses were carried out for the two different scales. The small-scale feature data were analysed as described by Huang *et al.* (2007), whereas the smoothed large-scale feature was used to make possible a simpler and more like-to-like comparison of the experimental data and the modelling result.

### 6.2.1. The output of the large scale fit

Six characteristic parameters calculated from the large-scale fit (LSF) data are used to compare the experimental data with the numerical predictions. The parameters are: fitted crest height, volume of the fit, the global measure of length in the stream-wise direction ($L_x$) and in the cross-flow direction ($L_y$), global measure of height ($H$), and a measure of the conservation of volume throughout the test (the product of $L_x$, $L_y$, $H$).

$$L_x = \frac{\sqrt{2\pi}}{S_x};\quad L_y = \frac{\sqrt{2\pi}}{S_y};\quad H = V_{00}\sqrt{\frac{S_x S_y}{\pi}} \tag{6.1}$$

where $V_{00}$ is the fit of the volume of the mound using only the Gaussian function and $S_x$ and $S_y$ are the $x$ and $y$ coordinates that make $V_{00}$ fit to the experimental volume. For further detail of fitting of the data see Taylor *et al.* (2008).

### 6.2.2. Suitability of the LSF of the experimental data to represent the experimental data.

The quality of the method used to represent the experimental data was checked by applying the large-scale fit to the experimental data and comparing the results to the raw experimental data. The 3D-surface, 2D-contours and cross sections through the stream-wise and cross-flow centrelines were plotted to consider the suitability of the fit.

The experimental fitted volumes and the raw contour volumes (Tables 6.1, 6.2 and 6.3) show very good agreement. The errors between the raw and fitted volumes are of the order of 1 % or less in Test GS and Test GT, and < 3 % in Test GSM. Figures 6.2 to 6.4, show the contours of the raw data (a) and the large scale fit (b), and the 3D-surfaces of the raw data (c) and fitted data (d). During the early stages of the tests the mound and the small-scale features can be identified at first glance. With the increasing elapsed time, the two scales are more difficult to identify and separate from each other (e.g. Figure 6.4 GT, $t$ = 4 hr). Figures 6.2, 6.3 and 6.4 also indicate that the large scale fit captures the general shape of the mound and smoothes out the small scale features, in both tidal and steady flow cases. When the mound migrated downstream, in the steady flow case the large scale fit migrated in the same direction. Removal of small scale features helps us follow the evolution of the large-scale mound, and then carry out a comparison with the numerical modelling predictions. Figures 6.5, 6.6 and 6.7 present cross sections of the raw experimental and the fitted experimental bed profile data along the stream-wise ($y$ = 0) and cross-flow ($x$ = 0) basin centrelines. Different lines represent the bed profiles at different times, typically: $t$ = 0, 20 min, 1 hr, 3 hr and so on. The bed profile cross section of the fit and the raw data agree very well, in some cases overlying each other ($t$ = 0, 20 min in Figure 6.6). In the later stages of the tests, when ripples become more important ($t$ = 300 min in Figure 6.7) the fit properly reproduces the general shape of the mound while removing the ripples.

For the GS test (Figure 6.5) the general shape of the mound is well represented/described by the fit; the ripples disappear and the fit captures the overall shape of the large scale feature;

with time the mound decreased in height and migrated downstream, and this evolution is captured by the fit. However the fit is not so successful in representing the sharp back edge present in the experimental data from $t$ = 20 min onwards. Figure 6.6 presents the results for the comparison between the fit and the raw data in Test GSM. The fit shows satisfactory agreement with the raw data. As in Test GS, at $t$ = 2 hr (Figure 6.5), in order for the fit to capture the volume of the mound, the fit artificially smoothes the very sharp back step. At $t$ = 3 hr (Figure 6.5), the back edge of the mound is not visible in the images, and some of the mound volume is lost. The large scale fit made up for this and approximated the entire shape. The results for Test GT also show close agreement (Figure 6.7). At $t$ = 20.3 hr the mound seems mostly composed of ripples at first glance; the fit removes the detail and leaves the underlying shape of the mound.

## *6.3. Model set up*

The hydrodynamic model domain covered the width of the central area of the basin and 10 m either side of the centreline. The domain area was 20 by 9 m (Figure 6.8) with a refined region with approximate grid cell size between 0.2 to 0.25 m (from -10 to 3 m in the $x$-axis), and a coarser zone with grid cell size between 0.45 and 0.5 m (from 3 m to 10 m along the $x$-axis). The reason for the selective refinement was to take into account the direction of the mound migration in the steady flow (and the slight asymmetry in the tidal flow field), and to decrease the computational costs. Three cases were modelled with PISCES: i) a Gaussian mound in steady flow on a mobile bed (Test 13); ii) a Gaussian hill in steady flow on a fixed bed (Test 9); and iii) a Gaussian hill under tidal flow conditions on a fixed bed (GT, Test 8).

**Boundary conditions**

In the steady flow case, the boundary conditions were: (i) a prescribed upstream discharge, ramped to ~ 1 $m^3/s$ for the first 50 min and (ii) a constant level (0.20 m) downstream boundary (Figure 6.9). In the tidal case, the boundary conditions at both ends of the model grid were defined as discharges, in phase. These were derived from the reconstructed upstream flow velocity recorded during the experiments by the two ADVs. The values of the recorded velocity were increased by 5 % in order to obtain a value of flow velocity closest to the experimental in

the central area of the basin (as calibration parameter). The used of the recorded velocity helped to capture the influence of the slight asymmetry of the flows in the morphology (Figure 6.10).

**Model parameters**

The bed roughness coefficient ($f$) is a function of the Nikuradse equivalent grain roughness ($k_s$), is given by:

$$f = \frac{1}{32} \frac{1}{\left[\log_{10}\left(14.8/ks\right)\right]^2} \tag{6.2}$$

and was calculated using the conditions of the experimental set up.

The representation of the turbulence in the model was through an ELDER scheme. The ELDER model (Telemac2d user manual, 2002) offers the possibility of specifying different viscosity values along and across the current ($K_l$ and $K_t$ respectively). The formulae used are:

$$K_l = a_l u_* H \quad \text{and} \quad K_t = a_t u_* H \tag{6.3}$$

Where $u_*$ is the friction velocity and $H$ the water depth, and $a_l$ and $a_t$ are the dimensionless dispersion coefficients equal to 6 and 0.6 respectively.

**Fixed and mobile bed representation**

In the case of the mobile bed, the bed was defined as a layer of material of 10000 kg/m$^2$, using a sediment of typical density 2650 kg/m$^3$ should be equivalent to a layer of 3.77 m. The sediment in this layer could be eroded or deposited. In the case of the fixed bed, the mound was represented with a layer of mobile sediment, but the bed was defined in such a way that could not be changed and was not erodible.

## *6.4. Model results*

The performance of the model was assessed with respect to the benchmark data of the evolution of a bed mound for a small range of varying conditions, GS, GSM and GTM. The evolution of the mound (model vs. experiments) was studied by comparing a number of integral mound properties: the evolution of the centroid coordinates; the decay in height and volume of the mound; the stream-wise and cross-flow centreline cross-sections of the large scale fit from the experimental and model data; and the six characteristic parameters of the large scale fit.

### 6.4.1. Gaussian mound in steady flow over a fixed bed (GS, Test 9)

Figure 6.11 presents the time evolution of the *x*, *y* and *z* centroid coordinates of the experimental and the predicted mounds. The predicted migration of the centroid after 3 hr was 1.5 m, in that time the experimental mound migrated 2.5 m. The model under-predicts the migration of the centroid along the stream-wise direction (*x*-axis) by a factor of about 1.5. The evolution of the *y* centroid coordinate gives an idea of the asymmetry in the cross-flow spread of the mound. Surprisingly the model predicted a slight migration towards the positive *y*-axis, whilst the experiments showed the centroid remained very close to $y = 0$. The model differs from the experiments by a factor of ten (the values being: 0.25 and 0.025 m); it should be noted however that the values are very small. After 3hr the model predicted a height of 0.009 m, whilst the measured height was 0.018 m. The decay of the centroid height over time was more pronounced in the model, a factor of two smaller than the experiment. From the model results (Figure 6.11), a faster decrease in centroid height and lower predicted migration in *x* indicates higher generalised erosion rates, hence the poor agreement of migration rate along the *x*-axis.

Figure 6.12 presents a comparison between the experimental and model predictions of the integral parameters of the LSF. The model overestimated the rate of decrease in crest height, also the volume decrease through the test. The predicted LSF crest height and volume evolution in Figure 6.12 showed a striking similarity with the experiments. The prediction of $L_x$ saturated at about 12 m, whilst for the experimental mound was ~3.4 m. $L_x$ was thus overestimated by a factor of 3.5. The mound is predicted to expand less in the stream-wise direction than in the experiments. The prediction of $L_y$ was underestimated by a factor of ~1.5. The prediction of the decaying trend of *H* differed with the experiments by a factor that grows with time up to three, as the values decreased to become smaller the prediction was reasonable. With regard to the product $H\text{-}L_x\text{-}L_y$ the model performs well, the volume (mass) of the mound is conserved.

### 6.4.2. Gaussian mound in steady flow over a mobile sand bed (GSM, Test 13)

Figure 6.13 presents the time evolution of the centroid coordinates. The simulation ran for an hour longer than the experiment, so the prediction for 2 hr could be investigated. Regarding the migration of the centroid along the *x*-axis, there is almost total agreement. The measured and

predicted migrations along the *y*-axis were also very similar (the variations were of the order of 0.0025 m, hence the error between measurement and prediction is not significant). The initial prediction of the centroid height did not coincide with the experimental value, and the decrease in height after 20 min was over-predicted, the overall decrease in height of the centroid after 1 hr was predicted correctly. The influence of the mobile bed (i.e. bed roughness and input of sediment) seemed able to damp the accelerated decrease of the vertical position of the centroid, in comparison to the fixed bed case (GS). Overall the predicted migration of the centroid was very satisfactory in comparison to the experimental migration. Figure 6.14 compares the LSF characteristic properties for the experiments and model predictions. The prediction of decay of mound crest height agreed with the experiment. The evolution of the experimental volume was not well represented by the model. The model predicted an initial increase of the volume, and over-predicted the volume by a factor of ~1.5. The reason for this disagreement was not clear. The plot of predicted evolution of crest height and volume in a log-log scale indicated that the crest height was in relatively close agreement with the experiments, but the volume was consistently over-predicted by the model by a factor of two. The stream-wise global measure of length of the mound ($L_x$) was reasonably well predicted by the model, and so was the global measure of width. The evolution of $H$ was well predicted by the model, although the value is slightly overestimated at the end of the test (1 hr). The prediction of conservation of mass differed from the experiments by a factor of about two, and the reason for this was not understood.

### 6.4.3. Gaussian mound in tidal flow over a fixed bed (GT, Test 8)

Figure 6.15 shows the time evolution of *x*, *y* and *z* centroid coordinates of the experimental and predicted evolution of the mound over a fixed bed (GT). The centroid migration in the *x*-axis (stream-wise direction) was slightly over-predicted by the model, although the overall prediction was reasonable (Figure 6.15). The prediction beyond 10 hr (long-term) was slightly deceptive, as by that time there was hardly any sediment left in the numerical simulation. The migration of the centroid in the cross-flow direction was very small, just a few centimetres. The model predicted well the near lack of migration in the *y*-axis. The decaying rate of the centroid height (*z* coordinate) was over-predicted by the model. The last three experimental values indicate that the rate of decrease in height of the centroid converges and slows down after some time (the

mound adapts to the conditions). The predicted centroid height decreased about twice as fast as the experiment. However, the simulation overestimated greatly the decay in mound height. Reasons for this will be discussed in Section 6.4.4.

Figure 6.16 indicates the evolution of the characteristic properties of the LSF. The model predicted a higher decay rate for the height and volume than the experiment. The crest height (GT) predicted at 10 hr was equivalent to the experimental height at the end of the test (20.3 hr); this meant there was a factor of 2 difference between the decay rate of the experiments and predictions. The predicted volume after 5 hr was similar to the experimental volume after 20.3 hr (this is clear from the log-log plot of volume). The decay of height and volume in the log-log plots shows that the GT predictions diverged greatly from the experiments after 5 hr. GT prediction gave larger $L_x$ than the experiments in the first few hours, although the last value (20.3 hr) was under-predicted. GT predicted a varying $L_y$ that decreased with time (the modelled mound spread further). The decay trend of $H$ was reasonably well represented up to 5 hr. After 2 hr the experimental results and model prediction for the product $H\ L_x\ L_y$ started diverging from the experimental values, and continued diverging further with time.

### 6.4.4. Discussion

The fitting method of the raw experimental data is successful in that it smoothes and removes the small detail and provides a good representation of the underlying mound. The fit in the current state, captures well the volume and the general shape of the mound, although does not reproduce properly the mound's sharp back step. If the number of derivatives and coefficients were to be increased, the fit would improve. The LSF provides a number of integral parameters that can be used to compare experimental data with model results.

There was no doubt that, 3-D flow features occurred over, and in the proximity of the mound during the experiments. These were typically connected to ripples and lateral dents of the mound where flow separation and wakes occurred. The 3-D processes were important in the evolution of local features on the mound, and affected the long-term ($t$ > 3 hr) overall shape of the mound and its final fate. The 2-DH model, however simplistic, reproduces well the overall morphodynamic evolution of the mound. It provides a reasonable prediction of the general shape, migration and volume changes with lower computational cost than a fully 3-D model.

The use of analytical solutions (Chapter 5) can be used to provide a first estimate, and a 2-DH model can provide non-detailed account of the evolution of the mound.

The sediment transport model uses a total load formula developed by Van Rijn (1984). The total load transport is calculated from:

$$q_t = q_b + q_s \tag{6.4}$$

where $q_t$ is the total load sediment transport, $q_b$ is the bedload transport and $q_s$ is the transport due to suspended load, which are defined as follows:

$$q_b = 0.005\ \overline{U} H \left( \frac{\left(\overline{U} - \overline{U}_{cr}\right)}{\left((s-1)\ g\ d_{50}\right)^{1/2}} \right)^{2.4} \left( \frac{d_{50}}{H} \right)^{1.2} \tag{6.5}$$

and

$$q_s = 0.012\ \overline{U} H \left( \frac{\left(\overline{U} - \overline{U}_{cr}\right)}{\left((s-1)\ g\ d_{50}\right)^{1/2}} \right)^{2.4} \left( \frac{d_{50}}{H} \right) \left(D_*\right)^{-0.6} \tag{6.6}$$

where $D_*$ is the dimensionless grain size, $H$ is the water depth, $d_{50}$ is the median grain size, $s$ is the ratio between densities of sediment and water, $\overline{U}$ is the flow velocity, and $\overline{U}_{cr}$ is the threshold velocity defined as:

$$\overline{U}_{cr} = 0.19\ \left(d_{50}\right)^{0.1} \log_{10}\left( \frac{4H}{d_{90}} \right) \quad \text{for } 0.1\ \le d_{50} \le 0.5 \text{ mm} \tag{6.7}$$

where $d_{90}$ is the grain diameter for which 90 % of the grains are finer. The total load model calculates the suspended and bedload transport fractions. It assumes most of the transport occurs as suspended load, and the bedload is a small percentage of the total transport. However, the transport during the experiments was mainly by bedload. To investigate the difference in sediment transport with the assumption of total load and only bedload, the results from Eq. 6.4 were compared to those from Eq. 6.5. Using Van Rijn's sediment transport method, the calculated ratio $q_b/q_s$, or $q_b/q_t$ is about 10 %. This can partly explain the predicted higher rates of decay in mound crest height and volume in comparison to the experiments.

The existence of ripples and other small bed features in the experiment increased the roughness of the bed. Hence, the near-bed currents experienced a degree of energy loss due to these features, which affect the sediment loading capacity of the flow. Ripples are sub-cell scale features, therefore they were not represented in the model and the change in bed roughness that

they yield was not included in the model calculations. Therefore their effect in the sediment transport capacity of the flow was not taken into account, and a higher rate of erosion/transport would be expected in the model in comparison to the experiments. Furthermore, at the end of the experiment the ripples became a storage zone for the sediment. The mound lost its integrity, although a sizeable portion of the sand remained. This was not the case in the model results where the mound decreased in height and dispersed leaving a footprint similar to the initial footprint of the mound.

| Time (hr) | Raw Volume ($m^3$) | % of initial volume raw | Large-scale-fit volume (LSF) ($m^3$) | % of initial volume LSF | % error |
|---|---|---|---|---|---|
| 0 | 0.659 | 100.0 | 0.658 | 99.7 | 0.3 |
| 0.33 | 0.693 | 105.1 | 0.687 | 104.2 | 0.8 |
| 1 | 0.587 | 89.0 | 0.583 | 88.4 | 0.7 |
| 2 | 0.489 | 74.2 | 0.489 | 74.2 | 0.0 |
| 3 | 0.344 | 52.1 | 0.342 | 51.9 | 0.5 |

**Table 6.1 Volume of the mound for experimental raw data and large scale fit, Test 9 (GS)**

| Time (hr) | Raw Volume ($m^3$) | % of initial volume raw | Large-scale-fit volume (LSF) ($m^3$) | % of initial volume LSF | % error |
|---|---|---|---|---|---|
| 0 | 0.625 | 100.0 | 0.629 | 100.6 | -0.6 |
| 0.33 | 0.505 | 105.1 | 0.518 | 82.9 | -2.6 |
| 1 | 0.448 | 89.0 | 0.440 | 70.4 | 1.9 |

**Table 6.2 Volume of the mound for experimental raw data and large scale fit, Test 13 (GSM)**

| Time (hr) | Raw Volume ($m^3$) | % of initial volume raw | Large-scale-fit volume (LSF) ($m^3$) | % of initial volume LSF | % error |
|---|---|---|---|---|---|
| 0 | 0.682 | 100.0 | 0.680 | 99.7 | 0.3 |
| 0.33 | 0.723 | 106.0 | 0.726 | 106.5 | -0.5 |
| 1 | 0.627 | 92.0 | 0.626 | 91.7 | 0.4 |
| 2 | 0.591 | 86.7 | 0.587 | 86.2 | 0.6 |
| 4 | 0.588 | 86.3 | 0.583 | 85.5 | 0.9 |
| 5 | 0.596 | 87.5 | 0.591 | 86.6 | 1.0 |
| 19.3 | 0.463 | 67.9 | 0.462 | 67.8 | 0.1 |

**Table 6.3 Volume of the mound for experimental raw data and large scale fit, Test 8 (GT)**

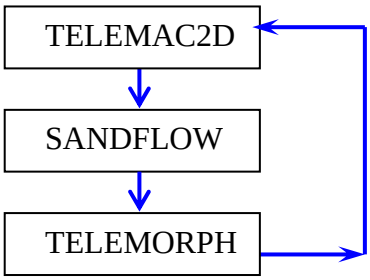


Figure 6.1 Diagram of the framework of PISCES

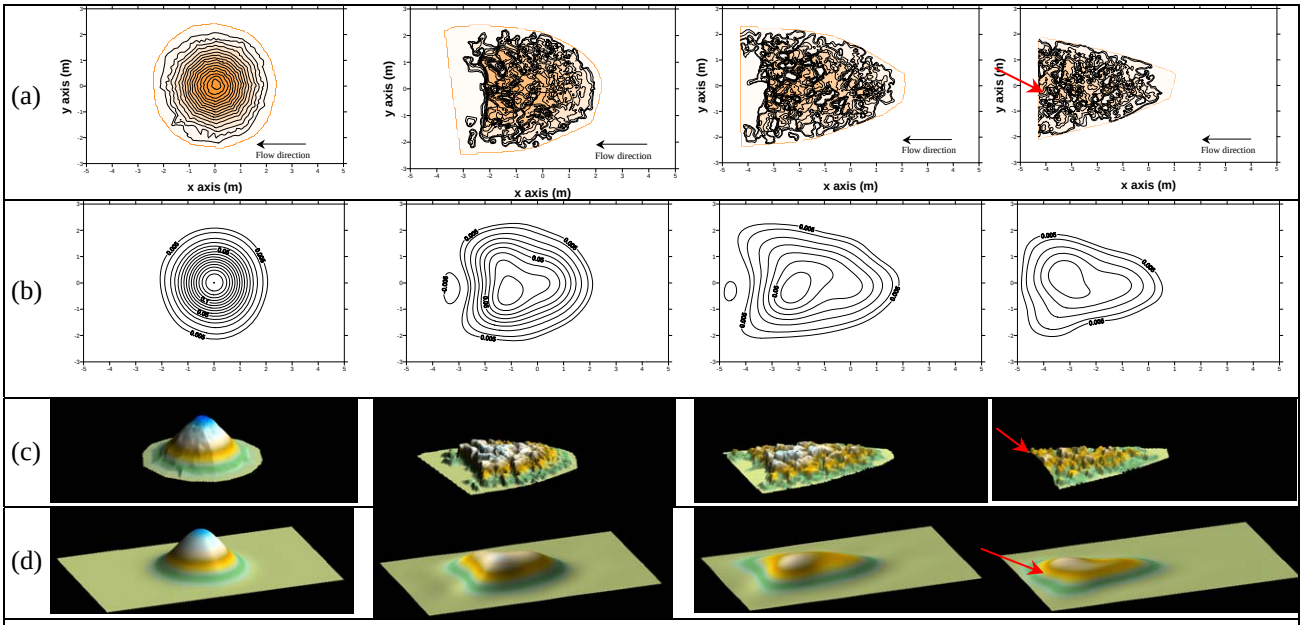


Figure 6.2 Test GS, comparison of profile contours between raw data (a) and fitted data (b), and between 3-D surface of profile raw data (c) and fitted data (d). $t$ =0, $t$ = 20 min, $t$= 1 hr, $t$ = 3 hr. Arrows point at sharp back edge

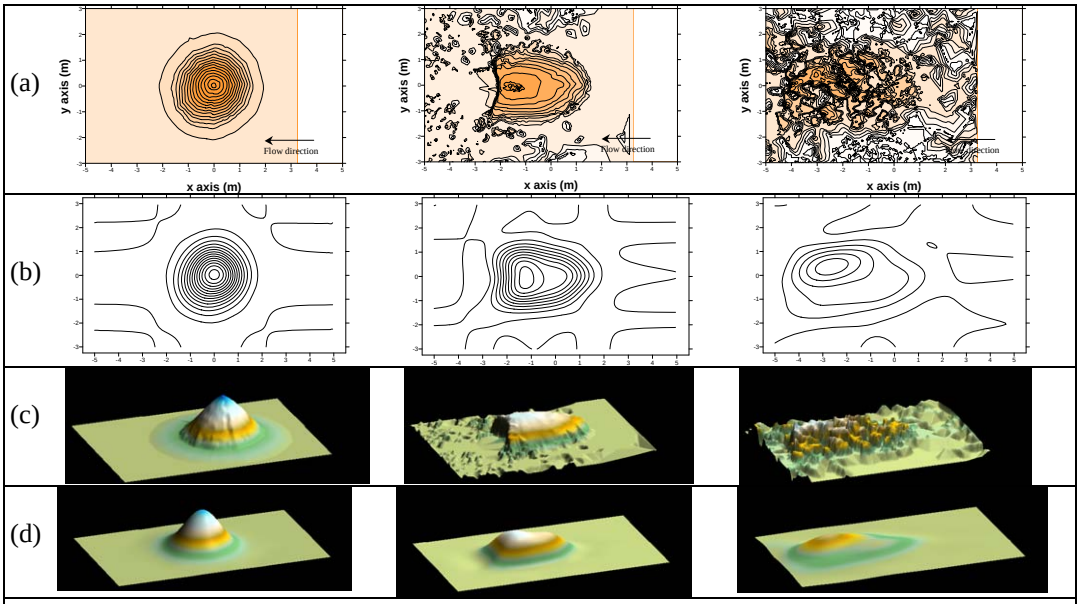


Figure 6.3 Test GSM, comparison of profile contours between raw data (a) and fitted data (b), and between 3-D surface of profile raw data (c) and fitted data (d). $t$ = 0, $t$= 20 min, $t$= 1 hr.

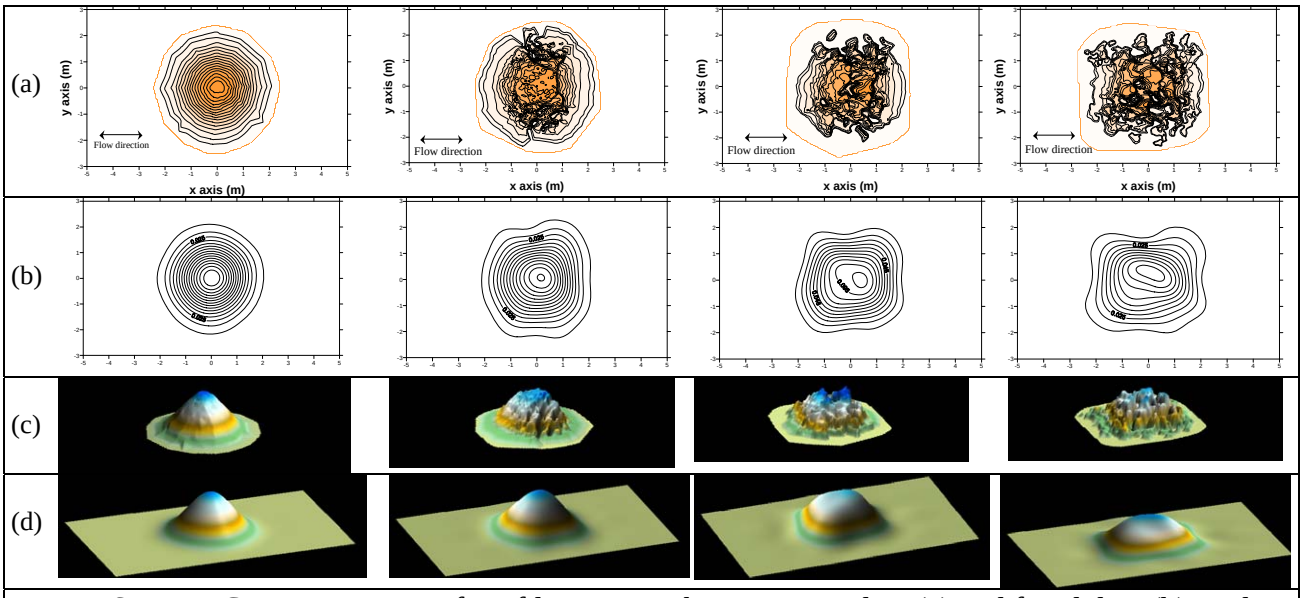


Figure 6.4 Test GT, comparison of profile contours between raw data (a) and fitted data (b), and between 3-D surface of profile raw data (c) and fitted data (d). t =0, *t* = 20 min, *t*= 1 hr, *t* = 2 hr.

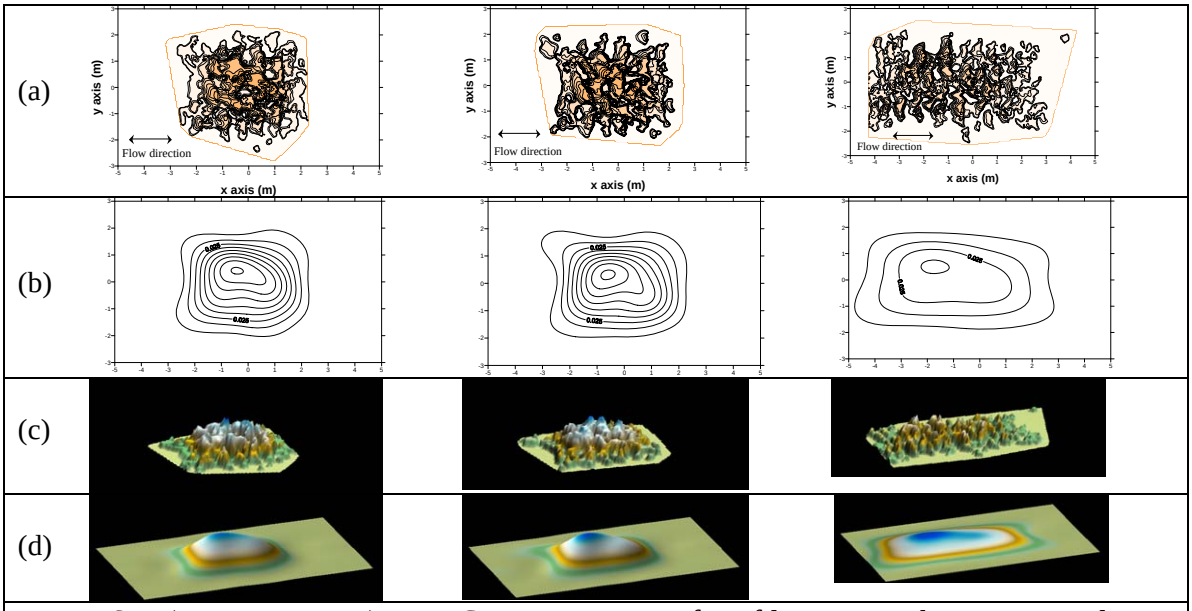


Figure 6.4 (continuation…) Test GT, comparison of profile contours between raw data (a) and fitted data (b), and between 3-D surface of profile raw data (c) and fitted data (d). *t* = 3 hr, *t* = 5 hr, *t*= 20.3 hr.

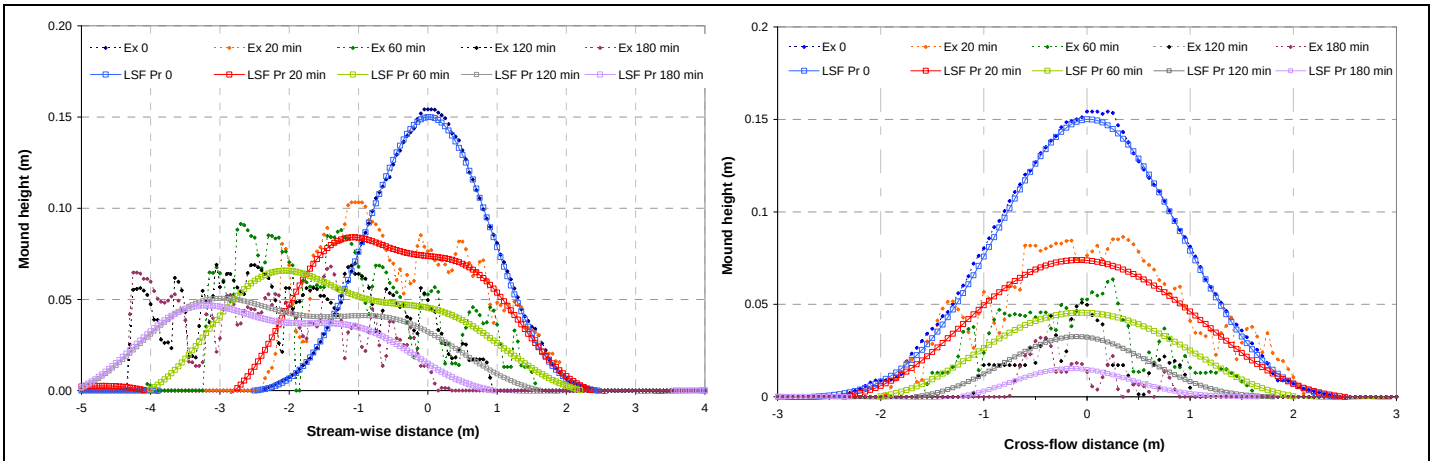


Figure 6.5 Test GS comparison of experimental raw and fitted bed-profiles (y=0 and x=0), (Test 9).

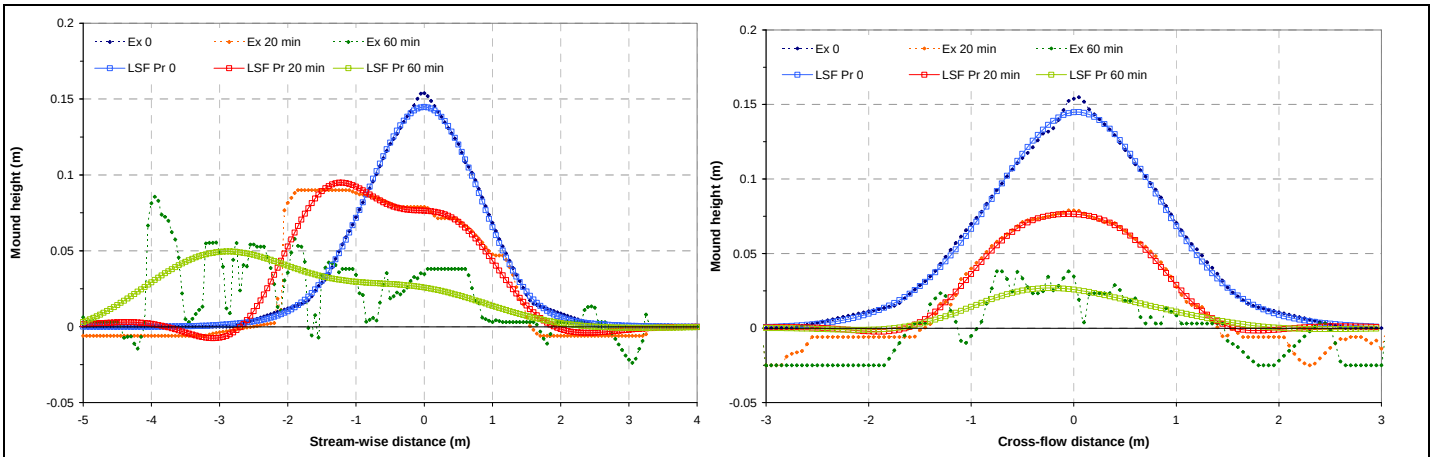


Figure 6.6 Test GSM comparison of experimental raw and fitted bed-profiles (y=0 and x=0), (Test 13).

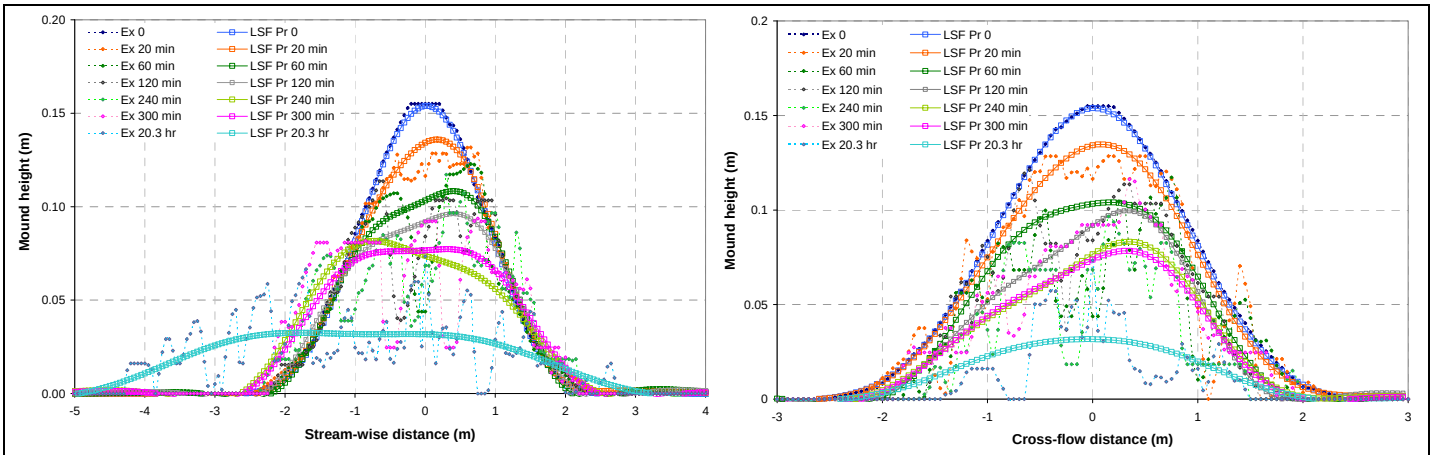


Figure 6.7 Test GT comparison of experimental raw and fitted bed-profiles (y=0 and x=0), (Test 8).

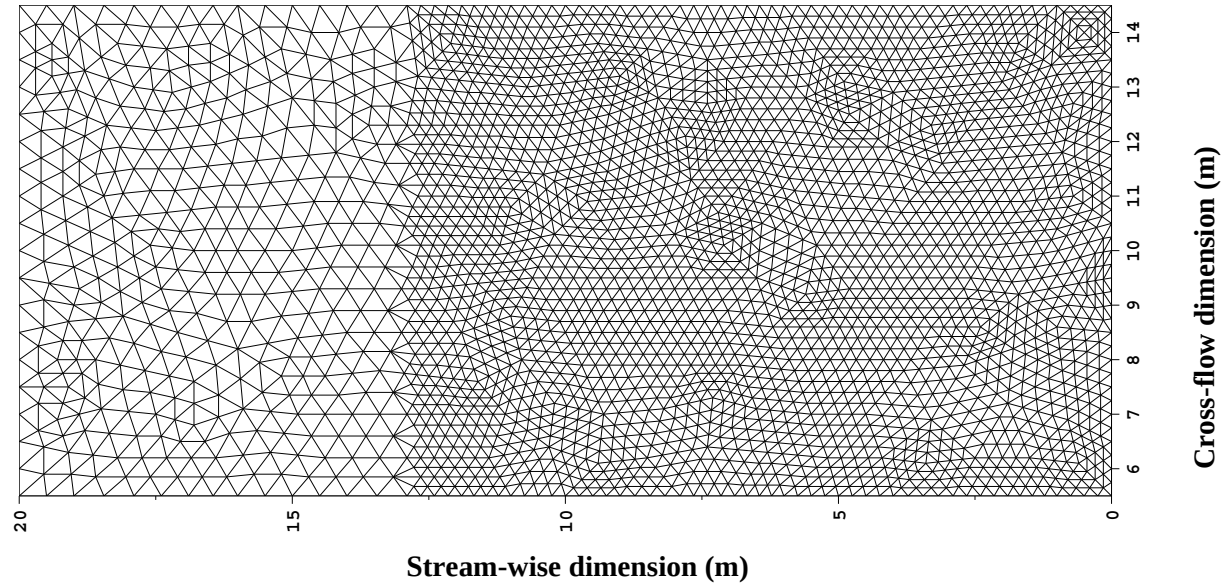


Figure 6.8 Telemac2D grid representing the UKCRF

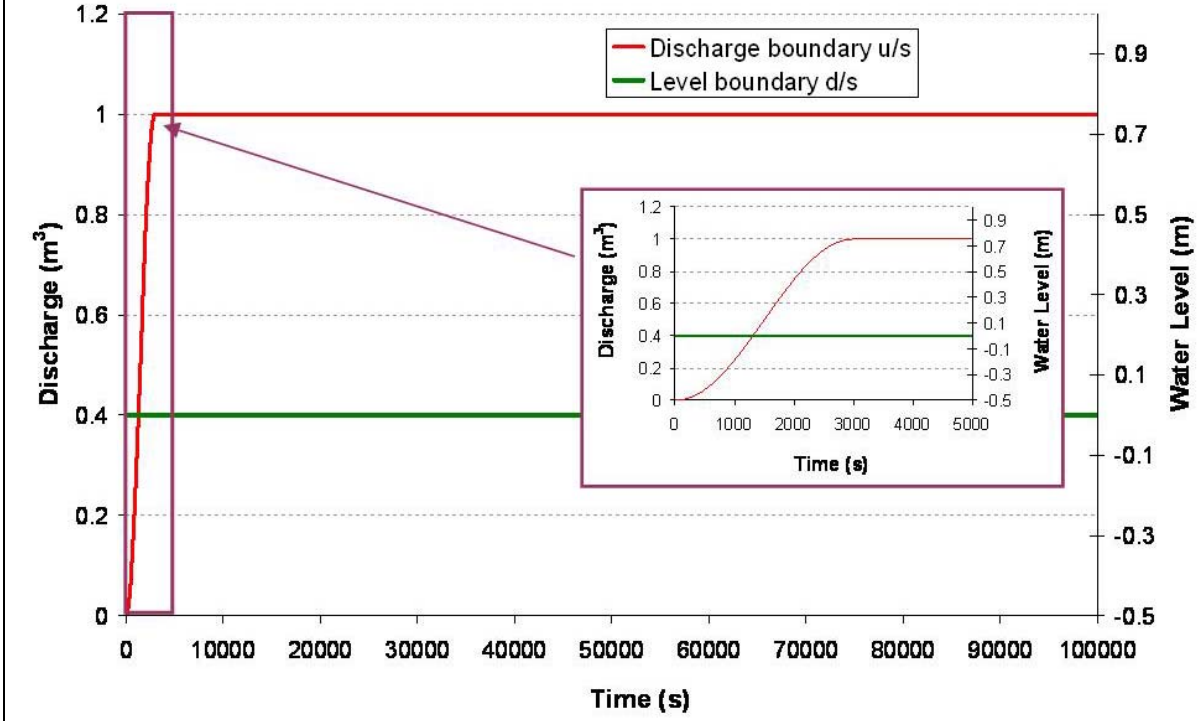


Figure 6.9 Plot of steady flow boundary conditions used in Tests 9 and 13 (inset: detail of ramping)

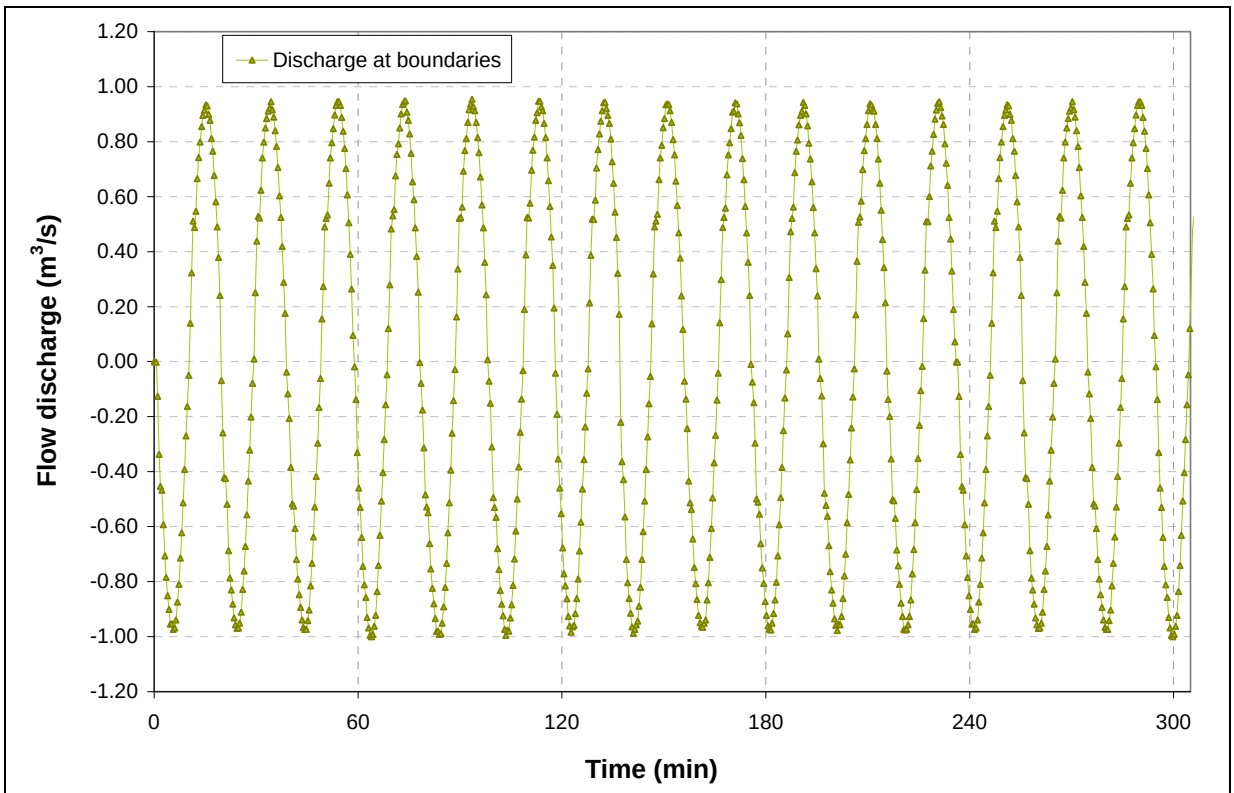


Figure 6.10 - Boundary condition GT, discharge from reconstructed flow velocity

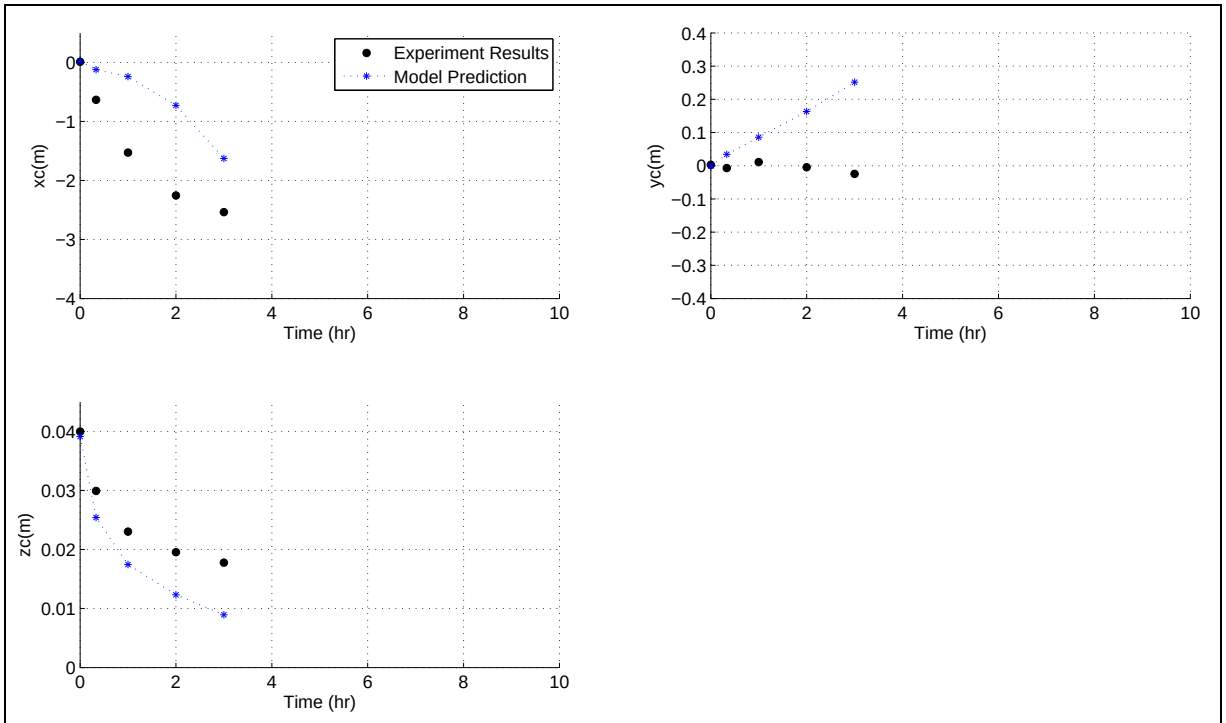


Figure 6.11 Evolution of centroid coordinates with time Test GS

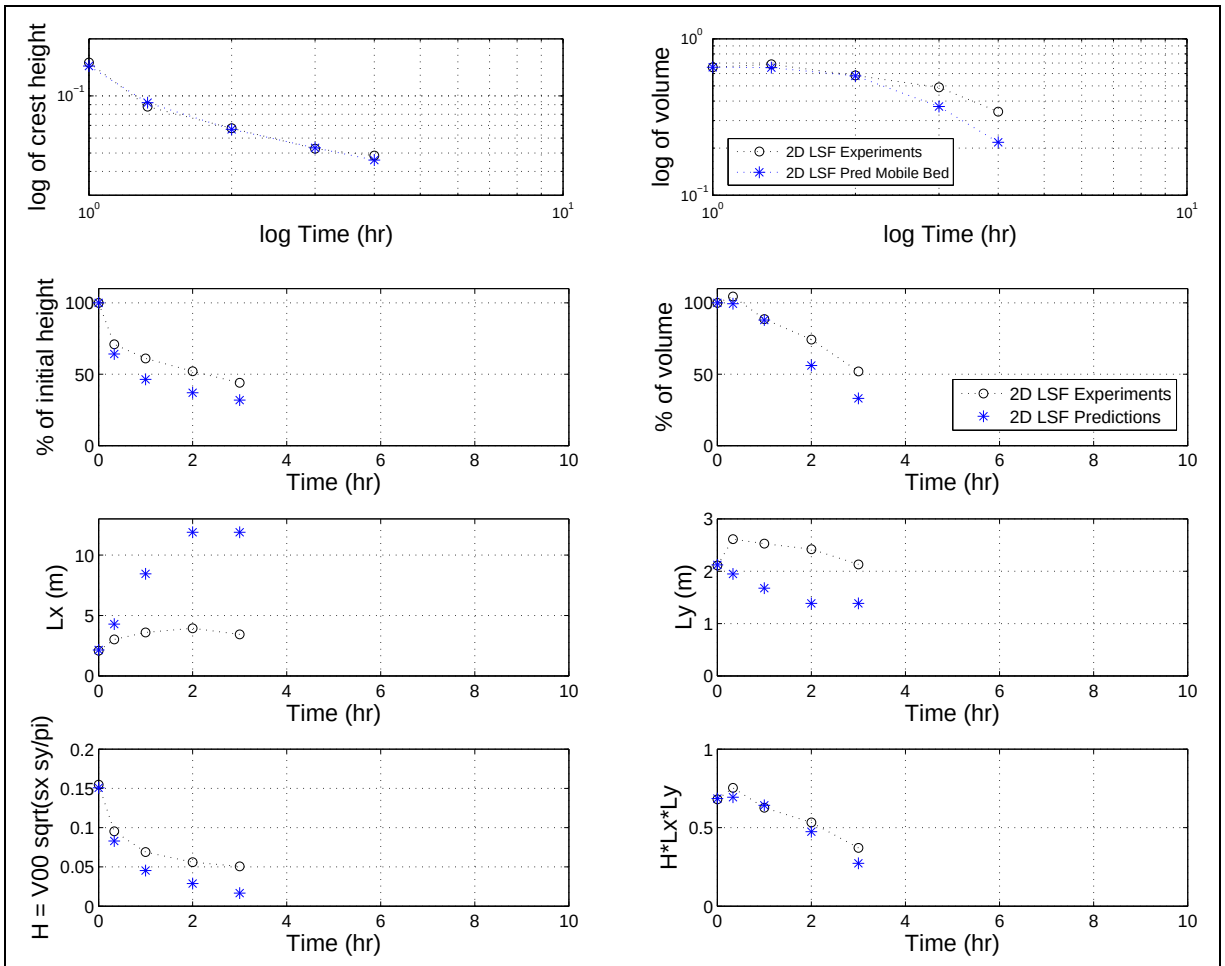


Figure 6.12 Characteristic parameters of the LSF for Test GS

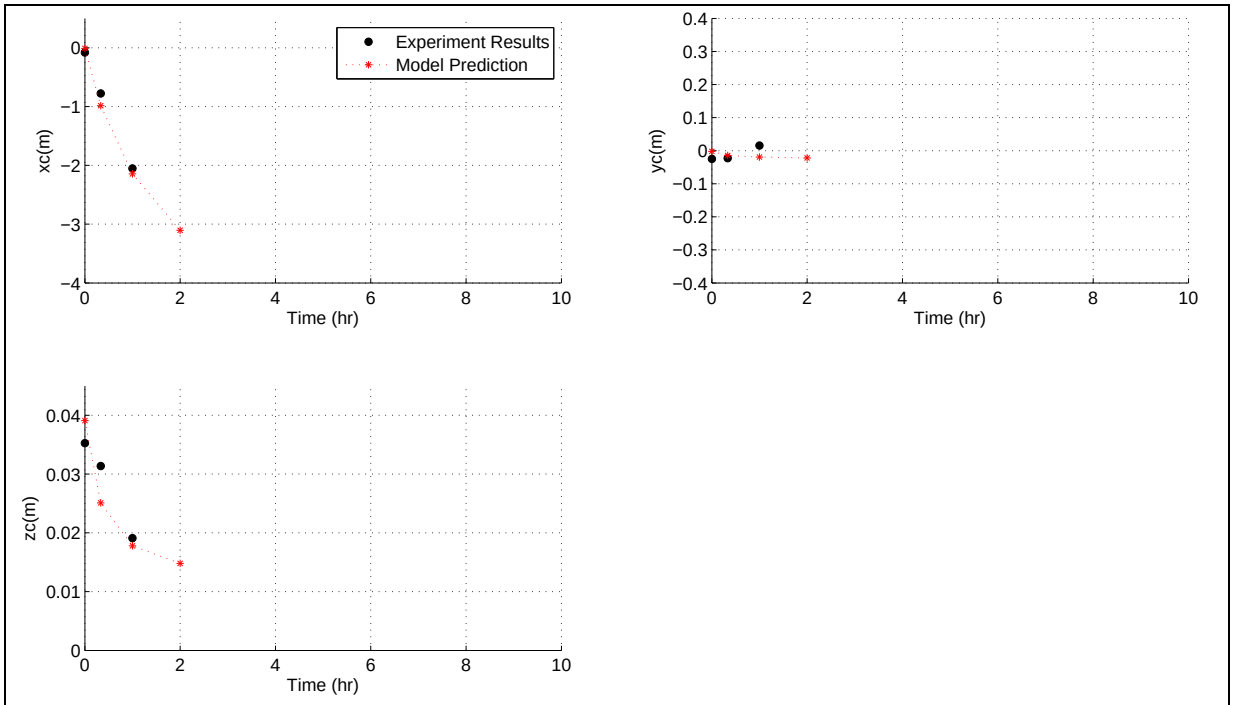


Figure 6.13 Evolution of centroid coordinates with time Test GSM

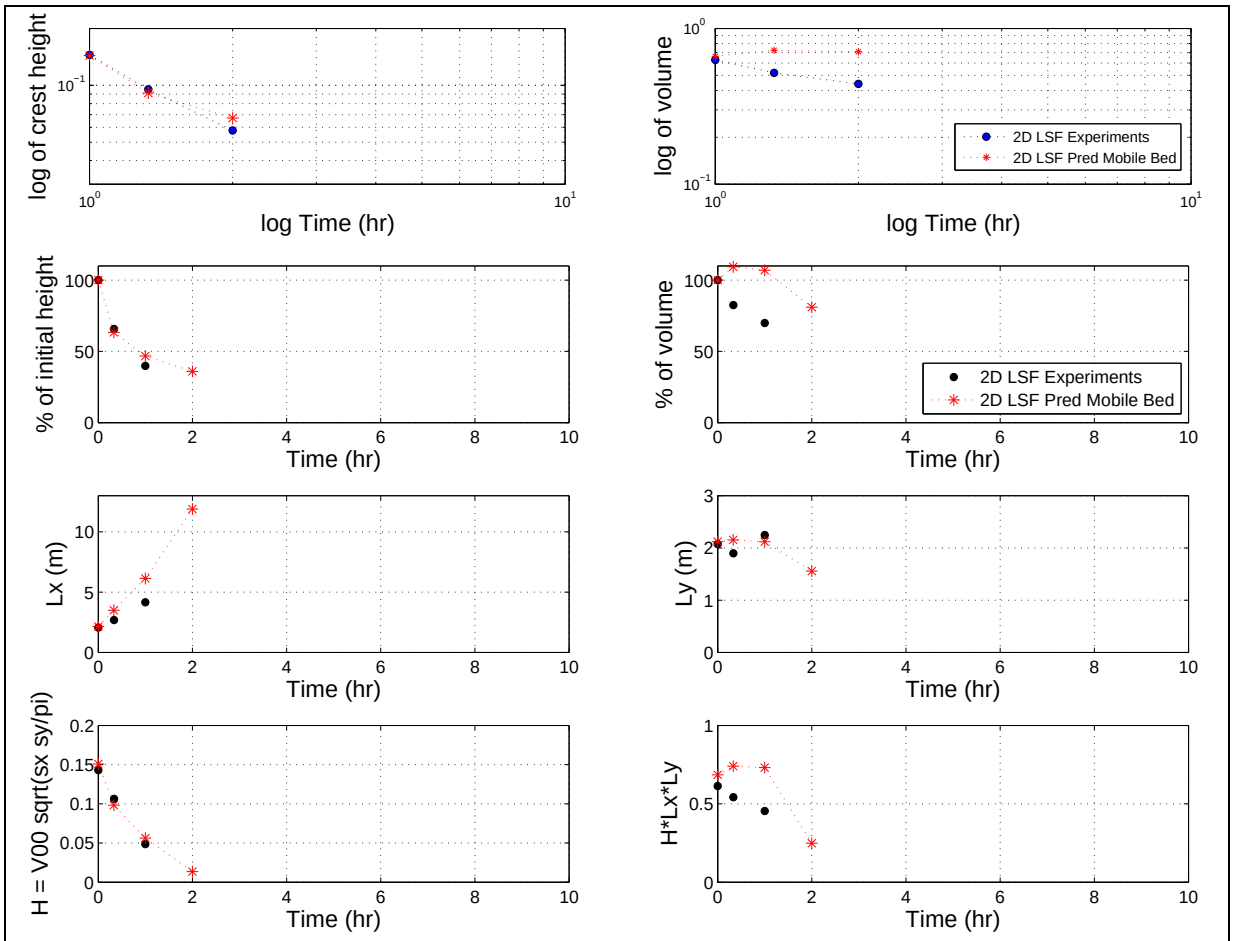


Figure 6.14 Characteristic parameters of the LSF for Test GSM

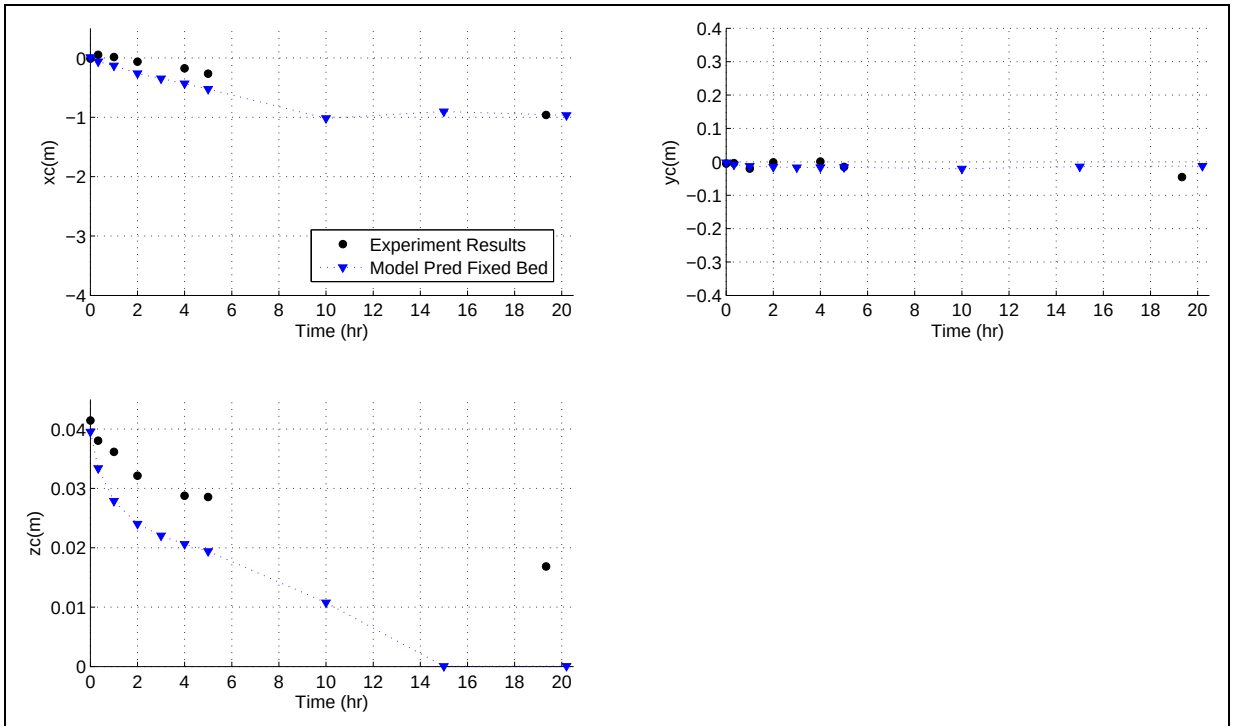


Figure 6.15 Evolution of centroid coordinates with time Test GT

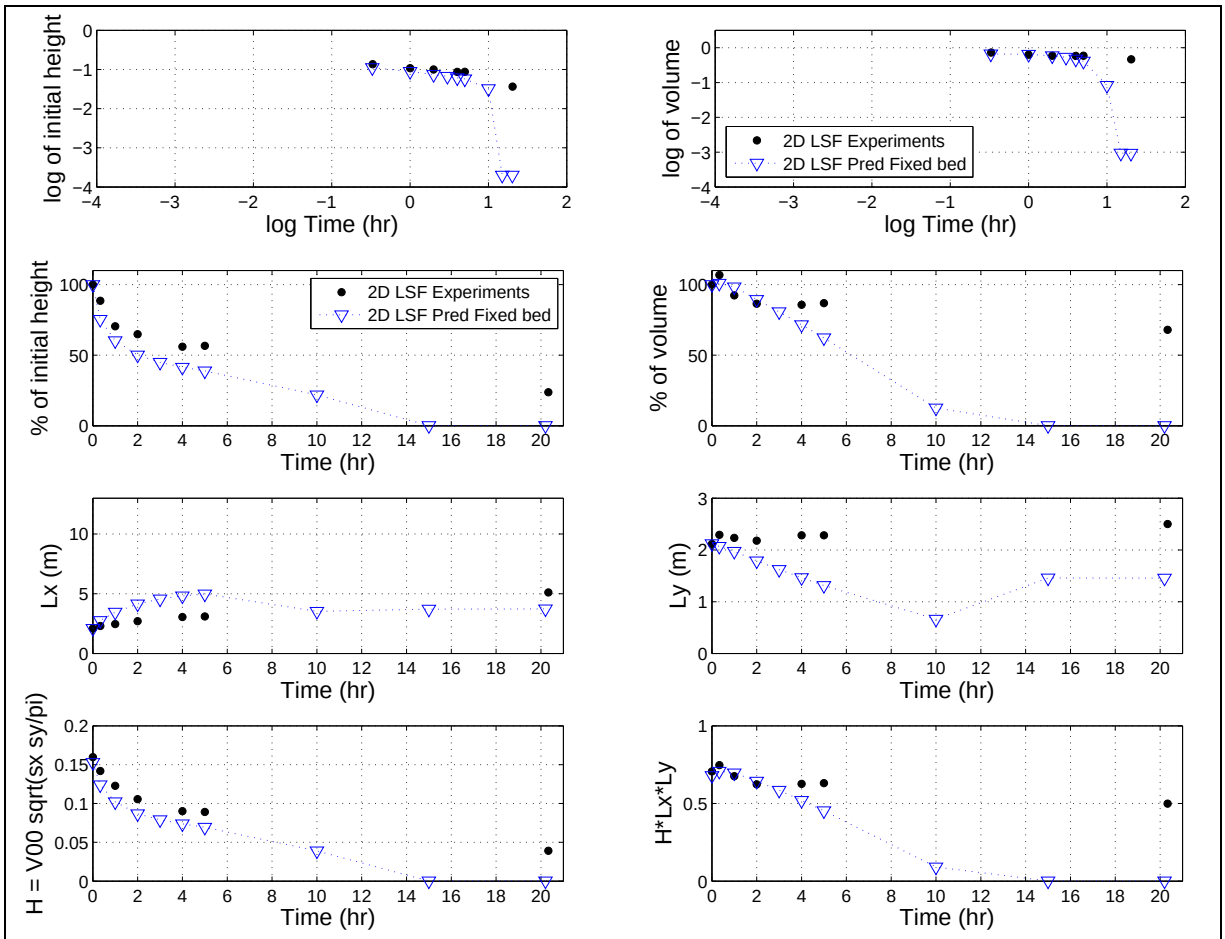


Figure 6.16 Characteristic parameters of the LSF for Tests GT

# 7. CONCLUSIONS AND FUTURE WORK

This chapter describes the outcomes from the research and summarises the findings from the investigation. The general conclusions provide insight into the morphodynamics of spoil heaps and sandbanks. The section on future work presents suggestions for further research following from the research here described.

## *7.1. Outcomes of the research*

- Collection of a benchmark dataset of the morphodynamic evolution of a mound of sand under a variety of steady and tidal flows, shapes and heights of mound, to be used in the validation and testing of morphodynamic numerical models. To the author's knowledge this is the only dataset of this kind available at present.
- Interpretation of the morphodynamic changes of a bed mound, and the interactions between the hydrodynamic conditions and sediment transport.
- Identification of the experimental threshold of motion for sediment transport for sand of $d_{50}$= 0.454 mm.
- Comparison between the migration rates of ripples on a mobile bed and the net migration of the centroid of the bed mound (Table 4.3). The maximum ripple migration is between 4 and 6 times that of the centroid of the mound, depending on whether it is on mobile or fixed bed. The average ripple migration was about 2.5 m/h, about three times faster than the migration of the centroid.
- Estimation of experimental sediment transport rates through cross sections of the mound (in the cross-flow direction). Comparison of these with transport rates using well known formulae and estimates of water depth and velocity values from numerical simulations representing the mound evolution.
- Comparison of the results from the analytical solution developed by de Vriend (1987) using characteristics analysis of the 2-D depth-averaged shallow-water equations with experimental data from the UKCRF experiments (i.e. back-edge migration, spreading rates and angles of spreading).
- Comparison of theoretical morphodynamic timescales derived by Hudson (2005) and Huang (2008) with experimental results.

- Application of a filtering technique to remove the small noise (sub grid scale features) and laboratory scale ripples to help compare the experimental results to numerical model predictions.
- Application of a commercial numerical model (Telemac/PISCES) to simulate some of the tests, comparison with observations and interpretation of results.

## *7.2. General conclusions*

**Pilot experiments**

The pilot experiments, described in Chapter 2, helped delineate the practical constraints for the large scale experiments in terms of sediment grain size, flow velocity, oscillation period and morphodynamic behaviour of the bed mound. The elapsed time influenced the morphodynamic evolution more than the oscillation period. The sediment size was chosen so that the sediment transport occurred mainly as bed load, while allowing sufficient mobility of the sediment. The slopes of the mound (1 in 3) generated strong secondary flow structures that affected the evolution of the mound. The repeatability of the tests varied, though the results were reasonably similar within the first two to three cycles. The threshold of motion for sand of $d_{50}$= 0.454 mm was identified using criteria devised by Delft Hydraulics (1972) cited by Van Rijn (1993, pp 4.8) and was higher than the theoretical.

**UKCRF data**

From the large-scale experiments, a range of parameters was tested and the response of the bed mound was investigated in terms of changes in integral properties (volume, height and centroid coordinates), as well as morphological changes. Fourteen tests were carried out in the UKCRF, six of which were fully analysed to understand the factors that dominate the evolution and decay of bed mounds (Chapter 4). A parameter study was undertaken over a range of initial, morphological and flow conditions.

The effect of the mobile bed and the mound on the downstream flow velocity differed from that of the fixed bed. For the fixed bed, the velocity downstream of the mound was markedly smaller than upstream, but for the mobile bed the upstream and downstream measured flow velocities are almost the same. It is not self-evident what causes this, although it could be due to the enhanced blockage effect of the mound and the mobile bed on the flow, or the attenuation of the turbulence downstream of the mound due to the effect of

the roughness of the mobile bed. The surface-piercing/touching, mound on a fixed bed exhibited a similar small downstream velocity deficit.

The secondary flow was more stable in the steady flow case than in the tidal flow, where the flow structures had limited time to develop due to the unsteady conditions. Flow unsteadiness had an impact on the sediment transport. In the steady case the velocity exceeded the threshold of sediment motion for the duration of each flow period, whilst in the tidal case it was only for about 50 % of each tidal cycle.

Comparison of the evolution of the mound built on an underlying mobile sandy bed of finite thickness with that on a concrete non-erodible bed, showed that the volume and height decayed slightly faster in the mobile bed case, though the test run was too short for this finding to be conclusive.

**Mound shape changes**

During the tests the shape of the mound evolved to adapt to the hydrodynamic conditions, reaching dynamic equilibrium. The mound evolved into a barchan dune shape in steady flow. A barchan dune shape developed in the mobile and fixed bed cases. The mobile bed provided a way to visualise the feedback effect of the mound on the free surface (the disturbance of the mobile bed, on the bed downstream of the mound, Figures 4.29 and 4.43b). However, on a fixed bed there was no record of this feature. In the tidal flow case the shape can be interpreted as two superimposed barchan dunes, migrating through each other in opposing directions (Figures 4.74 and 4.77).

Under tidal flow the mound retained features that mark the history of the previous cycles (such as the collapse line, step). Due to the periodic flow reversals, the flow did not have enough time in half a cycle to erase the steep step that developed in the previous half-cycle (Figure 4.71).

The slopes of the mound were asymmetric, in both steady and tidal cases. In the steady flow case the front and back slopes remained asymmetric for the duration of the test, whilst in the tidal case the steep slope alternated location with the reversing flow. The migration of the mound followed the leading edge (i.e the steepest slope). Dunes, ripples and sandbanks showed the same type of migration. The distance that the mound migrated was more noticeable in the steady flow case, than in the tidal case.

An unintended slight asymmetry in the tidal flows was found, which in the long-term resulted in a net mound migration towards the direction of the strongest flow. If this asymmetry were not considered, predictions could differ significantly from observations.

This is an example of how processes that *a priori* may be considered unimportant and hence be left out, can influence the final evolution of the bed mound.

The Gaussian mound created a larger obstruction to the flow than the more streamlined elliptical mound. The effect of secondary flows was smaller in the latter. The velocity deficit was more variable in the Gaussian case, as the mound had to evolve further to become more streamlined. The effects of secondary flow at the lateral edges were stronger in the Gaussian case than in the elliptical case. The pattern of the flow tracks over the mound appeared similar for both cases. The long term evolution of the mound was not highly dependent on the initial shape, in both cases the mound broke down into ripples of varying wavelengths (Figures 4.78 and 4.93), although after about 20 hr in the elliptical case the mound seemed slightly more compact.

The effect of the mound on the flow was longer-lasting for the surface piercing and surface touching cases than for the submerged case (to the point where the downstream velocity is very similar to the upstream undisturbed velocity). Once the crest became submerged the flow velocity downstream of the mound was lowest for the surface piercing, then the surface touching, then the submerged case. This difference could be related to an acceleration of the flow around the surface piercing mound due to a higher blockage effect. The shape of the mound was reworked by the flow, the crest travelled downstream (the wake followed) and eventually the mound became submerged, tending to an equilibrium with the present hydrodynamic conditions (minimum energy).

The long-term evolution of the mound therefore depends on both the initial volume of the mound and the blockage effect that it poses to the flow. A larger initial volume can play a more important role in allowing the mound to retain its identity for longer. The larger blockage effect (of the surface piercing mound) accelerates the flows further around the crest, inducing stronger secondary flows (which dent the sides of the mound more deeply). Stronger wake flows enhance the sediment transport capacity, decreasing the volume of the mound further and contributing to its destruction. For submerged mounds the blockage effect is reduced, and hence the secondary flows are less important, though due to a smaller initial volume of sediment, the identity of the mound might be dissipated in a shorter timescale than the surface touching/piercing.

The tests were relatively repeatable, in terms of general evolution and the effect of the mound on the velocity. The general shape of the mound and its overall evolution was highly repeatable in the short- to mid-term, although the small features were not repeatable. However, it is unclear whether a process that has not been identified in the short-term

evolution (e.g. how the effect of irregularities in the bed affects the roughness, and the 3-D flow features) can have an effect on the long-term evolution.

Sediment transport rates were calculated for two steady flow cases, through cross-sections of the mound at fixed points in the *x*-axis (Figure 4.144). Two sediment transport formulae were used: Meyer-Peter-Muller (1948) and Van Rijn (1984). From the calculations of the transport rates (Section 4.3) it was evident that the results depended strongly on the choice of transport formula. The formulae provided estimates that were in varying degrees of agreement with the experimental rates. The transport rates decreased with time as did the volume of the mound while it evolved to adapt to the existing conditions. The mobile bed case maintained higher transport rates than the fixed bed case. The effect of bedforms on the experimental transport rates could not be quantified.

**Comparison to the analytical solution**

The evolution of the mound in steady flow on a mobile bed was compared directly to the 2D analytical solution of the shallow water equations for the evolution of a bed disturbance described by De Vriend (1987) (discussed in Section 5.1). There was reasonable agreement between analytical and experimental data. A star-shape pattern developed in steady flow conditions (dashed line in Figure 4.7), from this and the results from the experiments, an empirical interpretative shape was proposed in Chapter 4. Figure 4.74 shows a near-equilibrium shape, that is non-stationary due to the unsteady conditions of tidal flows. The numerical model results confirm this. The evolution of the mound is a highly turbulent process and secondary flow patterns develop that affect the free surface and the mobile bed (discussed earlier).

**Morphodynamic timescales**

The comparison of the predicted and experimental morphodynamic timescales [defined by Hudson *et al*. (2005) and Huang *et al*. (2008)], and also derived from the decay of volume showed reasonable agreement, although the assumptions for the analytical formulae were not fully met (the bed disturbance occupied ¾ of the water depth). The expressions to calculate timescales of change (migration of back edge, crest and decay of volume) described in Chapter 5 can be used in the planning stage of experimental testing of bed mounds, trenches or other bed features, or in consultancy scoping studies. The experimental evidence supports the analytical solutions, and their use to validate numerical models. There is a great benefit in the use of analytical expressions to get a first estimate of migration rates and decay of bed

features (highly applicable to spoil heaps). When there is the need for further information (i.e. the evolution of the shape) numerical models provide finer detail.

**Smaller scale features**

The ripples superimposed on the mound evolved from incipient to straight- and sinuous- crested to linguoid ripples through the test (classification from Baas, 1993). The presence of the mound had an effect on the ripples, and the presence of the ripples had an effect on the sediment transport, and the evolution of the mound. The form and evolution of the ripples were different in tidal and unidirectional flow cases. In the steady flow, ripples reached equilibrium with the flow conditions. Due to the unsteady conditions in the tidal case, there was not enough time for the ripples to reach the theoretical equilibrium wavelength and height given the grain size. McDowell and O'Connor (1977) considered that part of the energy of the flow in tidal conditions is invested in reversing the bedform orientation and this process affects the sediment loading capacity.

Baas (1993) developed an expression to predict equilibrium ripple lengths on a flat bed. The predicted ripple dimensions (h = 0.02 m, L = 0.17 m) using the Baas expression were significantly smaller than those observed in the UKCRF, where ripple lengths reached values of 0.5 m on the flat mobile bed and were the same size or larger superimposed on the mound. From experimental observations, the average ripple migration speed was about 2.5 m/s, approximately three times faster than the centroid of the mound.

From the results gathered whilst studying still and moving images (see the discussion in Chapter 4), there seems to be a change in behaviour/regime at a certain threshold time. For example in Baas' (1993) experiments, the evolution of the ripples occurred in two stages until equilibrium was reached. During the UKCRF experiments, similar behaviour may be inferred, in this case related to the evolution of the mound, and when the mounds ceased to behave as large-scale features and instead behave as multiple ripples.

**Model comparison**

Data from three of the six fully analysed tests were used to test a commercial 2-D morphodynamic numerical model (PISCES). In most cases PISCES was able to predict the general integral parameters that characterise the mound in the experiments with reasonable agreement. However, the evolution of the Gaussian mound on a mobile bed under steady flow conditions was reproduced by the model. The representation of the mobile bed in the tidal case was not entirely satisfactory. In the steady flow case, migration is an important

process, whereas in the tidal case the migration of the mound was small, the dispersion and decay of the height and volume became more important.

The morphodynamic evolution of the bed mound is extremely complicated, involving 3-D processes (related to secondary flow structures). However, the general evolution of a bed mound can be reasonably well predicted with a depth-averaged model, which saves computational cost. The present tests have provided a standard means of assessing the performance of a morphodynamic model, by which the understanding of the physical processes is improved.

## 7.3. Findings in the context of sandbanks and spoil heaps

Timescales of change in linear sandbanks are the order of tens to hundreds of years. For a sandbank to maintain its existence today, it has to be in a long-term stable equilibrium and thus withstand the effect of the hydrodynamic processes acting upon it. Thus, there has to be a dynamic equilibrium between the destruction and creation mechanisms (though only destruction in the experiments reported in this thesis), otherwise banks would decay and eventually disappear. Assuming the sandbank is in equilibrium, the rate of growth should be equal to the rate of decay. For the UKCRF experiments the decay rates of bed mound height and volume were estimated, which provide quantitative information on the evolution of sandbanks occurring in tidally dominated environments.

The blockage effect experienced by the bed mound should not normally occur *in situ*, unless there is a flow constriction as might happen should a number of banks be aligned relatively parallel to each other. *In situ* sandbanks do not evolve into a barchan shape because they are subject to tidal conditions. The scale of the motion of the particles is typically shorter than the length scale of the bank and there is sediment input. During the experiments the mound was aligned to the main flow direction; a qualitative assessment of the coloured sand tests showed the cross-flow transport component was small.

If the mound were of the same scale as a sandbank, there would be a sufficient internal supply of sand for the mound to remain an entity through time (not degenerate), and become progressively streamlined while having small-scale ripples superimposed. In practice, a typical tidal period is sufficiently long for the conditions to change gradually (length scales of particle motion are smaller than the length of the sandbank). The flow would resemble an accelerating unidirectional flow, and so it is reasonable to expect that

sand transported from the upstream seabed should continuously replenish sand leaving the trailing edge of a sandbank.

Similarities in the behaviour of the mound and sandbanks can be sustained up to the critical time when the effect of the ripples on the flow is of the same scale to that of the mound. After this time the dynamics become different and further evolution of the mound no longer corresponds to that of a sandbank. Even moribund mounds would take too long to decay, and due to their structure (a harder core) their decay would not be so similar to the experiments.

Sandbank crests remain near the surface or become emerged during spring tides. At this time, wave action and currents reshape the bank more efficiently. The surface-piercing mound represents an emerged bank, the submerged mound represents submerged stages of the bank. The surface-piercing mound decreases in height due to the action of the flow, and becomes submerged, converging to a shape adapted to the existing conditions.

The sand movement over the experimental mound (occupying about ¾ of the water depth) appears to be like an uneven layer of sediment sweeping over it. In the case of submerged sandbanks only the sediment from the upper area moves (if the flow exceeds the threshold of motion). When the crest of the bank is close below the water surface the sand movement may reach deeper parts and be more generalised, and flows will be accelerated over the crest, and the transport capacity will be enhanced.

The surface sediment layer of the mound is very mobile. Ripples act to store sediment, in the experiments there were some parts of the mound where sand was undisturbed until the end of the test (when the mound was broken into ripples). Features superimposed on the mound have an effect on the flow, the overall shape, evolution (and maintenance) of the mound. However, their relevance has not been quantified. Bed features superimposed on full-scale sandbanks also have an effect on the regional flow structure, modifying the boundary layer and sediment transport.

Waves affect sandbank evolution, but have not been taken into account in the work reported in this thesis for practical reasons (mentioned in Section 1.2.5). In practice however, current effects are usually more important than episodic extreme wave events because of the much higher frequency of occurrence, and the different time-scales involved (sand in the bank takes years to move, whereas a storm lasts a few hours).

The evolution and long-term fate of the experimental bed mound under steady and tidal flow resembles that of a spoil heap. The morphological evolution of the mound in plan and cross section is representative of the conceptual evolution of a non-cohesive spoil heap

(Posford Haskoning, 2003): i.e. the bulk of the sediment remains in one area, and the flow shifts the sediment, forming dunes in the vicinity of the heap, whilst further afield ripples develop, and further away the sand features decrease in wavelength and height. In a steady flow environment the dunes and ripple field extend downstream as shown in Figure 5.4, whilst in a tidal flow environment the sediment becomes either side of the centre of the mound (predominantly in the reversing stream-wise direction) as Figures 4.76 and 4.78 show. The analytical solution and morphodynamic timescales can be used to predict rates of migration, spreading and decay of features such as spoil heaps in steady flows (and with some interpretation to tidal flows).

## *7.4. Future Work*

- Only three experimental datasets were used to test the numerical model in this study. Further research is recommended to use the four other datasets that have been analysed and interpreted to test numerical models for other conditions, and to digitise, analyse and interpret data from the remaining datasets collected.
- The benchmark data should be used to validate other numerical models (perhaps more sophisticated 3-D models). As a result it should be possible to find more appropriate parameterisations of the emerged crest in the surface-piercing and -touching cases.
- Additional research is needed in order to translate the findings from laboratory-scale to the modelling of prototype banks in the field. It should of course be borne in mind that the experimental data cannot be directly scaled to prototype condition, but the numerical models should be able to be scaled forward.
- Further experimental work could improve understanding of headland associated banks. New tests are needed on the effect of the mobile bed (as a source of sediment) in the evolution of the bed mound. It is recommended that laboratory experiments be undertaken with a bank and a beach in order to investigate their interaction, followed by tests involving a number of banks to assess the interaction processes between them.
- Further tests would be desirable, involving coloured sand, of spoil heaps and trenches to complete the benchmark data available to numerical modellers. New tests are recommended to investigate the mechanisms of saltation transport and the effect of sediment transport.
- To improve understanding of Type 2 banks, as suggested previously by Dyer and Huntley (1999) after validation of numerical Coastal Area Models, a parameter study

could be carried out to assess the relevance of ebb-flood dominated channels in the dynamics of sandbanks.

- Developing a particle model of near bed saltation may be valuable for application to a bed mound in order to assess the non-linear sand dynamics in an oscillatory flow over a large-scale bedform.

# 8. REFERENCES


Allen, J. R. L. (1968). *Current ripples*. North Holland Publishing Company, The Netherlands.

Baas, J.H. (2003) Ripple, Ripple Mark, Ripple Structure. *Encyclopedia of sediments and sedimentary rocks* (Ed. by G.V. Middleton), Kluwer Academic Publishers, Dordrecht, Netherlands, 565-568. (http://www.bangor.ac.uk/~oss40d/download/Baas%20(Encycl%202003).pdf)

Baas, J. H. (1993). *Dimensional analysis of current ripples in recent and ancient depositional environments*. PhD Thesis. University of Utrecht, The Netherlands.

Battjes, J. A. (2005). Developments in coastal engineering research. J. of Coastal Engineering, 53, 121 – 132.

Belderson, R.H. (1986). Offshore tidal and non-tidal sand ridges and sheets: differences in morphology and hydrodynamic setting. In Knight, R.J. and McLean, J.R. (eds), *Shelf Sands and Sandstones*. Canadian Society of Petroleum Geologists. Memoir II. 293-301.

Besio, G., Blondeaux, P. and Vittori, G. (2006). On the formation of sand waves and sand banks. J. of Fluid Mechanics, V 557, 1-27.

Carbajal, N., Piney, S. and Gomez Rivera, J. (2005). A numerical study on the influence of geometry on the formation of sandbanks. Ocean Dynamics, 55, 559-568.

Caston, V.N. (1972). Linear sandbanks in the southern North Sea. Sedimentology, 18, 63 - 78.

Caston, V.N.D. and Stride, A.H. (1970). Tidal sand movement between some linear sandbanks in the North Sea off northeast Norfolk. Marine Geology, 9, 38 - 42.

Chen, D. and Jirka, G. H. (1995). Experimental study of plane turbulent wakes in a shallow water layer. Fluid Dynamics Research, 16, 11-41.

Chesher, T. J., Wallace, H. M., Medowcroft, I.C. and Southgate, H, N. (1993). *PISCES, A Morphodynamic Coastal Area Model, First annual report*. SR 337 HR Wallingford Report.

Chow, V T., (1973). *Open channel hydraulics*. McGraw Hill. International Editions. Civil Engineering Series.

Collins, M.B.,Shimwell, S.J.,Gao, S.,Powell, H., Hewitson, C., Taylor, J.A. (1995). Water and sediment movement in the vicinity of linear sandbanks: the Norfolk Banks, southern North Sea. Marine Geology. 123. 125-142.

Coughlan, C., Vincent, C. E., Dolphin, T. J., and Rees, J. M. (2007). Effects of tidal stage on the wave climate inshore of a sandbank. J. of Coastal Research, SI 50 (Proceedings of the 9th International Coastal symposium), 751-756. Gold Coast (Australia).

Damgaard, J. and Chesher, T. (1997). *Morphodynamic simulation of Helwick Bank*. HR Wallingford Report TR 31, August 1997.

De Vriend, H. J., Campobianco, M., Chesher, T., de Swart, H. E., Latteux, B., and Stive, M. J. F. (1993). Approaches to long-term modelling of coastal morphology: a review. J. of coastal Engineering, 21, 225-269.

De Vriend, H. J. (1987). 2DH Mathematical modelling of morphological evolutions in shallow water. Coastal Engineering, 11, 1-27.

Dodd, N., Blondeaux, P., Calvete, D., De Swart, H. E., Falques, A., Hulscher, S. J. M. H., Rózynski, G., and Vittori, G. (2003). Understanding coastal morphodynamics using stability methods. J. of Coastal Research, 19(4), 849-865. West Palm Beach (Florida).

Dolphin, T. J., Vincent, C. E., Coughlan, C., and Rees, J. M. (2007). Variability in sandbank behaviour at decadal and annual time-scales and implications for adjacent beaches. J. of Coastal Research, SI 50 (Proceedings of the 9th International Coastal symposium), 731-737. Gold Coast (Australia).

Drapeau, G., Jean Munro, J. and Nellis, P. (2003). Long term fate of dredged sediments at Ile Madame dumping site (St Lawrence Estuary): a basic assessment. Proc. to 2nd International Symposium on Contaminated Sediments, Quebec City, Quebec, Canada.

Dronkers, J. (2005). *Dynamics of coastal systems*. Advanced Series on Ocean Engineering, Vol. 25. World Scientific Publishing Co. Pte. Ltd., London.

Dyer, K.R. and D.A. Huntley, 1999. The origin, classification and modelling of sand banks and ridges. Cont. Shelf Res., Vol. 19, 1285-1330.

Escarameia, M. (1999). *Scour around structures in tidal flows*. HR Wallingford Report SR 521, April 1999.

Garcia-Hermosa, M. I., and Borthwick, A. G. L. (2006). Sandbank morphodynamics: experimental data recorded at the UKCRF. Internal report. University of Oxford, Department of Engineering Science, Parks Road, Oxford, OX1 3PJ, U.K.

Gunawardena, Y., Ilic, S., Pinkerton, H. and Romanowicz, R. (2007). Prediction of beach morphological changes using a data-based approach. Proc. 30th ICCE, San Diego, September 2006, 3168-3177.

Harris, P.T., Pattiaratchi, C.B., cole, A.R. and Keene, J.B. (1992). Evolution of subtidal sandbanks in Moreton Bay, eastern Australia. Marine Geology. 103. 225-247.

Hayes, M.O. and Nairn, R.B. (2004). Natural maintenance of sand ridges and linear shoals on the U.S. gulf and Atlantic continental shelves and the potential impacts of dredging. J. of Coastal Research, 20(1), 138–148. West Palm Beach (Florida).

Hervouet, J. (2003). *Hydrodynamique des écoulements à surface libre: Modelisation numerique avec la methode des elements finis.* Presses de l'école nationale des ponts et chaussées, France.

Horrillo-Caraballo, J. M. (2005). *Investigation of the long-term evolution of the offshore sandbanks at Great Yarmouth, UK*. PhD thesis, School of Civil Engineering, University of Nottingham.

Horrillo-Caraballo, J. M., Reeve, D. E., and Li, B. (2002). Eigenfunction analysis of complex estuary morphology. Proc. of 5th International Conference of Hydroinformatics, Cardiff, UK.

Hu, K. and Cooke, I. (1997). *Sandbanks: Basic processes and effects on long-term morphodynamics*. Report on Geographical Database. Postford Duvivier, Peterborough, October 1997.

Huang, J., Borthwick, A. G. L. and Soulsby, R. L. (2008). 1-D modelling of fluvial bed morphodynamics. Accepted by J. of Hydraulic Research.

Hudson, J., Damgaard, J., Dodd, N., Cheshes, T. and Cooper, A. (2005). Numerical Approaches for 1D morphodynamic modelling. Coastal Engineering, Vol. 52, 691-707.

Hulscher, S.J.M.H., De Swart, H.E. and De Vriend, H.J. (1993). The generation of offshore tidal sandbanks and sand waves. Continental Shelf. Res., Vol. 13, No. 11, 1183 - 1204.

Hulscher, S.J.M.H. (1996). Tide-induced large-scale regular bed form patterns in a three dimensional shallow water model. J. of Geophysical Research. C9, 101. 20727-20744.

Huthnance, J.M. (1982a). On one mechanism forming linear sand banks. Estuarine, Coastal and Shelf Science 14, 79-99.

Huthnance, J.M. (1982b). On the formation of sandbanks of finite extent. Estuarine, Coastal and Shelf Science 15, 277-299.

Huthnance, J.M. (1973). Tidal current asymmetries over the Norfolk sandbanks. Estuarine, Coastal and Shelf Science 1, 89-99.

Idier, D., van der Veen, M. H. and Hulscher, S. J. M. H. (2007). Influence of grain size on sandbank dynamics. Proc. of River, Coastal and Estuarine Morphodynamics: RCEM 2007. Ed. Dohmen-Janssen and Hulscher. Taylor & Francis Group, London.

Idier, D. and Astruc, D. (2003). Analytical and numerical model of sandbank dynamics. J. of Geophysical Research, 108 (C3), 3060.

Jones, O. P. (2007). *Modelling headland sandbank processes.* PhD thesis, Department of Civil and Environmental Engineering, University College London, London.

Jones, O. P., Simons, R. R., Jones, E. J. W. and Harris, J. M. (2006). Influence of seabed slope and Coriolis effects on development of sandbanks near headlands. J. of Geophys. Research, Vol. 111, C03020.

Kemp, J., and Brampton, A. (2007). The development of a time trend analysis tool for GIS and its application in the assessment of Nash Bank, South Wales. J. of Hydroinformatics, 09.3.

van Lankver V., Honeybun, S. D. and Moerkerke, G. P. M. (2000). Sediment transport pathways in the Broes Bank - Westdiep coastal system, preliminary results. In: Trentesaux, A.; Garlan, T. (Ed.) (2000). *Marine Sandwave Dynamics (Dynamique des dunes sous-marines),* Proc. of an International Workshop, March 23-24 2000, University of Lille 1, France.

Lesser, G. R., Roelvink, J. A., van Kester, J. A. T. M., and Stelling, G. S. (2004). Development and validation of a three-dimensional morphological model. Coastal Engineering, 51, 883-915.

Lloyd, P. H., Stansby, P. K. and Chen, D. (2001). Wake formation around islands in oscillatory laminar shallow-water flows. Part 1: Experimental investigation. J. of Fluid Mechanics, 429, 217-238.

Lloyd, P. H. and Stansby, P. K. (1997a). Shallow water flow around model conical islands of small side slope. I: Surface piercing. J. of Hydraulic Engineering, Dec 1997, 1057-1067.

Lloyd, P. H. and Stansby, P. K. (1997b). Shallow water flow around model conical islands of small side slope. II: Submerged. J. of Hydraulic Engineering, Dec 1997, 1068-1077.

Lopez de San Roman Blanco, B (2008). *Further development to HR SANDFLOW.* HR Wallingford Report IT 555, June 2008.

McDowell, D M and O'Connor B A (1977). Hydraulic Behaviour of Estuaries. Civil Engineering Hydraulics Series. Editor E. M Wilson.

Meyer-Peter, E. and Müller, R. (1948). Formulas for bed load transport. Rep. 2nd Meet. Int. Assoc. Hydraul. Struct. Res., Stockholm, 39-64.

Nielsen, P. (1992). *Coastal* b*ottom boundary layers and sediment transport.* Advanced Series on Ocean Engineering, Vol. 4. World Scientific Publishing, Singapore.

O'Connor, B. (Ed). (1996). *Circulation and sediment transport around banks (CSTAB) Handbook, Vol I and II*. Department of Civil Engineering, University of Liverpool, UK.

Off, T. (1963). Rhythmic linear sand bodies caused by tidal currents. Bull. Of the American Assoc. of Petroleum Geologists. 47, 324-341.

Paintal, A S. (1971). Concept of critical shear stress in loose boundary open channels. J. of Hydraulic Research, vol. 9, N1, 90-113.

Pattiaratchi C., Collins M.B. (1987). Mechanisms for linear sandbank formation and maintenance in relation to dynamical oceanographic observations. Progress in Oceanography. 19. 117-176.

Posford Haskoning Ltd. (2003). *Regional environmental assessment for aggregate extraction in the eastern English Channel*. Report to the Eastern Channel Association.

Reeve, D., Li, B. and Thurston, N. (2001). Eigenfunction analysis of decadal fluctuations in sandbank morphology at Gt. Yarmouth. J. of Coastal Research, 17 (2). West Palm Beach (Florida, USA).

Reynolds, O. (1887). *On certain laws relating to the regime of rivers and estuaries, and on the possibility of experiments on a small scale*. Reports and Transactions of the British Association for the Advancement of Science, 555-562.

Roos, P. C. (2004). *Seabed pattern dynamics and offshore sand extraction.* PhD thesis. Water Engineering Management, University of Twente, Enschede (The Netherlands).

Roos, P. C., Hulscher, J. M. H., Knaapen, M. A. F. and Van Damme, R. M. J. (2004). The cross-sectional shape of tidal sandbanks: Modeling and observations. J. of Geophysical Research, 109, F02003, 1-14.

Schinaia, S. A., Momiji, H., Bishop, S. R., Simons, R. R. and Freeman, S. (2007). Towards a cellular automata model to predict the impacts of aggregate extraction on biological recoverability. Proc. 30th ICCE, San Diego, September 2006, 1989-1999.

Seminara, G., (1995). Effect of grain sorting on formation of bedforms. Applied Mechanics Review, 48(9), 549-563.

Shields, A. (1936). Anwendung der Ähnlichkeits-Mechanik und der Turbulenz-forschung auf die Geschiebebewegung. Preussische Versuchsanstalt für Wasserbau und Schiffbau, vol. 26, Berlin. [Application of similarity principles and turbulence research to bed-load movement. Translation by W.R. Ott and J. C. van Uchelen]

Signell, R. P., and Harris, C. K. (2000). Modelling sand bank formation around tidal headlands. Estuarine and Coastal Modelling, 6th International Conference, ASCE, New Orleans, LA, November 3 – 5, 1999. Ed. M. L. Spaulding and A. F. Blumberg, 209– 222, Am. Soc. of Civ. Eng., Reston, Va.

Soulsby, R. L., (1997). *Dynamics of marine sands. A manual for practical applications.* Thomas Telford.

Stride, A.H. (ed.) (1982). *Offshore tidal sands. Processes and deposits*. Chapman and Hall, London.

Sumer, B. M. (2007). Mathematical modelling of scour: A review. Invited Paper. J. of Hydraulic Research. Vol. 45, No 6, 723-735.

Sumer, B. M. and Fredsøe, J. (1997). *Hydrodynamics around cylindrical structures.* Advanced Series on Ocean Engineering Vol. 12. World Scientific Publishing, Singapore.

Swift, D.J.P. (1975). Tidal sand ridges and shoal-retreat massifs. Marine Geology. 18. 105-134.

Talmon, A. M., Struiksma, N., and Van Mierlo, M. C. L. M. (1995). Laboratory measurements of the sediment transport on transverse alluvial-bed slopes. J. Hydraul. Res., 33, 519-534.

Taylor, P. H., Huang, J., Garcia-Hermosa, I., Stansby, P. K., Borthwick, A. G. L. and Soulsby, R. L. (2008). Separation of large-scale structure and ripples on sand mounds using Hermite functions. (Submitted to J. of Engineering and Computational Mechanics).

Telemac2D (2002). Telemac2D Modelling system: User Manual, version 5.2. June 2002.

Van der Veen, M. H., Hulscher, S. J. M. H. and Pérez Lapeña, B. (2007). Seabed morphodynamics due to offshore wind farms. Proc. of River, Coastal and Estuarine Morphodynamics: RCEM 2007. Ed. Dohmen-Janssen and Hulscher. Taylor & Francis Group, London.

Van Rijn, L C. (1993). *Principles of sediment transport in rivers, estuaries and coastal seas*. Aqua publications, Amsterdam.

Van Rijn, L. C. (1984). Sediment transport: part I - bed load transport; part II - suspended load transport; part III - bed forms and alluvial roughness. J. Hydraul. Div., Proc. ASCE. 110 (HY10), 1431-56; (HY11), 1613-41; (HY12), 1733-54.

Vanvesenbeek, V. and Lanckneus, J. (2000). Residual sediment transport paths on a tidal sand bank: a comparison between the modified McLaren model and bedform analysis. J. of Sedimentary Research, Vol. 70, No. 3, May 2000, 470-477.

Velegrakis, A., Collins, M.B, Owrid, G. and Houghton, A. (2000). *Submerged sandbanks in European shelf waters*. Report to the WWF Global Environment Network. School of Ocean and Earth Science, University of Southampton. December 2000.

Whitehouse, R.J.S. (editor), (2001). *Understanding the behaviour and engineering significance of offshore and coastal sand banks*. HR Wallingford Report SR 512, July 2001.

Whitehouse, R.J.S., Mitchener, H.J., Soulsby, R.S., (1998). *Laboratory experiments on ripple development and bed roughness in tidal flow*. HR Wallingford Report TR 66, October 1998.

Wijnberg, K.M. and Terwindt, J. H. J. (1995). Extracting decadal morphological behaviour from high-resolution, long-term bathymetric surveys along the Holland coast using eigenfunction analysis. Marine geology, 126, 301-330.

Wild, B. R (1988). *A numerical sand transport model with time dependent bed exchange*. HW Wallingford Report No SR 148.

Williams, J.J., MacDonald, N.J., O'Connor,B.A. and Pan, S. (2000). Offshore sand bank dynamics. J. Marine Systems, 24, 153-173.

# Appendix 1

Tabulated experimental results

| Time (hr) | Crest height (m) | Volume ($m^3$) | % Initial volume |
|---|---|---|---|
| **0** | 0.154 | 0.659 | 100 |
| **0.3** | 0.115 | 0.693 | 105.1 |
| **1** | 0.097 | 0.587 | 90.0 |
| **2** | 0.080 | 0.489 | 74.2 |
| **3** | 0.068 | 0.344 | 52.1 |

**Table A1 Evolution of crest height and volume through Test 9**

| Time (hr) | Volume ($m^3$) ю | $x_c$ (m) | $y_c$ (m) | $z_c$ (m) |
|---|---|---|---|---|
| **0** | 0.659 | 0.010 | 0.003 | 0.040 |
| **0.33** | 0.693 | -0.633 | -0.007 | 0.030 |
| **1** | 0.587 | -1.527 | 0.011 | 0.023 |
| **2** | 0.488 | -2.255 | -0.005 | 0.020 |
| **3** | 0.343 | -2.535 | -0.025 | 0.018 |

**Table A2 Evolution of centroid coordinates through Test 9**

| Time (hr) | Volume ($m^3$) Test 13 * | % initial volume Test 13 | Crest height (m) Test 13 * |
|---|---|---|---|
| **0** | 0.625 | 100.0 | 0.155 |
| **0.3** | 0.504 | 80.5 | 0.090 |
| **1** | 0.438 | 70.0 | 0.071 |
| **2** | - | - | - |
| **3** | - | - | - |

Theoretical volume Gaussian mound 0.679 $m^3$

**Table A3 Crest height and mound volume for Test 9 and 13**

| | Test 9 | | | Test 13 | | |
|---|---|---|---|---|---|---|
| **Time (hr)** | $x_c$ (m) | $y_c$ (m) | $z_c$ (m) | $x_c$ (m) | $y_c$ (m) | $z_c$ (m) |
| **0** | 0.010 | 0.003 | 0.040 | -0.079 | -0.025 | 0.035 |
| **0.3** | -0.633 | -0.007 | 0.030 | -0.776 | -0.022 | 0.031 |
| **1** | -1.527 | 0.011 | 0.023 | -2.052 | -0.016 | 0.019 |
| **2** | -2.255 | -0.005 | 0.020 | - | - | - |
| **3** | -2.535 | -0.025 | 0.018 | - | - | - |

**Table A4 Centroid coordinates for Test 9 and 13.**

| | Test 8 Gaussian | | Test 11 Ellipse | |
|---|---|---|---|---|
| **Time (hr)** | **Crest height (m)** | **% initial crest height** | **Crest height (m)** | **% initial crest height** |
| **0** | 0.155 | 100.0 | 0.154 | 100.0 |
| **0.33** | 0.138 | 89.0 | 0.130 | 84.4 |
| **1** | 0.130 | 83.9 | 0.129 | 83.8 |
| **2** | 0.129 | 83.2 | - | - |
| **3** | - | - | 0.116 | 75.3 |
| **4** | 0.122 | 78.7 | - | - |
| **5** | 0.120 | 77.4 | - | - |
| **20.1** | 0.082 | 52.9 | 0.09 | 58.4 |

**Table A5 Evolution of the initial crest height time (Tests 8 and 11)**

| | Test 8 Gaussian | | Test 11 Ellipse | |
|---|---|---|---|---|
| **Time (hr)** | **Volume ($m^3$)** | **% of total volume** | **Volume ($m^3$)** | **% initial volume** |
| **0** | 0.682 | 100.0 | 0.592 | 100.0 |
| **0.33** | 0.724 | 106.2 | 0.552 | 93.3 |
| **1** | 0.629 | 92.3 | 0.546 | 92.3 |
| **2** | 0.592 | 86.8 | - | - |
| **3** | - | - | 0.522 | 88.2 |
| **4** | 0.588 | 86.3 | - | - |
| **5** | 0.596 | 87.5 | - | - |
| **20.1** | 0.463 | 67.9 | 0.429 | 72.5 |

**Table A6 Evolution of the mound volume with time (Tests 8 and 11)**

| | Test 8 Gaussian | | | Test 11 Ellipse | | |
|---|---|---|---|---|---|---|
| **Time (hr)** | **Xc (m)** | **Yc (m)** | **Zc (m)** | **Xc (m)** | **Yc (m)** | **Zc (m)** |
| **0** | -0.013 | -0.005 | 0.041 | -0.030 | 0.003 | 0.038 |
| **0.3** | 0.053 | -0.004 | 0.038 | -0.053 | 0.005 | 0.036 |
| **1** | 0.013 | -0.020 | 0.036 | -0.093 | -0.001 | 0.036 |
| **2** | -0.063 | -0.002 | 0.032 | | | |
| **3** | | | | -0.192 | 0.006 | 0.031 |
| **4** | -0.174 | 0.001 | 0.029 | | | |
| **5** | -0.265 | -0.015 | 0.029 | | | |
| **20.3** | -0.960 | -0.046 | 0.017 | -1.165 | 0.007 | 0.019 |

**Table A7 Evolution of the centroid coordinates for Tests 8 and 11**

| Test 11 (SM) | | | | | |
|---|---|---|---|---|---|
| **Time (hr)** | **Crest height** | **% initial crest height** | **Volume ($m^3$)** | **% of initial volume** | |
| **0** | 0.154 | 100.0 | 0.592 | 100.0 | Theoretical volume 0.730 $m^3$ |
| **0.33** | 0.130 | 84.4 | 0.552 | 93.3 | |
| **1** | 0.129 | 83.8 | 0.546 | 92.3 | |
| **3** | 0.116 | 75.3 | 0.522 | 88.2 | |
| **20.3** | 0.090 | 58.4 | 0.429 | 72.5 | |

Table A8a

| Test 4 (ST) | | | | | |
|---|---|---|---|---|---|
| **Time (hr)** | **Crest height** | **% initial crest height** | **Volume ($m^3$)** | **% of initial volume** | |
| **0** | 0.20 | 100.0 | 0.730 | 100.0 | Theoretical volume 0.536 $m^3$ |
| **0.33** | 0.159 | 79.5 | 0.762 | 104.4 | |
| **1** | 0.152 | 76.0 | 0.754 | 103.3 | |
| **2** | 0.146 | 73.0 | 0.719 | 98.4 | |
| **4** | 0.142 | 71.0 | 0.698 | 95.6 | |

Table A8b

**Table A8 Comparison of crest height and volumes for Tests 11 (SM), Test 4 (ST) and Test 3 (SP) (continues..)**

| Test 3 (SP) | | | | |
|---|---|---|---|---|
| **Time (hr)** | **Crest height** | **% initial crest height** | **Volume ($m^3$)** | **% of initial volume** |
| **0** | 0.248 | 100.0 | 1.112 | 100.0 |
| **0.33** | 0.248 | 100.0 | 0.993 | 89.3 |
| **1** | 0.165 | 66.5 | 0.993 | 89.3 |
| **2** | 0.158 | 63.7 | 0.877 | 78.9 |
| **3** | 0.151 | 60.9 | 0.888 | 79.9 |
| **4** | 0.140 | 56.5 | 0.845 | 76.9 |
| **19.3** | 0.108 | 43.5 | 0.658 | 59.1 |

Theoretical volume 0.894 $m^3$

Table A8c

**Table A8 Comparison of crest height and volumes for Tests 11 (SM), Test 4 (ST) and Test 3 (SP).**

| | Test 3 (SP) | | | Test 4 (ST) | | | Test 11 (SM) | | |
|---|---|---|---|---|---|---|---|---|---|
| **Cycle No.** | **$x_c$ (m)** | **$y_c$ (m)** | **$z_c$ (m)** | **$x_c$ (m)** | **$y_c$ (m)** | **$z_c$ (m)** | **$x_c$ (m)** | **$y_c$ (m)** | **$z_c$ (m)** |
| **0** | -0.030 | 0.003 | 0.038 | 0.106 | 0.011 | 0.049 | -0.023 | 0.003 | 0.065 |
| **0.33** | -0.053 | 0.005 | 0.036 | 0.107 | -0.017 | 0.047 | -0.034 | -0.002 | 0.058 |
| **1** | -0.093 | -0.001 | 0.036 | 0.075 | -0.016 | 0.045 | -0.102 | 0.026 | 0.054 |
| **2** | -0.192 | 0.006 | 0.031 | 0.015 | -0.017 | 0.041 | -0.131 | -0.022 | 0.045 |
| **3** | | | | | | | -0.197 | -0.018 | 0.043 |
| **4** | | | | -0.170 | -0.017 | 0.037 | -0.260 | -0.039 | 0.040 |
| **19.3** | | | | | | | -1.567 | -0.075 | 0.025 |
| **20.3** | -1.165 | 0.007 | 0.019 | | | | | | |

**Table A9 Centroid coordinates for Tests 3 (SP), 4 (ST) and 11 (SM),**

| Slice No. | Distance (m) | Volumetric sediment transport rate (kg/ m$^3$ s) | |
|---|---|---|---|
| | | MPM | VR bd |
| **1** | 2 | 0.0448 | 0.0366 |
| **2** | 1 | 0.0638 | 0.0540 |
| **3** | 0 | 0.0974 | 0.0880 |
| **4** | -1 | 0.1271 | 0.1206 |
| **5** | -2 | 0.1319 | 0.1265 |
| **6** | -3 | 0.0792 | 0.0723 |
| **7** | -4 | 0.0642 | 0.0563 |

Predictions at $t$ = 20 min

| Slice No. | Distance (m) | Volumetric sediment transport rate (kg/ m$^3$ s) | |
|---|---|---|---|
| | | MPM | VR bd |
| **1** | 2 | 0.0460 | 0.0375 |
| **2** | 1 | 0.0514 | 0.0423 |
| **3** | 0 | 0.0622 | 0.0524 |
| **4** | -1 | 0.0758 | 0.0656 |
| **5** | -2 | 0.0888 | 0.0789 |
| **6** | -3 | 0.0981 | 0.0890 |
| **7** | -4 | 0.0981 | 0.0897 |

Predictions at $t$ = 1 hr

**Table A10 Bedload sediment transport rates (kg/ m$^3$ s) estimated from model simulations of Test 13 using methods from MPM and Van Rijn (bed load).**

| Slice No. | Distance (m) | Volumetric sediment transport rate (kg/ m$^3$ s) | |
|---|---|---|---|
| | | MPM | VR bd |
| **1** | 2 | 0.0087 | 0.0068 |
| **2** | 1 | 0.0286 | 0.0239 |
| **3** | 0 | 0.0602 | 0.0547 |
| **4** | -1 | 0.0852 | 0.0813 |
| **5** | -2 | 0.0887 | 0.0847 |
| **6** | -3 | 0.0354 | 0.0306 |
| **7** | -4 | 0.0000 | 0.0000 |

Predictions at $t$ = 20 min

| Slice No. | Distance (m) | Volumetric sediment transport rate (kg/ m$^3$ s) | |
|---|---|---|---|
| | | MPM | VR bd |
| **1** | 2 | 0.0095 | 0.0077 |
| **2** | 1 | 0.0174 | 0.0143 |
| **3** | 0 | 0.0276 | 0.0234 |
| **4** | -1 | 0.0395 | 0.0346 |
| **5** | -2 | 0.0515 | 0.0462 |
| **6** | -3 | 0.0547 | 0.0496 |
| **7** | -4 | 0.0510 | 0.0457 |

Predictions at $t$ = 1 hr

**Table A11 Bedload sediment transport rates (kg/ m$^3$ s) estimated from model simulations of Test 9 using methods from MPM and Van Rijn (continues…).**

| Slice No. | Distance (m) | Volumetric sediment transport rate (kg/ m$^3$ s) | |
|---|---|---|---|
| | | **MPM** | **VR bd** |
| **1** | 2 | 0.0000 | 0.0000 |
| **2** | 1 | 0.0104 | 0.0085 |
| **3** | 0 | 0.0159 | 0.0132 |
| **4** | -1 | 0.0218 | 0.0185 |
| **5** | -2 | 0.0172 | 0.0146 |
| **6** | -3 | 0.0188 | 0.0162 |
| **7** | -4 | 0.0197 | 0.0170 |

Predictions at $t$= 2 hr

| Slice No. | Distance (m) | Volumetric sediment transport rate (kg/ m$^3$ s) | |
|---|---|---|---|
| | | **MPM** | **VR bd** |
| **1** | 2 | 0.0000 | 0.0000 |
| **2** | 1 | 0.0030 | 0.0025 |
| **3** | 0 | 0.0090 | 0.0075 |
| **4** | -1 | 0.0154 | 0.0129 |
| **5** | -2 | 0.0164 | 0.0139 |
| **6** | -3 | 0.0195 | 0.0167 |
| **7** | -4 | 0.0247 | 0.0214 |

Predictions at $t$ = 3 hr

**Table A11 Bedload sediment transport rates (kg/ m$^3$ s) estimated from model simulations of Test 9 using methods from MPM and Van Rijn.**

# Appendix 2

Derivation of the expressions for Tu and Th using Nielsen's bedload sediment transport formula and a power-law velocity profile.

$$S_{tot} = A_N \overline{U}\left(\overline{U}^2 - \overline{U}_{cr}^2\right) \tag{1}$$

$$\Phi = 12\ \theta^{1/2}\left(\theta - \theta_{cr}\right) \tag{2}$$

$$\frac{q_b}{\sqrt{g(s-1)d^3}} = 12\frac{u*}{\sqrt{g(s-1)d}}\left(\frac{u_*^2 - u_{*cr}^2}{g(s-1)d}\right) \text{ where } q_b = 12\frac{\sqrt{g(s-1)d^3}}{\left(g(s-1)d\right)^{3/2}} u_*\left(u_*^2 - u_{*cr}^2\right) =$$

$$= \frac{12}{g(s-1)} u_*\left(u_*^2 - u_{*cr}^2\right) \tag{3}$$

$$\text{We use } u_* = \frac{1}{7}\left(\frac{d}{H}\right)^{1/7}\overline{U} \text{ so, then } q_b = \frac{12}{g(s-1)}\frac{1}{7^3}\left(\frac{d}{H}\right)^{3/7}\overline{U}\left(\overline{U}_*^2 - \overline{U}_{*cr}^2\right) \tag{4}$$

$S_{\text{tot}}$ includes pore space, hence $S_{\text{tot}} = \frac{qb}{(1-\varepsilon)}$ where $\varepsilon \cong 0.4$. Therefore,

$$S_{tot} = \frac{12}{(1-\varepsilon)\ g(s-1)}\frac{1}{7^3}\left(\frac{d}{H}\right)^{3/7}\overline{U}\left(\overline{U}_*^2 - \overline{U}_{*cr}^2\right) \tag{5}$$

and $A_{\text{N}}$ in Eq. 1 is: $A_N = \frac{12}{g(s-1)(1-\varepsilon)}\frac{1}{7^3}\left(\frac{d}{H}\right)^{3/7}$ (6)

$$\frac{\partial S_{tot}}{\partial \overline{U}} = A_N\left(3\overline{U}^2 - \overline{U}_{cr}^2\right), \tag{7}$$

$$\text{so } T_u = \frac{\overline{U}}{A_N\ \overline{U}\ \left(\overline{U}^2 - \overline{U}_{cr}^2\right)} A_N\left(3\overline{U}^2 - \overline{U}_{cr}^2\right) - 1 = \frac{2\overline{U}^2}{\overline{U}^2 - \overline{U}_{cr}^2} \tag{8}$$

$$\frac{\partial S_{tot}}{\partial H} = \frac{\partial A_N}{\partial H}\overline{U}\left(\overline{U}^2 - \overline{U}_{cr}^2\right), \text{ where } \frac{\partial A_N}{\partial H} = -\frac{3}{7}\frac{A_N}{H} \tag{9}$$

$$\text{therefore } T_h = -\frac{10}{7} \tag{10}$$